The cold and dense interstellar medium of M 33

CHRISTOF BUCHBENDER

Universidad de Granada
Departamento de Física Teórica y del Cosmos

Instituto de Radioastronomía Milimétrica

Granada, Octubre 2013

Director/Supervisor: Dr. Carsten Kramer

El doctorando Christof Buchbender y el director de la tesis Dr. Carsten Kramer,

Declaran:

Garantizamos, al firmar esta tesis doctoral, que el trabajo ha sido realizado por el doctorando bajo la dirección del director de la tesis y hasta donde nuestro conocimiento alcanza, en la realización del trabajo, se han respetado los derechos de otros autores a ser citados, cuando se han utilizado sus resultados o publicaciones.

Granada, 9 de Octubre de 2013

Director de la Tesis

Fdo.:
Dr. Carsten Kramer

Doctorando

Fdo.:
Christof Buchbender

Summary

This thesis embarks on a study of the molecular line emission of HCN, HCO$^+$ and ^{12}CO in the nearby spiral SA(s)cd galaxy M 33. The goal of this thesis is to add to the understanding of these tracers of the diffuse and dense molecular gas of the interstellar medium and their dependence on environmental factors such as metallicity, optical extinction, density, far-ultraviolet field as well as the star formation rate.

Molecular tracers yield insight into the very regime where star formation happens: the cold and dense region of the interstellar medium. However, an all-encompassing theory of the dependence of molecular abundances and emission lines on the numerous physical and chemical parameters that govern the state of the interstellar medium, has yet to emerge. The correct interpretation of molecular line emission is further complicated because the physical and chemical properties vary within as well as between galaxies. The present study is motivated by a range of topical questions related to molecular emission in the field of star formation in galaxies, amongst which are: What are good tracers of the dense gas? What are good molecular tracers of star formation in galaxies? Which impact have metallicity and/or cloud parameters (optical extinction, density, FUV field strength,...) on the interpretation of molecular tracers?

To address these question the object of choice is M 33, the closest spiral galaxy after the edge-on Andromeda Galaxy. Its low inclination ($i = 56°$) and proximity ($D = 840$ kpc) yields a low line-of-sight depth through its disk and allows us to study the structure of the same as well as to resolve individual molecular cloud complexes. Furthermore, the sub-solar metallicity of M 33 – a factor of 2 lower than the solar one – offers the possibility to study the impact of metallicity onto the emission and abundance of molecular tracers. Nearby galaxies like M 33, with a low inclination, where individual molecular cloud complexes can still be resolved and the structure of the disk is observable, provide important stepping stones to relate observations in the Milky Way to observations of galaxies farther away. Therefore, conclusions drawn from M 33 are valuable information for the interpretation of observations of the interstellar medium of galaxies in general.

Note that this project is settled in the framework of the "*Herschel* open-time key program" `HerM33es`, a study of the major gas cooling lines ([C ɪɪ] [O ɪ] . . .) as well as the dust continuum emission with the *Herschel* satellite (Kramer et al., 2010). This affiliation gave access to an exhaustive complementary data set, collected by the `HerM33es`-consortium, which includes, amongst others, maps of H ɪ, ^{12}CO (2–1), Hα, the far and near ultra-violet, as well as of the dust continuum. Therefore, ancillary information about the interstellar medium in M 33 is available and environmental factors, such as the star formation rate, or the far-ultraviolet field strength can be deduced.

The data-set is used to investigate the dust-spectral energy distribution (SED) in the disk of M 33. This work has been published in Kramer, Buchbender et al. (2010) and in Xilouris et al. (2012), and is also briefly presented in this thesis. In these studies, we

used a two-component modified black-body model (MBB) of cold and warm dust to describe the dust-SED at wavelengths longer than 24 μm. Averaging the dust continuum over galacto-centric rings, we found that a a dust-emissivity exponent of $\beta = 1.5$ describes the data best at all radii. Furthermore, the temperature of the cold dust component declines with radius from 25 K in the center to about 13 K in the outskirts of M 33, while the warm dust component decreases from 77 K to 51 K.

The study of the HCN, HCO$^+$ and CO line emission in this thesis follows a two-fold approach. First, in a sample of seven giant molecular clouds with varying properties and environments the emission of the ground state transitions of HCN, HCO$^+$, ^{12}CO and ^{13}CO is observed with the IRAM[1] 30 m telescope in single pointings with a spatial resolution of ~ 115 pc. The observed GMCs are situated at galacto-centric radii of up to 4.6 kpc and cover a wide range of physical parameters. The molecular gas masses of the clouds vary by a factor of 130 between 0.1×10^5 and 13×10^5 M$_\odot$, the star formation rates traced by Hα and 24 μm emission by a factor of 50, and the total infrared luminosities by a factor more than 20. The temperatures of the cold-dust component of the GMCs lie between 19 K and 25 K. All of the clouds were identified in a systematic ^{12}CO survey of M 33 by Gratier et al. (2012), who classified four clouds as evolved clouds, i.e. showing signs of exposed and embedded star formation (Hα, FUV, 24 μm, and 8 μm emission). Two clouds only show embedded star formation (24 μm and 8 μm), while for one cloud the evolutionary stage is unclear. The data is analyzed, amongst others, using models of photon-dominated regions (PDRs) of the Meudon PDR code (Le Petit et al., 2006; Gonzalez Garcia et al., 2008). Note that a large part of the results of the analysis of this sample of GMCs has been published in Buchbender et al. (2013). In the following this sample of GMCs is referred to as "sample 1".

In a second step information on the small scale spatial distribution as well as the velocity structure of the dense gas tracers is obtained. To this end one individual giant molecular cloud from the sample was observed in HCN (1–0), HCO$^+$ (1–0) and ^{12}CO (1–0) at a high resolution of ~ 25 pc (5-7″) with the IRAM Plateau de Bure Interferometer (PdBI). The 30 m telescope was used to add information on the extended emission. The field of view of the obtained maps is about 300 pc. The velocity resolution of the HCN and HCO$^+$ data is 2 km s^{-1} the one of the ^{12}CO data is 0.5 km s^{-1}. The chosen giant molecular cloud (GMC no3) is an H II-region[2] giant molecular cloud interface region, located at 2.2 kpc galacto-centric distance in the North of M 33. It is an evolved cloud, with exposed, as well as embedded star formation as traced by Hα, 24 μm and 8 μm emission (Gratier et al., 2012). A young star cluster, (cluster number 16 in Bedin et al. (2005)) has likely formed recently from the cloud as its position coincides with the peak of Hα, 24μm, and FUV emission. The PdBI observation data reveals five-to-six "clouds" in HCN and HCO$^+$ within GMC no3, which will be referred to as "sample 2" in the following. At the time of writing, the analysis of the interferometric data is still work in progress and in only a first insight is given in this thesis.

---

[1]Instituto de Radioastronomia Milimétrica

[2]The H II-region is BCLMP 302 (Boulesteix et al., 1974).

A comparison of the HCN and HCO$^+$ lines strengths shows that the HCO$^+$ emission is on average stronger than that of HCN. The observed HCO$^+$/HCN line intensity ratios vary within the resolved giant molecular cloud GMC no3 in the range of 0.5–1.75 and for the GMCs of sample 1 between 1.1 and 2.5. Therefore, significant variations of the HCO$^+$/HCN line intensity ratio are found locally and globally along the major axis of M 33. The average ratios of the GMCs in M 33 are larger than values found for GMCs in M 31 of 0.5–1.5 (Brouillet et al., 2005), and comparable or lower than values obtained for GMCs in the Large Magellanic Cloud (LMC), where ratios up to 3.5 are observed (Chin et al., 1997, 1998). Further, the ratios in sample 1 lie at the upper end of the distribution of ratios obtained for the disks of (ultra-) luminous infrared galaxies (ULIRGs), where values as low as 0.4 are observed (Baan et al., 2010; Costagliola et al., 2011).

The HCN/CO and HCO$^+$/CO ratios of sample 1 are found to vary between 0.4 – 2.9% and 0.6 – 3.5%, respectively. Compared to ratios in GMCs of the spiral arms of M 31 (Brouillet et al., 2005), the observed range is slightly larger. In comparison, the HCN/CO and HCO$^+$/CO line intensity ratios in sample 2 are on average large in the range of 1.4–6.3% and 1.4–5.7%, respectively. The observed fraction of dense gas is higher in this sample probably because the dense gas covers a larger relative area in the smaller beam of 25 pc. Within the giant molecular cloud it is found that the dense gas fraction as traced by HCN/CO and HCO$^+$/CO increases steadily towards the young star cluster (see above), which is situated in the south in direct vicinity to the cloud. This is interpreted to indicate that the dense gas, as traced by HCN and HCO$^+$, can better resist the photo-ionizing radiation from the O/B stars of the cluster than the more diffuse gas traced by ^{12}CO, with the due change in relative filling factors of the two components. This shows that evolutionary processes affect the observed dense gas fraction.

From the emission lines of sample 1 the abundances of the molecules are estimated under the assumption of local thermodynamic equilibrium. To do so, the temperatures of the cold-dust component in the range of 19–25 K are used as an estimate for the excitation temperatures of the gas. It is found that HCN is more abundant than HCO$^+$ with [HCN]/[HCO$^+$] abundance ratios of 2–5. The derived abundances of HCO$^+$ and HCN agree with those found in the Large Magellanic Cloud within 0.5 dex. In contrast, the Orion Bar, a galactic massive star-forming region, shows significantly higher abundances of all three tracers by 0.7 dex to 1.8 dex (Omont, 2007, also for LMC). These striking differences may reflect the factor two subsolar metallicities of both the LMC and M 33.

Despite the lower abundance of HCO$^+$ in the giant molecular clouds its emission is found to be more extended than that of HCN in the PdBI-observations of GMC no3. Together with the on average stronger emission of HCO$^+$, this reflects that the critical density of the HCO$^+$ (1–0) transition ($n_{\mathrm{crit}} = 3 \times 10^4 \, \mathrm{cm}^{-3}$) is an order of magnitude lower in comparison with the one of HCN (1–0) ($n_{\mathrm{crit}} = 2 \times 10^5 \, \mathrm{cm}^{-3}$). Therefore, the HCO$^+$ (1–0) line can become stronger than HCN (1–0) for volume densities below the critical density of HCN (1–0), even if it is less abundant. For the same reason HCO$^+$ might have systematically larger area/volume filling factors. Note that a difference in area filling factor may result in a bias towards higher ratios of HCO$^+$/HCN, because a larger beam filling factor increases the antenna temperature of a radio-telescope. Here,

this effect manifests itself in a larger HCO$^+$/HCN line intensity ratio in the 30 m single pointing than in the higher resolution PdBI observations towards GMC no3. This is due to different relative area filling factors of the two molecules in the different resolution elements.

In the PdBI observation of GMC no3 the spatial extent of HCO$^+$ is found to be similar to that of ^{12}CO. The emission of HCO$^+$ is, however, more clumpy with five "condensations" (referred to as clouds in the following) on top of a more diffuse emission. In contrast, HCN does not show extended emission and is confined to six clouds, which are associated with those seen in HCO$^+$. The small clouds are not resolved with the 25 pc spatial resolution of the observations. From the average spectra of the individual clouds it is found that the lines of ^{12}CO and HCO$^+$ are well aligned in velocity and similar in line-width in the range of $\Delta v \approx 6$–10 km s^{-1}. In contrast the individual hyperfine structure components of HCN – which are partly resolved – have much smaller line widths of $\Delta v = 3$–5 km s^{-1}. The difference in line widths indicate that HCN comes from less turbulent gas than the other two tracers. This is interpreted to hint at an unresolved ensemble of clouds within the 25 pc beam. Here, a scenario is proposed in which only a sub-set of the cloud-ensemble has densities sufficiently high (i.e. $n_H > 1 \times 10^4$–1×10^5 cm^{-3}) to become luminous in the HCN (1–0) transition. The HCO$^+$ (1–0) emission in this scenario emanates in addition to these dense clouds also from clouds with lower densities ($n_H > 1 \times 10^3$). The similar line-width of HCO$^+$ and ^{12}CO shows that both molecules emit from a similar cloud ensemble with a similar velocity dispersion. This scenario is supported by observations of HCN and HCO$^+$ in individual clumps within GMCs in the LMC by Seale et al. (2012). There, it is found that only the densest, most massive, clumps emit in HCN and HCO$^+$, while much more clumps are detected only in HCO$^+$. The constraints on the densities of the different cloud ensembles in this scenario are anticipated from the results of the investigation of excitation and chemical formation conditions of HCN and HCO$^+$, which are summarized in the following paragraphs.

To investigate the effects of variations of temperature and density onto the excitation conditions of HCO$^+$ and HCN the statistical equilibrium radiative transfer code RADEX (van der Tak et al., 2007) is used. Temperature estimates for the GMCs are obtained from the cold-dust temperature of the GMCs (see above) in the range of 19–25 K; however, a larger range of temperature 10–50 K is studied to account for regions in which the dust and the gas temperature is not coupled. The RADEX results are evaluated for typical [HCN]/[HCO$^+$] abundance ratios derived for the GMCs of sample 1 in the range of ∼ 2–5. The exploited density range is 1×10^3 cm^{-3}–7×10^4 cm^{-3}, which corresponds to the mean densities that are obtained for sample 1 and sample 2 from the PDR-analysis, which is described further below. It is found for a given abundance ratio the range of dust-temperatures can not account for the observed variation of the HCO$^+$/HCN line intensity ratios between the GMCs. Further, significant variations in mean density between the clouds are unlikely to be a major influence for variations in the ratio. This is because a systematic increase in mean density should be reflected in a decrease of the HCO$^+$/HCN line intensity ratio combined with an increase of the HCN/CO line intensity ratios, which is not observed.

Nevertheless, it is difficult to disentangle the effects of variations in the excitation conditions and the abundances of the molecules because both are interleaved by their

simultaneous dependence on the numerous underlying physical parameters (metallicity, density, temperature, ...). Therefore, to get a handle onto the combined influence of the lower metallicity in M 33 as well as the optical extinction, density and FUV-field strength onto emission from HCN, HCO$^+$ and ^{12}CO, models of photon-dominated regions (Meudon PDR-code) have been employed. Two models have been constructed that reflect the sub-solar metallicity of M 33 as well as the metallicity of the solar neighborhood. A grid for both models has been calculated for volume densities $n_{\rm H}$ = 0.1, 0.5, 1, 5, 10, 50, $10^2 \times 10^4$ cm^{-3}, FUV field strengths G_0 = 10, 50, 100 in Habing units, and optical extinctions $A_{\rm v}$ = 2 – 50 mag, i.e. in steps of $\log A_{\rm v} \sim 0.2$.

Investigating the modeled grid of photon-dominated regions it was found that at low optical extinctions[3] ($A_{\rm v} \leq 5$ mag) the lower metallicity models have larger HCO$^+$ abundances, while HCN is slightly depleted with respect to the solar models. This is mainly due to the lower carbon abundance, which is the main source for free electrons. HCO$^+$ reacts strongly to the free electron abundance, because – being an ion – it is readily destroyed by dissociative recombinations. HCN, on the other hand, is formed in a recombination reaction of HCNH$^+$ at low optical extinctions and thus its formation rate is lowered if fewer electrons are present.

In general from the models it can be deduced that an HCO$^+$/HCN line intensity ratio above unity indicates that the medium, which gives rise to the line emission, has a low mean optical extinction ($A_{\rm v} \leq 5$ mag) as well as a low mean gas density ($n_{\rm H} \lesssim 5 \times 10^4$ cm^{-3}). Furthermore, the lower the FUV-field strength is, the lower also the HCO$^+$/HCN line intensity ratio for a given density and optical extinction becomes.

To compare the observations with the models, HCO$^+$/HCN and HCN/CO line intensity ratios are obtained from the models and compared to the observed ones with the method of least squares. It is found that both models – the solar and the sub-solar one – allow to reproduce the observed range of line ratios found globally in the GMCs and locally for the clouds within GMC no3. Interestingly, this suggests that changes in metallicity do not need to be invoked to describe the observed ratios. However, the best-fitting densities are larger for the sub-solar models. This reflects the larger modeled [HCO$^+$]/[HCN] abundance ratio under lower elemental abundances. The best-fit optical extinctions for both metallicity models are however comparable. The observations of sample 1 can be described by subsolar models with optical extinctions of 2–5 mag (edge-to-center). This falls into the regime of translucent clouds (e.g. Burgh et al., 2010) and is somewhat lower than typical optical extinctions found in the Milky Way of $A_{\rm v} \leq$ 8 mag (Hollenbach & Tielens, 1999). The best fitting densities are moderate $n_{\rm H} \leq 3 \times 10^4$ cm^{-3}. It is found that the optical extinction has a pronounced impact on the modeled ratios, while FUV field strength, metallicity and even density play minor roles. For the clouds within the PdBI observations yield nearly exclusively higher densities in the range of 3×10^4 cm^{-3}–7×10^4 cm^{-3} than for the GMCs in sample 1. Also on average larger optical extinction in the range of 3–9 mag for the cloud centers are found. Note that despite the fact that the HCN/CO and HCO$^+$/HCN ratios overlap between sample 1 and sample 2 their best-fitting values of the PDR-analysis differ. This is however due to the fact that sample 1 hosts largely low HCN/CO ratios in combination with large HCO$^+$/HCN ratios, while sample 2 exhibits high HCN/CO ratios

---

[3]Given here for the center of the cloud, as the models assume a 1-D slab of gas and are irradiated from two sides.

in combination with low HCO$^+$/HCN ratios. The modeled lines of HCN and HCO of the best-fitting models are found to be optically thin with optical depths $\tau \leq 0.1$.

Also the relation between the observed tracers and the star formation rate is studied. Recent findings have revealed a tight correlation between the star formation rate – as traced by the total infrared luminosity (L_{TIR}) – and the line luminosity of HCN that holds over 7-8 orders of magnitude in L_{TIR}, from galactic dense cores over normal galaxies to ultra luminous infrared galaxies ((U-)LIRGs)(e.g. Wu et al., 2010; García-Burillo et al., 2012). Motivated by these findings the relation between the total infrared luminosity and the emission of ^{12}CO, HCN and HCO$^+$ in both samples is investigated. In sample 1 the emission of HCO$^+$ shows a good correlation between the two quantities; however, not so the HCN nor the ^{12}CO emission. Further, the ratios between total infrared luminosity and the line luminosity of HCN are particular high in the GMCs of M 33 and lie in the range of $L_{\mathrm{TIR}}/L'_{\mathrm{HCN}}$=$1.3 \times 10^3$–$3.5 \times 10^3$ $L_\odot$/K km s^{-1} pc^2, which corresponds to the very high end of ratios found in massive star forming clumps of the Milky Way (Wu et al., 2010) and in LIRGs/ULIRGs (García-Burillo et al., 2012). This indicates that the HCN emission in the observed giant molecular clouds in M 33 is under-luminous with respect to the total infrared luminosity. The gas-to-dust mass ratios measured for sample 1 lie in the range of 170–290 and thus are higher than typical galactic values of 100-150 (Draine et al., 2007). A higher gas-to-dust mass might reduce the fraction of the giant molecular clouds at high optical extinctions, which is where HCN is efficiently produced and excited and thus might result in a lower HCN luminosity. Alternatively, selection effects of the sample might play a role as it includes mostly evolved giant molecular clouds (Gratier et al., 2012), i.e. clouds that show exposed star formation in Hα and FUV. These clouds might have consumed a significant amount of the dense gas traced by HCN in the star formation process. Therefore, the sample might include considerable regions traced in HCN that are not (yet) associated with star formation. This is in contrast to the objects for which the HCN–L_{TIR} correlation is found, which are massive star forming clumps and entire galaxies. Under the same conditions, however, HCO$^+$ emission proves to be related with the star formation rate of the gas. This is possibly due to the fact that it additionally traces regions with lower densities ($n_\mathrm{H} \geq 1 \times 10^3$ cm^{-3}) and/or lower optical extinctions (A_v<5 mag) than HCN. These gas reservoirs might be less affected if stars have formed from the clouds, because only the gas with densities above n_H=10^5 cm^{-3} is estimated to be the fuel for star formation (Krumholz & McKee, 2005). Further, from the PDR-analysis HCO$^+$ is found to be less sensitive to photo-ionization than HCN and thus possibly less affected by a change in extinction due to higher gas-to-dust ratios.

In the high-resolution observations in GMC no3 no relation of the total infrared luminosity with the emission of HCN and HCO$^+$ exists. This is in contrast to the good correlation found for HCO$^+$ on the larger spatial scales observed in the sample of giant molecular clouds. Therefore, at the spatial resolution of 25 pc, a break-down of this relation is observed. This indicates that at this resolution the feedback from newborn stars and the corresponding dense gas, from which they have formed, do not anymore fall into the same resolution element.

Finally, it is found that the HCO$^+$/HCN line intensity ratio is correlated with the total infrared luminosity, which is due to the good correlation of HCO$^+$ with L_{TIR}. However, one cloud – GMC 1 with the largest total infrared luminosity – deviates clearly from

this correlation because its HCO$^+$/HCN line intensity ratio of 1.1 is to low. This shows that the physical and/or chemical properties of this cloud might be different. It is argued that this behavior might be due to an influence from the ultra-luminous X-ray source M33-X8 with a luminosity of $L_X = 2.2 \times 10^{39}$ erg s^{-1} in a distance of about 110 pc from GMC 1 Weng et al. (2009). This source induces an energy input per hydrogen atom averaged over the 30 m beam of $P = F_X/n_H = 2 \times 10^{-7}$ erg cm s^{-1}. A second source, GMC no6, is found to be affiliated with the luminous and massive X-ray binary M33-X7. This source is weaker than M33-X8 with a luminosity of $L_X = 5 \times 10^{37}$ erg s^{-1}, but it is located within the GMC. Therefore, its energy input per hydrogen atom is larger with $P = 2.2 \times 10^{-5}$ erg cm s^{-1}. In comparison with models of X-ray dominated regions by Meijerink & Spaans (2005) and Meijerink et al. (2007) the parameters of the two sources fall tentatively in the regime where low HCO$^+$/HCN ratios are produced by the X-ray driven chemistry. However, the exact conditions of the clouds are not covered by these models. Further, it is likely that the chemistry in GMC 1 and GMC no6 is a mix of XDR- and PDR-chemistry due to the presence of far-ultraviolet and Hα emission in both GMCs. Therefore, an investigation of a dedicated model that includes both types of chemistries and reflects the exact properties of both sources, is pending to confirm the hypothesis of the presence of X-ray dominated regions in these two clouds.

In general the observations and analysis in this thesis add valuable information for the interpretation of HCN and HCO$^+$ as tracers of dense, star forming gas. The PDR-analysis demonstrated that the HCO$^+$/HCN line intensity ratio probes the mean density and mean optical extinction in a medium dominated by photon-dominated regions. A ratio above unity indicates a medium of low mean optical extinctions ($A_v \lesssim 5$ mag) as well as a low mean gas density ($n_H \lesssim 5 \times 10^4$ cm^{-3}) if the filling factors for both molecules are equal. HCN is found to be a robust tracer of dense gas with $n_H \geq 1 \times 10^4$–1×10^5 cm^{-3}. HCO$^+$ traces also less dense gas ($n_H \geq 1 \times 10^3$ cm^{-3}) and/or gas with lower optical extinctions ($A_v < 5$ mag). However, HCN ceases to trace star forming gas in the evolved and/or low-metallicity giant-molecular clouds observed in M 33, while HCO$^+$ might prove to be a substitute under these conditions.

This thesis is structured in four parts. Part I gives an introduction to the thesis and discusses basic physical principles of molecular physics, radiative transfer and photon-dominated regions to build the theoretical foundation of the following data-analysis. In Part II the analysis of the observation of HCN, HCO$^+$ and CO in the seven GMCs along the major axis of M 33 with the 30 m is presented. Part III concentrates on the analysis of the PdBI data obtained towards GMC no3. The last Part IV merges the insight from Part II and Part III in a discussion that focuses on the mutual influences of physical properties onto the emission characteristics of HCN and HCO$^+$. Part IV further summarizes the key conclusions of this thesis and gives a short outlook for further work.

Resumen en Español

Esta tesis profundiza en el estudio de la emisión de las líneas moleculares de HCN, HCO$^+$ y ^{12}CO en la galaxia espiral cercana de tipo SA(s)cd M 33. El objetivo de esta tesis es avanzar en el conocimiento de estos trazadores de gas molecular difuso y denso y su dependencia en factores ambientales, tales como la metalicidad, extinción óptica, densidad, campo ultravioleta lejano así como la tasa de formación estelar.

Los trazadores moleculares permiten explorar las zonas donde se produce formación estelar: las regiones frías y densas del medio interestelar. Aún no existe una teoría global acerca de la dependencia de las abundancias moleculares y las líneas de emisión con los numerosos parámetros físicos y químicos que gobiernan el estado del medio interestelar. Además de esto, la correcta interpretación de la emisión de líneas moleculares es compleja, puesto que las propiedades físicas y químicas de las regiones emisoras varían dentro de las propias galaxias, así como de una galaxia a otra. El presente estudio está motivado por un cierto número de preguntas de actualidad relacionadas con la emisión molecular en el campo de la formación estelar en galaxias entre las que se encuentran las siguientes: ¿Qué moléculas son buenos trazadores de formación estelar en galaxias? ¿Qué impacto tienen la metalicidad y/o los parámetros de las nubes (extinción óptica, densidad, intensidad del campo ultravioleta lejano) en la interpretación de los trazadores moleculares?

Para encarar estas preguntas el objeto elegido es M 33 la galaxia espiral más cercana después de la Galaxia de Andrómeda. Su baja inclinación ($i = 56°$) y proximidad ($D = 840$ kpc) dan como resultado una pequeña línea de visión a través del disco y nos permite estudiar la estructura del mismo y resolver complejos de nubes moleculares individuales. Además, la metalicidad subsolar de M 33 – un factor 2 por debajo de la metalicidad solar – ofrece la posibilidad de estudiar el impacto de una baja metalicidad en los trazadores moleculares. Las galaxias cercanas como M 33, con una baja inclinación, en las cuales se pueden resolver complejos de nubes individuales, mientras que la estructura del disco es observable, funcionan como un paso intermedio para relacionar las observaciones en la Vía Láctea con observaciones de galaxias lejanas. Por lo tanto, las conclusiones obtenidas a partir de M 33 suponen una información muy valiosa para la interpretación de observaciones del medio interestelar de galaxias en general.

Esta tesis se enmarca en el "*Herschel* open-time key program" `HerM33es`, un estudio con el satélite *Herschel* de las más importantes líneas de enfriamiento del gas ([C II] [O I] . . .) así como de la emisión continua del polvo (Kramer et al., 2010). Esto dio acceso a una base de datos complementaria exhaustiva, obtenida por el consorcio `HerM33es`, que incluye, entre otros, mapas de H I, ^{12}CO (2–1), Hα, ultravioleta lejano y cercano, asi como de emisión contínua de polvo. De esta manera, disponemos de información auxiliar acerca del medio interestelar de M 33, por lo que es posible deducir factores ambientales, tales como la tasa de formación estelar o la intensidad del campo ultravioleta lejano.

Estos datos permiten investigar la distribución espectral de energía del polvo en el disco de M 33. Este trabajo ha sido publicado en Kramer, Buchbender et al. (2010) y en Xilouris et al. (2012), y es brevemente presentado en esta tesis. En estos estudios, usamos un modelo de cuerpo negro modificado de dos componentes con diferentes temperaturas para describir la distribución espectral de energía del polvo a longitudes de ondas mayores de 24 μm. Promediando el continuo del polvo sobre anillos galactocéntricos se deduce que un exponente de emisividad del polvo de $\beta = 1{,}5$ consigue describir correctamente los datos para todos los radios. Además, la temperatura de la componente de polvo frío disminuye con el radio, desde 25 K en el centro hasta unos 13 K en la periferia de M 33, mientras que la componente templada varía desde 77 K a 51 K.

El estudio de las líneas HCN, HCO$^+$ y CO presentado en esta tesis sigue una doble estrategia. En primer lugar, se observó una muestra de siete nubes moleculares gigantes con distintas propiedades en las transiciones de base de HCN, HCO$^+$, ^{12}CO y ^{13}CO con el telescopio de 30 m de IRAM [4] en observaciones de tipo "single point" (punto único) con una resolución espacial de ~ 115 pc. Las nubes moleculares gigantes observadas están situadas en radios galactocéntricos de hasta 4.6 kpc y cubren un amplio rango de parámetros físicos. Las masas de gas molecular de las nubes varían en un factor 120 entre 0.1×10^5 y 13×10^5 M$_\odot$, las tasas de formación estelar trazadas por Hα y la emisión a 24 μm en un factor 50 y las luminosidades totales infrarrojas en un factor mayor de 20. Las temperaturas de la componente fría del polvo de las nubes moleculares gigantes se encuentran entre 19 K y 25 K. Todas las nubes fueron identificadas en un sondeo con ^{12}CO de M 33 hecho por Gratier et al. (2012), quien clasificó cuatro nubes como nubes evolucionadas, es decir, mostrando signos de formación estelar incrustada y expuesta (Hα y emisión a 24 μm y 8 μm). Dos nubes muestran únicamente formación estelar incrustada (emisión a 24 μm y 8 μm), mientras que para una de las nubes el estado evolucionario no está claro. Los datos son analizados, entre otros, utilizando modelos de regiones fotodominadas (PDRs, a partir de las siglas en inglés de "Photon Dominated Regions") del código PDR de Meudon (Le Petit et al., 2006; Gonzalez Garcia et al., 2008). Una gran parte de los resultados de los análisis de esta muestra de nubes moleculares gigantes ha sido publicado en Buchbender et al. (2013). A partir de ahora nos referiremos a esta muestra como "sample 1".

En segundo lugar, obtenemos información de la distribución espacial a pequeña escala, así como de la estructura en velocidad de los trazadores de gas denso. Para ello se observó una nube molecular gigante individual (GMC, a partir de las siglas en inglés "Giant Molecular Cloud") de la muestra en HCN (1–0), HCO$^+$ (1–0) y ^{12}CO (1–0) a una alta resolución de ~ 25 pc (5-7″) con el interferómetro del Plateau de Bure de IRAM (PdBI) así como con el telescopio de 30 m para añadir información acerca de la componente extensa. El campo de visión de los mapas es de unos 300 pc. La resolución en velocidad de los datos de HCN y HCO$^+$ es 2 km s^{-1}, mientras que la de los datos de ^{12}CO es 0.5 km s^{-1}. La nube molecular gigante elegida (GMC no3) es una interfaz entre una región H II [5] y una nube molecular gigante, situada a una distancia galactocéntrica de 2.2 kpc al norte de M 33. Es una nube evolucionada con formación

---

[4]Instituto de Radioastronomá Milimétrica

[5]La región H II es BCLMP 302 (Boulesteix et al., 1974).

estelar expuesta e incrustada, como trazan la emisión de Hα, 24 μm y 8 μm (Gratier et al., 2012). Un cúmulo estelar joven, (cúmulo número 16 en Bedin et al. (2005)) se ha formado recientemente a partir de la nube, puesto que su posición coincide con el pico de Hα, emisión a 24μm, y ultravioleta lejano. Las observaciones con el PdBI revelan entre cinco y seis "nubes" en HCN y HCO⁺ dentro de GMC no3, al que nos referiremos como "sample 2" a partir de ahora. En el momento de escribir esta tesis, el análisis de los datos interferométricos sigue en proceso, por lo que sólo daremos los primeros resultados.

Una comparación entre las intensidades de línea de HCN y HCO⁺ muestra que la emisión de HCO⁺ es en media mayor que la de HCN. La proporción entre las intensidades de línea de HCO⁺/HCN varía dentro de la GMC resuelta GMC no3 en el rango de 0.5–1.75 y para las GMCs del sample 1 entre 1.1 y 2.5. De esta manera, se encuentran variaciones locales y globales significantes a lo largo del eje mayor de M 33 del ratio de intensidades de línea de HCO⁺/HCN. Los ratios medios de las GMCs en M 33 son mayores que los valores encontrados para las GMCs en M 31 (Brouillet et al., 2005), y comparables, o menores que los valores obtenidos para las GMCs en la Gran Nube de Magallanes (LMC, a partir de las siglas en inglés "Large Magellanic Cloud"), donde se observan ratios de hasta 3.5 (Chin et al., 1997, 1998). Es más, los ratios del sample 1 se sitúan en el límite superior de la distribución de ratios obtenida para los discos de (ultra-) luminous infrared galaxies (ULIRGs), donde se observan valores tan bajos como 0.4 (Baan et al., 2010; Costagliola et al., 2011).

Los ratios de HCN/CO y HCO⁺/CO del sample 1 varían entre 0.4 − 2.9 % y 0.6 − 3.5 %, respectivamente. Comparados con los ratios en GMCs de los brazos espirales de M 31 (Brouillet et al., 2005), el rango observado es ligeramente mayor. En comparación, los ratios de HCN/CO y HCO⁺/CO en el sample 2 son, en media mayores en el rango de 1.4–6.3 % y 1.4–5.7 %, respectivamente. La fracción observada de gas denso es mayor en esta muestra probablemente porque el gas denso cubre un área relativamente mayor en el beam de 25 pc (que es más pequeño). Dentro de la nube molecular gigante se encuentra que la fracción de gas denso trazado por HCN/CO y HCO⁺/CO aumenta continuamente hacia el cúmulo estelar joven (véase arriba), que se sitúa en el Sur en la vecindad de la nube. Esto indica que el gas denso, trazado por HCN y HCO⁺, puede resistir la radiación fotoionizante de las estrellas O/B del cúmulo mejor que el gas difuso trazado por ¹²CO, con el debido cambio en filling factors relativos a los dos componentes. Esto muestra que los procesos evolutivos están afectando la fracción de gas denso observado.

A partir de las líneas de emisión de sample 1 se estiman las abundancias de las moléculas, asumiendo que se encuentran en equilibrio termodinámico local. Para ello, se utilizan las temperaturas de la componente fría del gas en el rango 19–25 K como una estimación para la temperatura de excitación del gas. Se encuentra que HCN es más abundante que HCO⁺ con ratios de abundancia de [HCN]/[HCO⁺] de 2–5. Las abundancias derivadas de HCO⁺ y HCN coinciden con ellas encontradas en la Gran nube de Magallanes en un factor 0.5 dex. En cambio, la barra de Orion, una región de formación estelar masiva, muestra abundancias de los tres trazadores significativamente altas de 0.7 dex a 1.8 dex (Omont, 2007, tambien válido para la Gran nube de Magallanes). Estas llamativas diferencias pueden estar reflejando las metalicidades en la Gran nube de Magallanes y M 33 por debajo de un factor dos de la metalicidad solar.

Pese a la menor abundancia de HCO$^+$ en los giant molecular clouds se encuentra que su emisión es más extensa que la de HCN en las observaciones del PdBI en GMC no3. Junto a la emisión de HCO$^+$ (más fuerte en media), esto refleja que la densidad crítica de la transición HCO$^+$ (1–0) ($n_{\text{crit}} = 3 \times 10^4 \, \text{cm}^{-3}$) es un orden de magnitud más baja en comparación con la de HCN (1–0) ($n_{\text{crit}} = 2 \times 10^5$, cm^{-3}). Por lo tanto, la línea de HCO$^+$ (1–0) puede volverse más fuerte que la de HCN (1–0) para densidades más bajas que la densidad crítica de HCN (1–0), incluso si es menos abundante. Por la misma razón HCO$^+$ puede tener sistemáticamente "filling factors" (factor de relleno) de área/volumen más altos. Nótese una diferencia en el filling factor del área puede conducir en un sesgo hacia mayores ratios de HCO$^+$/HCN, ya que un mayor filling factor del "beam" (haz) aumenta la temperatura de antena de un radiotelescopio. Aquí, este efecto en sí se manifiesta como un mayor ratio de intensidad de línea HCO$^+$/HCN en las observaciones de single point en el 30 m que en las observaciones de mayor resolución del PdBI de GMC no3. Esto se debe a diferentes factores de filling factor de área de las dos moléculas en los distintos elementos de resolución.

En las observaciones de GMC no3 del PdBI la extensión espacial de HCO$^+$ es similar a la de ^{12}CO. La emisión de HCO$^+$ es, en cambio, más grumosa con cinco "condensaciones" (a las que nos referiremos como nubes de aquí en adelante) sobre una emisión más difusa. En contraste, HCN no muestra emisión extendida y está confinada en seis nubes, que a su vez están asociadas a las que se ven en HCO$^+$. Las nubes pequeñas no están resueltas con la resolución de 25 pc obtenida en las observaciones. A partir de espectros medios de las nubes individuales se observa que ^{12}CO y HCO$^+$ están bien alineados en velocidad, con similares anchuras de línea en el rango de $\Delta v \approx 6$–10 km s^{-1}. En contraste las componentes de estructura hiperfina individuales de HCN – que están parcialmente resueltas – tienen anchuras de línea mucho menores de $\Delta v = 3$–5 km s^{-1}. La diferencia en las anchuras de línea indica que HCN viene de una parte del gas menos turbulenta que los otros dos trazadores. Esto se interpreta como un indicio de un conjunto no resuelto de nubes dentro del beam de 25 pc. En este trabajo se propone un escenario en el cual sólo un subgrupo del conjunto de nubes tiene densidades suficientemente altas (es decir $n_{\text{H}} > 1 \times 10^4$–$1 \times 10^5$ cm^{-3}) como para brillar en la transición HCN (1–0). En este escenario la emisión de HCO$^+$ (1–0), además de las nubes densas, procede de nubes con menor densidad ($n_{\text{H}} > 1 \times 10^3$). Los anchos de línea similares de HCO$^+$ y ^{12}CO muestran que ambas moleculas emiten a partir de un conjunto de nubes similares con velocidades de dispersión parecidas. Este escenario es respaldado por observaciones de HCN y HCO$^+$ en grumos individuales dentro de GMCs en la Gran nube de Magallanes por Seale et al. (2012). En este trabajo se encuentra que sólo los grumos más densos y masivos emiten en HCN y HCO$^+$, mientras que muchos más grumos se detectan sólo en HCO$^+$. Las restricciones a los valores de la densidad de los distintos conjuntos de nubes en este escenario están tomados a partir de los resultados de la investigación de la excitación y las condiciones de formación química de HCN y HCO$^+$, que se resumen en los siguientes párrafos.

Para investigar los efectos de las variaciones de temperatura y densidad sobre las condiciones de excitación de HCO$^+$ y HCN se u tiliza el código de transferencia radiativa en equilibrio estadístico RADEX (van der Tak et al., 2007). Se obtienen temperaturas de excitación para las nubes moleculares gigantes a partir de la temperatura de la componente fría del polvo de éstas, en el rango de 19–25 K; pese a todo, se esti-

ma que un gran rango de temperaturas de 10–50 K es factible para las regiones en las que la temperatura del gas y del polvo no están a la par. Los resultados de RADEX se evalúan para ratios de abundancia típicos de [HCN]/[HCO$^+$] derivados para las GMCs del sample 1 en el rango de ~ 2–5. El rango de densidad explotado es de $1 \times 10^3 \, \text{cm}^{-3}$–$7 \times 10^4 \, \text{cm}^{-3}$, lo que se corresponde con las densidades medias que se obtienen para sample 1 y sample 2 a partir del análisis de PDR descrito más tarde. Se encuentra que para un ratio de abundancias dado el rango de temperaturas de polvo no puede explicar la variación observada del ratio de intensidad de línea de HCO$^+$/HCN entre las GMCs. Además, no es probable que las variaciones significativas en la densidad media entre las nubes sean una influencia importante como para producir variaciones en el ratio. Esto es porque un aumento sistemático en la densidad media debería verse reflejado en una disminución del ratio de intensidad de línea HCO$^+$/HCN combinado con un aumento de los ratios de intensidad de línea de HCN/CO, lo que no se observa.

Sin embargo, es difícil separar los efectos de las variaciones en las condiciones de excitación y las abundancias de las moléculas, puesto que ambas están interrelacionadas por su dependencia simultánea en los numerosos parámetros físicos subyacentes (metalicidad, densidad, temperatura, ...). Para lidiar con la influencia combinada de la baja metalicidad de M 33 así como la extinción óptica, la densidad y la intensidad del del campo ultravioleta sobre la emisi'on de HCN, HCO$^+$ y ^{12}CO, se han empleado modelos de regiones de fotodisociación (código PDR de Meudon). Se han construido dos modelos, que reflejan la metalicidad subsolar en M 33 y la metalicidad en la vecindad solar. Se ha calculado una red para ambos modelos con densidades de $n_H = 0.1, 0.5, 1, 5, 10, 50, 10^2 \times 10^4 \, \text{cm}^{-3}$, intensidades del campo ultravioleta $G_0 = 10, 50, 100$ en unidades de Habing y extinciones ópticas de $A_v = 2 - 50 \, \text{mag}$, en pasos de $\log A_v \sim 0.2$.

Investigando la red de modelos de photon-dominated regions se encontró que a bajas extinciones ópticas[6] ($A_v \lesssim 5$ mag) los modelos de baja metalicidad tienen mayores abundancias de HCO$^+$ mientras que HCN está ligeramente depletado con respecto a los modelos solares. Esto es debido principalmente a la menor abundancia de Carbono, que es la principal fuente de electrones libres. HCO$^+$ reacciona fuertemente a la abundancia de electrones libres, puesto que –siendo un ión– es rápidamente destruido por recombinaciones disociativas. Por otro lado, HCN, se forma en una reacción de recombinación de HCNH$^+$ a baja extinción óptica y así su tasa de formación disminuye si hay menos electrones.

En general a partir de los modelos se puede deducir que un ratio de intensidades de línea de HCO$^+$/HCN alrededor de la unidad indica que el medio, que genera la emisión de la línea, tiene una baja extinción óptica media ($A_v \lesssim 5$ mag) así como una baja densidad media del gas ($n_H \lesssim 5 \times 10^4 \, \text{cm}^{-3}$). Además, cuanto más baja sea la intensidad del campo ultravioleta más bajo se vuelve el ratio de intensidades de línea HCO$^+$/HCN para una cierta densidad y extinción óptica.

Para comparar las observaciones con los modelos se obtuvieron ratios de intensidad de línea de HCO$^+$/HCN y HCN/CO a partir de los modelos y se compararon con los observados mediante el método de mínimos cuadrados. Se observa que ambos modelos –el solar y el subsolar– permiten reproducir el rango de ratios de líneas encontrados globalmente en las GMCs y localmente para las nubes dentro de GMC no3. Esto su-

---

[6]Dadas aquí para el centro de la nube, ya que los modelos asumen una capa de gas 1-D y están irradiados por ambos lados.

giere que no es necesario invocar cambios en la metalicidad para describir los ratios observados. Pese a todo, las densidades que mejor ajustan los datos son mayores para los modelos subsolares. Esto refleja el mayor ratio de abundancias [HCO$^+$]/[HCN] modelado con abundancias elementales. Las extinciones ópticas que mejor ajustan los datos para ambos modelos de metalicidad son pese a todo comparables. Las observaciones de sample 1 se pueden describir por modelos subsolares con extinciones ópticas de 2–5 mag (del borde al centro). Estas características son típicas del regimen de nubes translucientes (e.g. Burgh et al., 2010) y son algo menores que las extinciones ópticas típicas encontradas en la Vía Láctea de $A_v \leq 8$ mag (Hollenbach & Tielens, 1999). Las densidades que mejor ajustan las observaciones son moderadas $n_H \leq 3 \times 10^4$ cm^{-3}. Se observa que la extinción óptica tiene un pronunciado impacto en los ratios modelados, mientras que la intensidad del campo ultravioleta, la metalicidad y la densidad juegan un papel menor. Para las nubes observadas con el PdBI se encuentran casi exclusivamente mayores densidades en el rango de 3×10^4 cm^{-3}–7×10^4 cm^{-3} que para las GMCs de sample 1. También se encuentran mayores extinciones ópticas en media, en el rango de 3–9 mag (del borde al centro). Nótese que a pesar del hecho de que los ratios de HCN/CO y HCO$^+$/HCN se solapen entre sample 1 y sample 2 sus mejores valores de ajuste en el análisis de PDR difieren. Esto se debe al hecho de que sample 1 alberga ratios de HCN/CO altamente bajos en combinación con grandes ratios de HCO$^+$/HCN, mientras que sample 2 muestra altos ratios de HCN/CO en combinación con bajos ratios de HCO$^+$/HCN. Las líneas modelizadas de HCN y HCO de los modelos que mejor se ajustan a los datos son ópticamente delgadas con profundidades ópticas de $\tau \leq 0.1$.

También se estudia en esta tesis la relación entre los trazadores observados y la tasa de formación estelar. Recientes estudios han revelado una estrecha correlación entre la tasa de formación estelar –trazada por la luminosidad infrarroja total (L_{TIR}) – y la luminosidad de la línea de HCN que se mantiene alrededor de 7-8 órdenes de magnitud en L_{TIR}, desde núcleos galácticos densos de galaxias normales hasta galaxias infrarrojas ultraluminosas ((U-)LIRGs)(e.g. Wu et al., 2010; García-Burillo et al., 2012). Debido a estos hallazgos se investiga la relación entre la luminosidad infrarroja total y la emisión de ^{12}CO, HCN y HCO$^+$ en ambas muestras. En sample 1 la emisión de HCO$^+$ muestra una buena correlación entre las dos cantidades; pese a ello, no ocurre lo mismo con la emisión de HCN ni con la de ^{12}CO. Además los ratios entre la luminosidad total infrarroja y la luminosidad de la línea de HCN son particularmente altos en las GMCs de M 33 y se mueven en el rango de $L_{TIR}/L'_{HCN}=1.3 \times 10^3$–$3.5 \times 10^3$ $L_\odot$/K km s^{-1} pc^2, lo que corresponde al límite máximo de los ratios encontrados en regiones de formación estelar de la Vía Láctea (Wu et al., 2010) y en LIRGs/ULIRGs (García-Burillo et al., 2012). Esto indica que la emisión de HCN en las nubes moleculares gigantes observadas en M 33 es subluminosa con respecto a la luminosidad infrarroja total. Los ratios de masa entre gas y polvo medidos para sample 1 caen en el rango de 170–290 y por lo tanto son mayores que los valores galácticos típicos de 100–150 (Draine et al., 2007). Un ratio gas-polvo mayor puede reducir la fracción de los giant molecular clouds a altas extinciones ópticas, que es donde el HCN se produce y excita eficientemente, lo que puede conducir a a una luminosidad de HCN más baja. Alternativamente, efectos de selección de la muestra pueden influir puesto que incluye principalmente giant molecular clouds evolucionados (Gratier et al., 2012), es decir, nubes que presentan formación

estelar expuesta en Hα y ulravioleta lejano. Estas nubes pueden haber consumido una parte significativa del gas denso trazado por HCN en el proceso de formación estelar. Por lo tanto, la muestra puede incluir regiones considerables trazadas en HCN que no están asociadas (todavía) con procesos de formación estelar. Esto está en contraste con los objetos para los que se encuentra la correlación HCN–L_{TIR} que son regiones de formación estelar masivas y galaxis enteras. Aun así bajo estas condiciones la emisión de HCO$^+$ aún prueba estar relacionada con la tasa de formación estelar del gas. Esto se debe probablemente al hecho que adicionalmente traza regiones con menores densidades ($n_H > 1 \times 10^3$ cm^{-3}) y/o extinciones ópticas más bajas ($A_v < 5$ mag) que HCN. Estos depósitos de gas pueden ser les afectadas si estrellas se hayan formado a partir de las nubes, porque se estima que sólo el gas con densidades por encima de $n_H = 10^5$ cm^{-3} es capaz de alimentar el proceso de formación estelar (Krumholz & McKee, 2005). Además, a partir del análisis de los modelos de PDR se encuentra que HCO$^+$ es menos sensible a la fotoionización que HCN, con lo que posiblemente se ve menos afectado por un cambio en la extinción debido a mayores ratios gas-polvo.

En las observaciones a alta resolución en GMC no3 no existe ninguna relación de la luminosidad infrarroja total con la emisión de HCN y HCO$^+$. Esto contrasta con la buena correlación encontrada para HCO$^+$ en las grandes escalas espaciales observadas en la muestra de nubes moleculares gigantes. Así, a la resolución espacial de 25 pc se observa una descomposición de esta relación. Esto indica que a esta resolución la emisión de las estrellas recién formado y el gas denso correspondiente a partir del que se han formado no están incluido en el mismo elemento de resolución.

Finalmente se encuentra que el ratio de intensidad de líneas HCO$^+$/HCN está correlado con la luminosidad infrarroja total, lo que se debe a la buena correlación de HCO$^+$ con L_{TIR}. Pese a todo, una nube – GMC 1 con la mayor luminosidad infrarroja total – se desvía claramente de esta correlación porque su ratio de intensidad de líneas HCO$^+$/HCN es demasiado bajo. Esto muestra que las propiedades físicas y/o químicas pueden ser diferentes. El argumento es que este comportamiento puede ser debido a una influencia de la fuente de rayos X ultraluminosa M33-X8 con una luminosidad de $L_X = 2.2 \times 10^{39}$ erg s^{-1} en una distancia de alrededor de 110 pc desde GMC 1 (Weng et al., 2009). Esta nube induce un aporte de energía por átomo de Hidrógeno promediado sobre el beam del 30 m de $P = F_X/n_H = 2 \times 10^{-7}$ erg cm s^{-1}; asumiendo una densidad media de 1×10^4 cm^{-3} como la derivada a partir de los modelos de PDR para GMC 1. Una segunda fuente, GMC no6, está asociada con la binaria de rayos X luminosa y masiva M33-X7. Esta fuente es más débil que M33-X8 con una luminosidad de $L_X = 5 \times 10^{37}$ erg s^{-1} pero se encuentra situada dentro de la GMC. Por lo tanto, su aporte de energía por átomo de Hidrógeno es mayor $P = 2.2 \times 10^{-5}$ erg cm s^{-1} para la densidad media derivada para los modelos de PDR de 6×10^3 cm^{-3}. En comparación con los modelos de regiones dominadas por rayos X de Meijerink & Spaans (2005) y Meijerink et al. (2007) los parámetros de las dos fuentes caen tentativamente en el régimen donde se producen bajos ratios de HCO$^+$/HCN por la química conducida por rayos X. Pese a todo, las condiciones exactas de las nubes no están cubiertas por estos modelos. Así, es probable que la química en GMC 1 y GMC no6 sea una mezcla de químicas de PDR y XDR debido a la presencia del ultravioleta lejano y emisión Hα en ambas GMCs. Por lo tanto, queda pendiente hacer una investigación de un modelo específico que incluya ambos tipos de químicas y refleje las propiedades exactas de

ambas fuentes, para confirmar la hipótesis de regiones dominadas por los rayos X en estas dos nubes.

Globalmente las observaciones y el análisis de esta tesis añaden una información valiosa para la interpretación de HCN y HCO$^+$ como trazadores de gas denso, relacionado con la formación estelar. El análisis de los modelos de PDR demuestra que el ratio de intensidad de líneas de HCO$^+$/HCN explica la densidad y extinción óptica medias en un medio dominado por regiones de fotodisociación. Un ratio por encima de la unidad indica un medio de baja extinción óptica media ($A_v \lesssim 5$ mag) así como una baja densidad media del gas ($n_H \lesssim 5 \times 10^4$ cm^{-3}), si los "filling factors" para ambas moléculas son iguales. Se encuentra que HCN es un trazador robusto de gas denso con $n_H \geq 1 \times 10^4 - 1 \times 10^5$ cm^{-3}. HCO$^+$ traza también gas menos denso ($n_H \geq 1 \times 10^3$ cm^{-3}) y/o gas con menores extinciones ópticas ($A_v < 5$ mag). Pese a todo, HCN deja de trazar gas de formación estelar en las nubes moleculares gigantes evolucionadas y/o de baja metalicidad observadas en M 33, mientras que HCO$^+$ puede probar a ser un sustituto en esas condiciones.

Esta tesis está estructurada en cuatro partes. Part I introduce la tesis y discute principios básicos de física molecular, transferencia radiativa y regiones fotodominadas para construir los fundamentos teóricos del posterior análisis de datos. En Part II se presenta el análisis de las observaciones de HCN, HCO$^+$ y CO en las siete GMCs a lo largo del eje mayor de M 33 con el 30 m. Part III se concentra en el análisis de los datos del PdBI obtenidos para GMC no3. La última parte IV combina el conocimiento de Part II y Part III en una discusión que pone el foco en las influencias físicas mutuas de las propiedades físicas sobre las características de emisión de HCN y HCO$^+$. Por último, Part IV resume las conclusiones clave de esta tesis y propone las bases del trabajo futuro.

Contents

Part I.

Introduction and basic physical principles

Chapter 1.

Introduction

This thesis comprises a multi-wavelength study of the cold and dense phase of the interstellar medium (ISM) in the nearby spiral galaxy M 33. The study is performed with the aim to characterize the emission of the tracer molecules HCN, HCO$^+$ and CO with respect to the physical and chemical conditions within their host environments. Specific topical astronomical questions that this thesis aims to address are listed below after a general motivation of the study.

The existence of the Interstellar Medium (ISM) has been accepted globally by the astronomical community mere 80 years ago in the 1930s. Since then astronomy has come a long way in understanding the nature of the ISM and its decisive role in star- and galaxy-formation as well as their evolution. Nevertheless, many aspects remain poorly understood. For instance, while the formation of single stars over small scales has been put on a good observational and theoretical basis (Shu et al., 1987; McKee & Ostriker, 2007), large scale star formation (SF), averaged over ensembles of molecular clouds (MCs), and eventually entire galaxies, lacks a thorough physically based characterization (Genzel et al., 2010; Kennicutt & Evans, 2012).

The knowledge of star formation on large scales is mainly based on scaling relations. This information is continuously refined due to the continuously increasingly extensive multi-wavelength data-sets of dust, gas, and star formation tracers in nearby galaxies, which are, amongst others, obtained in surveys of: ^{12}CO (2–1) (HERACLES Leroy et al. (2009)), H I (THINGS Walter et al. (2008)), far-infrared continuum and line emission (SINGS and KINGFISH Kennicutt et al. (2003, 2011), and far- and near-ultraviolet emission (NGS Gil de Paz et al. (2007). Together, these data allow a general study of the relation of star formation to the underlying gas and dust content of the ISM (see e.g Leroy et al., 2013). Nevertheless, the existence of an universal star formation law, valid between different galaxy populations, is still a matter of debate. However, recent findings of good correlations between dense gas traced by HCN and the star formation rate (SFR) over a wide range of objects – from Milky Way giant molecular clouds (GMCs) to (ultra-)luminous infrared galaxies ((U-)LIRGs) – promise deeper insight into large scale star formation (e.g. Wu et al., 2010; García-Burillo et al., 2012).

A thorough understanding of the dynamics of large scale star formation and the related feedback processes is crucial to develop a self-contained theory of galaxy formation and evolution (Kennicutt & Evans, 2012). Star formation occurs within molecular clouds – in the cold and dense phase of the ISM. These regions are marked out by molecular lines as well as millimeter dust emission which makes these types of radiation indispensable diagnostic tools to advance the understanding of SF on all spatial scales. Nowadays over 170 molecules are known to exist in the interstellar medium

or circumstellar shells (CDMS Müller et al., 2001, 2005). In external galaxies, however, so far only a subset of these molecules has been detected, due to the often low abundances of the molecules and large distances to the galaxies. Nevertheless, a few molecules can be seen even in sources with high red-shifts, among these, the most prominent is ^{12}CO; however HCN, HCO$^+$, and CN (amongst others) are detectable as well[1]. This renders these very molecular species important tracers to study and compare the gaseous content and its relation with star formation over a large range of objects from the Milky Way to high-z galaxies.

One key requisite to use these tracers as genuine diagnostic tools and eventually employ them to improve the understanding of (large-scale) star formation, is the ability to correctly interpret their emission characteristics. However, the physical conditions in the ISM are diverse and vary inside galaxies as well as between galaxies. This renders the correct interpretation of emission non-trivial and a complete scheme of the dependence of molecular abundances and emission lines on the numerous of physical parameters, governing the state of the ISM, has yet to emerge. Metallicity, temperature, pressure, dust composition, density, column density and the interstellar radiation field (ISRF) are but a few examples of parameters that vary from molecular cloud to molecular cloud and in between galaxies. Furthermore, observational limitations impose additional complications. Naturally, telescopes do not have an infinitely high resolution with the consequence that the farther away an object is, the more emitting material falls into the spatial resolution element, which eventually may include multiple molecular clouds and even entire galaxies. Thus, a variety of largely different environments are averaged in the observations. The information encoded in such data are but the collective effects of a more or less large variety of processes. All in all, one has to be cautious not to over-simplify the interpretation of a specific tracer and assume that it behaves in the same way, if it is observed with different spatial resolutions or in different sources.

The "danger" of mixing multiple environments in one spatial resolution element is less severe for observations within our Milky Way[2]. Here, small scale structure can more easily be observed, and detailed case studies of individual regions are possible. On the other hand, observations in the Milky Way often have large line-of-sights making it difficult to disentangle information from different objects along the line-of-sight. Subsequently, it is difficult to deduce accurate distances and obtain a large-scale view. Astronomical research on star formation has been mainly divided into two distinct communities: a galactic and an extra-galactic one. Nevertheless, it is acknowledged that a combination of results from both communities is mandatory for further advances towards understanding large-scale star formation (Kennicutt & Evans, 2012). For this purpose, nearby galaxies like M 33 with a low inclination, where individual molecular cloud-complexes can still be resolved while the structure of the disk is observable, provide important stepping stones between the two realms of investigation.

In the following a selection of topical questions related to the field of star formation in galaxies, that this thesis hopes to address in one or another way, are raised:

1. **What are good tracers of the dense gas?** Dense gas is the fuel for star formation. Therefore, reliable tracers are needed to characterize its properties. A range

---

[1]For example in the Cloverleaf Quasar at $z = 2.56$ (Barvainis et al., 1997; Riechers et al., 2011).
[2]The Milky Way is also often referred to as the "Galaxy".

of molecular transition are considered to be dense gas tracers due to their high critical densities. However, the abundance and line emission of each molecule react differently to environmental conditions (metallicity, ISRF, X-rays, . . .) and a possible quantitative conversion factor between line intensity and dense gas column density, similar to the X_{CO} factor, is subject to these changes in environment (Graciá-Carpio et al., 2006, 2008a).

How do the different tracers of dense gas compare to each other?
Do they have the same spatial distribution?
Under which conditions do they trace dense gas reliably?

2. **What are good molecular tracers of star formation in galaxies?** The Schmidt-Kennicutt law (Schmidt, 1959; Kennicutt, 1998) shows that the gas mass surface density, determined from H I and ^{12}CO emission, is linearly related with the star formation surface density, while newer work shows that CO is far better correlated with SF than H I (Leroy et al., 2008, 2013). A series of recent papers[3] discusses a much tighter linear[4] correlation found between HCN (and partly HCO^{+}) and the SFR. This correlation seems to hold from galactic GMCs over centers of nearby galaxies to (ultra-)luminous galaxies (LIRGs/ULIRGs) and proposes a constant star formation efficiency of the dense gas in all these objects. A picture that is however complicated by other findings (see e.g. Graciá-Carpio et al., 2006; Costagliola et al., 2011; Rosolowsky et al., 2011).

What is the underlying physical reason for these correlations?
What about other tracers of dense gas to study the star formation efficiency?
What happens on local scales?

3. **Which impact has metallicity on the molecular tracers?** Elemental depletion in low-metallicity environments may have a strong effect on the abundance of molecules. This is due to the subsequent lower dust content that allows the energetic photons to penetrate deeper into the cloud and thus photo-dissociate more molecules. Further, the chemical formation/destruction rates of the molecules are different due to changes of the elemental abundances.

4. **How do cloud parameters control the properties of molecule emission?** Metallicity is not the only agent that determines the abundance and emission characteristics of molecules, which are controlled by a range of parameters, such as visual extinction, density, interstellar radiation field, ... With respect to this models of photon-dominated regions (PDRs) are pivotal tools to shed light on the processes within the ISM.

5. **Does the HCO^{+}/HCN line intensity ratio indicate the prevalent type of chemistry (XDR/PDR)? Is the HCN/CO line intensity ratio a tracer of the dense gas fraction?**
How does the interpretation of line intensity ratios depend on the environment?

---

[3]Gao & Solomon (2004a,b); Wu et al. (2005); Gao et al. (2007); Baan et al. (2008); Graciá-Carpio et al. (2008a); Wu et al. (2010); García-Burillo et al. (2012); Liu & Gao (2012)
[4]and maybe bimodal (see e.g. García-Burillo et al., 2012)

With these questions in mind this thesis embarks on an in-depth study of Carbon Monoxide (CO), Formylium (HCO$^+$) and Hydrogen Cyanide (HCN) in the nearby local group spiral galaxy M 33.

M 33 is – due to it's proximity and low inclination – ideally suited to investigate the behavior of molecular tracers over size scales of giant molecular clouds ($\approx 100\,$pc) and individual clouds therein ($\lesssim 25\,$pc) throughout its disk, with present-day instrumentation. It is the closest spiral galaxy after the edge-on Andromeda Galaxy (M 31) and seen at a moderate inclination, which yields a low line-of-site depth through the disk and allows us to study the structure of its disk and to resolve individual molecular cloud complexes.

One goal of this thesis is to characterize the observed tracers over different spatial scales and link their global behavior within the disk to local variations that occur in an individual GMC. To this end the strategy of this thesis is two-fold:

- First, in Part II, a sample of GMCs, observed in HCN, HCO$^+$ and CO at 115 pc spatial resolution, is investigated to characterize the properties of HCN and HCO$^+$ along the major axis of M 33. The sample has been chosen to cover different galacto-centric radii and a wide range of cloud properties (cloud mass, SFR, infrared luminosities as well as dust content). In detail this part investigates:

  - the behavior of the dust spectral energy distribution (SED) within the disk of M 33 and the sample of observed GMCs in Chapter 6.

  - the relation between the molecular emission and the SFR in M 33 in Chapter 7.

  - a range of line intensity ratios (in particular the I_{HCO^+}/I_{HCN}) and their relation to each other to test their use as "diagnostic tools" for conditions in the ISM (Chapter 8).

  - the influence of metallicity and other cloud parameters onto the line emission by means of models of photon-dominated regions that have been tailored to reflect the metallicity of M 33 (Chapter 9).

- Second, in Part III, high-resolution images of ^{12}CO, HCN, and HCO$^+$ resolving one GMC from the above sample with $\sim 25\,$pc resolution are analyzed. These observations add information onto the spatial as well as velocity structure of the molecular tracers. The analysis investigates:

  - the spatial distribution of the different molecules and their line ratios (Section 11.3).

  - the velocity structure of the HCO$^+$ and ^{12}CO line emission (Section 11.3).

  - the morphological relation between the observed molecules and complementary data at high resolution including dust, Hα, [C II] H I and FUV emission as well as an optical image at 5300 Å (Section 11.4).

  - the spectra of the molecular line emission at individual HCN peaks (Chapter 12).

  - the variation of the I_{HCO^+}/I_{HCN} as well as HCN/CO and HCO$^+$/CO ratios over small scales within the GMC (Sections 12.3 and 12.4).

– the effect of metallicity and cloud parameters onto the line emission within this GMCs (Section 12.5).

The insights of both parts are merged in a concluding discussion (Chapter 14) with the aims to develop an understanding for the dependence of the HCN and HCO$^+$ emission on physical and chemical parameters and to characterize the HCN, HCO$^+$, and ^{12}CO emitting gas in M 33.

This thesis was performed in the framework of the Herschel Open-time key program `HerM33es` (Kramer et al., 2010), a study of the major gas cooling lines [CII] 158 μm, [OI] 63 μm, [N ɪɪ], as well as the dust continuum emission in M 33 with a large consortium, which collected a wide range of complementary data of M 33. The access to this extensive multi-wavelength data set allows for an in-depth investigation of the properties of the molecular, atomic and ionized ISM in M 33.

Chapter 2.

The interstellar medium, galaxies, and M 33

2.1. A short introduction to the interstellar medium

In most galaxies the interstellar medium only contains a fraction of the total mass. For example in our galaxy, the Milky Way (MW), most of the visible baryons are locked away in stars and stellar remnants and only 10% of the visible baryons are found in the interstellar medium (Draine, 2011). In spite of this, the ISM is of immense importance for galaxies. It is the cold gas and dust of the ISM where and from which stars form. Old generations of stars re-inject processed matter trough supernovae and stellar winds, which in turn enrich the ISM with "heavy elements"[1]. These energetic events govern the structure of the ISM and trigger new sites of SF through shock-waves and subsequent compression of the interstellar clouds. New – more metal-rich – stars are born from the remainders of old generations of stars and thus the life cycle of matter in galaxies closes. This recycling of matter is driving the evolution of galaxies and constantly changes their emission characteristics as well as physical properties (Tielens, 2005).

A variety of objects belong to the ISM. Among these are H II-regions, reflection nebulae, supernova remnants, dark clouds and photo-dissociation regions. These objects are made up of a variety of particles: ionized and neutral atomic gas, molecular gas as well as dust, but also energetic cosmic rays, magnetic fields and the interstellar radiation field belong to the ISM (Tielens, 2005; Draine, 2011).

The interstellar baryons, i.e. the gas and dust particles of the ISM, are found in a variety of temperatures and densities that in general make up certain "phases" where the temperatures and densities are in specific ranges. The temperature in the different phases range from the so called hot ionized medium (HIM) or "coronal gas" heated by shocks from supernova explosion with temperatures of $T \geq 10^{5.5}$ K to the gravitationally bound dense molecular clouds with densities of $n_{\mathrm{H}} \geq 10^3 \mathrm{cm}^{-3}$ and very low temperatures of $T = 10 - 50$ K. Between these two extreme phases the warm ionized medium (WIM) exists, which is found e.g. in H II-regions. The latter are named after the ionized hydrogen atoms they host, which are ionized by ultraviolet photons from hot massive O-type stars. Further, there is the neutral medium that makes up two phases, the warm and cool atomic gas, were warm and cold refers to temperatures of

---

[1]Heavy elements refers to all elements heavier than Helium.

(a)   **(b)**
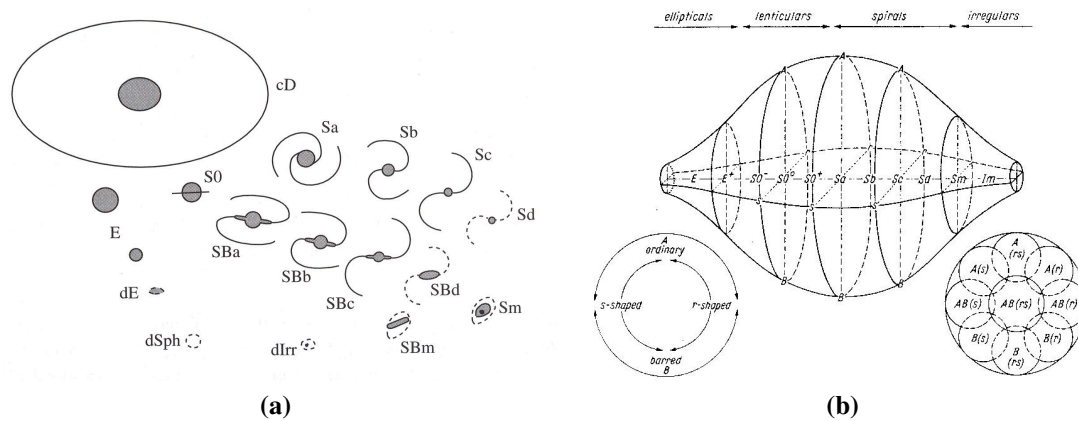
Figure 2.1.: Galaxy Classification: *a)* A modified form of the Hubble scheme with an overview of the morphological types (Sparke & Gallagher, 2000); *b)* The "classification volume" from de Vaucouleurs (1959).

around 6000 K and 100 K, respectively (Draine, 2011). The atomic gas consists mainly of HI. However molecular gas is also found in diffuse clouds (e.g. Liszt et al., 2010).

The stars themselves form in the densest regions of the ISM, the cold molecular clouds that can have diameters on a size scale of up to ~ 100–$200\,\mathrm{pc}$ and are often gravitationally bound (Blitz, 1993; Murray, 2011). Molecular clouds do not collapse entirely under the gravitation, but individual regions of high optical extinction or mass surface density form in which the actual star-formation occurs. As a consequence star formation is not distributed smoothly over molecular clouds. The dense star forming regions are commonly divided by size into two types. The bigger "Clumps" may form entire clusters of stars and high-mass stars, while "Cores" may produce individual stars or few multiple systems of stars. In nearby galaxies most of the mass is actually in regions with lower extinctions (Kennicutt & Evans, 2012).

Dust plays a crucial role in star formation and processes in the ISM although it makes up only $\sim 1\%$ of the mass of the ISM. The dust absorbs at least 30% of star-light emitted in the Universe and re-emits it in the infrared (Draine, 2003). The actual amount absorbed in individual sources can vary from about 10% in metal-poor dwarf-galaxies to up to more than 99% in circumnuclear regions in infrared-luminous galaxies (Kennicutt, 2008). The attenuation of the radiation field by the dust allows molecular clouds to become sufficiently cool to be gravitationally bound. Also dust is needed to build up the bulk mass of the molecular material because it acts as a catalyst in the formation of H_2 – the most prominent molecular species (cf. also Section 4.4.4) – that does not form efficiently in the gas phase.

2.2. Morphology of galaxies and the Local Group of galaxies

Galaxies exist in different shapes, sizes, masses, luminosities, and evolutionary stages. Fig. 2.1a gives and morphological overview. Although different classification schemes

and approaches exist, mainly two are used: the "Hubble Sequence" (Hubble, 1926; Sandage, 1975) and the "de Vaucouleur classification" de Vaucouleurs (1959)[2]. Both are based on the pure morphology of the galaxies at optical wavelengths; however, the Hubble scheme orders the galaxies along a sequence, while de Vaucouleurs (1959) uses a "classification volume"; shown in Fig. 2.1b. The latter allows "smooth" transitions between the different galaxy classifications and will used in the following. In both classifications schemes galaxies are divided into four morphological groups: the elliptical (E), lenticular (S0), spiral (S) and irregular (Irr) galaxies. Galaxies that belong to one of the groups, but are smaller than the archetype-galaxies that define the groups, are called dwarf galaxies[3].

Within each group further morphological distinctions are made. Here, however, only the spiral structure is discussed. Spirals come in two groups: those that have a bar (SB) and those that do not (SA). Each group is further distinguished by the compactness of their spiral arms which is denoted by the letters **a-d** where **a** being the most compact and **d** the loosest configuration.[4] Further, spiral galaxies may have ring structure which is denoted with with an **r**. In absence of a ring the letter **s** is used. Galaxies come in intermediate states between these classifications and combinations of letters of the two adjacent states are used[5]. As such SAB denotes a galaxies with a bar of medium strength, or **rs** a so called "pseudo-ring". To give an example, M 33 is classified as SA(s)cd and therefore a bar- and ring-less spiral galaxy with a loose to very loose configuration of its spiral arms.

Galaxies are however not statically frozen in their morphology, but are ever changing systems, driven by the violent effects of star formation, supernova explosions and interaction with their neighboring galaxies. As a consequence galaxies do evolve, while they use up their gas reservoirs to form stars and merge with other galaxies. Eventually, a galaxy may turn from one morphological form into another. Elliptical galaxies are thought to be the evolutionary end-points of this process. The reason is that ellipticals comprise mainly old stellar populations where most, if not all, of the gas has been exhausted by star formation.

2.2.1. The Local Group

Nearby galaxies where individual GMC complexes can still be resolved with nowadays instrumentation are ideal laboratories for the detailed investigation of star formation and the ISM over galactic scales. The closest neighbors to our Galaxy are the members of the "Local Group" (LG) of galaxies, cf. Fig. 2.2 for a 3-D representation of the Local Group. The Local Group is a small group of galaxies that contains about 54 galaxies; a number that is not final because the sample of more distant faint local group members

---

[2]Which is actually a revision and extension of the Hubble sequence.

[3]Dwarf galaxies are the most common form in the present day universe and were probably even more common at past epochs. Dwarf galaxies are much fainter and more difficult to detect than "normal" galaxies and most dwarf galaxies have been detected only in the local group (Mateo, 1998). Which is why most group-defining galaxies are large and bright galaxies.

[4]The Large Magellanic Cloud is the archetype of an additional group of small galaxies that show some spiral structure. Such galaxies have an extra status and their morphology is denoted by the letter **m**.

[5]To stress that the galaxy is closer to one state than the other one may underline the more prominent feature.
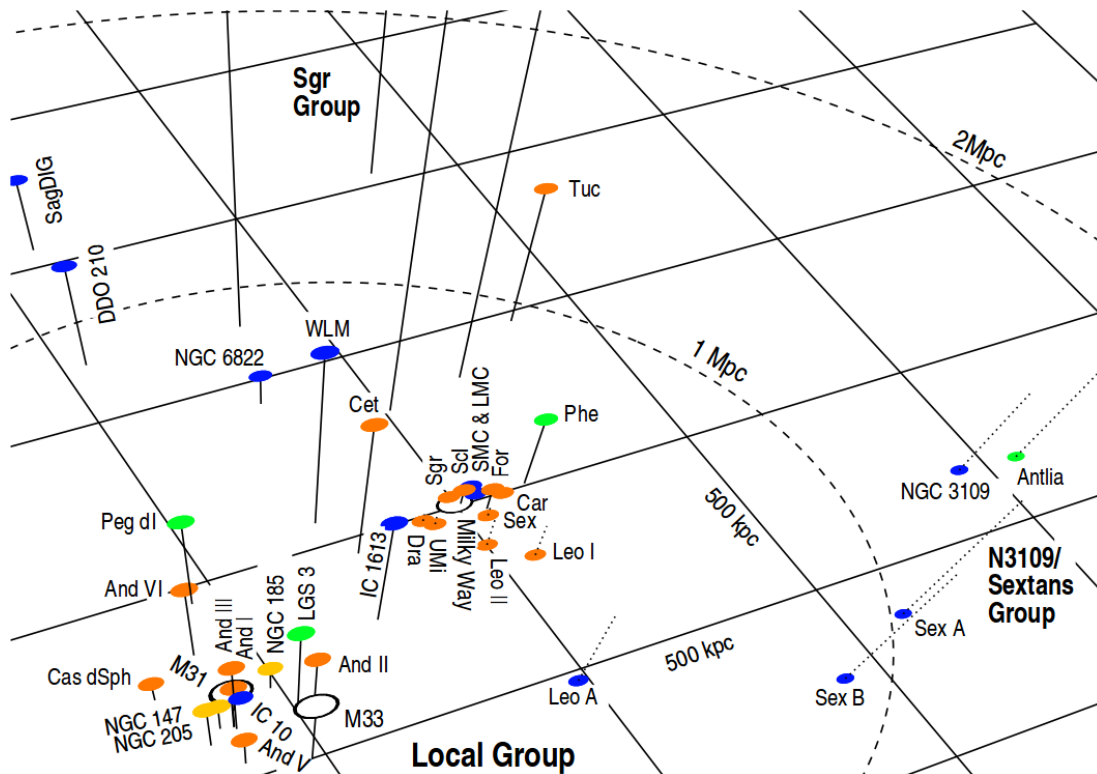
Figure 2.2.: The Local Group in a 3-D representation. The distances of the galaxies to the arbitrarily chosen plane are indicated by *solid lines* if they are above the plane and *dotted lines* if they are below. The *dashed ellipsoids* mark the distance to the assumed barycenter of the LG at $462 \, \mathrm{kpc}^{-2}$ distance from the MW. Note the binary structure of the local group centered on the grand-design spirals M 31 and the MW. (Grebel, 2001).

is still incomplete (van den Bergh, 2000). Such groups are common in the universe and the majority of nearby galaxies can be found in groups or clusters that resemble the Local Group (van den Bergh, 2000). Most of the major types of galaxies, with exception of giant ellipticals, are present in the Local Group. Its most prominent and luminous members are the Milky Way, the early-type[6] spiral galaxy Andromeda (M31) and the smaller and less-luminous late-type spiral M 33. M 33 is introduced in detail in the next section. Together these three spiral galaxies account for 90% of the total luminosity of the local group (Sparke & Gallagher, 2000). The other members of the local group galaxies are (dwarf-)irregular galaxies as well as dwarf-elliptical and dwarf-spheroidal galaxies.

Substructure exists in the Local Group. It resembles a binary system with two sub-groups centered on its two grand-design spirals: the Andromeda galaxy (M31) and the Milky Way (van den Bergh, 2003). Our source of interest in this thesis, M 33, belongs to the M 31 subgroup together with a range of dwarf galaxies. However not all galaxies are bound to either of these galaxies such that free flying galaxies exist.

Within the sub-group of the Milky Way, the Magellanic clouds – although not the nearest to us – are the most luminous and prominent members, apart from the MW.

---

[6]One speaks of late and early galaxy types with respect to the place of a galaxy on the Hubble sequence. This term does reflect an evolutionary state.
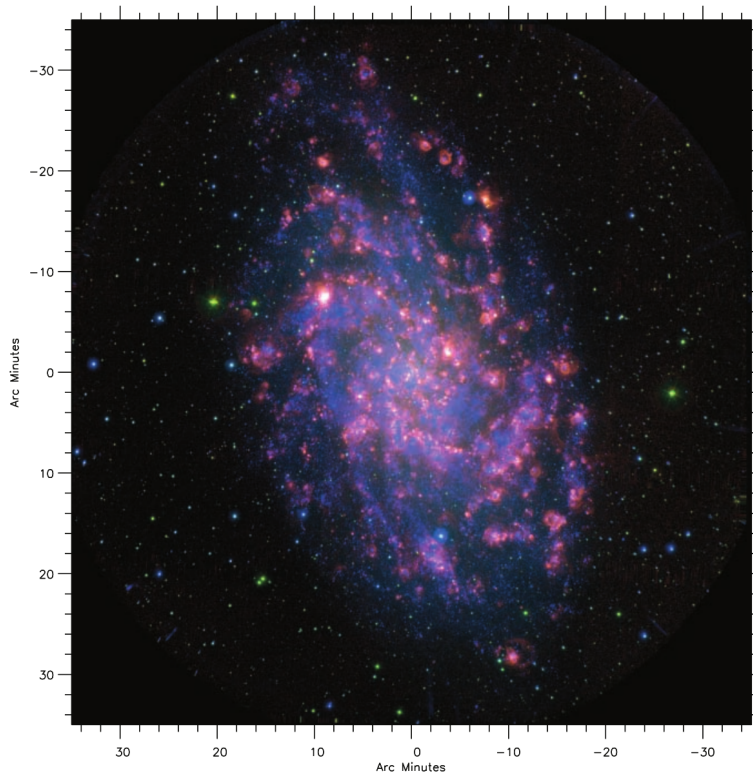
Figure 2.3.: A Multi-wavelength composite view of M 33 with a FOV of 11.4 kpc width. The colors in the image show: Hα + continuum (*red*), continuum (*green*), *GALEX* NUV (*blue*). (Thilker et al., 2005).

They have a substantial lower metallicity than the Milky Way and, due to their proximity, prove to be valuable laboratories in which to study star formation and the ISM. The Milky Way itself is a spiral galaxy that has most likely a bar and an SBbc morphology (e.g. Benjamin et al., 2005). This classification is due to the presence of a prominent bulge that favors a Sb type, while the high star formation rate of the Milky Way speaks for a Sc type galaxy. Since we are situated within the galactic disk it is not easy to deduce the overall morphology of the MW and the number of spiral arms (2 or 4?). Also the distance of the sun to the galactic center (R_0) as well as its rotation speed (Φ_0) are not known with high accuracy; recent values are $R_0 = 8.3 \pm 0.23$ kpc and $\Phi_0 = 239 \pm 7$ km s^{-1} (Brunthaler et al., 2011). The Andromeda galaxy is classified as an Sb galaxy. Is has a similar mass as the Milky Way (Reid et al., 2009). Currently its star formation activity is low due to a low hydrogen-gas content. The long-term fate of M31 and the Milky Way is most probably a head-on collision of both galaxies in a few (≈ 4) Gigayears in which they might form a giant elliptical galaxy. This elliptical galaxy will by then also includes M 33 as well as the Magellanic clouds and several other satellites of both spirals (see e.g. van der Marel et al., 2012).

2.3. M 33

M 33, shown in Fig. 2.3, is a small late type spiral galaxy of type SA(s)cd after the de Vaucouleur classification scheme. The main properties of M 33 are shown in Table 2.1. It has probably the dwarf galaxy LGS 3 as a satellite. Its total mass is with $\approx 5 \times 10^{10}$ M$_\odot$ (Corbelli, 2003) about 20 times lower than that of the Milky Way or the M 31. In contrast to the Andromeda galaxy, which is seen highly inclined, M 33 has a

low inclination of 56° (Zaritsky et al., 1989), which allows us a good view onto its disk with short line-of-sight depths. Therefore, M 33 is the closest spiral galaxy in which individual cloud complexes in the disk can be observed. It is located at a distance of about 730-840 kpc (Brunthaler et al., 2005; Galleti et al., 2004; Freedman et al., 1991) from the Milky Way and about 200 kpc from M 31 (Brunthaler et al., 2005). For consistency throughout this work and with work from the `HerM33es` consortium a distance of 840 kpc (Freedman et al., 1991) is used. The metallicity of M 33 is subsolar by a factor of 2 with an overall Oxygen abundance of 12 + log O/H = 8.27 (Magrini et al., 2010). This makes M 33 interesting in comparison with the Milky Way as well as with the Large Magellanic Cloud[7] (LMC) which has a similar oxygen abundance (Hunter et al., 2007).

Its structure includes three principal components that are certain: an exponential disk, a semi-stellar nucleus and a halo containing RR lyrae variables as well as globular clusters (van den Bergh, 2000). Furthermore there is evidence for a weak bar in M 33 (Corbelli & Walterbos, 2007). The existence of a small nuclear bulge is still controversial (see e.g. Colin & Athanassoula, 1981; Minniti et al., 1993). The absence of a stellar bulge in late type spiral galaxies is however common (Böker et al., 2002). As determined from Hubble Space Telescope surface photometry by Lauer et al. (1998) the nucleus of M 33 is very compact with a core radius of about 0.13 pc. Furthermore, Lauer et al. (1998) derives the upper limit for the mass of a hypothetical central black hole to be 2×10^4 M$_\odot$. This low mass implies that M 33, unlike M 31 and the Milky Way, does not contain a massive black hole in its center. The center of M 33 however hosts an ultra-luminous X-ray (ULX) source (M33-X8 RA = 01:33:50.89, DEC = +30:39:37.2) that is supposedly a binary star with a black-hole primary of around 10 M$_\odot$ and a secondary of around 70 M$_\odot$ (Takano et al., 1994; Peres et al., 1989; Weng et al., 2009, see e.g.). M33-X8 is the most powerful, steady X-Ray source in the local group (Peres et al., 1989) with an X-ray luminosity of about 2.2×10^{39} erg s^{-1} (Weng et al., 2009). M 33 further hosts the massive Giant H II-region NGC604[8] which is estimated to be young ~ 3 Myr (González Delgado & Pérez, 2000) and driven by a massive young cluster with $\gtrsim 200$ O and Wolf-Rayet stars (Maíz-Apellániz et al., 2004). NGC604 is the second most massive Giant H II-region in the local group after 30 Doradus in the LMC.

Naturally, the extent and morphology of the disk of M 33 depends on the wavelengths at which it is observed. The optical length of the major axis is 20 kpc, while neutral hydrogen can be observed up to 33 kpc (van den Bergh, 2000). The rotation curve of M 33 is measured out to 16 kpc where it is still rising which implies a dark matter halo with a total mass of about 5×10^{10} M$_\odot$ (Corbelli & Salucci, 2000). The ISM in M 33 on average more fragmented and irregular than in the Milky Way (Sánchez et al., 2010). Indeed the appearance of the disk is flocculent and depending on the wavelength it is difficult to define spiral arms. This is again a feature of late type spiral galaxies that have an open and not very well developed spiral structure which is often best outlined by H II-regions (Boulesteix et al., 1974). The outermost parts of M 33 disk are strongly warped (e.g. Corbelli et al., 1989). This feature is most likely due to a close encounter between M 33 and M 31, a few Gyr ago. This encounter also

---

[7]An irregular local group galaxy

[8]Visible in Fig. 2.3 as the brightest Hα peak (*red*), located to the upper left of the center of M 33.

Table 2.1.: Basic properties of M 33 (Buchbender et al., 2013)

	M 33	References
RA(2000)	01:33:51.02	
DEC(2000)	30:39:36.7	
Type	SA(s)cd	1
Distance [kpc]	840	2
Total Mass	$5 \times 10^{10}\,M_\odot$	3
5″ (PdBI @ 230 GHz) equal to	25 pc	
11″ (30m @ 230 GHz) equal to	45 pc	
21″ (30m @ 115 GHz) equal to	86 pc	
28″ (30m @ 89 GHz) equal to	114 pc	
LSR velocity [km s^{-1}]	−180	
Position Angle [deg]	22.5	4
Inclination [deg]	56	5
R_{25}	30.8′ or 7.5 kpc	

References. (1) de Vaucouleurs et al. (1991); (2) Galleti et al. (2004); Freedman et al. (1991); (3) Corbelli (2003); (4) Paturel et al. (2003); (5) Regan & Vogel (1994); Zaritsky et al. (1989).

formed a giant H i-bridge between both galaxies from material that has been ejected from M 33 by M 31 (see e.g. Bekki, 2008; McConnachie et al., 2009; Putman et al., 2009; Lockman et al., 2012). M 33 is therefore not an isolated galaxy, but in gravitational interaction with M 31, which will likely absorb M 33 in the future and bring new fuel for star formation in M 31; however, only if M 33 does not consume it's gas reservoirs before. M 33 exhibits a very high star formation efficiency deduced by comparing the actual star formation rate with the available H_2 mass content traced by CO (e.g. Gardan et al., 2007). M 33's SFE is comparable to that of intermediate redshift galaxies and larger than that of most large local universe spiral galaxies (Magrini et al., 2010). However, the high-star formation efficiencies deduced for M 33 might be an artifact of the conversion factors used to derived the H_2 mass content from CO, as will be shortly discussed in Chapter 14.

More information onto the ISM in M 33 is newly added or discussed by this thesis. In Chapter 6 the spectral-energy-distribution (SED) of the dust throughout the disk of M 33 is considered. Restricted to the observed positions along the major axis of M 33 further the star formation rate (Chapter 7), the atomic (Section 5.5) and molecular (Section 5.6) gas mass, the far-ultraviolet field strength (Section 5.8) and the optical extinctions (Section 5.7) are discussed. In general information onto the emission of the dense-molecular-gas tracers HCN and HCO$^+$ within M 33 is added by this thesis.

Chapter 3.

Probing the interstellar medium with molecular tracers

Until now more than 170 molecules have been detected in the interstellar medium or circumstellar shells (CDMS[1] Müller et al., 2001, 2005). In extragalactic sources 53 molecules of these molecules have also been detected. The different molecules naturally have different properties and chemical creation pathways that make them sensitive to distinct physical conditions and thus environments. Hence, choosing the appropriate molecule and transition between energy levels therein it is possible to investigate specific aspects of the ISM.

The information about the ISM that can be learned from molecular transitions is vast and exclusive. Especially the low lying rotational levels of some molecules have low excitation energies that can be overcome by the kinetic energies present in the cold, dense, molecular regions of the ISM. As a consequence, these transitions open observational windows into the realm where the actual star formation happens.

Molecules can be used as "diagnostic-tools" to study the:

- **Spatial distribution of gas** The most prominent tracer used to observe molecular gas is carbon monoxide (CO), the second most abundant molecule in the interstellar medium. The low lying rotational ground state transition of ^{12}CO is the "workhorse" to trace molecular gas. On the other hand to observe dense regions in the ISM, one may resort to molecules with higher critical densities, for which Hydrogen Cyanide (HCN) and Formylium (HCO$^+$), the molecules of interest of this thesis, are but two examples.

- **Temperature and density** When multiple transitions of the same molecule or lines with fine- and hyperfine-structure are available, the excitational state of the molecule tells about the physical state, temperature and density, of the emitting gas.

- **Mass and column density** If the emission from the molecules is optically thin it traces the column density of the emitting gas and thus also its mass.

- **Velocity structure** The line-shape of molecular emission as well as possible shifts of molecular lines with respect to their rest frequency tell about motions of the emitting particles and reveal turbulence within the gas. The line-shape may also reveal the geometry of clouds, as for example in shells.

---

[1]Cologne Database for Molecular Spectroscopy

- **Presence of certain physical or chemical processes** The mere presence of emission from certain molecules already tell about certain physical or chemical processes. For example shocks are such a process as they change the chemistry and sputter dust grains. Molecules formed in the changed chemical conditions are, e.g. OH or H_2O and serve therefore as tracers of shock. However, also FUV-photons, X-rays, and turbulence/shear imprint their presence in the composition and excitation of molecules and thus may be studied through them.

However, to be able to deduce physical parameters from molecular emission a thorough understanding of the physics of molecules and the radiative transfer of the emitted line radiation is needed. In this chapter essential concepts needed for the later analysis and discussion are outlined. The principles of the quantum-mechanical description of molecules are sketched in Section 3.1. In Sections 3.1.2 and 3.2 the level population and radiative transfer of molecules is sketched.

3.1. Molecular physics

In the following the physics of rotational ground-state transitions of diatomic molecules is outlined to provide a basis for the interpretation of the observations presented later in the text. Naturally, a detailed treatment of the physics of molecules is complex and beyond the scope of this thesis. In-depth treatments can be found in varying depths in e.g. Banwell (1983); Brown & Carrington (2003); Tielens (2005); de Boer (2007); Draine (2011). This section follows the line of argument in Brown & Carrington (2003).

Molecules are compounds of atoms and as such also more complex of nature than single atoms. For the observer this complexity is a benefit as molecules do not only possess electronic, but also vibrational and rotational energy levels. These additional energy levels altogether provide more means to characterize the physical state (temperature, density, velocity distribution, ...) of emitting molecules than are available for atoms. Typically the rotational and vibrational transitions generate radiation in the radio and infrared domains of the electromagnetic spectrum.

To identify a certain molecule in an observed spectra the frequencies of the transitions that arise between energy levels of this molecule have to be known. Two methods to deduce these frequencies exist. The first is to describe the molecule quantum-mechanically as closely as possible to calculate the level diagram of the molecule. The second is to measure the spectrum of a molecule in the laboratory. In general a twofold approach is used combining both methods which complement one another. Here only the theoretical calculation of the rotational levels of a rigid diatomic molecule will be discussed.

To describe an molecule quantum mechanically the Schrödinger equation $H\psi = E\psi$ is used, where E the energy, ψ the wave function and H the Hamiltonian, which is the operator corresponding to the total energy. In the most general case the kinetic energy of the electrons and nuclei of a molecule can be described by the Hamiltonian:

$$H = \sum_{\alpha} \frac{1}{2M_{\alpha}} P_{\alpha}^2 + \sum_{i} \frac{1}{2m} P_i^2, \qquad (3.1)$$

where M_α and m the masses of the nuclei and electrons, respectively, and P_α and P_i their momenta that are expressed in a space-fixed axis system of arbitrary origin. As presented in detail in Brown & Carrington (2003) one can show through appropriate coordinate transformations, that this equation contains the rotational and vibrational motions of the nuclei as well as the kinetic energies of the electrons.

A full mechanical treatment of the motion of a molecule can become very complex. Therefore the Hamiltonian as well as the wave function is divided into sub-parts corresponding to the translational, vibrational, rotational as well as electronical motions inside a molecule. However, coupling between the different motions exist and must be considered to deduce accurate values of the resulting energy levels. The subdivision of the total wave function into nuclear and electronic wave functions is called the Born-Oppenheimer Approximation (BOA). Motivated by the fact that the electrons are much lighter and move much faster than the nuclei, the BOA assumes that the motion of the nuclei can be neglected. As a result the electronic wave function depends only on the position of the nuclei that defines their Coulomb Potential, but not on the momenta of the nuclei. A convenient form of the wave function can be found for a coordinate system that gyrates together with the nuclei about a molecule-fixed axes. In this coordinate system one coordinate (R) is the internuclear distance and the other two coordinates two of the three Euler angles ϕ and θ. In this system the total wave function can be written in the BOA as

$$\psi_{\text{rve}} = \sum_n \psi_e^n(\boldsymbol{r}_i, R)\psi_{\text{rv}}^n(R, \phi, \theta), \tag{3.2}$$

where n numerates all possible electronic wave functions, $\boldsymbol{r}_i$ the coordinates of the electrons and the subscripts r, v, and e denote which motion – (r)otational, (v)ibrational or (e)lectronical – is included in the specific wave function.

Similarly, the Hamiltonian can be sub-divided into nuclear and electronic Hamiltonians $H = H_{\text{nucl}} + H_{\text{el}}$. In the following discussion the electronic states are neglected and only terms including motions of the nuclei are considered. The Hamiltonian of the nuclei can be expressed as:

$$H_{\text{nucl}} = -\frac{\hbar^2}{2\mu R^2}\frac{\partial}{\partial R}\left(R^2\frac{\partial}{\partial R}\right) + \frac{\hbar^2}{2\mu R^2}(\boldsymbol{J} - \boldsymbol{P})^2 + V_{\text{nucl}}(R), \tag{3.3}$$

where μ the reduced nuclear mass $M_1 M_2/(M_1 + M_2)$, $\boldsymbol{J}$ the total angular momentum and $\boldsymbol{P}$ the total electronic angular moment, which is the sum of the orbital and spin angular moments $\boldsymbol{L} + \boldsymbol{S}$. Please note that because this equation involves the operator $\boldsymbol{P}$, which acts upon the electronic wave function, the nuclear Hamiltonian is actually not independent from the motion of the electrons.

The Hamiltonian in Eq. (3.3) includes the vibrational and rotational kinetic energy of the nuclei. In case of the Born-Oppenheimer approximation the nuclear wave function can be further decomposed in wave functions that describe the vibrational and rotational motion separately:

$$\phi_{rv}^n = \chi^n(R)e^{iM_J\phi}\Theta^n(\theta)e^{ik\chi}, \tag{3.4}$$

where χ^n and Θ^n are the vibrational and rotational wave functions, χ the third, redundant, Euler angle not used in Eq. (3.2), and M_J and k constants that take integral or half-integral values. Applying the Hamiltonian of Eq. (3.3) one obtains the wave equation of the "vibrating rotator":

$$\frac{\hbar^2}{2\mu R^2}\frac{\partial}{\partial R}R^2\frac{\partial \chi^n(R)}{\partial R} + \left\{E_{\text{rve}} - V - \frac{\hbar^2}{2\mu R^2}(J(J+1))\right\}\chi^n(R) = 0, \qquad (3.5)$$

where V the potential energy term of the nuclei and E_{rve} the total (rotational, vibrational and electronical) energy of the molecule. The description of the potential energy term can be problematic and is in its generalized form (see e.g. Eq. 2.175 in Brown & Carrington (2003)) difficult to manage. Therefore, often restricted forms are used. One is the Morse potential:

$$V = D\left(1 - e^{-\beta(R-R_e)}\right)^2, \qquad (3.6)$$

with D the dissociation energy of the molecule, R_e the equilibrium nuclear separation[2] and β a constant. Using this form for the potential energy term the energy of the "vibrating rotator" is finally given by:

$$\begin{aligned}
E_{v,J} &= \omega_e(v+1/2) - \omega_e\chi_e(v+1/2)^2 + B_e J(J+1) \\
&\quad - D_e J^2(J+1)^2 - \alpha_e(v+1/2)J(J+1),
\end{aligned} \qquad (3.7)$$

where v and J are the vibrational and rotational quantum numbers, ω the vibrational energy, B_e the rotational constant D_e the expansion constant, χ_e the anharmonicity constant and α_e molecular specific constant describing the coupling between rotation and vibration of the molecule. The first two terms of this equation describe the vibrational – the next two the rotational energy. The last term includes the ro-vibrational interaction. Note that the first vibrational and the first rotational term are the quantum mechanical solutions for a harmonic oscillator and a classical rotor. The second terms are first order perturbations.

3.1.1. Rotational transitions

As shown in the previous section the wave equation and Hamiltonian of a molecule can be decomposed approximately into parts for the electronic, vibrational and rotational kinetic energies. Based on this description the rotational energy levels of a rigid rotating diatomic or linear molecule in its electronic and vibrational ground state is calculated to first order in the following. Subsequently, the frequencies of the transitions between these levels can be deduced, which will be demonstrated at the example of ^{12}CO. This section is based on Sec. 2.2 of Banwell (1983). Note, that all lines observed in this thesis are rotational transitions of linear molecules.

First, the term "electronic and vibrational ground-state" needs some explication. The ground-state of a molecule depends on its configuration and not all molecules have the same ground-state in terms of quantum numbers. To designate the electronic energy

---

[2]The value of R_e for that the potential energy is a minimum.
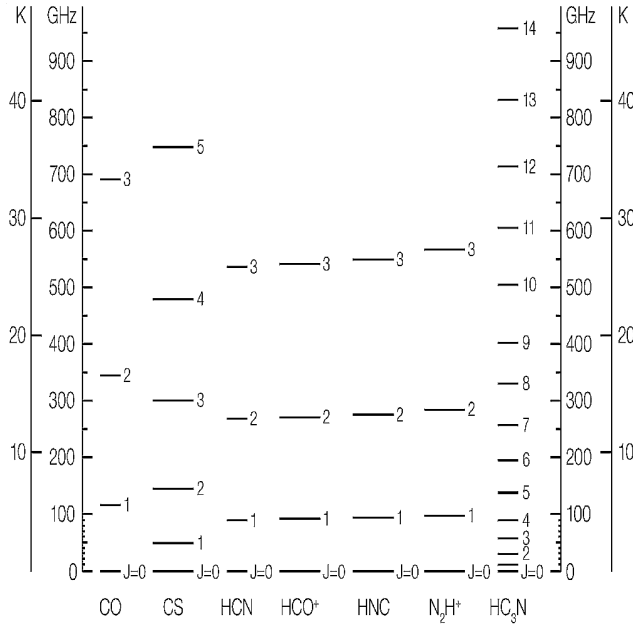
Figure 3.1.: Rotational ladder of interstellar molecules. Only the predominant isotopic species are shown. (Wilson et al., 2009)

levels of molecules with an axial symmetric Coulomb potential[3] the term symbols $^{(2\Sigma+1)}\mathcal{L}_{J_{e,z}}$ are used. $\mathcal{L}$ denotes the value of Λ, that is to say the absolute value of the electron angular momentum with $\mathcal{L} = \Sigma, \Pi, \Lambda, \ldots$ for $\Lambda = 0, 1, 2, \ldots$. Σ denotes the absolute value of the total electron spin and $J_{e,z}$ the total electronic angular momentum ($|\Lambda - \Sigma|$ or $\Lambda + \Sigma$). All three values are in terms of projection onto the internuclear axis divided by $\hbar$. In case of ^{13}CO, ^{12}CO, HCN and HCO^+ the electronic ground states have the same term symbol $^1\Sigma$, indicating that the absolute value of the projection of the electron angular momentum as well as the total electron spin onto the internuclear axis is 0. The vibrational ground state of these molecules is $v = 0$.

The energy of a rigid rotor is described by the first term related to the rotational energy in Eq. (3.7),

$$E_J = B_e J(J + 1) \text{ where } J = 0, 1, 2, \ldots \tag{3.8}$$

with,

$$B_e = \frac{h}{8\pi^2 I_B c} \, cm^{-1}, \tag{3.9}$$

where I_B the moment of inertia of the molecule. For a diatomic molecule I_B can be written in terms of the above introduced reduced mass and $I_b = \mu R^2$ (Banwell, 1983). The rotational energy levels of a rigid rotor can be deduced by evaluating Eq. (3.8) for the individual quantum numbers. In the lowest state $J = 0$ the energy is $E_J = 0$; no rotation takes place. For the next three values of $J = 1$, 2, and 3 one calculates $E_J = 2B_e, 6B_e$, and $12B_e$, respectively.

The energy of a transition is the difference in energy of the levels between which it occurs. All transitions between energy levels must follow so called selection rules, i.e. only certain changes in quantum number are allowed. For diatomic and linear molecules with a dipole moment, the rotational quantum number can only change

---

[3]Linear and diatomic molecules fall into this regime.

Table 3.1.: Molecule parameters of key species discussed in this thesis

	Electronic Ground State	ν [GHz]	μ [Debye]	E_u/k_b [K]	n_{cr} [cm^{-3}]
C$_2$H(1–0, 3/2-1/2)	$^2\Sigma^+$	87.2841050	0.77	4.19	1×10^5
HCN (1–0)	$^1\Sigma$	88.6316022	2.99	4.25	2×10^5
HCO$^+$ (1–0)	$^1\Sigma$	89.1885247	3.90	4.28	3×10^4
HOC$^+$ (1–0)	$^1\Sigma$	89.4874140	2.77	4.29	3×10^4
HNC (1–0)	$^1\Sigma$	90.6635680	3.05	4.35	2×10^5
^{12}CO (1–0)	$^1\Sigma$	115.2712018	0.11	5.53	4×10^2
^{13}CO (1–0)	$^1\Sigma$	110.2013543	0.11	5.28	4×10^2

Notes. Values except n_{cr} taken from CDMS (Müller et al., 2001, 2005). n_{cr} for collisions with H$_2$ at a temperature of 20 K neglecting opacity effects taken from the *Leiden Atomic and Molecular Database* (Schöier et al., 2005).

by $\Delta J = \pm 1$. The energy difference between the first two states of a rigid rotor – the $J = 1$–0 transition – is $\Delta E_{1-0} = 2B_e$. For the $J = 2$–1 transition the energy is $\Delta E_{2-1} = 4B_e$. Note the increase of $2B_e$ with respect to the $J = 1$–0 transition. Comparing the energy differences for the next higher transitions one can see that for each subsequent transition the energy increases by $2B_e$ with respect to the previous one such that:

$$\Delta E_{J'''-J''} = \Delta E_{J''-J'} + 2B_e \qquad (3.10)$$

holds, where $\mathrm{J}''' = \mathrm{J}'' + 1 = \mathrm{J}' + 2$ for $\mathrm{J}' \geq 0$. See Fig. 3.1 for the rotational "ladder" of some common molecules in the ISM, among them HCN, HCO$^+$ and ^{12}CO.

When the rotational constants of a molecule are known the frequencies of the individual levels can be calculated. For ^{12}CO $B_e = 57.6356$ GHz (de Boer, 2007) and thus from Eq. (3.10) follows $\Delta E_{1-0}(^{12}$CO$) = 115.271$ GHz and $\Delta E_{2-1}(^{12}$CO$) = 230.542$ GHz. Note that the latter frequency differs 4 MHz from the official value 230.538 GHz reported for example in the CDMS. This difference is due to higher order effects, such as for example the rotational stretching of the molecule, which are neglected here. As mentioned above, the rotational constants include the moment of inertia of a molecule and thus depend on the masses of the individual nuclei. Therefore, the rotational constants are dependent on the actual isotopes that make up the molecule. For example the rotational constant of ^{13}CO is different from that of ^{12}CO and is $B_e = 55.1007$ GHz. Therefore the resulting frequency of the first transition is lower and has a frequency of $\Delta E_{1-0}(^{13}$CO$) = 110.201$ GHz.

3.1.2. Einstein and collision rate coefficients and critical density

Knowing about the frequency of certain transitions allows us to identify a certain molecule in a spectrum. However, without knowledge about the line strengths and radiative transfer, that both depend on the population of the different energy states, it is not possible to make statements about the physical conditions of the emitting medium.

In this section the physics of level population is discussed together with the concept of critical density following the lines of argument in (Weiss, 2000; Wilson et al., 2009).

For sake of simplicity consider a simple two-state system with an upper (u) and a lower (l) energy level that are populated by n_l and n_u particles, respectively. Further let the medium be exposed to an radiation field with an energy density $\bar{U}$ that in case of Thermodynamic Equilibrium (TE) is described by the Planck law

$$\bar{U} = \frac{8\pi h \nu_0^3}{c^3} \left(\exp\left(\frac{h\nu_0}{kT_{\text{rad}}} \right) - 1 \right)^{-1}, \qquad (3.11)$$

with the formal radiation temperature T_{rad}. In such a scenario transitions between the two levels can be caused by several different processes that have certain probabilities, which are formalized by the Einstein- and collision rate-coefficients. The coefficients and the processes they describe are:

- A_{ul} - **Spontaneous Emission** Probability of a spontaneous emission of a photon due to the transition from state u to l. The number of transitions per second per unit volume is $n_u A_{ul}$.

- B_{lu} - **Absorption** The probability of absorption of a photon and a subsequent change from state l to u, depends on the energy density of the radiation field and is $B_{lu}\bar{U}$. Therefore, the number of absorption per second and unit volume is $n_l B_{lu}\bar{U}$.

- B_{ul} - **Stimulated Emission** Photons can induce a transition from the upper to the lower level. This process is also depended on $\bar{U}$ and the probability is therefore $B_{ul}\bar{U}$. The number of emitted photons per second per unit volume is $n_u B_{ul}\bar{U}$.

- C_{lu}/C_{ul} - **Collision between molecules** The collision rates for molecules are defined by $C_{ij} = \sum_x n_x K_{ij} = \sum_x n_x \int_0^\infty \sigma_{ij}^X(\nu)\nu f^X(\nu)\mathrm{d}\nu$ where K_{ij} the collision coefficient, x denotes the species of collision partner (atoms or molecules), σ_{ij}^x the specific collision cross section and $f^x(\nu)$ the velocity distribution function of the colliding particles which depends on the kinetic temperature T_{kin} and the reduced mass $m_r = m_a m_b/(m_a + m_b)$ of the colliding particles. For most astrophysical applications only the most abundant molecules and atomic species are included in the calculation of the collisional excitation. In first order these are H, H_2 and He and electrons (depending on the phase of the ISM). The number of collisions per second per unit volume are $n_u C_{ul}$ and $n_l C_{lu}$.

- F_i - **Chemical Formation** The chemical formation of a molecule in state u or l is a fifth way to populate a certain energy level. In elaborated models of photon dominated regions (see e.g. Chapter 4) this rate coefficient is included for the following discussion in this chapter it is, however, neglected.

The Einstein coefficients are related by the so called Einstein relations:

$$g_l B_{lu} = g_u B_{ul}, \qquad (3.12)$$

and

$$A_{ul} = \frac{8\pi h\nu_0^3}{c^3} B_{ul}.$$
(3.13)

where g_l and g_u are the statistical weights of the lower and upper state. For rotational transitions the statistical weights are given by the degeneracy of each level due to spin and are $g_J = 2J + 1$.

In case of rotational transitions in linear molecules the Einstein coefficient A_{ul} can be given in dependence of the permanent electric dipole moment μ of the molecule[4] and the rotational Quantum number (J) of the upper state:

$$A_{ul} = \frac{64\pi^4}{3hc^3} \nu^3 \mu^2 \frac{J}{2J + 1}.$$
(3.14)

For a stationary situation in which upward and downward transitions are in equilibrium one can write the rate equation as,

$$\frac{n_u}{n_l} = \frac{\bar{U}B_{lu} + C_{lu}}{A_{ul} + \bar{U}B_{ul} + C_{ul}}.$$
(3.15)

In the case of local thermodynamic equilibrium the population distribution is given by a Boltzmann distribution. Introducing a formal excitation temperature T_{ex} the Boltzmann distribution is given by,

$$\frac{n_u}{n_l} = \frac{g_u}{g_l} \exp\left(-\frac{h\nu}{kT_{ex}}\right).$$
(3.16)

Dependent on whether collisional or radiative transitions dominate the rate equation, T_{ex} corresponds to either the kinetic temperature of the gas (T_{kin}) or the radiative temperature (T_{rad}) (cf. Eq. (3.11)). In general T_{ex} is a complex function of both.

Now, consider an optically thick medium in which radiative processes play no role and the collisions dominate such that $n_u C_{ul} = n_l C_{lu}$ and

$$\frac{n_u}{n_l} = \frac{C_{lu}}{C_{ul}} = \frac{g_u}{g_l} \exp\left(-\frac{h\nu}{kT_{ex}}\right).$$
(3.17)

Under these circumstances, recalling the Einstein relations Eqs. (3.12) and (3.13), the rate equation Eq. (3.15) can be rewritten as

$$\frac{n_u}{n_l} = \frac{g_u}{g_l} \frac{k_\nu \bar{U} + \dfrac{C_{ul}}{A_{ul}} \exp(-h\nu/kT)}{1 + k_\nu \bar{U} + \dfrac{C_{ul}}{A_{ul}}}$$
(3.18)

where $k_\nu = c^3/8\pi\nu^3$ has been defined for sake of brevity. It is readily visible that this equation depends heavily on the value of the factor C_{ul}/A_{ul}. Recalling the definition of

---

[4]Normally measured in the laboratory and given in units of Debyes ($1\text{Debye} = 10^{-18} \sqrt{\text{erg cm}}$ cm).

the collision rates above and defining the total density $n = \sum_x n_x$ one can write C_{ul}/A_{ul} as:

$$\frac{C_{ul}}{A_{ul}} = \frac{n}{n_{crit}} \text{ where } n_{crit} \equiv \frac{A_{ul}}{\sum_x K_{ul}}. \tag{3.19}$$

n_{crit} is called the critical density and is different for every transition. It defines the density of the colliding particles for that the collisional de-excitation and the spontaneous emission (A_{ul}) are in equilibrium. Contemplating Eq. (3.18)) one can see that for $n \gg n_{crit}$ the level population becomes by a Boltzmann distribution. If this is the case the system maximizes its emission[5]. A system that fulfills this criterion is said to be "thermalized". Note that for $n \ll n_{crit}$ the system still emits radiation, however weaker. For a thermalized system the excitation temperature T_{ex} equals the kinetic temperature of the gas T_{kin}. Note, that the effective density n_{eff} that is needed to produce a line of 1 K may be much lower than n_{crit} and the common notion that molecules trace gas densities equal or larger than their critical density ($n \geq n_{crit}$) is not necessarily true (Evans, 1999).

3.2. Radiative transfer under local thermodynamic equilibrium

In this section the radiative transfer under Local Thermodynamic Equilibrium (LTE) conditions in a homogeneous medium is discussed. The changes to a light ray of intensity I_ν of a specific frequency ν that propagates through a medium are described by the radiative transfer equation:

$$dI_\nu = -\kappa_\nu(s)I_\nu(s)ds + \epsilon_\nu(s)ds, \tag{3.20}$$

where $\kappa_\nu(s)$ the extinction and $\epsilon_\nu(s)$ the emission coefficient. In general $\kappa_\nu(s)$ and $\epsilon_\nu(s)$ are functions of s, that is to say the position along the line of sight. However, in a homogeneous medium these quantities become independent of s. On an atomic and/or molecular basis the emission and extinction coefficient can be described using the Einstein coefficient A_{ul} and the Einstein relations (Eqs. (3.12) and (3.13)):

$$\epsilon_\nu = \frac{h\nu_0}{4\pi} n_u A_{ul} \varphi(\nu), \tag{3.21}$$

$$\kappa_\nu = \frac{c^2}{8\pi\nu^2} \frac{g_u}{g_l} n_l A_{ul} \left(1 - e^{-\frac{h\nu}{kT_{ex}}}\right) \varphi(\nu). \tag{3.22}$$

Inserting the formulation of the Einstein A_{ul} coefficient (Eq. (3.14)) into the previous equation and assigning the quantum number J to the (u)pper and $J-1$ to the (l)ower state such hat $g_u = g_J = 2J + 1$ and $g_l = g_{J-1} = 2J - 1$, the extinction coefficient κ_ν can be written in terms of the rotational quantum number J and the electric dipole moment as:

$$\kappa_\nu = \frac{8\pi^3\nu}{3hc} \frac{J}{2J - 1} n_l \mu^2 \left(1 - e^{-\frac{h\nu}{kT_{ex}}}\right) \varphi(\nu) \tag{3.23}$$

---

[5]This can be tested by inserting Eq. (3.18) into the definition of the emission coefficient in Eq. (3.21) of the next section.

Note that the discussion here neglects possible scattering of light by with the corresponding frequency by dust particles into or out of the line-of-sight. Before we attempt to solve the radiative transfer equation it is beneficial to introduce the optical depth τ_ν and the source function S_ν.

The optical depth determines the maximum path length a photon can travel before it is scattered or absorbed and is defined by:

$$\tau_\nu = \int \kappa_\nu \mathrm{d}s, \tag{3.24}$$

where $\mathrm{d}s$ is an infinitesimal small path length along the line of sight. For low values $\tau_\nu \ll 1$ the light can reach the observer from any point in the medium. For high values $\tau_\nu \gg 1$ only the surface of the medium at a given frequency or velocity is visible and information from its interior and especially the column density of the emitting particles remains unknown.

The source function S_ν is defined as the ratio of the emission to the extinction coefficient. With Eqs. (3.21) and (3.22) and substituting Eqs. (3.12) and (3.13) the source function can be written as

$$S_\nu = \frac{\epsilon_\nu}{\kappa_\nu} = \frac{2h\nu^3}{c^2} \left(\frac{g_u n_l}{g_l n_u} - 1 \right)^{-1}. \tag{3.25}$$

Under LTE the level population is described by a Boltzmann distribution and T_{ex} is independent of J. Therefore one can substitute n_u/n_l with Eq. (3.16). This results in a description of the source function that equals a Planck Function B_ν for a formal temperature T_{ex}:

$$S_\nu = B_\nu = \frac{2h\nu^3}{c^2} \left(\exp\left(\frac{h\nu}{kT_{\mathrm{ex}}} \right) - 1 \right)^{-1}. \tag{3.26}$$

With the definition of τ and Eq. (3.25) one can now rewrite the radiative transfer equation Eq. (3.20) as follows:

$$\frac{dI_\nu}{d\tau_\nu} = -I_\nu + S_\nu. \tag{3.27}$$

After integrating the previous equation and a subsequent multiplication with $e^{-\tau}$, under assumption of a homogeneous medium, the solution for the radiative transfer equation is:

$$I_\nu = I_\nu^0 + S_\nu[1 - e^{-\tau}]. \tag{3.28}$$

In this equation I_ν^0 is the intensity of an optional background source. This solution can also be written in terms of brightness temperature (using the not yet introduced Eq. (B.2)):

$$T_B(\tau_\nu) = T_B^0 e^{-\tau} + T(1 - e^{-\tau}), \tag{3.29}$$

where T_B^0, equivalent to I_ν^0, is the brightness temperature of the background source and T in case of line radiation the excitation temperature introduced in Eq. (3.16). In the case that no background source exists two limiting cases for extreme values of τ exist:

$$T_B = \begin{cases} T_{\text{ex}}, & \text{for } \tau_\nu \gg 1. \\ \tau_\nu T_{\text{ex}}, & \text{for } \tau_\nu \ll 1. \end{cases} \tag{3.30}$$

Please note that the same formula holds for the radiative transfer of dust in which case, however, κ and τ are different and T becomes the dust temperature T_{dust}. This case is discussed in the next Section 3.2.1.

3.2.1. Radiative transfer of a dust cloud at uniform temperature

Although the emphasis of this thesis lies on the analysis of molecular line radiation molecules, use is made of the extensive data set available for M 33 to deduce ancillary information. Especially the Spectral Energy Distribution (SED) information obtained by *Herschel* and *Spitzer* in the wavelength range $24 - 500\,\mu\text{m}$ is used to deduce the temperature and mass of the dust (see Chapter 6). Therefore, the radiative transfer calculations behind the employed SED-fitting routines is shortly presented here. For an in-depth treatment of this topic (Krügel, 2003) is a very complete source and serves as the general reference to this section.

As mentioned above Eq. (3.28) also holds for the radiative transfer of dust. For wavelengths larger than $10\,\mu\text{m}$ scattering by dust grains can be neglected (Krügel, 2003). Without scattering the only emission able to reach an observer is the (isotropic) emission of the dust grains as well as light from a background source. If the latter does not exist, the source function of dust grains at a temperature T_{dust} equals a Planck function of the same temperature:

$$S_\nu = B_\nu(T_{\text{dust}}). \tag{3.31}$$

Thus the flux coming from a solid angle Ω becomes:

$$F_\nu(\tau) = B_\nu(T_{\text{dust}}) + B_\nu(T_{\text{CMB}})[1 - e^\tau]\Omega \tag{3.32}$$

This type of flux is also called "modified blackbody" (MBB) or "greybody" in resemblance of the term blackbody. The optical depth can be described as follows:

$$\tau_\nu = \frac{\kappa_{\text{d}}(\nu)M_{\text{dust}}}{D^2\Omega_s}, \tag{3.33}$$

where M_{dust} is the dust mass, D the distance to the source and $\kappa_d(\nu)$ the dust extinction coefficient. The subscript ν to the optical depth τ signifies that it is wavelength-dependent. This dependency is due to the extinction coefficient $\kappa_{\text{d}}(\nu)$ that in turn is dependent on the type of dust and the dust grain distribution. In this thesis Krügel & Siebenmorgen (1994) is followed and:

$$\kappa_{\text{d}}(\nu) = 0.04(\nu/250Ghz)^\beta \text{ in units of } [\frac{m^2}{kg}] \tag{3.34}$$

3.3. Column densities under local thermodynamic equilibrium

In the following it is described how to calculate column densities from optically thin emission lines assuming LTE. This section follows the line-of-argument of Zielinsky (1999). The brightness temperature measured by a radio-telescope deviates from the one described by Eq. (3.29) in as much as that it is general practice to subtract a base-line from the observed spectra. This removes possible background continuum radiation and the measured brightness becomes:

$$T_B = (\mathcal{J}_\nu(T_{\text{ex}}) - \mathcal{J}_\nu(T_{\text{CMB}}))(1 - e^{-\tau})\Phi_b \tag{3.35}$$

where Φ_b is the beam filling factor and $\mathcal{J}$ defined by

$$\mathcal{J}_\nu(T) = \frac{c^2}{2k\nu^2}B_\nu(T). \tag{3.36}$$

The term $\mathcal{J}_\nu(T_{\text{CMB}})$ enters the equation due to the omnipresent Cosmic Microwave Background (CMB) radiation that resembles a Blackbody of temperature $\sim 2.7\text{K}$ (e.g. Fixsen, 2009).

For optically thin emission $\tau \ll 1$ Eq. (3.35) becomes:

$$T_B = (\mathcal{J}_\nu(T_{\text{ex}}) - \mathcal{J}_\nu(T_{\text{CMB}}))\tau\Phi_b \tag{3.37}$$

Let us further assume that the beam filling factor is unity $\Phi_b = 1$ then Eq. (3.37) can be solved for τ. Subsequent integration over the emission line, yields the following equation:

$$\int \tau_\nu d\nu = (\mathcal{J}_\nu(T_{\text{ex}}) - \mathcal{J}_\nu(T_{\text{CMB}}))^{-1} \int T_B d\nu. \tag{3.38}$$

Recalling the definition of κ in Eqs. (3.23) and (3.24) one can describe the integral of τ_ν over the emission line as:

$$\int \tau_\nu d\nu = \frac{8\pi^3\nu}{3hc} \frac{J}{2J-1} N_{J-1}\mu^2 \left(1 - e^{-\frac{h\nu}{kT_{\text{ex}}}}\right) \tag{3.39}$$

where $N_{J-1} = \int n_{J-1}ds$ the column density of the lower level with the rotational quantum number $J-1$.

Now, combining Eqs. (3.38) and (3.39) one can describe the column density of the lower level by:

$$N_{J-1} = \frac{3hc}{8\pi^3\nu} \frac{2J-1}{J} \frac{1}{\mu^2} \left(1 - e^{-\frac{h\nu}{kT_{\text{ex}}}}\right)^{-1} (\mathcal{J}_\nu(T_{\text{ex}}) - \mathcal{J}_\nu(T_{\text{CMB}}))^{-1} \int T_B d\nu. \tag{3.40}$$

The total column density can be defined with help of the partition function

$$Z = \sum_{J=0}^{\infty}(2J+1)\exp\left(-\frac{hB_eJ(J+1)}{kT_{\text{ex}}}\right) \tag{3.41}$$

and is for the $J - 1$ energy level:

$$N = N_{J-1}\frac{Z}{2J-1}\left(e^{\frac{h\nu}{kT_{ex}}}\right). \tag{3.42}$$

Combining Eqs. (3.40) and (3.42) the total column density can finally be expressed as a function of the two variables T_{ex} and brightness temperature T_B,

$$N = \frac{3h}{8\pi^3\mu^2}\frac{Z}{J}\frac{\exp(\frac{h\nu}{kT_{ex}})}{[1-\exp(-\frac{h\nu}{kT_{ex}})]}(\mathcal{J}_\nu(T_{ex}) - \mathcal{J}_\nu(T_{BG}))^{-1}\int T_b\mathrm{d}\nu. \tag{3.43}$$

Note that the following substitution was made:

$$\int T_B\mathrm{d}\nu = \frac{\nu}{c}\int T_B\mathrm{d}\nu. \tag{3.44}$$

Thus, in the end, the calculation of the column density of a certain molecule from one transition only via Eq. (3.43) requires that the excitation temperature, its permanent electric dipole moment, and the partition function Z of the molecule is known. Note, that the assumption of LTE is necessary as under these conditions the excitation temperatures of all levels of a molecule are the same.

3.3.1. Column density of neutral atomic hydrogen

Neutral atomic hydrogen (H I) has a hyperfine transition that emits at a wavelength near 21 cm. The transition is due to a change in the relative spin (parallel, anti-parallel) between nucleus and electron of the hydrogen atom. This system is a true two state system. The CMB plays a dominant role in the excitation of H I and it is safe to assume that interstellar H I follows a Boltzmann distribution in thermodynamic equilibrium for which $g_u = 3$ and $g_l = 1$ and consequently $n_u = 3n_l$. Thus, the total number of hydrogen atoms (per unit volume) are $n_H = \frac{4}{3}n_u$. Assuming a low optically thickness of the emitting gas and that T_{ex} stays constant along the line of sight one can solve the radiative transfer equation for H I, such that the column density of the emitting gas can be determined from the brightness temperature alone. This is for example shown in detail by de Boer (2007) and Rohlfs & Wilson (2000). The resulting relation is:

$$N_H = 1.823 \cdot 10^{18} \int T_{mb}\mathrm{d}\nu. \tag{3.45}$$

with $\int T_{mb}\mathrm{d}\nu$ in $\mathrm{K\,km\,s^{-1}}$. Due to the large amount of H I in the ISM the 21 cm line may become optically thick. In this case the line radiation may be afflicted by self-absorption, which has to be kept in mind when using this relation.

Chapter 4.

Photodissociation regions (PDRs)

Photodissociation regions are nearly omnipresent in the cold ISM. Their complex chemistry and structure governs the abundance of many molecules and provides the means for the gas to become dense and cool enough to eventually form stars. Nowadays complex computational models exist that allow us to interpret observed molecular data and determine physical conditions of the emitting regions. In the analysis presented in this thesis PDR-models are used to investigate the influence of metallicity on the observed tracers of gas. This chapter introduces the basic concepts of the physics and chemistry in photodissociation regions following work from Hollenbach & Tielens (1999); Zielinsky (1999); Tielens (2005); Draine (2011).

4.1. Introduction

The parts of the ISM in which far-ultraviolet photons (FUV) ($6\,\mathrm{eV} < h\nu < 13.6\,\mathrm{eV}$) dominate the chemistry and heating of the gas are called Photodissociation regions (PDRs). The classic example of a PDR is situated in the vicinity of hot, young, O and B[1] stars. Such a PDR resides just beyond the Strömgren-spheres of these stars in which ultra-violet photons $h\nu > 13.6\,\mathrm{eV}$ ionize hydrogen atoms and produce so called "H ɪɪ-regions". However, PDRs are not only present in these very energetic environments. The average interstellar radiation field (ISRF) caries already enough FUV-photons to produce PDRs on the surfaces of molecular clouds, even if these are not associated with star formation. Also planetary nebula, protoplanetary disks and regions around cool stars are examples of PDRs. In extragalactic studies, photon-dominated regions can be encountered as well, and active and interacting galaxies can develop large photon-dominated regions (e.g. M82 see Fig. 4.1). Indeed, PDRs are ubiquitous in the ISM and actually "all of the atomic and at least 90% of the molecular gas in the Galaxy is in PDRs" as stated by Hollenbach & Tielens (1999). The small part of the molecular gas that is not considered to belong to PDRs resides inside dense star forming cores of molecular clouds where the FUV-radiation is too strongly attenuated to play a role.

The structure of PDRs is controlled by the intensity of the FUV-radiation. The FUV-radiation dissociates and ionizes atoms and molecules and also heats dust-grains and large molecules[2], and therefore drives the chemistry inside a cloud. However, the

---

[1] Stars are classified by their spectral type into seven main categories, i.e. O, B, A, F, G, K, M. This order is a sequence in mass and temperature where O-type stars are the hottest and most massive ones. For comparison: our sun is a G star.

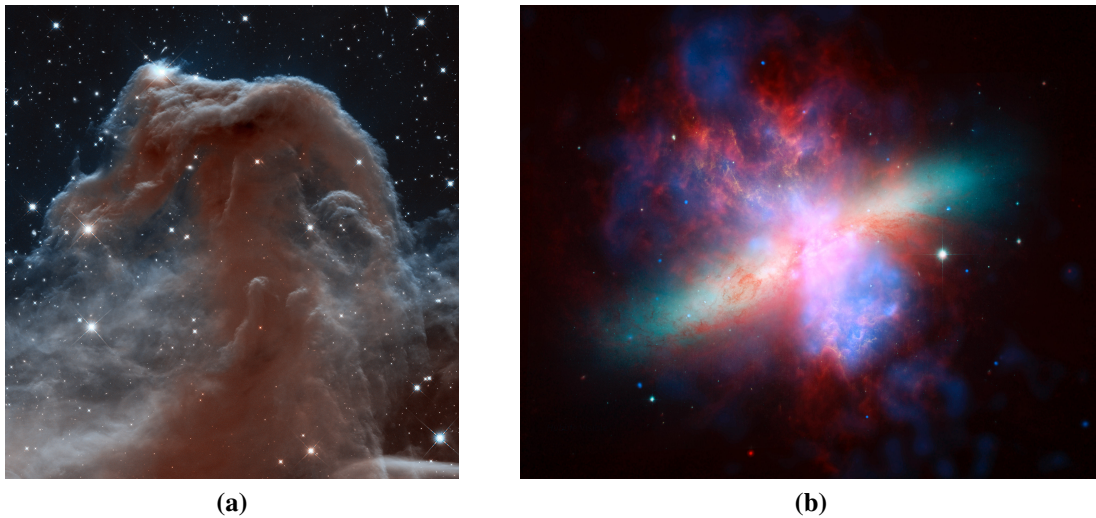[2] and subsequently the gas, as discussed in Section 4.3.1

(a)   (b)

Figure 4.1.: Examples of PDRs. a) The Horsehead Nebula observed with the Hubble Space Telescope (HST) in the near-infrared at 1.1 µm (*blue/cyan*) and 1.6µm (*red/orange*) with the Wide Field Camera 3 (NASA/ESA/Hubble Heritage Team (AURA/STScI)); b) the galaxy M 82 shown in a multi-color composite image combining Chandra x-ray (*blue*) *Spitzer-IRAC* infrared (*red*) and HST Hα (*orange*) as well as visible light (*yellow-green*) observations (NASA/JPL-Caltech/STScI/CXC/UofA/ESA/AURA/JHU).

deeper the FUV-radiation penetrates a cloud, the more it becomes attenuated through absorption by dust and self-shielding from molecules. This has direct influence on the abundances of molecular or atomic species in a specific point of the cloud. The abundances depend on the local balance between formation and destruction processes for the individual species, which in turn depend (seldom in a linear way) on the local FUV intensity. Although this holds for all atomic and molecular species present in a PDR, the three transitions zones in which the bulk of the hydrogen, carbon and oxygen content change from atomic/ionized to molecular form have the largest influence on the structure of a PDR. These transitions create distinct layers and give rise to the typical PDR structure depicted in Fig. 4.2. The different layers also resemble different chemical zones (Section 4.4.2).

Studying PDRs one has to be aware that the variations of a certain cloud parameter does seldomly affect the abundance and emissivity of a certain species in a linear or intuitive way. For example a lower elemental abundance of nitrogen does not necessarily lead to a lower abundance of all of the nitrogen-bearing molecules due to details in the chemical network (cf. Section 4.4). Even if the abundances are lowered the emissivity of these molecules does not have to be lower as well, since the excitation and radiative transfer conditions may change (cf. Section 4.3). To cope with this complexity, models of PDRs (cf. Section 4.5) are necessary that incorporate detailed chemical networks, full radiative transfer, dust-emission and heating, as well as the initial elemental abundances to produce predictions of line-strengths. These line-strengths can then can be compared to observations to deduce the physical properties of the PDR.

In the following sections, the properties of PDRs are introduced in detail. In Section 4.2 the concepts of the optical extinction and the interstellar radiation field that
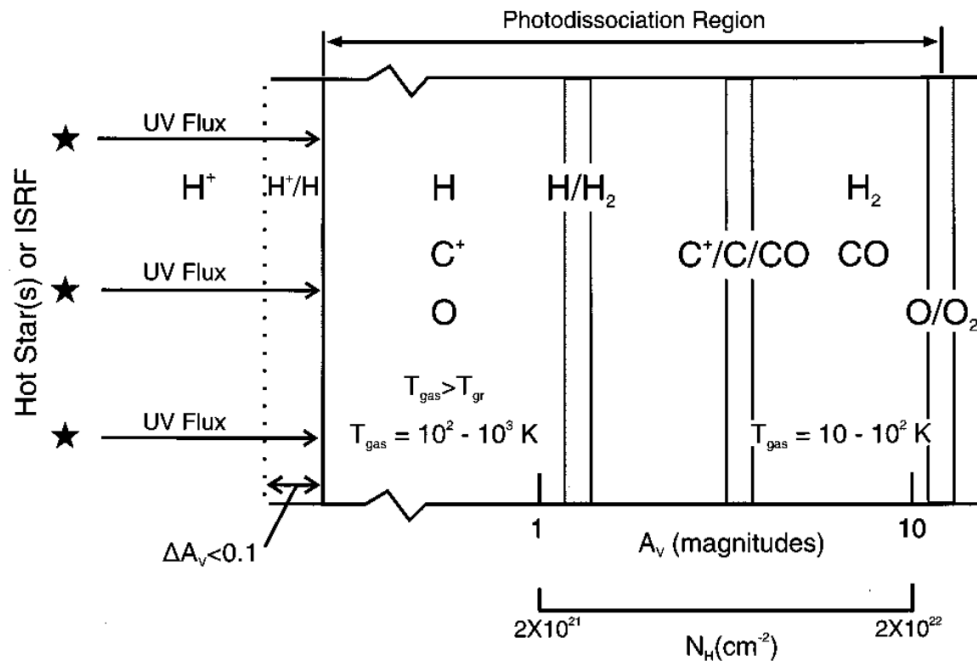
Figure 4.2.: Sketch of an photodissociation region that is illuminated from the left by an ultraviolet field. The PDR spans the regime from the mainly atomic surface to the depth $A_v \simeq 10$ at which photoionization of O_2 stops to be dominant. (Hollenbach & Tielens, 1999)

are needed for the description of PDRs will be introduced. The following Section 4.3 discusses the energy balance while Section 4.4 focuses on the chemistry inside PDRs. Section 4.5 discusses approaches to construct computational models of PDR regions and shortly introduces the Meudon PDR code that has been used later in this thesis.

4.2. Basic concepts

In this section the concept and nomenclature of the optical extinction A_v and the interstellar radiation field (ISRF) are introduced, which will be used in the discussion of PDRs in the following sections.

The visual extinction A_v It is common to parametrize the depth into a cloud in terms of the visual extinction A_v, i.e. the extinction measured at a wavelength $\sim 5550\,\text{Å}$. The extinction is caused by the dust column density that is present until a certain depth and can be expressed as:

$$I_V = I_{V0}10^{-(A_v v/2.5)}, \tag{4.1}$$

where I_V the visual intensity at a specific A_v, I_{V0} the incident intensity and, A_v expressed in magnitudes (mag). Therefore, $A_v = 1$ mag, for example, corresponds to a reduction of the intensity by a factor 2.5. If a constant gas-to-dust ratio is assumed one can correlate A_v with the hydrogen nucleus column density that is about $N_H = 2 \times 10^{21}$ cm^{-2} for $A_v = 1$ mag.

The interstellar radiation field   The far-ultraviolet range of the electromagnetic spectrum, which is of importance in PDRs is defined as light with energies in the range 6–13.6 eV. Light in this range comes from stars. The intensity of the FUV-radiation field is usually given in multiples of the average interstellar radiation field (ISRF) observed in the solar neighborhood. In the literature mainly the two estimates of the average ISRF presented by Habing (1968) and Draine (1978) are used for that purpose. Habing (1968) estimated the intensity of the UV-field from observations at $h\nu =$ 12.4 eV ($\lambda = 1000$Å) to be $\nu u_\nu \approx 4 \times 10^{-14}$ erg cm^{-3}. Habing (1968) further estimated the intensity of the UV-field at 1400, and 2200 Å. Integrating this spectrum between 6 eV and 13.6 eV results in an energy density of $u(6\text{–}13.6\,\text{eV}) = 5.29 \times 10^{-14}$ erg cm^{-3}. It is common to express other estimates of the radiation field relative to the estimates of Habing (1968) for which the following parameters;

$$\chi_{\text{habing}} = \frac{(\nu u_\nu)_{12.4\,\text{eV}}}{4 \times 10^{-14}\text{erg cm}^{-3}}, \tag{4.2}$$

and

$$G_0 = \frac{u(6\text{–}13.6\text{eV})}{5.29 \times 10^{-14}\text{erg cm}^{-3}}, \tag{4.3}$$

are defined. The first, χ, is used to describe estimates of the FUV-field around 12.4 eV and G_0 is used for the integrated spectrum between 6-13.6 eV.

The second estimate of the FUV flux that is often referred to in the literature is the "Draine field". Note that in the literature the letter χ is sometimes used as well to express the FUV-field strength in terms of the Draine field. In Draine (1978) the FUV-field is estimated from a best-fitting polynomial to a number of previously published estimations by other authors and the estimate result in $G_0 = 1.69$ and $\chi = 1.71$. Therefore, values given in multiples of the Draine-field are a factor of about 1.7 larger than values given in multiples of the Habing-field. In the analysis in Chapter 9 the Habing-field and G_0 is used to express the intensity of the FUV-fields used in our PDR-modeling analysis (cf. Section 9.1.4).

4.3. Energy balance

4.3.1. Heating

The FUV-photons entering a PDR heat the gas via multiple processes. These processes document the importance of dust for the physical processes inside a PDR as well as the manifold possibilities for FUV-photons to interact with the gas particles. Below the individual processes are discussed in detail.

Photo-electric effect   The photo-electric effect (PE) is the most important heating process in the neutral ISM. It takes place on large polycyclic aromatic hydrocarbon molecules (PAHs) and dust grains that absorb the FUV-photons. The absorbed energy is transmitted to an electron that gains kinetic energy equal to the photon energy minus the binding energy the electron had. If the kinetic energy is large enough to overcome the gravitational and the Coulomb potential of the PAH or dust grain the electron is

injected into the gas phase. Then its remaining energy is re-partitioned to other gas particles, atoms, molecules and dust grains, through collisions, which heat the gas.

In the case of PAHs all electrons having enough energy to leave the PAH will do so; however, in dust grains, which are much larger, this is not the case. The electron that absorbs the energy of the incident FUV-photon will begin to "wander" about the dust-grain. On its way it will collide with other electrons or atoms of the grain and will loose energy in each encounter. If it encounters the surface on its way, and has enough energy left to overcome the potential of the grain, only then it can leave the grain and participate in the heating of the gas. Actually only about 0.1–1% of the absorbed far-ultraviolet energy is converted into energetic electrons that heat the gas (Hollenbach & Tielens, 1999). The rest of the energy heats the dust grains and is subsequently re-emitted in the infrared (IR), giving rise to the dust-SED emission (cf. Section 3.2.1).

The efficiency of photoelectric heating (ϵ_{PE}) depends, among others, on the charge of the grain; the higher it is, the larger is the Coulomb potential that electrons have to overcome to leave the grain. Subsequently, those electrons that do leave the grain end-up with smaller kinetic energies. In other words, the heating efficiency depends on the rate of photoionization over recombination: $\gamma \propto G_0/n_e$ where n_e is the electron density. If the ratio is small, grains and PAHs are predominately neutral and the heating efficiency is largest. Therefore, ϵ_{PE} depends on the grain size distribution. Smaller grains are able to heat the gas more efficiently as their potential well is less deep and it is easier for the electrons to encounter the surface and leave the grain.

Photo-pumping[3] of H$_2$ In the predominantly atomic parts of a PDR, the existing H$_2$ molecules can be vibrationally excited through photo-pumping. In dense PDRs the accumulated energy can be released through collisional de-excitation that in turn leads to an increase in temperature of the gas. Similarly, at larger A_v photo-pumping of the [OI] fine-structure line becomes an important heating source.

Photo-dissociation of H$_2$ A second way for H$_2$ to participate in the heating processes is its own photo-dissociation, which results in two single H atoms with excess kinetic energy.

IR-radiation heating and gas-grain collisions   As mentioned above the dust is heated through the FUV-radiation. However, at the same time the dust attenuates the FUV-radiation, such that eventually in larger depths of PDRs the FUV-radiation field does not contribute significantly to the dust-heating anymore. In these parts the IR-radiation of the outer dust-layers can be an important dust heating-source. The gas and dust temperatures are coupled through collisions. If the temperature of the dust is higher than that of the gas, collisions between both parties lead to heating of the gas. However, if the dust is cooler this process is a cooling mechanism (cf. Section 4.3.2) for the gas.

Photoionization of C-atoms   Like the photo-electric heating, the photo-ionization of C-atoms produce electrons that are injected into the gas-phase. Since H atoms can

---

[3]Subsequent absorption of photons to populate higher levels of vibrational states.

not be ionized, this process is the main source of free electrons in PDRs (Tielens, 2005).

Cosmic rays   At large depth into clouds, where the FUV-radiation is largely extinct, ionization through cosmic-rays becomes important since cosmic-rays can penetrate clouds much deeper (up to $\sim 100\,A_\mathrm{v}$). Gas particles such as He, H_2 and HD can be ionized by cosmic-ray protons with high energies (2-10 Mev). Again the freed electrons collisionally heat the gas. The efficiency of this effect depends on the composition, ionization degree and density of the gas (Röllig et al., 2007).

Turbulence and chemical heating   are further possible heating mechanisms (cf. Röllig et al. (2007)).

4.3.2. Cooling

The most important gas coolants in the surfaces of PDRs are atomic fine-structure lines in the far-infrared of which [C II] 158 μm, [O I] 63μm, [O I] 146μm, [Si II] 35 μm, [C I] 609μm, [C I] 370 μm are the most prominent. At higher depths also molecular rotational transitions, especially of CO and H_2, but also from OH and H_2O, become important. Of the fine-structure lines the [CII] 158 μm is the most important. In denser ($n_\mathrm{H} > 10^4\,\mathrm{cm}^{-3}$) and warmer regions the [OI] 63 μm begins to dominate the cooling process (Röllig et al., 2006). The cooling efficiency via a certain line depends on the optical depth of the line as well as the density of the gas. If the transition is optically thin and the density low enough that collisional de-excitation plays no significant role, almost all excitations are followed by a spontaneous emission of a photon. This photon is then able to leave the cloud and take energy away. On the other hand, if the density is high such that collisional de-excitations begin to play a role (cf. critical density Section 3.1.2) or if the line-radiation is optically thick (as is often the case for ^{12}CO in the ISM) a more dedicated radiative transfer treatment is needed to deduce the actual cooling efficiency.

As mentioned above collisions of gas particles with cooler dust grains may become a possible cooling process. This mechanism is more effective at high gas densities. These collisions can heat up the dust, which then radiates the energy away via IR-radiation.

4.4. Chemistry

Although the chemistry in PDRs gradually converges with increasing A_v towards the ion-molecule chemistry (cf. Section 4.4.2) that takes place in dense molecular clouds, throughout most of the PDR it is different. For instance the FUV-photons keep part of the hydrogen in atomic form and carbon ionized throughout a significant part of the PDR. Due to its additional energy, UV-pumped H_2 can overcome activation barriers for certain reactions that are not accessible in the dense parts of molecular clouds. In the same way the higher temperatures in the outer layers of PDRs provide more kinetic energy to overcome the activation barriers of certain reactions.

In this chapter a short overview of the chemical reactions that take place in the ISM in general is given in Section 4.4.2. The change of the chemistry with rising A_v and development of chemical zones is discussed in Section 4.4.2. In Section 4.4.4 the importance of H_2 for PDRs is underlined and it's formation in and influence on the structure of PDRs is outlined. Note also the results of the later PDR analysis in Section 9.1.2 where the formation and destruction pathways of HCN and HCO^+ in a specific PDR cloud model from the Meudon PDR code (Section 4.5.1) are investigated in detail.

4.4.1. Chemical reactions in the ISM

This section is based on the line-of-arguments in Tielens (2005) and Draine (2011). Two classes of chemical reactions in the ISM exist, those that occur in the gas-phase and those happening on the surface of dust-grains. Formation in the gas-phase of the ISM basically occur through the following reaction types:

Neutral-neutral reactions have high activation barriers that can not be overcome by typical molecular gas with temperatures below $100\,\mathrm{K}$ and are therefore mainly of importance in warm gas. Such gas may be found, amongst others, in dense PDRs around luminous stars. Nevertheless, UV-pumping (cf. Section 4.3.1) can help to overcome the activation barrier by which certain neutral-neutral reactions may be aided. One example reaction is $O + H_2 \longrightarrow OH + H$.

Ion-molecule reactions occur, in contrast to neutral-neutral reactions two orders of magnitude faster and have lower activation barriers. These are the dominant form that take place in the cold gas-phase in molecular clouds. Due to the high reaction rates already a small ionization degree can effectively drive the chemistry. In cold, dense-regions where no or only few FUV-photons exist, ionization may be provided by cosmic rays.

Charge-transfer Only one such reaction is important in the chemistry of the interstellar medium: $H^+ + O \rightleftharpoons H + O^+$. It is however of importance as this reaction activates chemical pathways incorporating the oxygen ion O^+.

Dissociative electron recombination In these reactions molecular ions recombine with electrons and form an excited state of their neutral counterpart, which in turn can use its excess energy to dissociate.

Associative attachment The reaction takes place between anions and atoms which collide and stabilize through emission of an electron. The only such reaction that plays a role in ISM chemistry is $H^- + H \longrightarrow H_2 + e$, but cf. Section 4.4.4.

Radiative association When two atoms (say A and B) combine to an excited state AB^* they have to emit a photon or translate its excess energy to a third body through a collision to become stable and not dissociate again. A three-body encounter in the
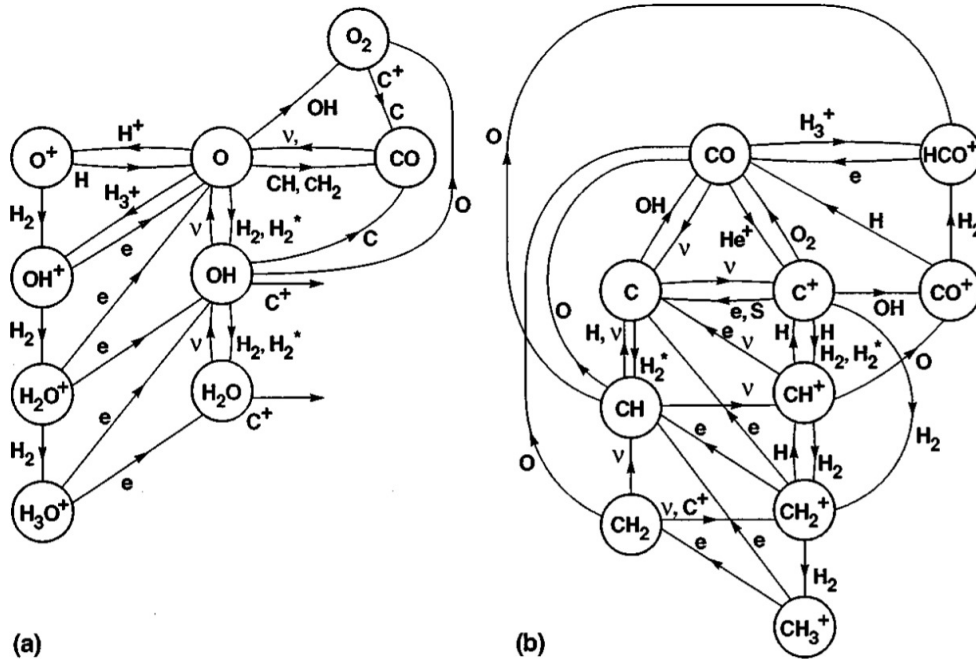
Figure 4.3.: Most prominent PDR chemistry reactions of (a) oxygen-bearing and (b) carbon-bearing compounds. Hollenbach & Tielens (1999)

ISM is, however, very unlikely due to the very low density. Therefore only molecules with excited states with allowed radiative transitions can form in the gas phase. This is where dust-grains comes into play. Since dust grains can act as a catalyst taking up excess energy, reactions on the surface of dust-grains make e.g. radiative association reactions possible. Thus, reactions that are not available in the gas phase can occur on the grains. The most prominent example is the formation of H_2 which is discussed in Section 4.4.4 and is used as an example for the formation process on the dust-grains.

4.4.2. Chemical zones

For this section (Tielens, 2005) serves as general reference.

Due to the changes of abundances of molecular and atomic species, differences in FUV-field as well as the ionization degree for different values of A_v, a PDR develops different chemical zones, in each of which chemical reactions occur with different priority. The major sign-post for changes in the chemistry are the three transition zones in that the bulk of hydrogen, carbon, and oxygen content change their predominant form from atomic to molecular, i.e. $H \rightarrow H_2$, $C^+ \rightarrow C \rightarrow CO$ and $O \rightarrow O_2$ (cf. Fig. 4.2).

The establishment of these transition zones results from the extinction of the FUV-field. With increasing depth the radiation field becomes more and more attenuated by the dust, the ionization degree as well as the photoionization rate decreases and eventually a molecular species can become abundant enough to become "self-shielding". This is to say that outer layers of the cloud block all of the photons that are able to photodissociate this molecule. If other destruction mechanisms do not play a major role, this molecular species can then become the predominant form over their atomic/ionized counterparts. The actual depths in that these transitions occur, depend on a variety of
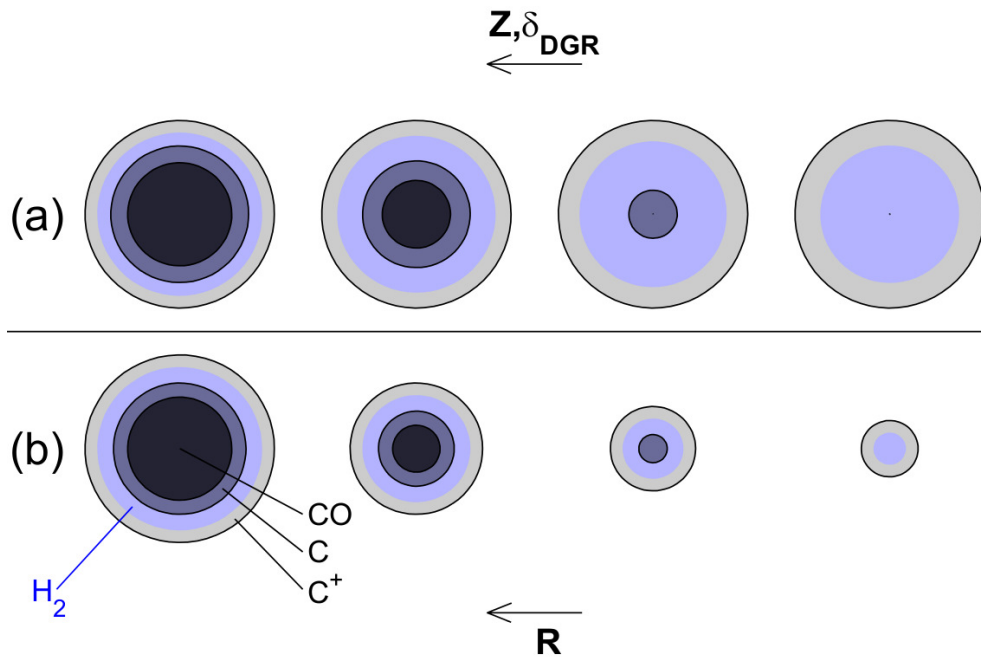
Figure 4.4.: Influence of metallicity and cloud size on the CO (*dark blue-grey*), C (*light blue-grey*), C$^+$ (*light gray*) , as well as H$_2$ (*blue*) content of a clump in a uniform radiation field. In (a) The effect of increasing metallicity (from *left to right*) for a cloud with constant size is shown, while (b) shows the effect of the increase in cloud size for a constant metallicity. (Bolatto et al., 2013)

parameters of the cloud; one major influence is the energy deposition per hydrogen nucleus $P = G_0/n_H$ but also the metallicity plays a role. The transitions occur approximated at $A_v \sim 2$ for H/H$_2$, $A_v \sim 4$ for C$^+$/C/CO and $A_v \sim 8$–10 for O/O$_2$ (Tielens, 2005). The change of chemical reactions between different zones in a PDR is therefore due to a variety of variations with increasing A_v that go hand in hand with variations in:

- the FUV-field strength,

- the elemental/molecular abundances,

- the ionization degree, i.e. amount of free electrons,

- changes in temperature and density.

In the surface of a PDR at, shallow depths where the FUV-flux is still high, mostly atomic species such as H, C$^+$ and O exist and radicals[4] dominate the chemical pathways. The abundance of molecules is restricted due to photodissociation. After the C$^+$/C/CO transition much less radicals are present and the temperature and abundance of vibrational excited H$_2$ has dropped, which means that reactions with higher activation barriers are less accessible. Finally, for very large depths, the chemistry becomes the typical ion-molecule chemistry of cold-dense molecular clouds that is mainly driven by comsic-ray ionization.

---

[4]A very reactive atom with an unpaired electron.

The chemistry in a PDR is a complex network of all possible reactions that are connected through their ingredients and products, which in turn may serve as ingredient to other reactions. In Fig. 4.3 (Hollenbach & Tielens, 1999) the most important chemical reactions of oxygen- and carbon-bearing molecules in PDRs are shown. This is however but a part of the possible reactions and nitrogen, sulfur and silicon compound chemical reactions are not shown at all.

4.4.3. Influence of metallicity

Changes in metallicity (Z) influence the elemental abundances as well as the abundance of dust in molecular clouds. Lower metallicity regions, have less dust and thus a higher gas-to-dust ratio. As a consequence the FUV-photons can penetrate the clouds deeper and drive the transition regions to larger depths. In the extreme case this means that in clouds of the same size, but different metallicity, the carbon atoms might be found in CO for a sufficiently high metallicity or as neutral C atoms for a somewhat lower metallicity. For a very low metallicity they might even remain ionized throughout the cloud. This process is depicted in cf. Fig. 4.4. C^+ is the main supplier of electrons and therefore the metallicity also affects the electron density of the clouds which in turn influences the recombination cooling efficiency (Röllig et al., 2006). Also, the heating efficiencies depend on the metallicity in a rather complex way (cf. Table 1 in Röllig et al. (2006)). One observational feature that hints at a lower metallicity is a higher [CII]/CO(1–0) line ratio due to the larger C^+ zones.

4.4.4. Molecular hydrogen

This section sketches the formation processes of molecular hydrogen H_2 based on the work from Tielens (2005).

A key role in interstellar chemistry falls to molecular hydrogen (H_2) as this molecule is an intermediary[5] for many gas phase species. Although H_2 can form in two ways in the gas phase, both reactions occur at very low rates. One possible way to form H_2 is radiative association (cf. Section 4.4.2) where two H atoms combine to an excited H_2^* molecule, which then has to get rid of the excess energy. Radiative transitions in homonuclear molecules are however strongly forbidden such that this reaction only occurs with a very slow rate $\lesssim 10^{-23} \text{cm}^3\text{s}^{-1}$ (Tielens, 2005). The second possibility is associative detachment, where an H atom reacts with an H^- ion to produce H_2 and an electron. This formation channel however is also very slow[6] and both processes together can not account for all H_2 present in the ISM. Therefore it is generally thought that H_2 forms to a large part on the surface of dust-grains. H-atoms that collide with a dust-grain may stick to it and afterwards "wander" about it's surface. If by chance two H-atoms meet they may form an excited form of H_2^*. The dust-grain serves as a catalyst taking up the excess energy of this compound. A part of this energy is used to evaporate the hydrogen molecule from the grain-surface back into the gas-phase. This is however only the short version of the story, as the details of this process are more

---

[5]A product of a reaction that is used in a following reaction to form the final product.

[6]Nevertheless, it may have been important to form the first H_2 molecules in the early universe before the presence of dust.

Table 4.1.: A selection of PDR codes that have been benchmarked against each other as presented in Röllig et al. (2007).

Model Name	Author
Cloudy	Ferland et al. (1998); Abel et al. (2005); Shaw et al. (2005)
COSTAR	Kamp & Bertoldi (2000); Kamp & van Zadelhoff (2001)
HTBKW	Tielens & Hollenbach (1985); Kaufman et al. (1999)
	Wolfire et al. (2003)
Kosma-τ	Stoerzer et al. (1996); Bensch et al. (2003); Röllig et al. (2006)
Lee96mod	Lee et al. (1996)
Leiden	Black & van Dishoeck (1987); Jansen et al. (1995)
	van Dishoeck & Black (1988)
Meijerink	Meijerink & Spaans (2005)
Meudon	Le Petit et al. (2006); Le Bourlot et al. (1993)
Sternberg	Sternberg & Dalgarno (1989, 1995)
	Boger & Sternberg (2005)
UCL_PDR	Taylor et al. (1993); Bell et al. (2005)
	Papadopoulos et al. (2002)

complex and not entirely well understood. This process depends on the temperature and the composition of the dust as well as the abundance of the reactants that all may change the sticking probability of the H-atoms on the grain and their mobility on the surface.

4.5. Models of photodissociation regions

PDRs are complex: the chemical network of PDRs depend on the radiative transfer of the gas and dust particles, which in turn are coupled through collisions. It is therefore by no means straightforward, to relate observed quantities with physical properties of PDRs. This makes computational models necessary, with which observations can be compared. This section gives a short overview over existing PDR models following the work of Röllig et al. (2007). In Section 4.5.1 the model that is used later in this thesis to analyze line emission from giant molecular clouds in M 33 – the Meudon PDR code – is introduced.

A number of different PDR models exist; see Table 4.1 for a selection. Most of these models have been developed with a different use-case in mind, e.g. to model a certain type of region such as planetary disks or diffuse clouds, or to include a detailed treatment of the physical and chemical processes. As described above, PDRs are complex regions with clumps of higher density gas embedded in a more diffuse medium. Therefore, every model needs to make simplifying assumptions in geometry and/or physical as well as chemical processes. This is not least due to computational limitations. The two most common geometries used in PDR models are shown in Fig. 4.5. The first assumes a 1-D slab of gas that is illuminated from one or both sides by an uni-directional (Fig. 4.5 a) or isotropic radiation field (Fig. 4.5 b); the second a spherical structure. For the latter only uni-directional illumination fields are used.
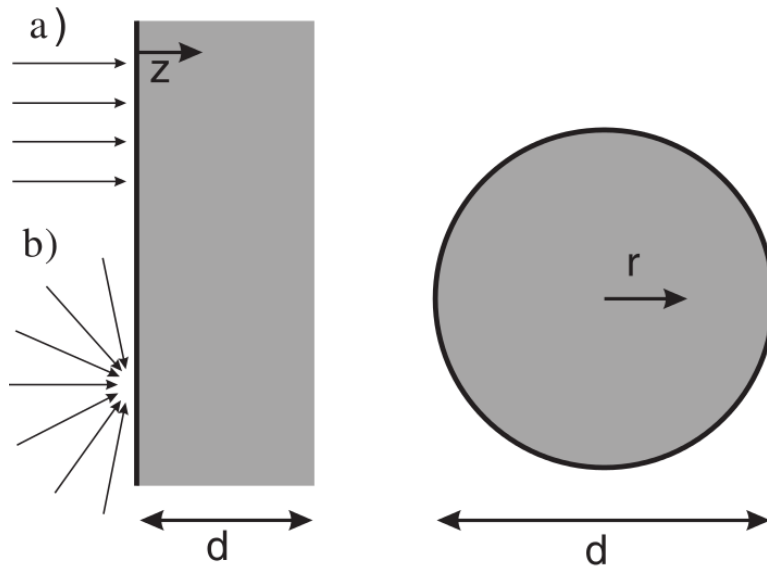
Figure 4.5.: The most common geometries used in PDR codes. *Left*: A one dimensional slab of gas that is a) illuminated by a uni-directional or b) by an isotropic radiation field. *Right*: a spherical model for that only uni-directional radiation fields are used. (Röllig et al., 2007)

Once settled for a geometry one has to make further choices of implementation for the model. *Is the radiative transfer to be wavelength dependent or treated effectively? To which detail self-shielding of molecules and mutual shielding between different species is to be taken into account?* Whether the chemical evolution is time-dependent or stationary and how much reactions the chemical network includes, is another variation between different models. The same holds for the inclusion of the heating and cooling of gas and dust as well as whether the contribution of dust to the radiative transfer is considered in the calculations or not. Finally, the models differ in the available input parameters as well as in the output parameters.

Due to the many differences between the existing models one has to be careful when using a certain model to interpret observations and be aware of its limitations. There has been however some work to benchmark a range of models (cf. Table 4.1), which is presented in Röllig et al. (2006). For comparison the models had to be restricted to a more or less common base-set of features. Although not all differences between the models could be removed, Röllig et al. (2006) have been successful to improve the agreement between the different codes for a set of benchmark models. The development of PDR models is still in progress, but as more and more computational power becomes available, models may become also more complex and detailed.

In the following one specific PDR code, the Meudon code, that has been used in this thesis to analyze the observed data and to investigate the influence of changes in metallicity on the emission of dense gas tracers and CO is introduced.

4.5.1. Meudon PDR code

In this section the Meudon code which was used in this thesis to analyze the observation data is introduced. For in-depth details please refer to Le Petit et al. (2006) and Gonzalez Garcia et al. (2008) which are the general reference for this section.

The Meudon code is together with Cloudy the most complex code of the ones listed in Table 4.1 (Röllig et al., 2007). It includes a detailed treatment of the chemistry, radiative transfer, detailed balance and thermal balance of the modeled PDR region and

provides column densities, level populations and intensities for a range of important molecules, together with detailed, position-dependent information of the parameters at every point in the cloud.

The geometry of the Meudon code is a 1-dimensional plane-parallel slab of gas and dust. The dust optical depth τ_ν perpendicular to the plane is used as the spatial coordinate defining the position in the cloud. The slab of gas may be illuminated by a FUV-field from either one or two sides and additionally by a star with a user-definable spectrum. The model is a steady-state code. This means that the calculated conditions represent the state of a cloud after infinite time has passed. The code further includes a sophisticated modeling of the absorption by dust as well as its thermal balance. The actual dust-grain properties e.g. gas-to-dust ratio, the grain mass density and grain size distribution are input parameters to the model (see Table 4.2 for a complete list of input parameters). The dust emissivity is additionally calculated through the DUSTEM code (Compiègne et al., 2008). The attenuation of the FUV-field not only takes the continuum absorption from dust into account but also the effects of photo-ionization of C and S, photodissociation of H_2 and HD as well as of the pre-dissociating lines of CO. A large chemical network it implemented in the code for which the initial elemental abundances can be defined by the user. This permits to model PDR regions with different metallicities.

The different processes that have to be solved, i.e. FUV-radiative-transfer, chemistry, thermal balance and level populations are all inter-dependent on each other. In the model they are, however, calculated sequentially (in the order they are listed here). Therefore the calculation of one model involves iterative calculation of all steps to reach a stable solution. The number of iterations is a user-definable parameter and defaults to 10.

A wide range of parameters of the model, some of which have already been mentioned above, are tuneable by the user see Table 4.2. This makes the code a very flexible tool to model different PDR-conditions. However the assumptions made in the design of the code restrict its usage in certain scenarios. Due to the steady-state nature of the code one can not apply the code to rapidly evolving regions such as young prestellar cores, where time-dependent processes may dominate (Le Petit et al., 2006). Considering the typical timescale of H_2 photodissociation, however, which is $1000/\chi$ yr (Le Petit et al., 2006) where χ is the FUV-field strength in multiples of the Draine field, the assumption of a stationary cloud is valid in most PDRs. For giant molecular clouds in the Milky Way, for example, Murray (2011) reports a typical life time of 27 ± 12 Myr. Last but not least, the geometry makes it impossible to compute strict edge-on PDRs because the line-of-sight becomes infinite in this case.

In Section 9.1.4 and Section 12.5 the Meudon PDR code is used to compare the results of two sets of models, one for solar elemental abundances, the other for M33-type metallicity, to investigate the influence of lower metallicity on the emission of HCN and HCO^+.

Meudon Grid

Long computation times (~6 hours for 10 iterations on a Desktop-PC[7]) are the price for the complexity of the Meudon model. It is therefore time consuming to compute

---

[7]Here, Intel® Core™2 Duo CPU E7300 @ 2.66GHz, 2Gbyte RAM.

larger grids of PDR models with varying physical properties. Therefore, a Python program `MeudonGrid` that employs many computers within a network as well as the individual cores of the CPUs of the PC in parallel to speed up the grid calculations, has been developed in within the work of this thesis. `MeudonGrid` has successfully been used to generate a grid of 336 PDR models for an analysis of HCN and HCO$^+$ emission in M33 presented in this thesis and Buchbender et al. (2013). Calculation of this grid on a single PC without `MeudonGrid` would have taken nearly 3 months of pure calculation time and a lot of effort to start the models by hand and to archive the results. With `MeudonGrid` and in total 16 available CPU-cores on different machines in the IRAM-Granada computer network, it was possible to calculate the grid in about 7 days without further interaction with the program once it was started.

Table 4.2.: User-tune-able parameters of the Meudon-PDR code.

Parameter	Default Value
Chemistry file	chimie08.chi
Number of global iterations	10
Integration limit (Av)	1.00e+00
Initial density	5.00e+02
Radiation field intensity (Left - minus side)	1.00e+00
Radiation field intensity (Right - plus side)	1.00e+00
Additional radiation field source (Star //)	none.txt
Star distance (pc) - negative: left, positive: right	0.000e+00
Cosmic rays ionization rate (10-17 s-1)	5
Initial temperature	70
State equation (0: Cte nH, 1: interpolation, 2: isobaric)	0
Temperature-density profile file	none.pfl
Initial Pressure	1.00e+06
Turbulent velocity (Doppler broadening only)	2.00e+00
Transfer (0: FGK, 2: Full line)	0
Use FGK approximation for J ¿= jfgkh2	0
Line of sight extinction curve	Galaxy
Rv = Av / E(B-V)	3.1
NH / E(B-V) (in cm-2)	5.8e+21
Dust albedo	4.2e-1
<cos(theta)>= g (diffusion anisotropy factor)	6.00e-01
Mass ratio of grains / gas	1.00e-02
grains mass density (g/cm3)	3.00e+00
grains distribution index (MRN)	3.50e+00
Grains minimum radius	3.00e-07
Grains maximum radius	3.00e-05
1 - Activate DUSTEM / 0 - Without DUSTEM	0
H2 formation on grains model (0 is standard)	0
H2 sticking on grain model (4 is standard)	4

Part II.

The dense molecular medium in M 33: A global view

Chapter 5.

Properties of selected giant molecular clouds in M 33

The goal of this thesis is to better understand the emission of HCN, HCO$^+$, ^{12}CO and ^{13}CO, molecular tracers of the molecular diffuse and dense gas, in giant molecular clouds and the influence that metallicity, optical extinction, density, far-UV field, star formation rate as well as spatial scale have on these tracers. To characterize the emission of these molecules over spatial scales of giant molecular clouds and in varying environments, seven GMCs in M 33 have been targeted at different galacto-centric radii. M 33 has been chosen as a target because its proximity (840 kpc) allows to achieve a high spatial resolution, while its low inclination (56°) yields low line-of-sight lengths through its disk.

Note that most extragalactic observations of HCN and HCO$^+$ have so far been restricted to the energetic nuclei of galaxies or to galaxy integrated fluxes. The few exceptions include a study in the disk of M 31 by Brouillet et al. (2005), LMC observations (Chin et al., 1996, 1997, 1998; Heikkilä et al., 1999; Seale et al., 2012), HCN maps of seven Seyfert galaxies by Curran et al. (2001a,b), and HCN mapping along the major axis in 12 nearby galaxies by Gao & Solomon (2004a,b) as well as study of HCN and CO and their ratios in M51 by Kuno et al. (1995).

This chapter presents the data that have been obtained with the 30 m telescope and the derivation of basic properties of the observed GMCs using this and ancillary data, that is available in the scope of the `HerM33es` project. Section 5.1 motivates the observations of the chosen sample of GMCs and sketches its properties. The following Section 5.2 presents the details of the 30 m observations and the data reduction. In Section 5.2 the subsequent results are discussed.

An extensive set of complementary data is available for M 33. Section 5.3 introduces the sub-set that that has been used as complementary data in the analysis in this part as well as in Part III.

In Section 5.4 column densities of the observed lines are derived under assumption of local thermodynamic equilibrium and compared with those found in other sources. The last four sections explain how the atomic (Section 5.5) and molecular mass (Section 5.6), the optical extinction (Section 5.7), and the FUV-field strength (Section 5.8) were calculated for the individual GMCs.
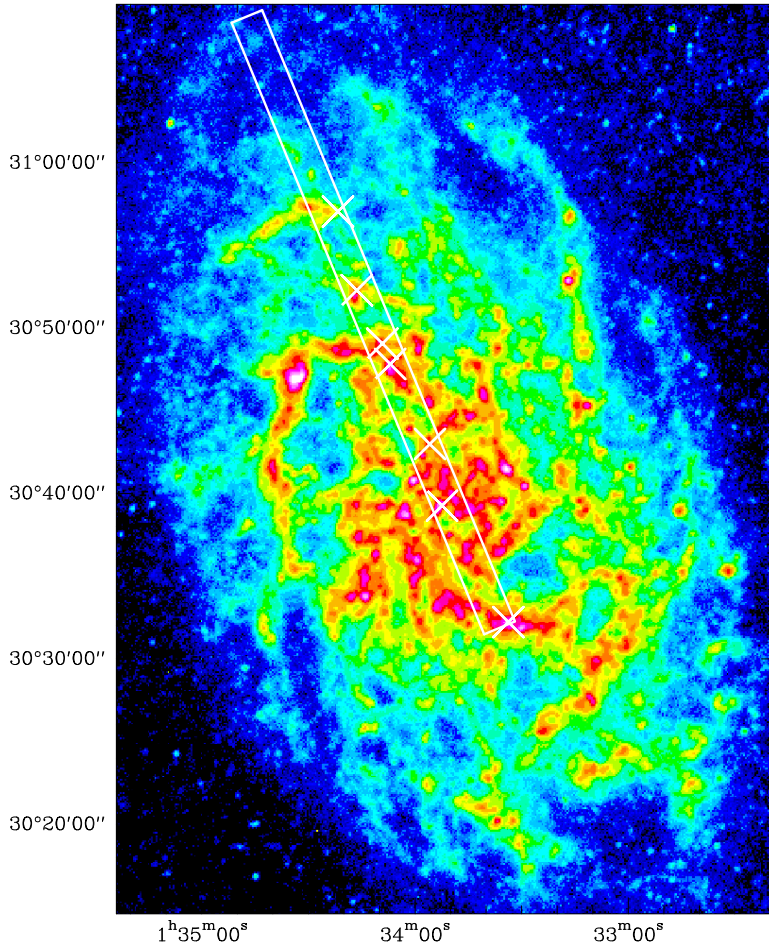
Figure 5.1.: SPIRE 250 μm map of M 33 (Xilouris et al., 2012). The rectangle delineates the $2' \times 40'$ wide strip along the major axis shown in Fig. 5.5. Crosses mark the positions of the observed GMCs. (Buchbender et al., 2013)

5.1. The sample of giant molecular clouds

The following text of this section was published in Section 3 of (Buchbender et al., 2013, B13) deviations are marked in italic fonts.

Motivated by the `HerM33es` project, the GMCs were selected to lie within a $2' \times 40'$ wide strip along the major axis of M 33 shown in *Figs. 5.1 and 5.5* at a range of galacto-centric distances of up to 4.6 kpc. This assures the largest overlap with the FIR line observations made with Herschel. Three of the GMCs (GMC 1, GMC 26, GMC 91) belong to the sample of CO-bright clouds studied by (Rosolowsky et al., 2011) in search of HCN emission. Four additional GMCs (no6, no3, no1, no2) were added to increase the range of studied galacto-centric radii, as well as physical conditions.

The physical condition of the chosen GMCs are diverse. The masses of the molecular gas traced by CO, calculated below using X_{CO}-factors derived individually for every cloud as a function of integrated $^{12}CO\,(1$–$0)$ intensities and total IR luminosity (cf. *Section 5.6*), vary by a factor 130 between 0.1×10^5 (GMC no2) and $13 \times 10^5\,M_\odot$ (GMC 1). The SFRs vary by more than a factor 50 and the far ultraviolet (FUV) field strengths by a factor larger than 20 *(cf. Chapter 7)*. The GMC near the nucleus, GMC 1, is the most massive and shows the strongest SFR, as well as the highest FUV flux, while the outermost GMC no2 at 4.6 kpc radial distance is the least massive in molecular mass and shows only weak activity.

Individual areas of the strip have been mapped in [C ɪɪ] and other FIR lines in the framework of the `HerM33es` project, which will yield additional insight into the properties of the ISM of M 33. The first `HerM33es` papers on [C ɪɪ] focus on the H ɪɪ region BCLMP 302 (Mookerjea et al., 2011) which is associated with GMC no3, and on BCLMP 691 ((Braine et al., 2012)), which lies near GMC no1.

Gratier et al. (2012) identified over three hundred ^{12}CO (2–1) clumps in M 33 and present a detailed view of each individual clump in Hα, 8 μm, 24 μm, and FUV, together with the corresponding HI and ^{12}CO (2–1) spectra and further complementary data. The seven GMCs discussed here are among the identified clumps. In Table 5.1 the corresponding clump numbers are listed.

5.2. ^{12}CO, HCN and HCO$^+$ in M 33

This section was published in Section 2 of B13.

The observations were carried out between December 2008 and July 2012, comprising a total of 109 hours of observing time. In 2008, the now decommissioned A100 and B100 receivers were used that had a bandwidth of 500 MHz and the 1MHz filterbank, to observe each of the four lines individually.

The bulk of the observations were carried out in 2009 employing the new eight-mixer receiver EMIR and its instantaneous bandwidth of 16 GHz in each polarization, connected to the wide-band WILMA autocorrelator backend with 2 MHz spectral resolution. This setup allowed simultaneous observation of HCN with HCO$^+$ and ^{12}CO with ^{13}CO. One advantage of the simultaneous observations is that the relative intensity calibration of the lines is very accurate. The observations were carried out in wobbler switching mode using the maximum available throw of $\pm 120''$ and a switching frequency of two seconds. This mode ensures more stable baselines than the position-switching mode. However, the velocity resolution of about $6\,\mathrm{km\,s^{-1}}$ in the 3 mm band only barely resolves the spectral lines of M 33, which are typically $10–15\,\mathrm{km\,s^{-1}}$ wide (Gratier et al., 2010). The beam sizes are 21″ at 115 GHz and 28″ at 89.5 GHz, corresponding to a spatial resolution of 86 pc and 114 pc, respectively, in M 33 (cf. Table 2.1).

The observations of ^{12}CO and ^{13}CO were repeated in June and July 2012 using position-switching and the FTS spectrometers with an off position outside of the disk of M 33 to exclude the possibility of self-chopping effects in the spectra. The latter were present in some of the earlier wobbler-switched ^{12}CO spectra. Due to the high critical density of the dense gas tracers HCN and HCO$^+$, as well as the observed velocity gradient along the major axis of M 33 (see Table 5.1), it is reckoned that self-chopping is less probable for these lines. Please note that the ^{12}CO data of GMC1, GMC91, and GMC26 are taken from RPG11 who also used position-switching.

All data were reduced using the GILDAS[1] software package. Each scan was inspected and scans with poor baselines or unreasonably high rms values were rejected. Before averaging, linear baselines were fitted and removed. The data were regridded to a common velocity resolution. Spectra were converted from the T_A^* to the T_{mb} scale by multiplying with the ratio of forward efficiency ($F_{\mathrm{eff}} = 95\%$) to main beam efficiency

---

[1]http://www.iram.fr/IRAMFR/GILDAS
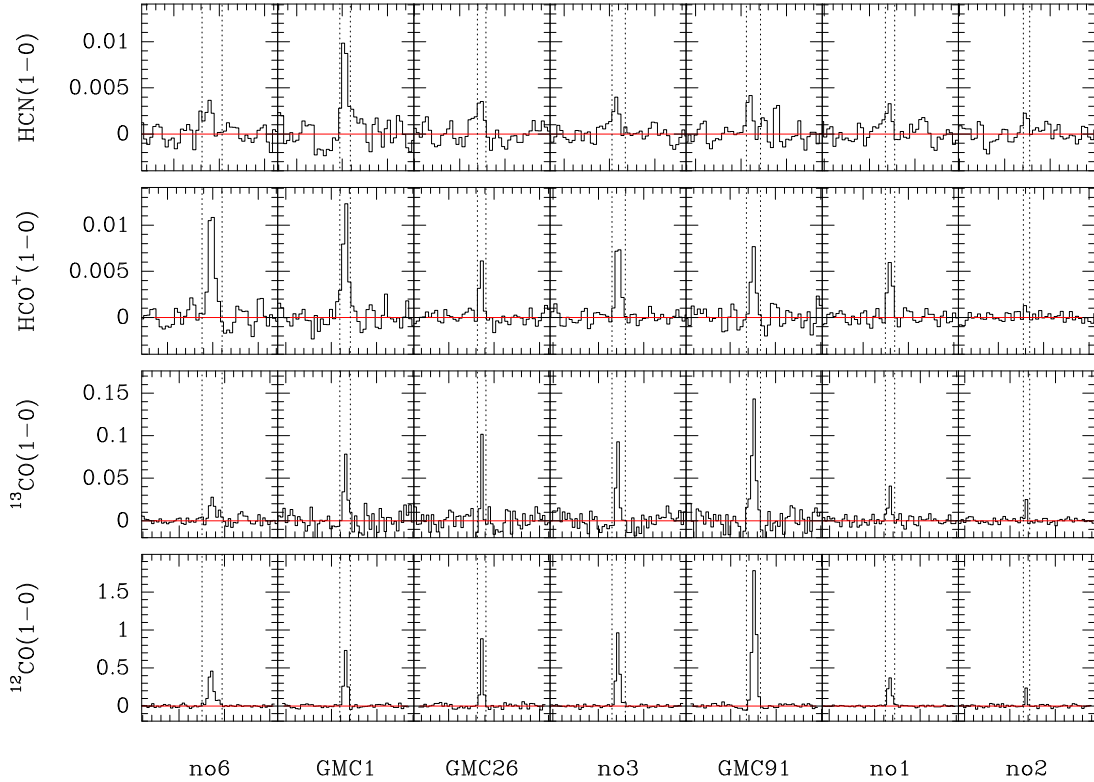
Figure 5.2.: Spectra of the ground-state transitions of HCN, HCO$^+$, ^{13}CO, and ^{12}CO at the positions of seven GMCs along the major axis of M 33 (cf. Fig. 1, 2). ^{12}CO and ^{13}CO have been observed in position switching; HCN and HCO$^+$ with wobbler switching. The spectra are shown on a main beam brightness temperature scale (T_{mb}). The velocity resolution is given by the spectrometer with the lowest resolution, i.e. WILMA, and is 5.4 km s^{-1} in case of ^{12}CO and ^{13}CO, and 6.7 km s^{-1} for HCN and HCO$^+$. Center velocities are listed in Table 5.1. The local standard of rest (`lsr`) velocity displayed covers 300 km s^{-1}. The same velocity range is used to determine the baseline (*red lines*), excluding the line windows determined from ^{12}CO (1–0) (*dotted lines*), cf. Fig. 5.3. (Buchbender et al., 2013).

(B_{eff} = 81%), taken to be constant for the observed 3 mm lines. The reduced spectra are shown in Fig. 5.2.

Integrated intensities were extracted from the spectra on a T_{mb} scale by summing all channels inside a velocity range around each particular line. The velocity range was determined by eye for each position from the full width to zero intensity (FWZI) of the ^{12}CO 1–0 line and is marked in Fig. 5.2. The σ uncertainties of the integrated intensities are determined by measuring the baseline rms ($T_{\mathrm{mb}}^{\mathrm{rms}}$) in a 300 km s^{-1} window centered on the particular line using the corresponding ^{12}CO 1–0 FWZI as baseline window and using

$$\sigma = T_{\mathrm{mb}}^{\mathrm{rms}} \; \sqrt{N} \, \Delta v_{\mathrm{res}} \tag{5.1}$$

with the number of channels N and the channel width Δv_{res}. In case the $1\,\sigma$ value is higher than the typical 10 % calibration error of the IRAM 30 m, the former is used to estimate the observational error for the following analysis. If the integrated intensities are lower than $3\,\sigma$, this value is used as an upper limit. Table 5.1 lists the observed
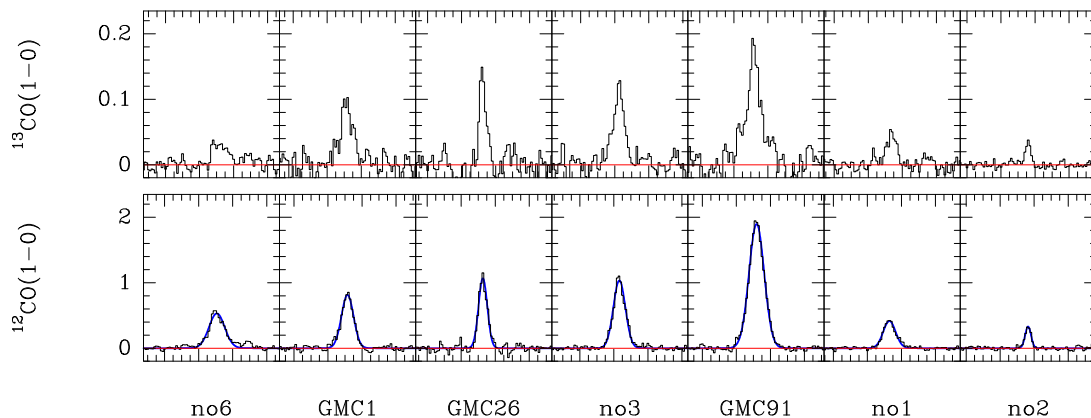
Figure 5.3.: ^{12}CO and ^{13}CO (1–0) spectra at the seven selected GMC positions at high-velocity resolution of $1\,\mathrm{km\,s^{-1}}$. The ^{12}CO spectra of positions GMC 91, GMC 26 and GMC 1 are taken from RPG11. The *blue lines* over-plotted on the ^{12}CO spectra show the Gaussian line fits used to deduce the FWHM of the lines which are listed in Table 5.1. (Buchbender et al., 2013)

intensities. Error estimates are given in parentheses after the integrated intensities in Table 5.1.

5.2.1. Spectra at individual positions: HCO$^+$ and HCN

The text of this section was published in Section 4.1 of B13.

HCO$^+$ is detected at six positions with 6 to $12\,\mathrm{mK}$ peak temperatures and with good signal-to-noise ratios of at least seven; position no2 has not been detected. HCN emission is detected at the same six positions with signal-to-noise ratios of four and better; position no2 is but tentatively detected at a signal-to-noise ratio of 3.5. The HCO$^+$/HCN ratio of line integrated intensities of positions where both molecules are detected varies between 1.1 and 2.5 (Table 5.1). Below, the observed ratios are compared in detail with ratios found in the Milky Way and in other galaxies. Although the integrated intensities for GMC26, GMC1, and GMC91 differ up to a factor of two from the values and upper limits given in RPG11 for the same positions, they are consistent within 3σ of the baseline rms of the observations from RPG11. This discrepancies may be a result of baseline problems in the RPG11 data.

5.2.2. Spectra at individual positions: ^{12}CO and ^{13}CO

The text of this section was published in Section 4.2 of B13.

Emission from ^{12}CO and ^{13}CO is detected at all seven positions, though varying by a factor of more than 15 between GMC no2 and GMC91. The ratio of line integrated ^{12}CO vs. ^{13}CO intensities varies between 9 for GMC no1 and 15 for GMC no6. In Fig. 5.3 show the ^{12}CO and ^{13}CO spectra are shown at a high resolution of $1\,\mathrm{km\,s^{-1}}$. The resolved line shapes are Gaussian and the corresponding FWHMs are given in Table 5.1.
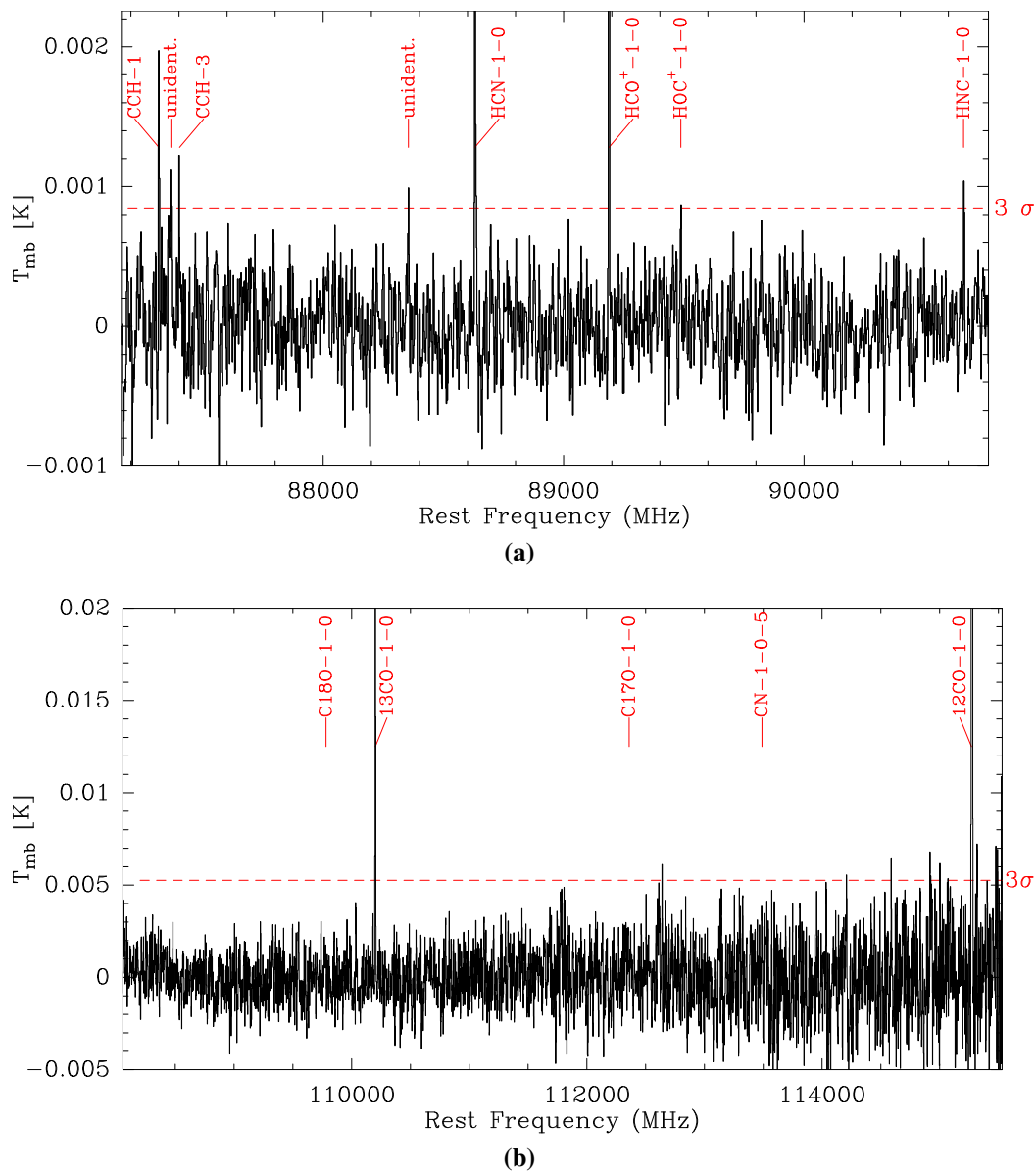
Figure 5.4.: **(a)** Stacked spectrum of all data taken in the frequency range between 87.2 and 90.8 GHz. The *red dashed* line denotes the 3σ value average over the entire baseline. The HCN and HCO$^+$ lines are not shown up to their maximum peak temperature. **(b)** Stacked spectrum of the wobbler switched data taken in the frequency range between 108.1 and 115.5 GHz. The average 3σ value is shown as *red dashed line*. The baseline noise increases with frequency because of the increasing atmospheric opacity. C^{18}O, C^{17}O, and CN are marked but not detected. The ^{12}CO and ^{13}CO lines are not shown up to their maximum peak temperature. (Buchbender et al., 2013)

Table 5.1.: Observed intensities and complementary data.

	GMC no6	GMC 1	GMC 26	GMC no3	GMC 91	GMC no1	GMC no2
Clump number [a]	42	108	128	256	245	300	320
RA [J2000]	01:33:33.77	01:33:52.40	01:33:55.80	01:34:07.00	01:34:09.20	01:34:16.40	01:34:21.77
DEC [J2000]	+30:32:15.64	+30:39:18.00	+30:43:02.00	+30:47:52.00	+30:49:06.00	+30:52:19.52	+30:57:4.99
V_{LSR} [km s^{-1}]	-133.0	-168.0	-227.0	-257.0	-247.0	-266.0	-264.0
R [kpc]	2.01	0.11	0.873	2.18	2.51	3.38	4.56
$I_{^{12}CO\,(1-0)}$[K km s^{-1}]	7.1 (10 %)	7.2 (10 %)	6.9 (10 %)	9.4 (10 %)	21.6 (10 %)	4.0 (10 %)	1.4 (10 %)
FWHM ^{12}CO (1–0)[km s^{-1}] [c]	11 (0.5)	8 (0.2)	6 (0.1)	8 (0.1)	11 (0.1)	9 (0.2)	4 (0.2)
$I_{^{12}CO\,(2-1)}$[K km s^{-1}] [d]	8.9 (15 %)	10.6 (15 %)	7.0 (16 %)	9.4 (15 %)	19.3 (15 %)	6.2 (15 %)	0.7 (15 %)
$I_{^{13}CO\,(1-0)}$[m K km s^{-1}]	468 (12 %)	799 (13 %)	541 (19 %)	772 (13 %)	1690 (10 %)	369 (12 %)	132 (15 %)
$I_{HCO^+\,(1-0)}$[m K km s^{-1}]	205 (10 %)	182 (10 %)	66 (10 %)	119 (10 %)	97 (15 %)	77 (10 %)	< 12
$I_{HCN\,(1-0)}$[m K km s^{-1}]	82 (20 %)	164 (10 %)	56 (16 %)	61 (16 %)	67 (24 %)	56 (17 %)	26 (28 %)
$I_{HNC\,(1-0)}$[K km s^{-1}]	< 43.9	< 44.8	< 15.6	< 22.3	< 47.5	< 25.9	< 20.4
rms [mK] [e]	1.0	1.4	1.0	0.7	1.1	0.9	0.8
$I_{HCO^+\,(1-0)}/I_{HCN\,(1-0)}$	2.5 (0.2)	1.1 (0.1)	1.2 (0.1)	1.9 (0.1)	1.4 (0.3)	1.4 (0.2)	< 0.5
$I_{HNC\,(1-0)}/I_{HCN\,(1-0)}$	< 0.5	< 0.3	< 0.3	< 0.4	< 0.7	< 0.5	< 0.8
$I_{HCN\,(1-0)}/I_{^{12}CO\,(1-0)}$ [%]	1.4 (0.3)	2.9 (0.4)	1.0 (0.2)	0.8 (0.2)	0.4 (0.1)	1.7 (0.4)	2.3 (0.7)
$I_{HCO^+\,(1-0)}/I_{^{12}CO\,(1-0)}$ [%]	3.5 (0.5)	3.2 (0.5)	1.1 (0.2)	1.6 (0.2)	0.6 (0.1)	2.3 (0.3)	< 1.0
$I_{^{12}CO\,(1-0)}/I_{^{13}CO\,(1-0)}$	15.1 (2.4)	9.0 (1.5)	12.8 (2.8)	12.2 (2.1)	12.8 (1.8)	10.8 (1.8)	10.6 (1.9)
L'_{CO} [10^3 K km s^{-1} pc^2]	87.7 (8.8)	85.4 (8.5)	87.9 (8.8)	114.6 (11.5)	248.9 (24.9)	49.8 (5.0)	17.3 (1.7)
L_{TIR}[10^6 $L_\odot$]	4.4 (0.1)	5.9 (0.2)	1.4 (0.0)	2.7 (0.1)	1.3 (0.0)	1.7 (0.1)	0.3 (0.0)
L_{TIR}/L'_{HCN} [10^3]	3.5 (0.7)	2.4 (0.3)	1.6 (0.3)	3.0 (0.5)	1.3 (0.3)	2.0 (0.4)	0.8 (0.2)
L_{TIR}/L'_{HCO^+} [10^3]	1.4 (0.1)	2.2 (0.2)	1.4 (0.1)	1.5 (0.2)	0.9 (0.1)	1.5 (0.2)	> 1.6
SFR [M$_\odot$ Gyr^{-1} pc^{-2}]	35.9 (4.3)	65.0 (7.8)	6.6 (0.8)	13.7 (1.8)	4.0 (0.6)	12.2 (1.7)	1.2 (0.1)
T_{dust} [K]	23.0	25.0	22.0	22.0	20.0	23.0	19.0
X_{CO}	5.1	6.9	1.6	3.2	1.5	2.0	0.3
M_{HI} [10^4 M$_\odot$]	93.9 (14.1)	57.6 (8.6)	40.5 (6.1)	80.0 (12.0)	88.1 (13.2)	52.0 (7.8)	47.8 (7.2)
M_{H_2} [10^4 M$_\odot$]	95.8 (9.6)	126.6 (12.7)	29.9 (3.0)	78.7 (7.9)	82.0 (8.2)	20.9 (2.1)	1.3 (0.1)
M_{dust}[10^4 M$_\odot$]	0.9	0.7	0.4	0.8	0.8	0.3	0.2
GDR	200.7 (18.0)	275.5 (22.9)	166.6 (16.0)	210.5 (19.0)	286.0 (26.2)	238.1 (26.4)	234.0 (34.2)
G_0	37.3 (1.2)	50.7 (1.6)	11.6 (0.4)	23.5 (0.8)	11.3 (0.4)	14.4 (0.5)	2.5 (0.1)
A_v	6.3 (0.6)	6.1 (0.5)	2.3 (0.2)	5.3 (0.5)	5.7 (0.5)	2.4 (0.3)	1.6 (0.2)

Notes. *Top panel*: line intensities are on the T_{mb}-scale and on their original resolutions: 12″ for ^{12}CO (2–1), 24″ for ^{12}CO and ^{13}CO (1–0) and 28″ for HCN and HCO$^+$ 1–0. *Bottom Panel*: line ratios and complementary data are on a common resolution of 28″. [a]^{12}CO (2–1) clump numbers from Gratier et al. (2012); [b]Rosolowsky et al. (2011); [c]FWHMs of Gaussian fits to the high resolution ^{12}CO 1–0 spectra (Fig. 5.3); [d]Gratier et al. (2010); [e]Baseline rms of HCO$^+$spectra at a velocity resolution of 6.7 km s^{-1}. (Buchbender et al., 2013)

5.2.3. Stacked spectra

The text of this section was published in Section 4.4 of B13.

Stacking of all spectra allows improvement on the signal-to-noise ratios and detection of faint lines. Figure Fig. 5.4a shows the stacked spectrum of all data taken near 89 GHz. It was created by shifting all spectra in frequency such that the emission lines align in frequency. Individual spectra were weighted by integration time. In addition to the lines of HCN and HCO$^+$, the resulting spectrum shows detections of CCH and HNC 1–0. The average baseline rms is 0.27 mK at 5.4 km s^{-1} resolution. HOC$^+$ is tentatively detected with an upper limit of 19 m K km s^{-1}, resulting in a lower limit to the HCO$^+$/HOC$^+$ratio of 5.8.

The stacked spectrum centered on 112 GHz (Fig. 5.4b) does not show additional detections other than ^{13}CO and ^{12}CO even after additional smoothing of the velocity resolution. Table 5.3 lists the integrated intensities and upper limits of all detected transitions in the stacked spectrum, as well as their corresponding LTE column densities and abundances, derived as explained in Section 5.4.
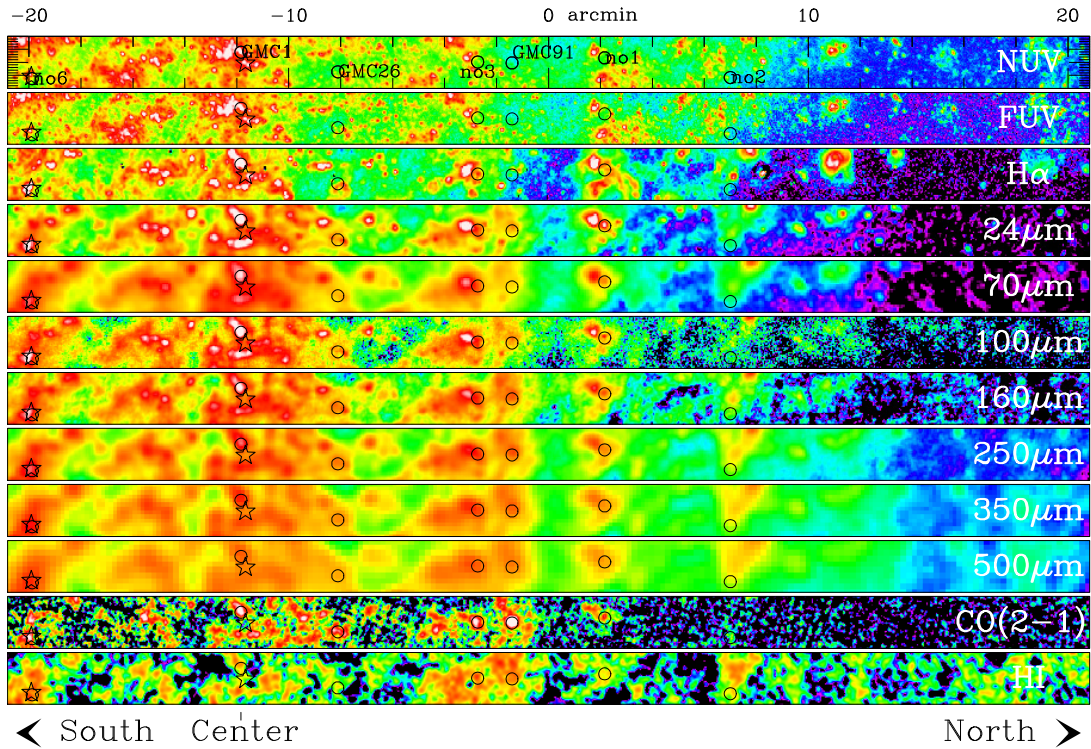
Figure 5.5.: Observed positions towards seven giant molecular clouds (GMCs) within a $2' \times 40'$ strip along the major axis of M 33. The strip extends from $10'$ south of the galactic center to $33.3'$ north. The center of the strip is at 01:34:11.8 +30:50:23.4 (J2000). Circles indicate the 30 m beam size of $28''$ at 90 GHz. Panels show from top to bottom: NUV and FUV *GALEX* data (Thilker et al., 2005); integrated intensities of Hα emission (Hoopes & Walterbos, 2000) 24; 70 μm emission observed with Spitzer (Tabatabaei et al., 2007); continuum emission between 100 μm and 500 μm observed with PACS and SPIRE in the framework of the `HerM33es` program (Kramer et al., 2010; Boquien et al., 2011; Xilouris et al., 2012); ^{12}CO (2–1) 30 mobservation and H I VLA data, both taken from Gratier et al. (2010). All data are shown at their original resolutions. The star symbol denotes the location of the X-ray binaries M 33-X8 near GMC 1 and M 33-X7 near GMC no6 (cf. Section 2.3 and Chapter 14 for more details.). (Buchbender et al., 2013)

5.2.4. Additional detections

The following text was published in Appendix D of B13.

The C_2H (1–0) transition is split into six hyperfine components. In the stacked spectrum, we detected the 3/2–1/2, 2–1 transition, which is the strongest one. To determine LTE column densities of CCH, we estimate the total integrated intensity of the C_2H (1–0) line including all hyperfine components by dividing the result of a Gaussian fit to the detected component by its relative strength, i.e. 0.416 (Padovani et al., 2009).

5.3. Ancillary data

The work of this thesis is settled within the framework of the `HerM33es` project which gave access to an extensive data set of M 33 with which the observations of HCN and

HCO$^+$ could be complemented. Here the data that is used to analyze the seven point-
ings with the IRAM 30 m and the PdBI maps of GMC no3 (Part III) are presented.
While some of the available data only covers small fields or single pointings within
M 33, many data-sets yield a full coverage of the disk of M 33. To analyze the seven
GMCs in the subsequent chapters only maps are used that cover all sources and can
be convolved to 28$''$, i.e. the resolution of the HCN and HCO$^+$ 30 m observations.
A compilation of most of the available maps is shown in Fig. 5.5. This figure shows
the cut along the major axis on that the PACS and HIFI/*Herschel* [C II] and [O I] ob-
servations within `HerM33es` have been concentrated. The rectangle is also shown in
Fig. 5.1 including the seven pointings of the IRAM 30 mobservations. In the following
an overview of the used data ordered declining in wavelength can be found, the last
three entries are maps only used in Part III:

- *GALEX* **Ultra-Violet** Near- and far-UV (NUV/FUV) maps measured with the
  Galaxy Evolution Explorer (*GALEX* (Martin et al., 2005)). The maps have been
  observed and presented by Thilker et al. (2005). The point-spread-function
  (PSF) of *GALEX* has a full width at half maximum (FWHM) of 5$''$. Typical
  1 σ limits for the rms flux sensitivity for the FUV and NUV data are 6.6 and
  2.8×10^{-19} erg s^{-1} cm^{-2} Å (Thilker et al., 2005).

- **KPNO Hα** A Hα emission map has been observed by Hoopes & Walterbos
  (2000) with the 0.6 m Burrel-Schmidt telescope at Kitt Peak National Observa-
  tory (KPNO). The field of view of the image is 1.75 deg$^2 \times$ 1.75 deg^2. The total
  Hα flux observed is 3.6×10^{-10} erg s^{-1} cm^{-2}. In the following an error of 10 % is
  assumed.

- *Spitzer* **MIPS** maps at 24 and 70 μm (Tabatabaei et al., 2007). The maps have
  been observed with the Multiband Imaging Photometer Spitzer (MIPS). The re-
  spective resolutions of the 24 and 70 μm maps are 6$''$ and 18$''$. The *Spitzer*
  Observers Manual v8.0 reports 5 % and 10 % accuracy of calibration, for 24 μm
  and 70 μm respectively.

- *Herschel* **PACS and SPIRE** Continuum emission maps at 100 and 160 μm ob-
  served with PACS and 250, 350 and 500 μm and SPIRE are available in the
  framework of the `HerM33es` *Herschel* key program (Kramer et al., 2010; Bo-
  quien et al., 2011; Xilouris et al., 2012). The resolution of the PACS maps are
  6.7$'' \times$ 6.9$''$ for 100 μm and 10.7$'' \times$ 12.1$''$ at 160 μm, the assumed uncertainty
  is 20 %. SPIRE has a poorer resolution with 18.7$'' \times$ 17.5$''$, 26.3$'' \times$ 23.4$''$, and
  38.1$'' \times$ 35.1$''$ at 250, 350, and 500 μm, respectively, while an error of 15 % is
  assumed (Kramer et al., 2010).

- **IRAM 30 m** ^{12}**CO (2–1)** A work in progress is a full map M 33 in ^{12}CO (2–1) at
  12$''$ resolution observed with the HERA receiver at the 30 m (Braine & Schus-
  ter). Although the final data product is not yet finished, the part of the regions of
  interest that are investigated in this thesis were already available at the time of
  writing, cf. Gratier et al. (2010).

- **H I VLA** data was presented by Gratier et al. (2010). Two version were available
  for this work one at 12$''$ and one at 5$''$. The latter has a much lower signal to

Table 5.2.: LTE column densities at the individual positions. (Buchbender et al., 2013)

	GMC no6	GMC 1	GMC 26	GMC no3	GMC 91	GMC no1	GMC no2
$N(^{12}CO\,(1\text{–}0)\,[\text{cm}^{-2}])$	1.19e+16	1.25e+16	1.14e+16	1.57e+16	3.53e+16	6.69e+15	2.27e+15
$N(^{12}CO\,(2\text{–}1)\,[\text{cm}^{-2}])$	5.82e+15	6.89e+15	4.60e+15	6.16e+15	1.29e+16	4.08e+15	5.05e+14
$N(^{13}CO\,(1\text{–}0)\,[\text{cm}^{-2}])$	1.67e+15	2.96e+15	1.90e+15	2.74e+15	5.87e+15	1.31e+15	4.54e+14
$N(HCO^+\,[\text{cm}^{-2}])$	4.13e+11	3.83e+11	1.32e+11	2.38e+11	1.89e+11	1.54e+11	< 2.29e+10
$N(HCN\,[\text{cm}^{-2}])$	8.64e+11	1.79e+12	5.72e+11	6.38e+11	6.78e+11	5.88e+11	2.59e+11
$N(H_2\,[\text{cm}^{-2}])$ - LTE	1.18e+21	2.09e+21	1.34e+21	1.94e+21	4.14e+21	9.28e+20	3.21e+20
$N(H_2\,[\text{cm}^{-2}])$ - X-factor	2.98e+21	3.95e+21	9.32e+20	2.45e+21	2.55e+21	6.51e+20	4.00e+19
$\log N(^{12}CO\,(1\text{–}0))/N(H_2)$	-5.00	-5.22	-5.07	-5.09	-5.07	-5.14	< -5.15
$\log N(^{12}CO\,(2\text{–}1))/N(H_2)$	-5.31	-5.48	-5.46	-5.50	-5.51	-5.36	< -5.80
$\log N(^{13}CO\,(1\text{–}0))/N(H_2)$	-5.85	-5.85	-5.85	-5.85	-5.85	-5.85	< -5.85
$\log N(HCO^+)/N(H_2)$	-9.46	-9.74	-10.01	-9.91	-10.34	-9.78	< -10.15
$\log N(HCN)/N(H_2)$	-9.14	-9.07	-9.37	-9.48	-9.79	-9.20	-9.09
$N(HCO^+)/N(HCN)$	0.48	0.21	0.23	0.37	0.28	0.26	0.09
$T_{ex}\,[K]$	23	25	22	22	20	23	19

noise ratio than the first, but allows comparison with the high resolution data of GMC no3 presented below in Part III. In Fig. 5.5 the 12″ version is shown. The calibration error for the H I data is assumed to be 15 %.

- **CII** *Herschel* **PACS** [CII] 158 μm maps of the H II region BCLMP302 related to GMC no3 (Mookerjea et al., 2011) are already published. The resolution is about 12″ near 158 μm and the field of view is 47″ × 47″.

- *Spitzer IRAC* maps at 3.6, 4.5, 5.8, and 8,μm (Verley et al., 2007). The maps have been observed with the Infrared array Camera (*IRAC*). The resolutions are 1.4,1.4, 1.5 and 1.7 ″, respectively (*Spitzer* Observers Manual v8.0).

- **555 nm HST** This image has been extracted from the Hubble Space Telescope legacy archive. It was obtained with the Wide Field and Planetary Camera 2 (WFPC2) using the F555W filter that has a central wavelength of 5300 Å and a bandwidth of 1000 Å. The image has been taken under the HST Proposal 11079 by Luciana Bianchi.

5.4. Molecular column densities

5.4.1. LTE Column densities of ^{12}CO,^{13}CO,HCN and HCO$^+$

As has been discussed in Section 3.3 one can estimate column densities from a single emission line under the assumption of LTE and optically thin emission as long as information about the excitational state of the molecules is available. In the following the column densities of HCN, HCO$^+$, ^{12}CO (1–0), ^{12}CO (2–1) and ^{13}CO (1–0) are deduced from their observed 1–0 transitions using Eq. (3.43). In this formulation the excitation is described by the theoretical excitation temperature T_{ex}. In cold and dense regions ($n_H \geq 1 \times 10^4$–1×10^5 cm^{-3}) regions of GMCs the dust temperature T_{dust} and the gas temperature T_{gas} may become coupled and equal (e.g. Goldsmith, 2001). Employing further the assumption that T_{gas} and T_{ex} are equal, here the deduced temperatures of

Table 5.3.: LTE column densities from the stacked spectra. (Buchbender et al., 2013)

	C_2H	HCN	HCO^+	HOC^+	HNC	$^{13}CO\,(1\text{–}0)$	$^{12}CO\,(1\text{–}0)$	$H_2{}^a$
$I\,[\text{m K km s}^{-1}]$	25.1	81.0	110.0	< 18.8	13.7	522.0	6280.0	-
$N[\text{x}]^b$	5.10e+12	8.03e+11	2.11e+11	< 7.10e+10	4.18e+10	1.80e+15	8.55e+15	8.47e+20
$N[\text{x}]/N_{\text{H}_2}{}^c$	-8.40	-9.20	-9.78	< -10.25	-10.48	-5.85	-5.17	1.00

[a] deduced from ^{13}CO; [b] column density; [c] logarithmic values.

the cold dust component from the modified black-body SED fits of each region, presented in Chapter 6, are used as an estimate for T_{ex}. For the stacked spectra the average temperature off all observed positions T_{ex}=21 K is used.

The remaining parameters that are needed to use Eq. (3.43) are the partition function Z and the permanent electric dipole moment μ, which both depend on the molecular species and can be measured in the laboratory. The "Cologne Database for Molecular Spectroscopy" (CDMS) (Müller et al., 2001, 2005) gathers such information and is used to look up the necessary molecule parameters. The molecular electric dipole moment of the observed species are compiled in Table 3.1. The partition function Z (not explicitly listed here) is available on CDMS for discrete temperatures in the range from 2.75 to 500 K for every molecule. The actual value of Z, used for the calculations, is interpolated to the assumed excitation temperature at each position. The resulting column densities for the different species and positions are given in Table 5.2 for the individual positions and in Table 5.3 for the stacked spectra.

Furthermore, the abundances of the individual molecules estimated with respect to the column density of H_2 are listed in Table 5.3. The column density of H_2 is estimated from $^{13}CO\,(1\text{–}0)$, assuming a $^{12}CO/^{13}CO$ abundance ratio of 60 (Langer & Penzias, 1993) and a H_2/CO abundance ratio of 8.5×10^{-5} (Frerking et al., 1982) both values measured in the MW. Note that the abundances are only lower limits in case the emission of the observed molecules would be optically thick. In comparison with the PDR-model analysis below (see Section 9.1.4) it is however found that for the best-fitting models to our observations the optical depths (τ) in the centers of the lines of HCN and HCO^+ are $\tau < 0.1$. This suggests that emission is likely to be optically thin in the observed clouds (cf. Section 9.2).

5.4.2. M 33 abundances in context

This section has been published in paragraph 2 and 3 of Section 5 from (Buchbender et al., 2013); deviations are marked in italics.

In Table 5.4, the abundances are compared with those found in other galaxies (LMC, NGC 253, M82, IC 342), in selected Galactic sources, the photon-dominated region Orion Bar, the dark cloud TMC-1, and a translucent cloud.

The abundances of HCO^+, HCN, and HNC found in M 33 are very similar to those found in the LMC cloud N159. The abundances derived from the stacked spectrum of M 33 agree to within 0.3 dex with those of N159. Galactic sources have values that are higher by more than an order of magnitude. The Orion Bar, for example, shows 1.8 dex to 0.8 dex higher abundances. The good agreement with the LMC may be driven by its similar metallicity of 0.3–0.5 relative to the solar metallicity (Hunter et al., 2007), which is only slightly lower on average than in M 33 (Magrini et al., 2007, 2010).

However, the C_2H abundance observed in M 33 and in the Orion Bar agree within 0.3 dex.

The LTE HCO^+/HCN abundance ratios in M 33 range between 0.2 and 0.5 (Table 5.2). Godard et al. (2010) measured an HCO^+/HCN abundance ratio of 0.5 in the diffuse ISM of the Milky Way, similar to the ratio found in the solar neighborhood, and similar to the higher ratios found in M 33.

5.5. Atomic mass

The atomic gas mass is determined from the H I emission of the clouds. To make the extracted fluxes from the VLA HI-cube compliant with the dense gas observations a moment-zero[2] map has been created from the $12''$ version of the H I-map and afterwards convolved to $28''$ resolution.

Under the assumption of optically thin emission and a constant excitation temperature for the clouds one may use Eq. (3.45) to derive the H I column density of H I (N_{HI}). The mass of the atomic hydrogen is calculated as follows:

$$M_{H_2} = 1.36\,N_{HI}\,m_p\,A \tag{5.2}$$

where m_p the mass of a proton, i.e. $1.672 \times 10^{-27}\,kg$[3]. The factor 1.36 takes the mass contribution of elements heavier than hydrogen into account. A is the surface area covered by the beam:

$$A = \frac{\pi}{4ln2} \cdot (4.848 \times 10^{-6} \cdot 28'' \cdot D_{M33})^2, \tag{5.3}$$

with D_{M33} the distance to M 33, i.e. 840 kpc (cf. Table 2.1), the factor 4.848×10^{-6} the conversion between arcseconds and radian, and the factor $\frac{\pi}{4ln2}$ due to the Gaussian shape of the beam (cf. e.g. Klein et al. (2006)). The uncertainties are estimated using Gauss error propagation and assume a 15% calibration error on the HI data. The resulting HI-mass values are listed in Table 5.1.

5.6. Molecular gas mass

The bulk mass of molecular clouds consist of H_2; however, this molecule is only readily observable in warm regions with temperatures exceeding 500K of the ISM. From cold and dense regions that are of interest in this project, no emission from H_2 is observable. Therefore, one has fall back to the second most abundant molecule in the ISM, which is CO[4]. This molecular can be observed even in very cold environments thanks to its low lying rotational transitions.

---

[2]Moment-zero means integration of the spectra at every pixel of the cube. Here the full-velocity range of the H I spectra has been used, i.e. $-340 - -60\,km\,s^{-1}$

[3]Note, that although the electrons contribute to the mass of an atom, their mass is with $9.1 \times 10^{-31}\,kg$ four orders of magnitude lower than that of a proton. This contribution is well below the accuracy of the 15% calibration accuracy of the HI-data and therefore neglected.

[4]Another possibility is the determination of the molecular gas mass via optically thin dust emission and the assumption of a constant gas-to-dust ratio.

Table 5.4.: Molecular abundances in M 33 and typical examples of galactic and extra-galactic sources. (Buchbender et al., 2013)

Source	HCO$^+$	HCN	HNC	C$_2$H	References
M 33 min	−10.3	−9.8	-	-	
M 33 stacked	−9.8	−9.2	−10.5	−8.4	
M 33 max	−9.5	−9.1	-	-	
LMC N 159	−9.7	−9.7	−10.2	-	1,2
NGC 253	−8.8	−8.3	−9.0	−7.7	1,3
M 82	−8.4	−8.4	−8.8	−7.6	1,3
IC 342 GMC-A			−8.7	−7.5	5
Orion Bar	−8.5	−8.3	−9.0	−8.7	1
TMC-1	−8.4	−7.7	−7.7	−7.1	1,6
Transl. Cl.	−8.7	−7.4	−8.6	-	1,4

Notes. Entries show log(N(X)/N(H$_2$)).
References. (1) Omont (2007); (2) Johansson et al. (1994); (3) Martín et al. (2006); (4) Turner (2000); (5) Meier & Turner (2005) and references therein; (6) Hogerheijde & Sandell (2000)

5.6.1. Techniques to derive the molecular gas mass

The data that is available for the observed clouds in M 33 yields two means to estimate the molecular gas column density of the individual clouds. The first has been already introduced above in Section 5.4 and consists in the transformation of measured column densities of ^{13}CO into a H$_2$ column density under the assumption of abundance ratios (^{13}CO $\rightarrow$ ^{12}CO $\rightarrow$ H$_2$). The second way uses the ^{12}CO intensity I_{CO} and employs a N(H$_2$)-I_{CO} conversion factor – also referred to as X_{CO}-factor – which transforms the measured brightness temperature directly into a H$_2$ column density. The necessity of a conversion factor instead of a more direct derivation of a ^{12}CO column density is due to the fact that in general ^{12}CO is optically thick. The conversion factor is widely used to get a handle on the molecular gas mass, since ^{12}CO is easier to observe than the often optical thin, but weaker, ^{13}CO or C^{18}O emission, especially in far-away galaxies. Despite the optically thickness of the ^{12}CO (1–0) transition the same can be used to trace the molecular mass of a cloud, which is due to the fact that the emission arises from the surfaces of an ensemble of ^{12}CO-emitting entities ("clumps") within the telescope beam. The ^{12}CO line intensity is therefore a proxy for the number of clumps and will be proportional to the total molecular mass of this ensemble, under general conditions (e.g. Dickman et al., 1986; Bolatto et al., 2008).

To yield sensible results, a conversion factor such as X_{CO} has to be gauged. And its application intrinsically assumes that the same conditions apply in the region where it was gauged and in the region to which it is applied. There is however a basic justification for the use of an X_{CO}-factor that is based on the observed relation between the CO luminosity and the viral mass of molecular clouds. This relation, measured in the Milky Way, is found to follow a power law $M_V \propto L_{CO}^{0.76}$ as reported by Solomon et al. (1987). The "standard" value of X_{CO} often used in the literature is also derived within the Milky Way disk and is 2×10^{20} (K km s^{-1})$^{-1}$ cm^{-2} as for example derived

from maps of molecular column density that have been derived from far-infrared and 21 cm surveys of the Galaxy Dame et al. (2001).

Caution is however required because the value of X_{CO} may change between clouds already within small parts of a galaxy and even more so between different environments/galaxies. This has multiple reasons. For instance X_{CO} may be metallicity dependent. Lower metallicity goes in hand with a lower dust-to-gas ratio (e.g. Leroy et al., 2013) and thus less absorption due to dust. In turn this pushes the transition zone of atomic carbon to CO to greater depths into the cloud. This results in a subsequent change in the ratio of CO to H_2 column density and thus a higher X_{CO} is needed to yield the correct result (see e.g. Bolatto et al., 1999; Leroy et al., 2013). Using the same X_{CO} for clouds with different metallicity but similar CO-brightness would therefore underestimate the total molecular gas mass of the cloud with the lower metallicity (cf. Fig. 4.4). Another effect in occurs in starburst environments where the local radiation fields are stronger than in more quiescent regions. This leads to a higher excitation state of the CO molecules and thus a larger emissivity per CO molecules. Hence, a standard X_{CO}-factor would overestimate the H_2 column density (Weiß et al., 2001). These are but two possible influences onto X_{CO}. Temperature and density differences may also affect X_{CO} (Maloney & Black, 1988; Wall, 2007).

One has to keep in mind that the value chosen for X_{CO} may significantly influence the subsequent analysis and results. For the reasons mentioned a wrong X_{CO} factor could lead to unreasonably high star formation efficiency (i.e. the ratio of star formation rate to the gas mass) (cf. Israel, 1997; Gardan et al., 2007). It further may affect basic scaling relations such as the Schmidt-Kennicutt law for which different slopes may be found depending if one uses a constant or a variable X_{CO} factor (e.g. Boissier et al., 2003; Buchbender, 2009). As a final example the choice of X_{CO} factor may change the dust-to-gas mass estimation.

5.6.2. A variable X_{CO} for the GMCs in M 33

In the present case of M 33 the ISM has a mostly sub-solar metallicity and the observed clouds vary largely in the degree of star formation. Therefore, the X_{CO}-factor of the individual clouds is likely different from the standard Milky Way value[5]. To account for variations between the clouds an individual value for X_{CO} is estimated for each cloud using the findings from Israel (1997). This study investigated a sample of low-metallicity environments in the LMC and SMC and for two clouds in M 33. They found that that the conversion factor X_{CO} (cf. Table 5.1) is a function of total infrared luminosity (L_{TIR}). In the following this relation is used to estimate an X_{CO} factor from the measured L_{TIR} (see Section 6.4).

The following two paragraphs have been published in Section C.4. of Buchbender et al. (2013) deviations are marked in italic.

Israel (1997) derived N_{H_2} for CO clouds in the LMC, the SMC, and other low-metallicity galaxies from their far-infrared surface brightness and H I column densities. He finds local X_{CO} values up to a magnitude higher than the widely used Galactic value

---

[5]Note however that averaged over large regions, i.e. the inner and the outer disk of M 33, the X_{CO} value of M 33 (and also that of the LMC) lies within the uncertainties of the Milky Way value (Leroy et al., 2011).

of 2×10^{20} $(\mathrm{K\,km\,s^{-1}})^{-1}\,\mathrm{cm}^{-2}$ (e.g. Dame et al., 2001). In particular he studies the two bright H II regions NGC 604 and NGC 595 in M 33, for which he derives X-factors of 22×10^{20} $(\mathrm{K\,km\,s^{-1}})^{-1}\,\mathrm{cm}^{-2}$ and 12×10^{20} $(\mathrm{K\,km\,s^{-1}})^{-1}\,\mathrm{cm}^{-2}$. Israel (1997) further finds a correlation between X_{CO} and the TIR-flux. For NGC 604 and NGC 595 a TIR luminosity of 27.18 and $7.82 \times 10^6\,L_\odot$ is estimated in this work *with the techniques explained in Section 6.4.* From this the local X_{CO} for our seven clouds is estimated from their TIR by using the mean of the $X_{\mathrm{CO}}/L_{\mathrm{TIR}}$ ratio of NGC 604 and NGC 595 as a conversion factor, i.e. $X_{\mathrm{CO}} = 1.17\,10^{20}\,10^{-6}\,L_\odot\,L_{\mathrm{TIR}}$. The thus derived X-factors vary between 7 and 1.5 in units of 10^{20} $(\mathrm{K\,km\,s^{-1}})^{-1}\,\mathrm{cm}^{-2}$ for the six positions with HCN and HCO$^+$ detections (*Table 5.1*). The values of $N_{\mathrm{H_2}}$ for the stacked values in *Table 5.3* are deduced using an average over the individual X_{CO} factors of the observed GMCs of 3.0×10^{20} $(\mathrm{K\,km\,s^{-1}})^{-1}\,\mathrm{cm}^{-2}$.

The mass of the molecular gas $M_{\mathrm{H_2}}$ is estimated from the intensity of the ^{12}CO 1–0 line using the X_{CO}-factor derived in the previous section and

$$M_{\mathrm{H_2}} = 2 \times 1.36\,N_{\mathrm{H_2}}\,\mathrm{m_p}\,A \qquad (5.4)$$

with the proton mass $\mathrm{m_p}$, the beam size A. The factor two accounts for the two protons of molecular hydrogen and 1.36 includes the contribution of heavy elements to the total mass. Errors follow from the measurement uncertainty of ^{12}CO The results are listed in *Table 5.1*. The derived X_{CO}-values range between 0.3 and 6.9 $\times 10^{20}$ $(\mathrm{K\,km\,s^{-1}})^{-1}\,\mathrm{cm}^{-2}$.

For comparison the values of $N_{\mathrm{H_2}}$ from the ^{12}CO (1–0) lines using the X_{CO}-factors derived for every cloud and from the column density of ^{13}CO (cf. above) are both listed in Table 5.2. Comparing both methods it is found that the results for $N_{\mathrm{H_2}}$ are consistent within a factor of 2.5 excluding position no2.

It is found that the observed clouds exhibit a range of molecular masses ranging from 0.1 (GMC no2) to $12.7 \times 10^5\,\mathrm{M_\odot}$ (GMC 1). GMC no2 – the cloud with the largest galacto-centric radius – has an L_{TIR} 20 times weaker, as well as a ^{12}CO luminosity 5 times weaker than GMC 1, it is the only clouds in which we did not detect HCO$^+$. In contrast GMC 1 is situated in the very center of M 33 and is the most TIR luminous. Therefore, this cloud also has the highest X_{CO} which renders it the most massive cloud. Interestingly, in our sample it is only the second most luminous cloud in CO with $I_{^{12}\mathrm{CO}}$=7.2 K km s^{-1}, while GMC 91 has CO luminosity of 21.6 K km s^{-1}. GMC 91 however is a very quiescent clouds with a weak total-infrared luminosity and relatively weak HCN and HCO$^+$ emission. This renders its $X_{\mathrm{CO}} = 1.5$ $\times 10^{20}$ $(\mathrm{K\,km\,s^{-1}})^{-1}\,\mathrm{cm}^{-2}$ similar to clouds in the Milky Way, but much lower than the X_{CO}=6.9 $\times 10^{20}$ $(\mathrm{K\,km\,s^{-1}})^{-1}\,\mathrm{cm}^{-2}$ or X_{CO}=5.1 $\times 10^{20}$ $(\mathrm{K\,km\,s^{-1}})^{-1}\,\mathrm{cm}^{-2}$ of GMC 1 and GMC no6.

5.7. Optical extinction

As has been discussed in Chapter 4, the depth into a PDR and/or GMC is commonly measured by the amount of optical extinction. This section explains how A_{v} has been estimated for the seven observed GMCs. The following paragraph has been published in Sec. C.5. in (Buchbender et al., 2013), deviations are marked in italic font.

Bohlin et al. (1978) showed that for the local ISM a correlation between the amount of hydrogen atom column density $N(H\,I + H_2)$ and the color excess exists; they estimate a conversion factor of $\langle N(H\,I + H_2)\rangle/E(B-V) = 5.8 \times 10^{21}$ atoms cm^{-2} mag^{-1}. The color excess and the optical extinction A_v are also linked. Bohlin et al. (1978) give a value for the interstellar average of R = $A_v/E(B-V)$ = 3.1. Here the optical extinction A_v for the observed clouds per beam is estimated using these formulas and the column densities $N_{H\,I}$ and N_{H_2} derived above. Note that for clouds not filling the 115 pc beam, local extinctions may be higher. The errors given for A_v (cf. Table 5.1) include the errors of $N_{H\,I}$ and N_{H_2}. We estimate the A_v for the stacked spectra by averaging the values of the individual positions, i.e. 4.2 ± 1.9 mag. *The range found for the seven GMCs is 1.6 – 6.3 mag.* The values of A_v are given in Table 5.1.

5.8. Far ultraviolet flux

The text of this section has been published in Section C.4 of Buchbender et al. (2013), deviations are marked in italic font.

The FUV flux G_0 impinging on the dusty cloud surfaces can be estimated from the emitted total infrared intensity assuming that all FUV photons are absorbed by the dust. We use $G_0 = 4\pi\,0.5\,L_{TIR}$ (cf. e.g. Mookerjea et al., 2011) with G_0 in units of the Habing field $1.6\,10^{-3}$ erg s^{-1} cm^2 (Habing, 1968) and the TIR intensity in units of erg s^{-1} cm^{-2} sr^{-1}. Errors follow directly from the errors on L_{TIR}. *Here far-ultraviolet field strengths in the range of 2.5 – 50.7 G_0 are found.* The FUV flux that we use to compare with values deduced from the stacked spectrum is the average FUV flux of all individual clouds, i.e. 21.6 ± 0.7 G_0.

Chapter 6.

Spectral energy distribution of the far infrared continuum

Dust and molecular gas are intermixed in the ISM and influence each other. As has been discussed in Chapter 4, the dust is of tremendous importance for the development of photo-dissociation regions and the mechanisms therein. As such, it serves as a catalyst during the formation of H_2 and attenuates the FUV-radiation with the consequence that molecules can form and become eventually self-shielding. The molecular transition regions and their volume filling factor depend, amongst others, on the gas-to-dust ratio (GDR) in the specific medium. Furthermore, the dust allows for heating of the gas via the photo-electric effect and therefore influences the excitation and formation of the molecules. Thus, for a thorough understanding of molecular line emission and the conditions that are traced by them, information about the dust properties of the specific sources is beneficial.

Having full-maps of M 33 at the wavelengths 24, 70, 100, 160, 250, 350 and 500 μm at hand, measured with the instruments MIPS/*Spitzer* and PACS and SPIRE/*Herschel* (cf. Section 5.3), it is possible to investigate the dust spectral energy distribution (SED) across the entire disk of M 33.

To add insight into the dust properties of the GMCs observed in HCO^+, HCN and CO in this chapter their dust spectral energy distribution (SED) is investigated. Section 6.1 gives a general introduction to modified black body fits that have been used to determine the temperature, mass as well as the extinction coefficient of the dust. The following Section 6.2 discusses the general SED properties found within the disk of M 33 by the `HerM33es`-consortium. In Section 6.3 the dust-SEDs of the individual GMCs that are the focus of this thesis are analyzed at a resolution of 28″. The dust temperatures derived here are used as a best-guess for the excitation temperature of the gas in the derivation of LTE-abundances of the observed molecules in Section 5.4. The derived massed of the cold-dust component are used in Section 6.4.1 to estimate the gas-to-dust ratio of the GMCs. In a final step the derivation of the total infrared luminosity (L_{TIR}) of the seven GMCs is discussed in Section 6.4.1. The L_{TIR} is used in Chapter 7 as a tracer of the star formation rate to study the relation between the same and the line intensities of HCN and HCO^+.

6.1. Introduction to modified black body fits

The dust makes up only about 1% of the ISM[1]. Nevertheless, it absorbs at least 30% of the light emitted by stars within a galaxy and re-radiates it at the infrared and sub-millimeter wavelengths (Draine, 2003). To extract the properties of the dust from measured SEDs, one has to assume a model incorporating the composition, geometry and grain-size distribution of the dust present in the observed region. Different compositions of the dust-grains are discussed in the literature that, after Draine & Li (2007), fall into three broad categories that describe dust as: a silicate-graphite composite; having a silicate-core and a carbonaceous mantle; or a composite of small silicate and carbonaceous particles. The dust-grains give rise to thermal emission at FIR ($42 - 122\,\mu$m (e.g. Helou et al., 1988; Dale et al., 2001)) and (sub-)millimeter wavelengths ($\sim 122 - 1.1$ mm). The dust in the ISM further contains polycyclic-aromatic-hydrocarbons (PAHs) that emit at wavelengths shorter than $42\,\mu$m. The emission characteristics of these two types of dust emission can be described separately and composite models exist that describe the full spectral range of dust emission such as the one presented in Draine & Li (2007). The (Draine & Li, 2007) however does not include variations of the slope of the Rayleigh Jeans part of the spectral energy distribution in the far-infrared (FIR). In the following, only the thermal emission from dust in the FIR between $24\,\mu$m and $500\,\mu$m is considered.

To describe the dust emission in this wavelength regime it is often assumed that the emission follows a modified black body (MBB)[2] and is optically thin (e.g. Dunne & Eales, 2001; Weiß et al., 2008). This model has been introduced in Section 3.2.1 as the solution of the radiative transfer equation for a optically thin dust cloud at uniform temperature. The emission characteristics of a MBB depend on the mass of the emitting material, its temperature and in particular the extinction coefficient κ. The value of κ depends on the assumed model of the dust and incorporates its characteristics. The value of kappa has a wavelength dependence which is typically described by a power law function with an exponent β, i.e. $\kappa \propto \nu^{\beta}$ (cf. Eq. 3.34). The value of β determines the slope of the SEDs in the "Rayleigh-Jeans tail". It is a matter of debate, not least because it is difficult to determine β in the laboratory. The estimation of β carries information about the characteristics of the dust and a better understanding of its behavior helps to improve dust models.

To compare the MBB approach with observations often a simple χ^2 fit is employed. In our work presented below (Kramer et al., 2010; Xilouris et al., 2012) we have used the Levenberg-Marquardt algorithm (Bevington & Robinson, 1992) to minimize the function:

$$\chi^2 = \sum ((S_{\nu,obs} - S_\nu)/\Delta S_{\nu,obs})^2. \tag{6.1}$$

by varying the modeled flux S_ν. After the minimal χ^2 is determined, its value is divided by the number of degrees of freedom, i.e. d.o.f $= n - 1$, to calculate the reduced χ^2, where n the number of observations.

For a single greybody component such a fit has three free parameters, i.e. the temperature of the dust (T_{dust}, cf. Eq. 3.32), its mass (M_{dust}, cf. Eq. 3.33) and the value

---

[1]In the Milky Way the interstellar medium itself accounts for $\sim$10% of all baryonic matter (e.g. Draine, 2011).

[2]Often also referred to as "greybody".

of β (cf. Eq. 3.34). Each free parameter reduces the degrees of freedom by one, i.e. d.o.f.=n-k-1, where k the numbers of free parameters of the fit. Therefore to fit a single-component greybody where all variables vary freely one needs at least four data points.

In many occasions, it is found that one dust component at a single temperature can not describe the observed galactic as well as extra-galactic SEDs in the FIR and sub-mm regime. Typically a cool component ($T_{cold} \sim 15 - 25\,K$) and a warm component ($T_{warm} > 30\,K$) are needed (e.g. Dunne & Eales, 2001; Weiß et al., 2008). The warm dust component, traced by the short wavelengths of the SED, is believed to be located in the vicinity of HII-regions and high-mass star formation and to be heated by Hα photons from young (OB) stars (Dunne & Eales, 2001). The cold component originates from more diffuse dust that is heated by the average interstellar radiation-field. See Section 11.4 for an vivid example of this behavior where interferometer maps of HCN, HCO$^+$ and ^{12}CO are presented next to images of the 8, 24, and 100μm dust as well as Hα emission.

The best-fit values of β to dusty clouds lie in the range of 1–2.5 (Chapin et al., 2011; Boselli et al., 2012). Interpreting the fit results and comparing them to each other, it is important to keep in mind which particular object has been observed: a sub-part of a GMC, a single cloud or an ensemble of clouds. This is because, for example, the measured β-value of an ensemble of many clouds may lead to a β-value that is different from the clouds intrinsic values even if all clouds have the same β simply through superposition of the individual emission characteristics of the clouds. Also a temperature deduced in the fits must not be the physical temperature of the dust-grains, which in any case have a, however finite, temperature distribution.

The value of β, the pure MBB approach as well as the ways to fit the model to measured data are a matter of debate. For example it is not certain that β stays constant with wavelength and a turnover between the FIR and the sub-mm regime is suggested (Paradis et al., 2011). Another caveat of the MBB-approach is that the very mathematical nature of the MBB-definition and the χ^2 procedure results in a degeneracy between the fitted β and T values and in a spurious β–T anti-correlation. The reason is that data inflicted with measurement-errors may be fitted equally well by different β–T pairs within the uncertainties (Kelly et al., 2012). Therefore, it is not possible to reliably determine both values independently with this technique. To improve the situation a hierarchical Bayesian multi-level fit approach is suggested by Kelly et al. (2012) that rigorously treats the measurement uncertainties. On the other hand, a real correlation of β with the dust-temperature might exist, because such a relation has been seen in laboratory experiments (Agladze et al., 1996; Boudet et al., 2005).

6.2. The spectral energy distribution in the disk of M 33

As stated above the data available to the `HerM33es` project allows to study the dust SED of M 33 throughout the disk. The smallest common resolution of the data-set is 40″. To get a first handle on the dust properties in M 33 we investigated in Kramer, Buchbender et al. (2010) the total dust-SED as well as the variation of the SED with
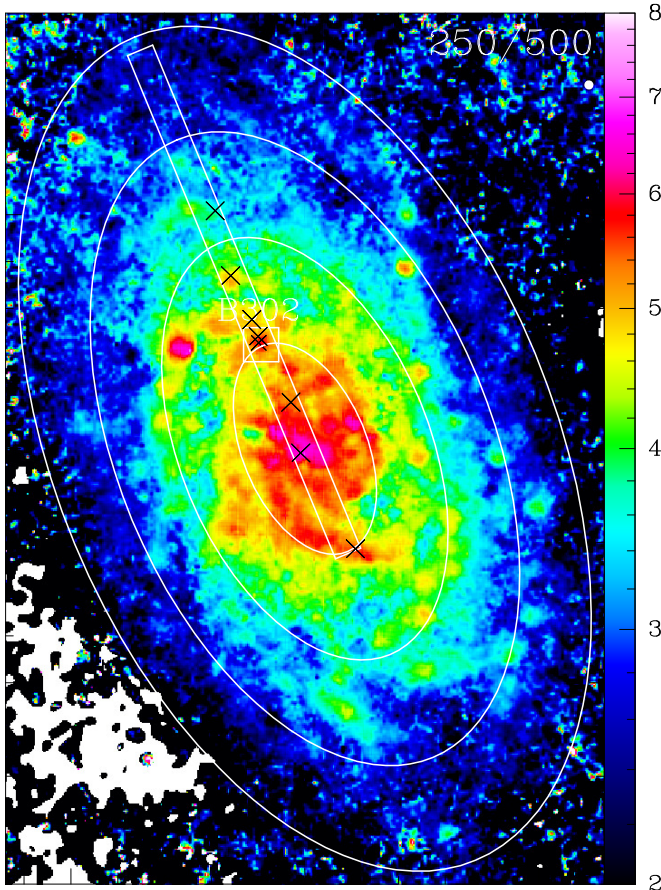
Figure 6.1.: Ratio map of the SPIRE/*Herschel* 250 μm over 500 μm emission of M 33. Ellipses denote 2, 4, 6, 8 kpc galacto-centric distances for the inclination of M 33 of 56° and position angle 22.5° (cf. Table 2.1). The elongated rectangle delineates the 2′ × 40′ wide strip along the major axis shown in Fig. 5.5. The small rectangle marks the region of BCLMP 302 and GMC no3 where PdBI data of HCN, HCO⁺ and ^{12}CO has been observed, which is analyzed in Part III. Crosses mark the positions of the observed GMCs. (Kramer et al., 2010)

galacto-centric radius. To do so we averaged the dust emission over four galacto-centric rings with a 2 kpc width each (r_i <R <r_i + 2 kpc with r_i = 0, 2, 4, 6 kpc). The rings are marked in Fig. 6.1 that shows a map of the 250/500 μm ratio. Note that this ratio is a first proxy for the slope of the SEDs. The ratio declines for larger radii and thus the slope of the SED becomes shallower.

Finding that a single-component greybody is unable to reproduce the SEDs well we settled for a two-component approach. In Fig. 6.2 the total and averaged SEDs are shown together with the best fit two-component MBB. The optical extinction κ that we assumed for the MBB is the same as in Eq. (3.34). Testing values of β = 1.0, 1.5 and 2.0 to found the best-fitting value, we find that for all radial averages as well as the total SED a value of β = 1.5 resulted in the best agreement with the data. This may however be due to the coarse sampling of the β parameter-range as well as due to the fact that we average over large areas. However the variation in β in M 33 shall be discussed in more detail later in this section. The resulting best fitting parameters for the β=1.5 model are shown in Table 6.1. We find that the temperatures of the cold (T_c) and warm (T_w) component decline from the center of the galaxy with temperatures of T_c=24 K and T_w=77 K, to T_c=13 K and T_w=51 K for the outermost ring. Further, it can be seen that the cold component dominates as it is much more massive than the warm one and the relative mass M_c/M_w is less then 0.3% for all cases. Nevertheless, the warm component is needed to fit the data short-ward of 100 μm, except for the inner-most region where the warm component is only constrained by the 24μm flux.
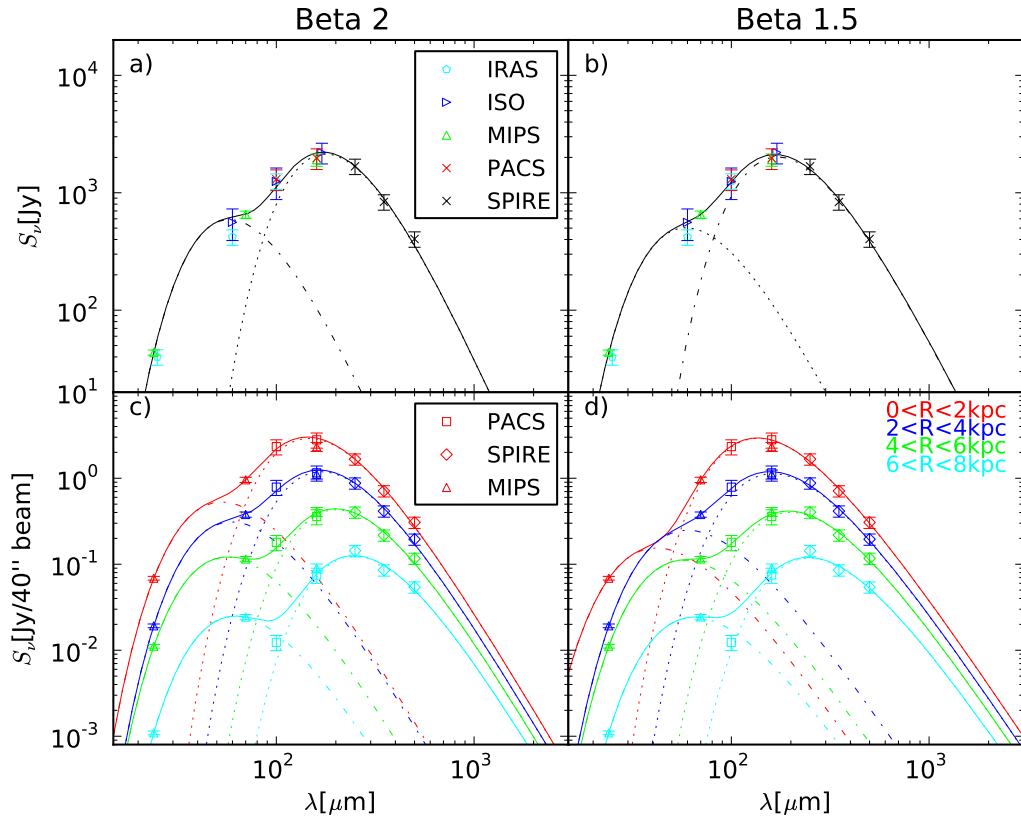
Figure 6.2.: Spectral energy distributions (SEDs) of M 33 at wavelengths between 24 μm and 500 μm. **a, b**: Total integrated SED of M 33, combining data of PACS & SPIRE, with data of MIPS/*Spitzer* (Tabatabaei et al., 2007), ISOCAM (Hippelein et al., 2003), and IRAS (Rice et al., 1990). **c, d**: Radially averaged SEDs in zones of 2 kpc width (cf. Fig. 5.1). Here, we show the MIPS, PACS, and SPIRE data. **a, c**: Drawn lines show the two-component greybody model fit results. The 100 μm PACS flux density, measured in the outermost zone, was not used for the fits. The dust emissivity index was set to $\beta = 2$. **b, d**: Drawn lines show two-component models for $\beta = 1.5$. **a-d**: All fits are weighted by the assumed uncertainties: 7 % for MIPS 24, 70 μm (*Spitzer* Observers Manual v8.0), 20 % for PACS, 15% for SPIRE. The SEDs have not been de-projected. (Kramer et al., 2010)

To get a handle on the errors of the fits we performed a Monte-Carlo analysis. To do so we generated 10000 new data sets by randomly drawing "data points" from a Gaussian distribution which is centered on the individual measurements and has a FWHM corresponding to the measurement error. Subsequently, we fitted our two-components MBB to each data-set and finally derived the standard deviation of the temperatures. We found that the cold temperatures is well determined to an accuracy of $\Delta T \sim 3$ K. The warm component is however less well constraint and may vary by $\pm$ 10 K.

In a next step of the analysis of the dust emission in M 33 within the `HerM33es`team, in Xilouris et al. (2012) we produced maps of the cold and warm dust component at a resolution of 40″ and with pixel sizes of 10″ using the same fitting algorithms as inKramer et al. (2010).With a finer spacing of β-values of 1, 1.3, 1.5, 1.7 and 2 we found that on average β=1.5 gives the best fitting results in accordance with the

Table 6.1.: MBB-fit parameters for β=1.5 of the total and radial averaged SEDs of M 33.

	Total	(1)	(2)	(3)	(4)
T_c/[K]	19	24	20	16	13
T_w/[K]	55	77	57	52	51
M_c/[10^6 M$_\odot$]	10	1.2	3.0	4.6	4.9
M_c/M_w	500	3800	480	730	2200
χ^2_{red}	0.14	0.10	0.12	0.20	1.8
M$_{\mathrm{gas}}$	200	190	150	120	160

Notes. The radial averaged SEDs noted (1) through (4) are measured in four galacto-centric rings with a 2 kpc width each; r_i <R < r_i + 2 kpc with r_i = 0, 2, 4, 6 kpc respectively. This is a sub-set of Table 1. from (Kramer et al., 2010).

earlier analysis over radial averages. Constructing radial averages with a finer spacing Xilouris et al. (2012) confirmed the decline of temperature with radius in M 33 and the results are within the measurement errors consistent with (Kramer et al., 2010).

It is found that the warm component for single pixels is often not well defined, especially in the bright regions. Comparing the scale-lengths of the dust emission in the far-infrared at $\sim$ 100 μm with that in the sub-mm regime at 500 μm we found that the emission at longer wavelengths have a larger scale-length and thus are more widely distributed than the shorter wavelength emission. Recalling that the longer wavelengths determine the temperature of the cold component, the latter is subsequently better constrained.

Furthermore, the galaxy was decomposed into a diffuse exponential disk and a spiral-arm network by fitting an exponential disk to all available bands. The emission of this disk is found to account for about 21% of the emission at 24 μm and rises to about 57% for sub-mm wavelengths (500 μm).

A future publication of the `HerM33es` team Tabatabaei (2013 in prep.) investigates the variation of β over the disk of M 33. This study uses the Newton-Raphson (Numerical Recipes) iteration method to solve the two-component MBB approach at each pixel for a range of fixed β for the cold component with the goal to reduce the $\beta - T$ degeneracy discussed above. The resulting map of the best-fitting β values for the cold component is shown in Fig. 6.3. One can see that β declines with radius and $\beta = 1.2-2$. Note that this results in a positive correlation of β and T in M 33 which is in contrast to the anti-correlation of the two-values found in other studies (Paradis et al., 2009; Ysard et al., 2012; Juvela & Ysard, 2012, e.g.). There are several possible reason for this decline to shallow beta values at larger radii and the low average value of 1.5 in the averaged SEDs. One might be the low metallicity of M 33 as galaxies with sub-solar metallicity have been found to exhibit flatter SEDs (Galliano et al., 2005; Planck Collaboration et al., 2011).
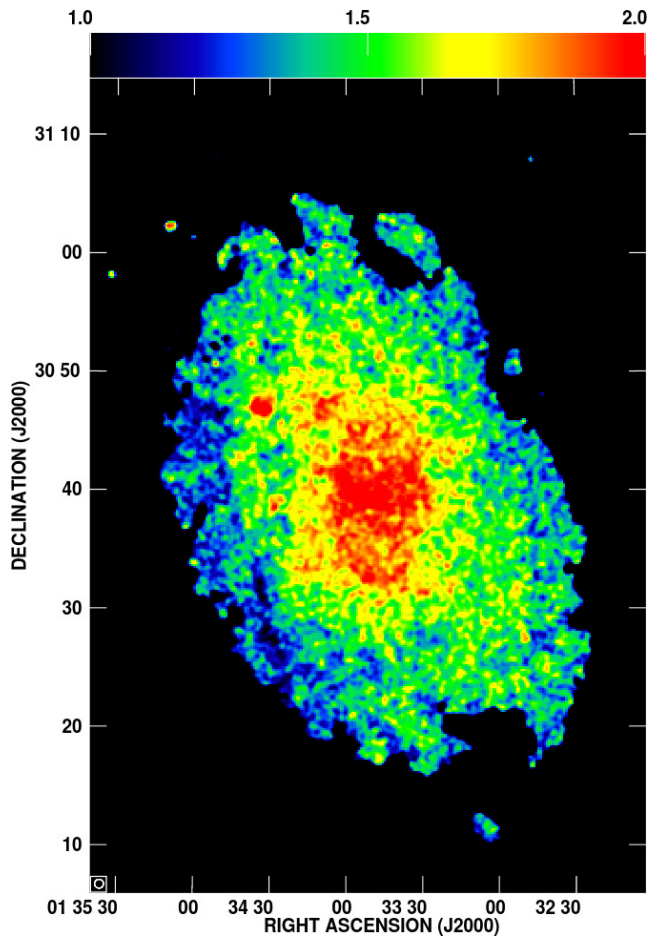
Figure 6.3.: Distribution of the dust emissivity index β_{cold} within the disk of M 33. β_{cold} has been obtained from a two-component modified black-body approach using the Newton-Raphson method (from Numerical Recipes), where β_{warm} = 2. Tabatabaei (2013 in prep).

6.3. Dust conditions of the observed giant molecular clouds

Using above results and discussed techniques the SEDs of the seven GMCs observed in HCN and HCO$^+$ can be investigated to determine dust temperatures as well as the total infrared luminosity (L_{TIR}). This adds valuable information for an in-depth analysis of the physics of these regions. As such the cold-dust temperature derived here will serve as an first estimation of the excitation temperature of the gas and is used to estimate its column densities via Eq. (3.43) in Section 5.4. Further, the total infrared luminosity (L_{TIR}) (see Section 6.4) will be used as a tracer of star formation by revealing star light that has been absorbed by the dust as discussed in Chapter 7.

To make the results of the SED-fits in the seven GMCs applicable for comparison with the dense gas observations, the SEDs are produced at a resolution of 28$''$, which is the resolution of the HCN and HCO$^+$ observations. The map with the lowest resolution within the set of FIR-maps is the SPIRE 500 µm map with 36.9$''$ resolution. All other maps have a resolution of 25.2$''$ or better. Therefore the 500µm map is neglected and all other maps are smoothed to 28$''$ resolution and converted to units of Jy/beam. The SEDs are generated for each observed cloud from the fluxes of the pixels that correspond with the coordinates of the 30 m pointings.
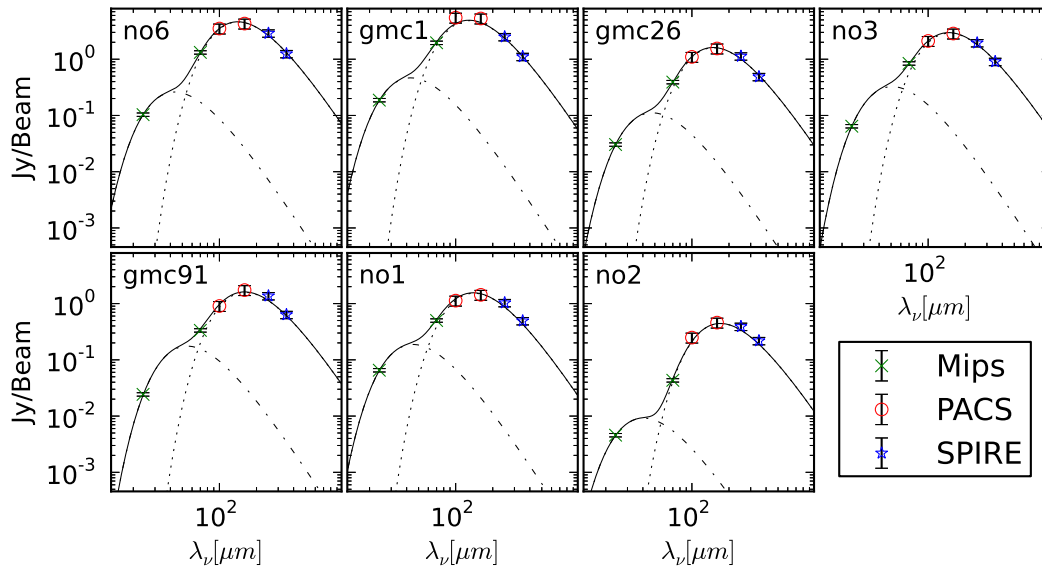
Figure 6.4.: Dust SEDs for the sample of GMCs combining data from PACS and SPIRE from *Herschel* as well as MIPS/*Spitzer*. All data has been convolved to a resolution of $28''$. The best-fitting two-component MBB-model for a dust emissivity index $\beta = 1.5$ are shown. The lines indicate the SED-fit of the cold component (*dotted*), of the warm component (*dash-dotted*) and their superposition (*solid*). Table 6.2 gives the fit-results.

At $28''$ resolution therefore, six data points are available, enough to perform a two-component fit with a variable beta that is the same for both components. Here, however, the findings from (Kramer et al., 2010; Xilouris et al., 2012, Tabatabaei 2013 in prep.) are used and a constant $\beta = 1.5$ for both component is assumed which has been found to best describe the disk-averaged emission of M 33. This renders our two-component greybody models to have five degrees of freedom. From the fitted SED the L_{TIR} values are determined by integrating the obtained dust SED over the total infrared wavelength range which is defined in Dale et al. (2001) to be between $3\,\mu$m to $1100\,\mu$m. Below, the TIR luminosity will be discussed in more detail. No corrections have been applied for the fitted-bandpasses of the different instruments, nor for any line emission in the fitted bands.

The resulting SED-fits are presented in Fig. 6.4 and the determined values in Table 6.2. As discussed above the warm dust-component is often only constrained by the $24\,\mu$m data point (see e.g. GMC no2 in Fig. 6.4). Subsequently, the fit of the warm component may give gives unphysical results, e.g. $T \gg 1000$. This was the case for the sources GMC 1, GMC 91, and GMC no2. In such a case, to constrain the fit only the masses were left to vary and the temperatures were set to good fitting values as evaluated by eye. Note that the values of the warm components are therefore rather ambiguous. In particular the fit of the warm component of GMC no2 does not yield a physical result as the large $M_{\text{cold}}/M_{\text{warm}}$ ratio shows, cf. Table 6.2. The fits of the cold component is however well constrained for all sources.

From Table 6.2, it can be seen that T_{cold} varies only slightly, between in the northernmost position GMC no2 with $T_{\text{cold}} = 19$K and $T_{\text{cold}} = 25$ K in GMC 1 in the most center of M 33. With 75 K the warm dust temperature is hottest in the center and the

Table 6.2.: MBB fit-results to the SEDs of the seven GMCs observed in HCN and HCO⁺.

Source	T_{cold} [K]	T_{warm} [K]	M_{cold} M$_\odot$	M_{warm} M$_\odot$	M_{cold}/M_{warm}	β	L_{TIR} $10^6 L_\odot$	χ^2
GMC no6	23	75	9452	3.00	3653.00	1.5	3.13	0.51
GMC 1	25	75	6684	5.00	1460.00	1.5	3.92	0.78
GMC 26	22	68	4227	2.00	2489.00	1.5	1.06	0.73
GMC no3	22	63	7541	7.00	1109.00	1.5	2.11	0.23
GMC 91	20	59	5945	5.00	1173.00	1.5	1.05	0.88
GMC no1	23	72	3062	2.00	1381.00	1.5	1.22	0.81
GMC no2	19	80	2098	0.00	30965.00	1.5	0.23	1.05

Notes. See Fig. 6.4 for the corresponding Fits.

southern arm position GMC no6. These two sources have the highest SFRs (cf. Table 5.1 and Chapter 7) in our sample. However, positions in the north and at higher galactic radii are with 59-72 K only slightly colder and within the estimated errors of T_{warm} of ~ 10 K. Further we find that the cold component contains substantially more mass than the warm component , i.e. $M_{cold}/M_{warm} \approx$ 1000-4000 . The clouds with the highest ratio are GMC no6 and GMC 26.

6.4. The total infrared luminosity

The total infrared luminosity determined from the integration of the SED underestimates most likely the true luminosity of the clouds between 3 μm and 1100 μm since the two-component MBB-model does not account for the emission of dust features short-ward of 24 μm, such as emission from PAHs.

To get a more reliable estimate of the L_{TIR} the results of another `HerM33es`-study of dust emission in M 33 by Boquien et al. (2011) are used. The authors used the *Spitzer* and *Herschel* data of M 33 between 8 and 500 μm to fit models by Draine & Li (2007) – that take dust emission at shorter wavelengths and from PAHs into account – to the SEDs at every pixel via a χ^2-fit. The best-fitting SED is then integrated between 1μm and 1 mm. Subsequently, they determine the best linear relation between L_{TIR} and any combination of the available IR bands. To do so they fit the obtained L_{TIR} at every pixel to a linear combination of the flux L_i in band i (Eq. 1 in Boquien et al. (2011)):

$$\log L_{TIR} = \sum_{i=1}^{n} a_i \log L_i + b. \tag{6.2}$$

They give the values for a_i and b for any possible combination of all bands at 8, 24, 70, 100, 160, 250, 350, 500 μm bands. Here, to determine L_{TIR} for the observed GMCs, the measured brightnesses[3] in W kpc^{-2} are added for all bands, except the 8μm band, weighted by the factors given Boquien et al. (2011). The resulting values for L_{TIR} are

---

[3]The determined brightnesses are converted to luminosities corresponding to the 28″ beam by multiplying with the beam size in kpc^{-2}.

given in Table 5.1; the errors on the derived L_{TIR} values are the σ values of the fits given by Boquien et al. (2011).

Comparing the results of both methods to derive L_{TIR}, i.e. integrating the flux of the fitted MBB SED and using the relation from Boquien et al. (2011), we find that the former underestimated L_{TIR} at all seven positions by less than 34%. In other words, both methods yield consistent results within $\sim 30\,\%$. Both results are very well correlated with an Pearson correlation coefficient of $r = 0.99$, so that both methods are consistent with each other.

In Chapter 7 we will discuss the usage of L_{TIR} as a tracer of star formation.

6.4.1. Gas-to-dust mass ratio

The gas-to-dust mass ratio has a large influence onto photon-dominated regions. A higher gas-to-dust mass ratio (GDR) results in an lower extinction and thus the chemical transition zones occur at larger depths. Also with less dust in comparison to gas particles the photo-electric heating rate (cf. Section 4.3.1) is lowered. Here the gas-to-dust mass ratio for the seven observed GMCs is derived.

With the total gas mass (M_{gas}) and the mass of the cold dust component (M_{dust}) derived in Section 5.6 and Section 6.3 respectively, it is possible to derive the gas-to-dust mass ratio $M_{gas}/M_{dust}$the values of which are given in Table 5.1. We find GDRs (cf. Table 5.1) in the range of $\sim 166 - 286$ (cf. Table 5.1) which is (moderately) higher than the typical values of 100–150 found in the Milky Way or in galaxies of solar metallicity (e.g. Draine et al., 2007). Note that a higher gas-to-dust mass ratio is expected in an environment with lower metallicity (Bolatto et al., 2008). The possible implications of such low gas-to-dust mass ratios onto the line emission of HCN and HCO^+ and our analysis of the following chapters are discussed in Chapter 14.

Chapter 7.

Star formation in M 33 and its relation to molecular tracers

Star formation occurs in the densest parts of the ISM. Gas that has densities that are above $n_{\mathrm{H}}=1\times10^{5}\mathrm{cm}^{-3}$ is estimated to be direct fuel for star formation (Krumholz & McKee, 2005). Therefore, tracers of the dense gas are of great interest as they allow us to study the gas directly related to star formation. This chapter aims to characterize the relation between the HCN and HCO^{+} emission and the star formation rate of the observed giant molecular clouds in M 33. This a comparison is motivated by the recently found tight and linear correlation between HCN and the star formation rate (as traced by L_{TIR}) that holds over 7–8 orders if magnitude in L_{TIR}. The objects for which this relation is found include galactic massive star forming clump, the centers of nearby galaxies and (ultra-) luminous infrared galaxies ((U-)LIRGs) (e.g. Gao et al., 2007; Wu et al., 2010). This relation is a strong contender for a more fundamental "star formation law" than the "Schmidt-Kennicutt law" which relates the SFR surface density (Σ_{SFR}) and the total (molecular and/or atomic) gas surface density (Σ_{gas}). It is however yet unclear what the underlying physical reasons for the good correlation are. Furthermore, a series of recent papers (e.g. Graciá-Carpio et al., 2006; García-Burillo et al., 2012) find deviations from a single linear correlation as well as raise doubt for the usefulness of HCN as a universal tracer of dense star forming gas. This chapter hopes to add to this discussion. First, Section 7.1 discusses how the star formation rate was deduced for the giant molecular clouds in M 33. In Section 7.2 the correlation of the HCN (and HCO^{+}) luminosity with the star formation rate of the giant molecular clouds is investigated and set in relation to other studies.

7.1. The star formation rate in M 33

The tracers used to estimate the rate of star formation are numerous and range from star counts in certain age-bins, over observation of the X-ray, UV and radio-continuum emission and line emission (e.g. Hα and [C II]) to thermal dust emission at infrared wavelengths (e.g L_{TIR}). Each tracer is sensitive to certain types of stars as well as physical processes and can only trace star formation that happened over a specific time-scale in the past. This is in part due to the fact that stars with different masses have different lifetimes, where the most massive stars are the most short-lived. For example, radiation in the NUV mostly emerges from stars with a few solar masses, which have formed over the past 10-200 Myrs. In contrast, much more massive stars
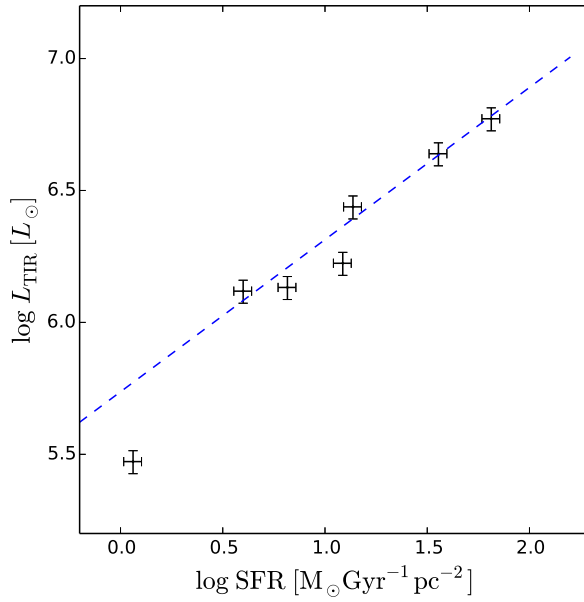
Figure 7.1.: The logarithmic values of the total infrared luminosity (L_{TIR}) and the star formation rate deduced from Hα and 24 μm, plotted against each other. The correlation coefficient is r=0.97.

are able to induce emission lines in the ionized gas surrounding them, such as the Hα emission, which is therefore a tracer of more recent star formation that occurred in the past 3-10 Myrs (Kennicutt & Evans, 2012). UV and Hα emission have been favored traditionally as SFR tracer for their easy accessibility, Hα mostly at low red-shifts and UV at intermediate to high redshifts where it is shifted into the optical wavelengths regime (Calzetti et al., 2007). However, a huge caveat for these two types of star formation tracer is their extinction due to dust that leads to an underestimation of the star formation rate. Therefore a range of composite star formation rate tracers have been developed to correct for the dust extinction, most of which combine UV or Hα with dust emission. The composite tracer of the SFR that is adopted in this work is presented in Calzetti et al. (2007, (Eq. 7)) and combines Hα and 24 μm continuum emission as follows:

$$\text{SFR} = 5.3 \times 10^{-42} \left[L(\text{H}\alpha) + (0.031 \pm 0.006) \, L(24 \, \mu\text{m}) \right]. \tag{7.1}$$

The data used to construct the SFRs for the M 33 GMCs are the 24 μm map (Tabatabaei et al., 2007) from MIPS/*Spitzer* and the Hα map (Hoopes & Walterbos, 2000) (cf. Section 5.3). The fluxes of both maps are extracted at 28″ resolution, such that they are comparable to the observations of HCN and HCO⁺. The resulting values of the SFRs for the seven GMCs are given in Table 5.1. The errors are deduced assuming calibration errors of 7 % for 24 μm (Spitzer Observers Manual v8.0) and 15 % for Hα (Hoopes & Walterbos, 2000) .

As mentioned above the luminosity of the total infrared (L_{TIR}) may also be used as a SFR tracer. There are however issues to be kept in mind when using this tracer. An obvious caveat is that the dust in general does not absorb all the starlight. The absorbed amount depends to a varying degree on the environment. Further, evolved stars with ages $\gtrsim$ 100-200 Myr may also contribute to the heating of the dust (e.g. Boquien et al., 2011). In this case L_{TIR}-based SFR-tracer likely overestimate the SFR of GMC-complexes which have shorter lifetimes of $\sim 27 \pm 12$ Myr (Murray, 2011). Therefore,

Table 7.1.: Linear least squares fit results.

	m	b
L_{HCN}	1.27 ± 0.1	2.5 ± 0.34
L_{HCN} w/o GMC 1	2.3 ± 0.29	-0.57 ± 0.88
L_{HCO^+}	1.35 ± 0.1	2.24 ± 0.3
L_{HCO^+} w/o GMC 1	1.07 ± 0.1	2.9 ± 0.35
HCN - Wu et al. 2005	1.02 ± 0.06	2.79 ± 0.16

the conversion factor between L_{TIR} and SFR thus is dependent on the stellar population mix in galaxies (Kennicutt & Evans, 2012). Thus, to use L_{TIR} as a reliable tracer it has to be calibrated first. It appears however that TIR-derived SFRs still are usable as they are in agreement with the SFRs that were derived from attenuation-corrected Hα line fluxes (Kewley et al., 2002; Kennicutt & Evans, 2012). However, Kennicutt & Evans (2012) question the use of L_{TIR} as a SFR tracer in low-metallicity galaxies with only little dust.

The L_{TIR}-values of the observed M 33-GMCs have already been derived in Chapter 6. Since M 33 has a sub-solar metallicity the viability of L_{TIR} as a SFR-tracer in M 33 is tested for the present sample of GMCs by comparing L_{TIR} with the star formation rate obtained via Eq. (7.1). The resulting scatter plot of the logarithmic values of both quantities is shown in Fig. 7.1. Clearly, the total infrared luminosity and the star formation rate are very well correlated with a Pearson correlation coefficient of r=0.97. Only GMC no2, with the lowest SFR and L_{TIR} value, does not follow the otherwise nearly linear trend. A linear least squares fit, taking into account errors in both quantities (chap. 8 Taylor, 1996) results in log(SFR) = 0.59±0.04 log(L_{TIR}) + 5.70±0.05. Due to the good correlation for the majority of the observed GMC, it is reckoned that it is safe to assume that in our sample L_{TIR} may be used as a proxy for the SFR, despite the sub-solar metallicity of M 33. This is a valuable result and enables the comparison of the results of this study with other studies that employ the TIR luminosity as a proxy for the star formation rate (Gao et al., 2007; Wu et al., 2010; García-Burillo et al., 2012, e.g.). Note that the use of the `HerM33es` *Herschel* PACS and SPIRE observations of M 33 to study of star formation and the total infrared luminosity has been investigated in more detail by Verley et al. (e.g. 2010); Boquien et al. (e.g. 2011).

7.2. HCO+ and HCN emission with respect to the star formation rate

This section aims to characterize the relation of HCN and HCO$^+$ with L_{TIR} in M 33 and sets the findings in comparison to the tight linear correlation between L'_{HCN} and L_{TIR} reported by Gao et al. (see e.g. 2007); Wu et al. (see e.g. 2010); Graciá-Carpio et al. (see e.g. 2008a); García-Burillo et al. (see e.g. 2012).

In Fig. 7.2 log(L_{TIR}) is plotted against the logarithmic line luminosities of HCN, HCO$^+$, and CO. The line luminosities L'_{HCN} L'_{HCO^+} and $L'_{^{12}\text{CO}}$ in units of K km s^{-1} pc^2, were derived by multiplying the integrated line intensities (cf. Table 5.1) with the beam
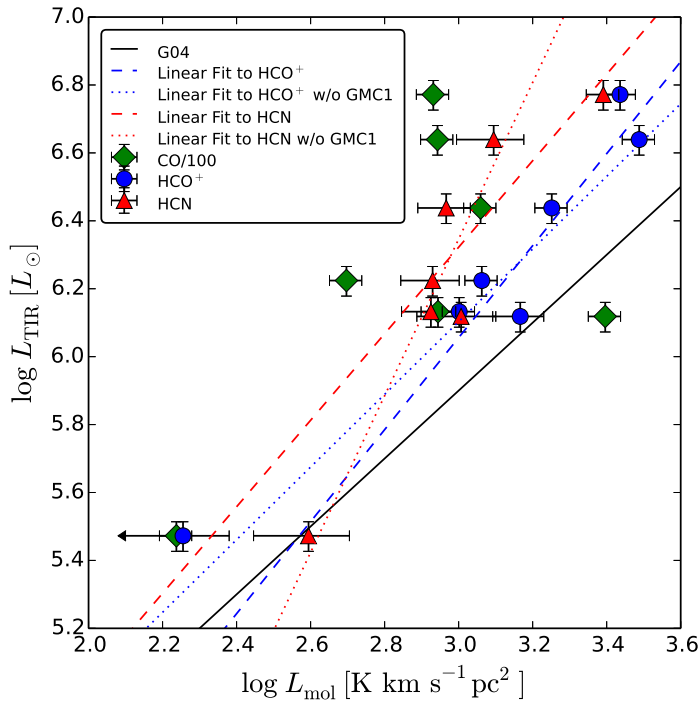
Figure 7.2.: Plot of L_{TIR} against the luminosities of the first transitions of HCO$^+$, HCN and CO for the seven positions observed in M 33. The *red* and *blue* lines are linear least squares fits to the HCN and HCO$^+$ data, respectively, where *dashed* lines show fits including GMC 1 and *dotted* line fits that exclude the same. The *black* line represents the fit by Gao & Solomon (2004a) to luminosities of HCN in LIRGS, ULIRGS and normal spiral galaxies.

size in pc^2 at the distance of M 33, i.e. $1.5 \times 10^4 \, \text{pc}^{-2}$ for a 28$''$ beam. Errors follow from the measurement uncertainties given in Table 5.1. For convenience in Fig. 7.2 the ^{12}CO (1–0) emission has been divided by a factor hundred. Linear least square fits of the form $\log(L_{TIR}) = m \log(L'(\text{mol})) + b$ – taking into account the errors in both axis (Taylor, 1996) – are performed where $L'(\text{mol})$ being the particular luminosities of either HCN, or HCO$^+$. Two fits are made for HCN and HCO$^+$: one including all sources except GMC no2[1] and one that additionally excludes GMC 1. The exclusion of GMC 1 from the analysis is motivated further below in this section and based on its peculiar behavior in Fig. 7.3 and Fig. 7.4, that sets it clearly apart from the other clouds. The linear fit results are shown in Table 7.1 as well as in Fig. 7.2.

For comparison, Fig. 7.2 (*black solid line*) shows further the linear relation between L'_{HCN} and L_{TIR} that was found by (Wu et al., 2005, also given in Table 7.1) over a range from individual dense cores in the Milky Way to entire galaxies, including normal, luminous and ultra-luminous galaxies.

Furthermore, the mutual Pearson correlation coefficients (r) are derived between: L_{TIR}, SFR, the HCN, HCO$^+$, ^{12}CO and ^{13}CO line intensities as well as the atomic, molecular, and total gas surface densities (Σ_{mol}, Σ_{atomic}, Σ_{gas}). The gas surface densities in units of $M_\odot \, \text{pc}^{-2}$ where derived from the atomic and molecular gas masses (cf. Section 5.5, Section 5.6 and Table 5.1) through division with the beamsize (28$''$) in pc^2 at the distance of M 33, i.e. $1.5 \times 10^4 \, \text{pc}^{-2}$. The data from GMC no2 and GMC 1 is excluded here as well for the above reasons. The resulting r-correlation coefficients are shown in Table 7.2. The sample size is $N = 5$. In this case a Pearson correlation coefficient that is higher than $r = 0.8$ can be considered to have significance level of ~90% (Taylor, 1996), such r-values are marked in green in Table 7.2. Note

---

[1]Excluded due to the non-detection of HCO$^+$ and the marginal detection of HCN.

Table 7.2.: Pearson r-correlation coefficients

	SFR	I_{HCN}	I_{HCO^+}	$I_{^{12}CO}$	$I_{^{13}CO}$	$\Sigma_{mol.}$	Σ_{atomic}	Σ_{gas}
L_{TIR}	0.97	0.81	0.96	-0.31	-0.39	0.65	0.62	0.64
SFR		0.80	0.92	-0.42	-0.50	0.50	0.50	0.50
I_{HCN}			0.94	0.19	0.09	0.83	0.83	0.84
I_{HCO^+}				-0.06	-0.15	0.79	0.77	0.79
$I_{^{12}CO}$					0.99	0.51	0.52	0.52
$I_{^{13}CO}$						0.44	0.46	0.45
$\Sigma_{mol.}$							0.96	0.99
Σ_{atomic}								0.99

Notes. All r-values have been derived under exclusion of the data points of GMC 1 and no2.

that $r \geq 0.9$ indicates a significant correlation with a 96% or higher probability that the correlation is genuine.

From the correlation coefficients it can be seen that HCN and HCO⁺ are correlated with L_{TIR} and the SFR. However, HCO⁺ is significantly better correlated with $r \geq 0.92$. This can also be seen in Fig. 7.2 and Table 7.1, where the fits under exclusion of GMC 1 shows a nearly linear behavior with a slope $m = 1.07 \pm 0.1$ similar to the HCN-L_{TIR} relation by (Wu et al., 2005). The slope of HCN is much steeper with $m = 2.3$. Note, that HCN is at all seven positions significantly weaker than expected from the linear relation reported by Wu et al. (2005). Further, the total infrared luminosity is for all clouds above the limit $L_{TIR} < 4 \times 10^5 \, L_\odot$ where the relation is reported to break down in galactic sources (Wu et al., 2005). This confirms and strengthens the key result of Rosolowsky et al. (2011) who first detected this behavior of HCN in four GMCs of M 33.

From the relation of ^{12}CO with L_{TIR} in Table 7.2 and Fig. 7.2 it can be seen that CO is not correlated with L_{TIR} (or any other quantity except $I_{^{13}CO}$) in the present sample. Therefore, the CO integrated line intensity seems to be independent of the SFR on the spatial scales of about 115 pc corresponding to the 28″ beam size. This is in concordance with the breakdown of the Schmidt-Kennicutt law in M 33 at a scale of ∼ 80 pc reported by (Onodera et al., 2010), which the authors attribute to differences in evolutionary stages and drifts of newborn clusters from their parent GMCs. Note that in M 33 a full ^{12}CO (2–1) map has recently been completed by Braine & Schuster, which will allow to study the correlation of CO with the SFR in detail with a spatial resolution of up to about 50 pc (see e.g. Gratier et al., 2012).

In a next step the HCO⁺/HCN line intensity and LTE abundance (cf. Section 5.4) ratios are compared with L_{TIR} with the goal to better understand the respective relation of both molecules with the total infrared luminosity. This comparison is shown in Fig. 7.3. The Pearson correlation coefficient for the intensity as well as the abundance ratios with L_{TIR} for all seven sources is $r = 0.45$, which is not a significant correlation for a sample size $N = 7$. However, looking at Fig. 7.3 one can see that the data points of GMC 1 show a peculiar behavior and deviates from the behavior of the other clouds. Indeed, excluding the data point of GMC 1 the correlation coefficient increases to $r \approx 0.97$, indicating a very good correlation within this sub-sample.
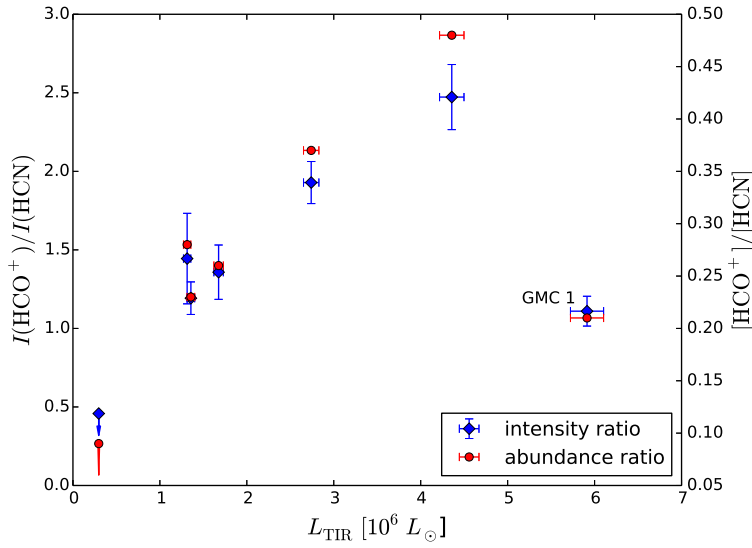
Figure 7.3.: Comparison of the HCO+/HCN integrated intensity ratios (*blue, left axis*) and the LTE [HCO+]/[HCN] abundance ratios (*red, right axis*) with the infrared luminosity L_{TIR}. Upper limits are denoted by arrows.

Interestingly, Graciá-Carpio et al. (2006, 2008b) and Imanishi et al. (2007) find a reversed trend where the HCO+/HCN luminosity ratio declines with increasing L_{TIR}. However they study objects with much higher TIR luminosities $L_{TIR} > 10^{10}$ in a sample of (U-)LIRGs including AGN and starburst galaxies. Baan et al. (2008) investigates the same relation in a similar but larger sample of galaxies. They do not find a simple declining trend but a more complicated picture that depends on the evolutionary stages of the individual galaxies. However, an increase of HCO+/HCN with L_{TIR} is not compatible with their findings either. This shows that the underlying physical and chemical properties in the observed GMCs of M 33 are different from the average conditions in AGNs and starburst galaxies.

To reveal whether the increase of HCO+/HCN with L_{TIR} seen for the other 5 GMCs is due to an increase of the HCO+ intensity, a decrease of HCN intensity or a combination of both, Fig. 7.4 plots the L_{TIR}/L'_{HCN} and the L_{TIR}/L'_{HCO^+} ratios against L_{TIR}. Note the peculiar behavior of GMC 1 that shows up also in this plot; again it is excluded in the following discussion for the above reasons. The plot reveals that the ratio of L_{TIR}/L'_{HCO^+} stays rather constant with L_{TIR}, indicating a linear increase of the HCO+ luminosity with the TIR-luminosity. On the other hand the increase in L_{TIR}/L'_{HCN} points out that L'_{HCN} is rather constant or only weakly increases with L_{TIR} between the clouds.

To test for subtle effects in the behavior of L'_{HCN}, Fig. 7.4 shows a linear relation for a hypothetical constant L'_{HCN} equal to the mean value of the clouds L_{TIR}/L'_{HCN}=2.1. This linear relation has been fitted to the data points in Fig. 7.4 to determine a sensible y-axis intersection. It can be seen that for GMC no6, L'_{HCN} seems to be larger with respect to the other clouds whose L_{TIR}/L'_{HCN} ratios increase roughly in parallel to the linear relation for the mean of the clouds. Indeed, from the HCN line intensities in Table 5.1, we see that the HCN intensity hardly varies between the sources GMC 26, GMC no3, GMC 91, and GMC no1 where $I_{HCN} = 56$–$67 K km s^{-1}$, while GMC no6 has a significantly larger flux $I_{HCN} = 84 K km s^{-1}$. The absence of an increase of L'_{HCN} with L_{TIR} raises doubts for its application in M 33 as a molecular tracer of the star formation rate. In contrast to the findings in galaxy averaged observations as well as in galactic massive star forming clumps as discussed above (e.g. Gao et al., 2007; Wu et al., 2010).
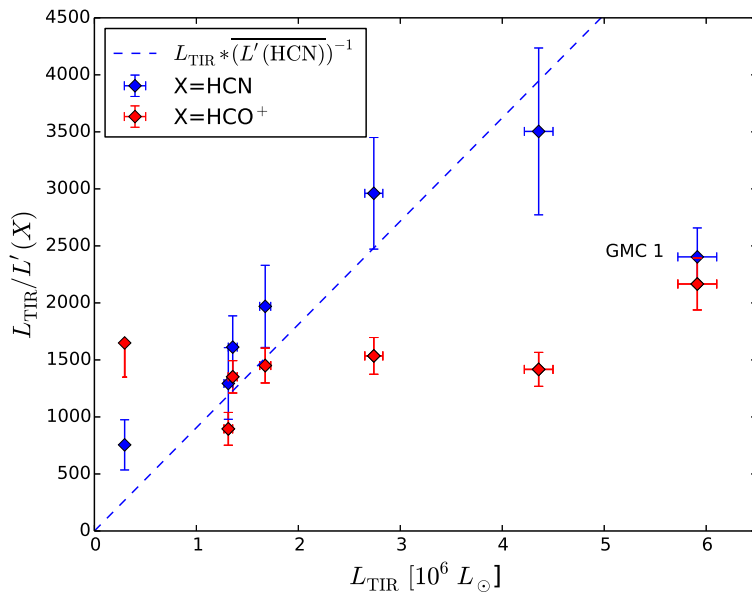
Figure 7.4.: Comparison of L_{TIR}/L'_{HCN} (*blue*) and L_{TIR}/L'_{HCO^+} (*red*) with the infrared luminosity L_{TIR}. Upper limits are denoted by arrows. The dashed blue line shows the hypothetical behavior of the relation for a constant value of L'_{HCN} equal to the mean over all clouds excluding GMC 1.

The following paragraph was published in Section 4.4.3 from (Buchbender et al., 2013).

The L_{TIR}/L_{HCN} ratios observed in M 33 (Table 5.1) fall into the range between 1300 and 3500 $L_\odot$/K km s^{-1} pc^2. These ratios lie at the upper end of the values found in Milky Way clouds (Wu et al., 2010). Normal galaxies show on average total L_{TIR}/L_{HCN} ratios of about 900±70 $L_\odot$/K km s^{-1} pc^2 (Graciá-Carpio et al., 2008a, GS04a,b). For (U-)LIRGs, higher values, in the range of $\sim 1100 - 1700 \, L_\odot$/K km s^{-1} pc^2, are found (Graciá-Carpio et al., 2008a, GS04a,b), while the highest reported ratios are found at the extreme end of the LIRG/ULIRG distribution, as well as in high-z galaxies, and range up to $\sim 3900 \, L_\odot$/K km s^{-1} pc^2 (Solomon et al., 2003; Gao et al., 2007; Graciá-Carpio et al., 2008a; Wu et al., 2010; García-Burillo et al., 2012). Thus the L_{TIR}/L_{HCN} ratios in M 33 are among the highest ratios observed.

Hypothesizing, that, despite the small sample size, the different behavior of GMC 1 is significant, its peculiar behavior might indicate that this cloud is governed by different physical or chemical mechanisms. Indeed, GMC 1 takes a special place within our sample of sources as it is located in the center of M 33. Although the center of M 33 is not strongly pronounced (cf. 2.3), GMC 1 is with 126.6 M_{H_2} the most massive cloud of the sample and is actively forming stars with a SFR of 65 $M_\odot$ Gyr^{-1} pc^2, which is two times larger than for the next active cloud GMC no6. Furthermore, it is closely located to the X-ray binary M33-X8 in a distance of about 110 pc. In the Discussion in Chapter 14 possible influences of this constellation onto the HCO⁺/HCN ratio are discussed.

The key conclusions of this chapter are:

- HCO⁺ is well correlated with the total infrared luminosity.

- HCN is poorly correlated with TIR.

- HCN is under-luminous relative to the tight linear relation between L'_{HCN} and L_{TIR} found to hold from galactic massive clumps over normal galaxies to (ultra-) luminous infrared galaxies (e.g. Gao et al., 2007; Wu et al., 2010).

- The above reasons indicate that in M 33 HCO$^+$ might be a more reliably tracer of the dense gas content related to star formation in M 33.

- The HCO$^+$/HCN ratio of GMC 1 – in the center of M 33 – shows a peculiar behavior in relation to the total infrared luminosity and the other sources. Its close proximity to a strong X-Ray binary M33-X8 might alter its emission and abundance characteristics.

What is the reason for the under-luminous HCN emission in M 33?   A variety of processes exist that alter the emission characteristics of HCN (and HCO$^+$). Especially the sub-solar metallicity of M 33 (e.g. Magrini et al., 2007) might play a role in the under-luminosity of HCN with respect to the larger and more metal rich spiral galaxies in the studies such as Gao et al. (e.g. 2007). To investigate the implications of lower elemental abundances onto the line ratios between CO, HCN, and HCO$^+$ in Chapter 9 dedicated models of photon-dominated regions are employed. These models take not only the chemical network into account, but also the detailed heating and cooling processes of a cloud as well as radiative transfer are used. In Chapter 14 further possible influences onto the emission characteristics of HCN and HCO$^+$ such as, amongst others, differences in chemistry and/or gas-to-dust content and also differences in the evolutionary state of the observed GMCs are discussed in more detail.

Chapter 8.

Molecular tracers in relation to each other

Molecular line intensity ratios may provide valuable diagnostic tools of physical properties of the emitting regions. A range of ratios that use the emission from HCN, HCO$^+$ and ^{12}CO can be found in the literature. Applications include the HCO$^+$/HCN and HCN/HNC ratio as a tracer to discriminate between PDR and XDR dominated sources (e.g. Krips et al., 2008; Baan et al., 2008) and the HCN/CO and HCO$^+$/CO ratios as tracers of the dense gas fraction (e.g. Brouillet et al., 2005). In this chapter the HCN, HNC, HCO$^+$ and CO emission in the GMCs in M 33 is set in context to each other and is compared to that found in other objects, near and far. In Section 8.1 the HCO$^+$/CO and HCN/CO ratios are investigated in comparison with findings in M 31, the Milky Way as well as normal galaxies. The next Section 8.2 investigates HCO$^+$/HCN and HNC/HCO$^+$ ratios in M 33 in comparison with a large range of sources ranging from the MW, over the LMC to total infrared luminosity ((U-)LIRGs). The ^{12}CO/^{13}CO line ratio is investigated in Section 8.4. The last Section 8.5 investigates the influence of variations in the excitation conditions onto the HCO$^+$/HCN line intensity ratio using the statistical equilibrium radiative transfer code RADEX (van der Tak et al., 2007).

8.1. HCO$^+$/CO vs. HCN/CO

The text of this section has been published in Sec. 4.4.1 of (Buchbender et al., 2013) with the exception of the last paragraph and Fig. 8.2. For the comparison of different tracers, all data were convolved to the same resolution of 28″. To account for the different intrinsic beam sizes of the CO, HCN, and HCO$^+$ (1–0) observations the data has been multiplied with beam filling factors determined from the ^{12}CO (2–1) map (Gratier et al., 2010). Fig. 8.1 compares the HCO$^+$/CO vs. HCN/CO line intensities ratios observed in M 33, with those observed at nine positions in the disk of the Andromeda galaxy M 31 (Brouillet et al., 2005, hereafter BR05). M 31 lies at a similar distance as M 33 of 780 kpc and had been observed with the 30 m telescope as well. Therefore, both studies obtain about the same spatial resolution of $\sim$ 114 pc.

For M 33, we find HCN/CO ratios in the range of 0.4 % – 2.9 % (mean: 1.5 ± 0.8 %) and HCO$^+$/CO ratios in 0.6 % – 3.5 % (mean: 1.9 ± 1.0 %). BR05 finds comparable values in the spiral arms of M 31: HCN/CO 0.75 % – 2.8 % (mean: 1.7 ± 0.5 %) and HCO$^+$/CO 1.1 % – 3.9 % (mean: 2.0±0.7 %). A linear least squares fit to the M 33 data results in HCO$^+$/CO = (1.14 ± 0.15 %) HCN/CO + (0.18 ± 0.14 %).
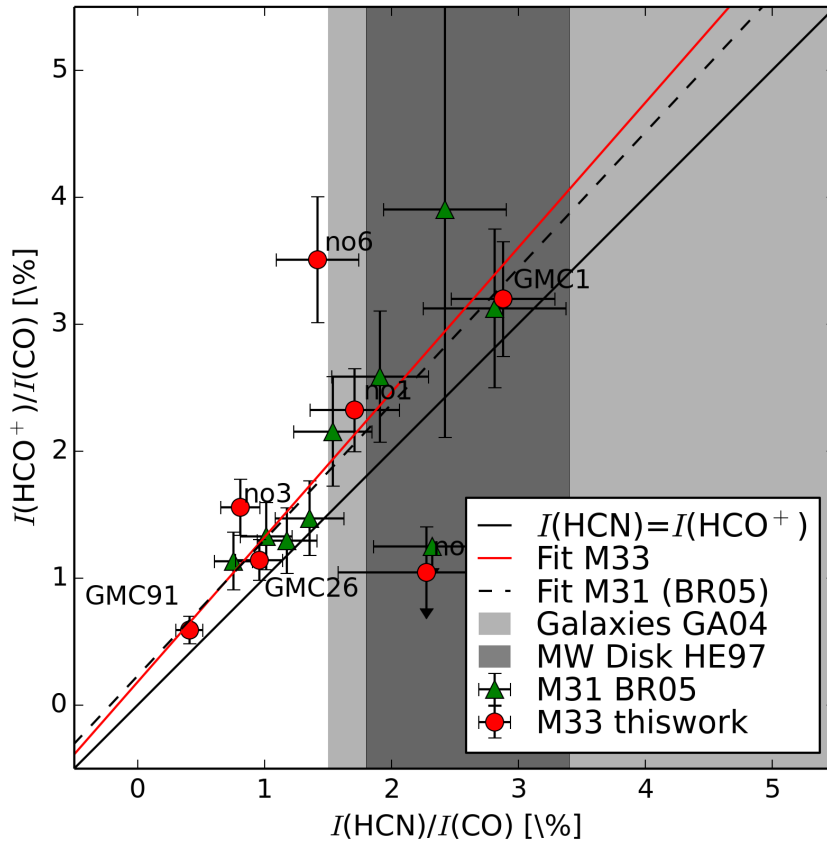
Figure 8.1.: Ratios of integrated intensities HCO⁺/CO vs. HCN/CO for M 33 (red points: this work) and for M 31 (green points: BR05). Upper/lower limits are denoted by arrows. Linear least squares fits to data from M 33 (red solid line) and M 31 (BR05, black dashed) are shown. Both fits exclude points with upper limits. The solid black line shows the angle bisector where $I(HCO^+) = I(HCN)$. The gray shaded areas display the range of the HCN/CO found in the disk of the Milky Way (MW) by (Helfer & Blitz, 1997, HE97) (darker gray) and in a sample of normal spiral galaxies (GA04b) (lighter gray). (Buchbender et al., 2013)

This is consistent within errors to the fit results obtained by BR05 for the M 31 data: HCO⁺/CO = 1.07 % HCN/CO + 0.23 %. We excluded positions with upper limits from the fit, i.e. position GMC no2.

In the Milky Way in the solar neighborhood values of HCN/CO are found between 0.7 % – 1.9 % (mean: 1.4 ± 2 %), while the Galactic plane hosts on average 2.6 ± 0.8 % (Helfer & Blitz, 1997). HCO⁺/CO values in the Galactic center range between 0.9 % and 7.6 % (Riquelme et al., 2010).

The HCN/CO ratios found in the LMC by Chin et al. (1998) and Heikkilä et al. (1999) lie between 3 % and 6 %, and are thus higher than any value found in M 33, M 31, and also M 51 where HCN/CO = 1.1 % – 2 % in the spiral arms are reported (Kuno et al., 1995). Unlike GS04b in a sample of normal galaxies, we do not find a systematic change in the HCN/CO ratio between regions in the center of M 33, i.e. the inner ∼ 1 kpc (here GMC1, GMC26) and regions at greater galacto-centric distances (cf. Table 5.1). GS04b reports that HCN/CO drops from ∼ 10% in the centers of normal galaxies to ∼ 1.5% – 3% in their disks ⪆ 4 kpc. In ULIRGs and AGNs the ratios
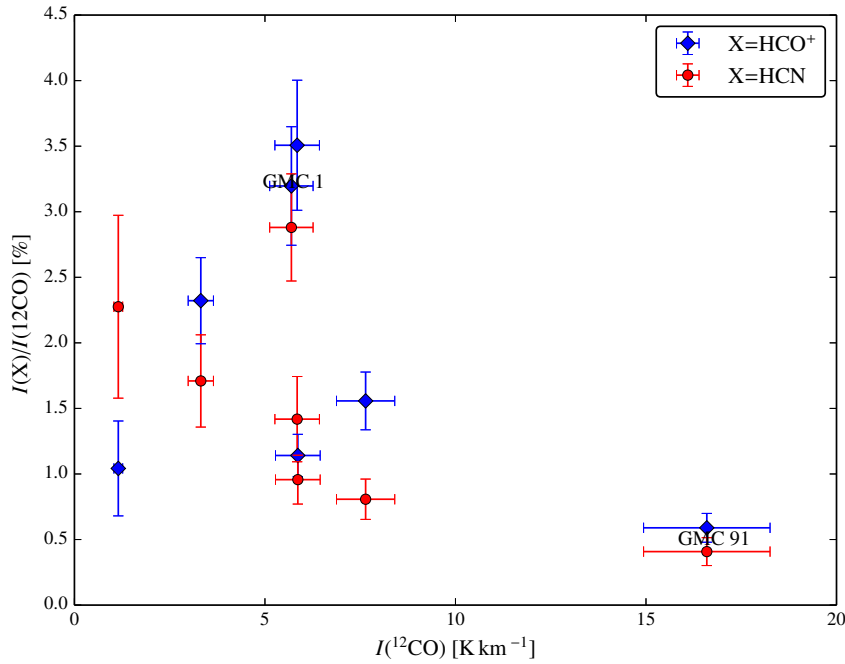
Figure 8.2.: Comparison of the HCN/CO and HCO⁺/CO line intensity ratios with the ¹²CO line intensity. HCN/CO ratios are shown in *red*, HCO⁺/CO ratios in *blue*.

may reach global HCN/CO values as high as 25% (GS04b and references therein). GS04b attribute these high ratios to the presence of starbursts and argue that HCN/CO may serve as a starburst indicator.

To investigate if a correlation between ¹²CO and HCN as well as HCO⁺ exists, the HCN/CO and HCO⁺/CO line intensity ratios are plotted against the ¹²CO line intensity in Fig. 8.2. A declining trend of the HCN/CO ratios with increasing ¹²CO line intensities exists. The data point of GMC 1 is an exception to this trend. Excluding this data point [1] a high correlation coefficient for HCN/CO vs. CO of $r = -0.9$ is found. Indeed, as has been discussed in Section 7.2 the HCN line intensity is rather constant independent of the cloud with few exception (GMC no6 and GMC 1). The HCO⁺/CO line intensity ratio, on the other hand, seems mostly independent of the ¹²CO line intensity and shows only a week correlation coefficient of $r = -0.4$ which is driven to some extent driven by the data point of GMC 91 with the largest ¹²CO intensity in our sample. This cloud seems to be rather quiescent as its SFR is very low with $4\,M_\odot\,\mathrm{Gyr}^{-1}\,\mathrm{pc}^{-2}$. Both relations show that the fraction of denser gas traced by HCN and HCO⁺ does not depend on the total amount of molecular gas of a specific GMC as traced by ¹²CO.

8.2. HCO⁺/HCN and HNC/HCO⁺

This section has been published in Sec. 4.4.2 of (Buchbender et al., 2013).

The HCO⁺/HCN ratios observed in M 33 vary between 1.1 and 2.5, while the upper limits derived for the HNC/HCO⁺ ratios vary between 0.2 and 0.5 (Fig. 8.3). The upper

---

[1] See Section 7.2 and the Discussion in Chapter 14 for a motivation to exclude GMC 1.
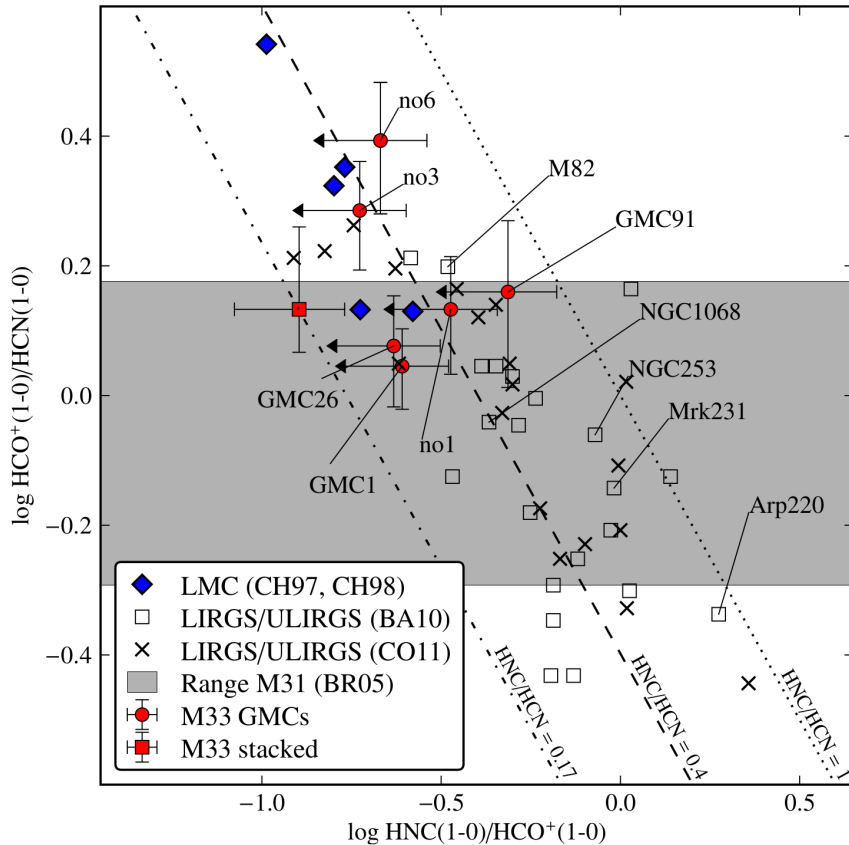
Figure 8.3.: Comparison of integrated intensities HCO$^+$/HCN vs. HNC/HCO$^+$ in M 33 (*red filled circles* and *square*; *arrows* indicate upper/lower limits) with values found in the LMC (Chin et al., 1997, 1998) (CH97, CH98; *blue diamonds*) and in luminous infrared galaxies compiled by Baan et al. (2008) (BA08; *open symbols*) and by Costagliola et al. (2011) (CO11; *crosses*). The *dotted*, *dashed*, and *dot-dashed* lines shows HNC/HCN = 1, 0.4, and 0.17 (stacked value of M 33), respectively. The *gray shaded* area shows the range of the observed HCO$^+$/HCN ratios in M 31 by BR05. (Buchbender et al., 2013)

limit of the HNC/HCN ratio is at maximum 0.7 (GMC91), while the stacked spectrum where HNC has been detected shows a HNC/HCN ratio of 0.17 (Fig. 8.3).

These ratios are compared with the ratios found in luminous infrared nuclei by Baan et al. (2008) and Costagliola et al. (2011) and in H ıı regions of the LMC by Chin et al. (1997, 1998) (cf. Fig.3a in Baan et al. (2010)). The HCO$^+$/HCN ratios are also compared to the range found in the disk of M 31 by BR05 (cf. Fig. 8.3).

The HCO$^+$/HCN ratios, found in M 33 in the six GMCs with clear detections, lie at the upper end of the distribution of values found in LIRGs. While the starburst galaxy M 82 exhibits a higher ratio than the AGN NGC 1068 (1.6 vs. 0.9), these ratios lie within the scatter of values and their errors observed in the disk of M 33.

The HCO$^+$/HCN ratios in M 33 lie in the overlap region between the ones found in M 31 and those found in the LMC. We find neither ratios as high as in the LMC, i.e. 3.5, nor ratios as low as in M 31, i.e. 0.51. Interestingly, all detected regions in the LMC are situated in the same parameter space as those detected in M 33. The detection of HNC in the stacked spectrum allows us to derive an average HCO$^+$/HNC ratio of

7.8 (Table 5.3) for the GMCs observed in M 33. This ratio lies at the very high end of the range of values found in any of the other samples plotted in Fig. 8.3.

More remarkably, the HCN/HNC value of 5.9 from the stacked spectra is higher than any from the other samples we compare with in Fig. 8.3. Furthermore, it is higher than ratios observed over the surface of IC 342 which are only $\sim 1-2$ (Meier & Turner, 2005), higher than the ratios in a range of galaxies found by Huettemeister et al. (1995) of < 4, higher than the typical ratios of 1 observed in starburst and Seyfert galaxies (e.g. Aalto et al., 2002), and also higher than ratios of 1-3 observed in Galactic molecular complexes (Wootten et al., 1978).

This extraordinary high ratio indicates that the physics or chemistry in M 33 may be different from that of AGNs and starbursts. The dominance of strong X-ray radiation in the nuclei of AGNs or even of starbursts may be important for the differences in the line ratios, since it creates X-ray-dominated regions (XDRs) that change the chemical abundances (e.g. Meijerink & Spaans, 2005).

The subsolar metallicity of M 33 may also play a role in creating such a high ratio between HCN and HNC. However, the HCN/HNC ratio obtained in M 33 is significantly higher than those observed in similar low-metallicity environments, such as N159, 30Dor in the LMC, as well as LIRS36 in the SMC, which are no higher than 3.6 (besides a lower limit of 4.7 in N27 in the SMC) (Chin et al., 1998; Heikkilä et al., 1999) and comparable to the values found in Galactic GMCs (Huettemeister et al., 1995). Therefore, a subsolar metallicity alone does not seem to be a guarantee for very high HCN/HNC ratios.

8.3. HCO⁺/HCN vs. HNC/CO

In Fig. 8.4 the HCN/CO line intensity ratio is plotted against that of HCO⁺/HCN. The plot is an adaptation of Figure 6 in Baan et al. (2010). It compares the values obtained in the GMCs in M 33 against a sample of (U-)LIRGs and starbursts galaxies as well as galaxies in late stages of starbursts (*grey symbols*) from Baan et al. (2010). Again – as in Fig. 8.3 – the HCO⁺/HCN ratios in M 33, are found at the upper end of the distribution. The HCN/CO ratios coincide and exceed the lower end of values found in the sample of Baan et al. (2010). In M 33 no correlation between both ratios is found ($r = -0.27$). This is in contrast to the good correlation found by (Baan et al., 2010) for the (U-)LIRGs and starbursts galaxies. This correlation is interpreted by (Baan et al., 2010) as follows: while the starburst progresses, more and more of the high density gas traced by HCN is consumed – as such the HCN/CO ratio serves as a evolutionary tracer. In this way also the mean density of the medium decreases. The HCO⁺/HCN ratio on the other hand is sensitive to the mean density of the medium. This is because on the one hand the critical density of HCO⁺ is an order of magnitude lower than that of HCN (cf. Table 3.1) such that at densities below the critical density of HCN ($2 \times 10^5 \, \text{cm}^{-3}$), HCO⁺ emits more strongly. On the other hand, the HCO⁺ abundance is sensitive to the density as its rate of recombinations with electrons – in which HCO⁺ is destroyed – is increased at higher densities (cf. also Section 9.1.2).

The lack of a correlation between the two ratios in the sample of GMCs in M 33 shows that a change in mean density does not govern the HCO⁺/HCN ratios of this sample. Furthermore, this indicates that in the GMC-sample HCN/CO does not equally
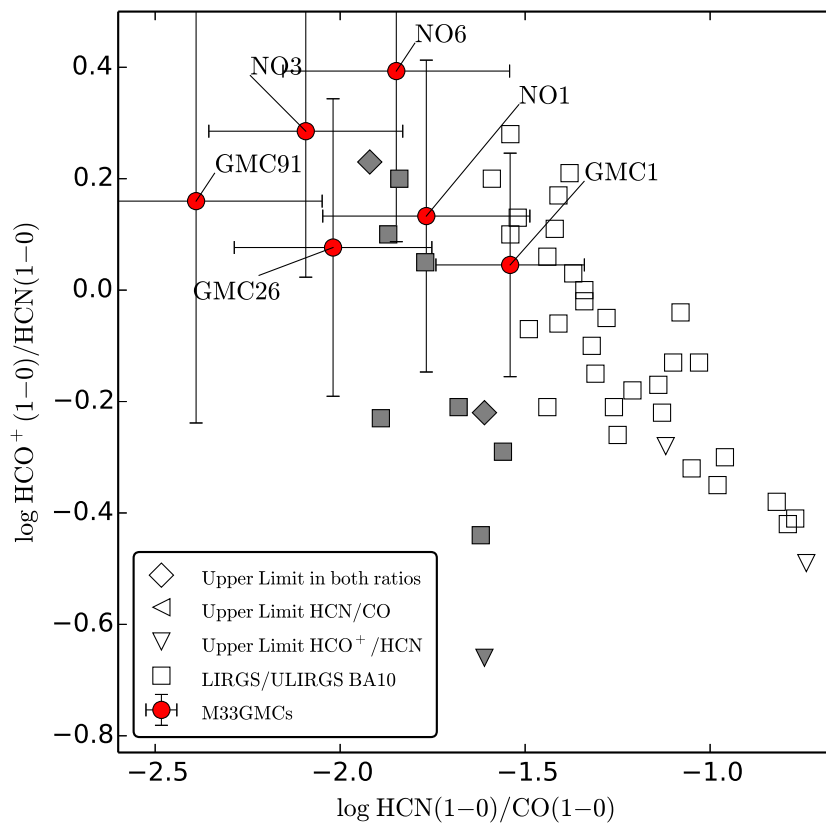
Figure 8.4.: Comparison of the HCN/CO and HCO+/HCN line intensity ratios. *Red circles* show the data for the M 33 GMCs. The *open symbols* show (U-)LIRGs and starburst galaxies; gray symbols sources at later stage of stages of starburst evolution (Baan et al., 2010). The same sample is shown in Fig. 8.3. This figure is an adaptation of Figure 6 from (Baan et al., 2010).

serve as a evolutionary tracer of the GMCs as it does in the galaxy averaged sample of (Baan et al., 2010).

8.4. ^{12}CO/^{13}CO line ratio

The text of this section has been published in Sec. 4.4.4. of (Buchbender et al., 2013). In our sample of GMCs in M 33 we find ^{12}CO/^{13}CO line intensity ratios between 9 and 15. There is no obvious correlation with galacto-centric distance, FUV strength, or SFR. In a study of eight GMCs in the outer disk of M 33, Braine et al. (2010) found similar ratios between 8.9 and 15.7. In the Milky Way, the isotopic ratio of ^{12}C/^{13}C varies between values of 80 − 90 in the solar neighborhood and 20 in the Galactic center (Wilson, 1999). Polk et al. (1988) studied the ^{12}CO/^{13}CO line ratio in the Milky Way, for several large regions of the plane in comparison with the average emission from GMCs and of the centers of GMCs. They find that the average value rises from three in the centers of GMCs, to 4.5 averaged over GMCs, to 6.7 for the Galactic plane, with peaks of ∼ 15. Their interpretation is that the higher ratios observed in the plane are caused by diffuse gas of only moderate optical thickness in ^{12}CO. A similar

Table 8.1.: RADEX HCO$^+$ (1–0)/HCN (1–0) line intensity ratios

T [K]\ n_{H}[cm^{-3}]	1×10^3	5×10^3	1×10^4	3×10^4	7×10^4
$N_{\mathrm{HCN}} = 3.8 \times 10^{11}$ and $N_{\mathrm{HCO^+}} = 1.8 \times 10^{12}$; [HCN]/[HCO$^+$]=4.8					
10	2.0	1.9	1.8	1.5	1.2
19	1.7	1.6	1.5	1.2	0.9
25	1.6	1.5	1.4	1.1	0.8
35	1.5	1.4	1.3	1.0	0.7
50	1.4	1.3	1.2	0.9	0.7
$N_{\mathrm{HCN}} = 8 \times 10^{11}$ and $N_{\mathrm{HCO^+}} = 2 \times 10^{11}$; [HCN]/[HCO$^+$]=4					
10	2.4	2.3	2.2	1.8	1.4
19	2.0	1.9	1.8	1.4	1.1
25	1.9	1.8	1.6	1.3	1.0
35	1.8	1.6	1.5	1.2	0.9
50	1.7	1.5	1.4	1.1	0.8
$N_{\mathrm{HCN}} = 8.6 \times 10^{11}$ and $N_{\mathrm{HCO^+}} = 4.1 \times 10^{11}$; [HCN]/[HCO$^+$]=2.1					
10	4.6	4.4	4.2	3.5	2.7
19	3.8	3.6	3.4	2.7	2.0
25	3.6	3.4	3.1	2.5	1.8
35	3.3	3.1	2.9	2.3	1.6
50	3.2	2.9	2.7	2.1	1.5

Notes. A line width of $10 \, \mathrm{km \, s^{-1}}$ for both lines is assumed.

interpretation may hold in M 33. The fraction of dense gas within the beam and optical depth effects may affect the ratios observed in M 33.

Ratios in the Magellanic clouds are observed by Heikkilä et al. (1999) to cover values between 5 and 18, a somewhat wider range than found in M 33. Unlike in M 33, a gradient is seen on larger scales in a set of IR-bright nearby galaxies, dropping from values of about ten in the center to values as low as two at larger radii (Tan et al., 2011). Although Aalto et al. (1995) finds variations with galacto-centric radius in some galaxies of their IR-bright sample, other galaxies exist where the ^{12}CO/^{13}CO stays constant with radius. They report a mean value of ~ 12 for the centers of most galaxies in their sample except for the most luminous mergers with ratios of $\gtrsim 20$ (see also Casoli et al., 1992).

8.5. Influence of excitation conditions onto the HCO$^+$/HCN ratio

Here the influence of variations of excitation conditions onto the HCO$^+$/HCN line intensity ratios are shortly investigated. To get a handle onto the impact of changing excitation conditions on the HCO$^+$/HCN line intensity ratio, the statistical equilibrium radiative transfer code RADEX (van der Tak et al., 2007)[2] is used. With this tool HCO$^+$/HCN line intensity ratios are derived for a set of temperatures and densities.

---

[2]Here the on-line version is used: http://home.strw.leidenuniv.nl/ moldata/radex.html .

The exploited range is motivated by the results of the analyses of the observations in M 33 in this thesis and also anticipates results obtained further below. The combined range of best-fitting densities from the PDR analyses for GMCs (Section 9.2) and "clouds" within GMC no3 (Section 12.5) is 1×10^3–$7 \times 10^4 \mathrm{cm}^{-3}$. The only estimates at hand for the average temperatures present in the seven giant molecular clouds are derived from their dust-SEDs and lie between 19 K and 25 K (cf. Section 6.3). Since, the gas and dust temperatures are expected to couple only in the densest parts of molecular clouds with densities exceeding 1×10^4–$1 \times 10^5 \mathrm{cm}^{-3}$ (Goldsmith, 2001), here a somewhat larger range in temperature is explored, i.e. 10–50 K. This is a typical range found for the excitation temperatures in dense molecular clouds (e.g. Snow & McCall, 2006). Finally, three different sets of column densities for HCN and HCO$^+$ are used, which span the observed range of [HCN]/[HCO$^+$] abundance ratios derived under assumption local thermodynamic equilibrium (LTE) (cf. Section 5.4). The three sets are: the lowest observed LTE-abundance ratio of GMC no6, i.e. [HCN]/[HCO$^+$]=2 with $N_{\mathrm{HCO^+}} = 4 \times 10^{11} \mathrm{cm}^{-2}$ and $N_{\mathrm{HCN}} = 8 \times 10^{11} \mathrm{cm}^{-2}$; the ratio of the average (stacked) spectra of all seven GMCs, with [HCN]/[HCO$^+$]=4 and $N_{\mathrm{HCO^+}} = 2 \times 10^{11} \mathrm{cm}^{-2}$ and $N_{\mathrm{HCN}} = 8 \times 10^{11} \mathrm{cm}^{-2}$; the highest abundance ratio found in GMC 1 (excluding GMC no2), i.e. [HCN]/[HCO$^+$]=4.8 with $N_{\mathrm{HCO^+}} = 3.8 \times 10^{11} \mathrm{cm}^{-2}$ and $N_{\mathrm{HCN}} = 1.8 \times 10^{12} \mathrm{cm}^{-2}$. The resulting line intensity ratios, calculated with RADEX within this parameter space, are given in Table 8.1.

From the table it can be seen that for all sets of column densities the line intensity ratio decreases steadily with an increase in temperature as well as density. The ratios are naturally higher in the case of a lower [HCN]/[HCO$^+$] abundance ratios. The ratios increase at most by 0.3 at all densities if the temperature increased from 19 K to 25 K, which span the range of deduced (dust-)temperatures of the GMC. These differences are comparable to the measurement uncertainties (cf. Table 5.1). Nevertheless, within the range of explored densities and temperatures the calculated HCO$^+$/HCN ratios cover the observed range of 0.8–2.5 for the GMCs and for the "clouds" with in GMC no3 (cf. Table 5.1 and Table 12.1). Naturally, it is found that the [HCN]/[HCO$^+$] abundance ratio has a strong influence onto the line intensity ratio and defines the ratio for a given temperature and density. Note that RADEX finds optically thin conditions for the HCO$^+$ and HCN lines in the explored parameter range. Thus no optically depth effects alter the ratios derived with RADEX.

To investigate the combined effect of changes in abundance and excitation conditions, in the next chapter models of photon-dominated regions are used.

Chapter 9.

Photodissociation regions and metallicity

The metallicity of the interstellar medium has a strong influence onto many processes within molecular clouds. Amongst others it influences the chemical reactions and the gas-to-dust ratio which controls the intensity of the radiation field at a given depth into a cloud. Subsequently, the metallicity is of immense importance for star formation itself.

To improve on the LTE analysis and to better understand why HCN is under-luminous in M 33 with respect to HCO$^+$ as well as L_{TIR} (cf. Chapter 7), we compare the observed HCO$^+$/HCN, HCN/CO, and HCO$^+$/CO line ratios with models of photon-dominated regions (PDRs) using the Meudon PDR code (Le Petit et al., 2006; Gonzalez Garcia et al., 2008). The models have been tailored to reflect the ISM in M 33 as well as that of the MW to get a handle on the influence of the metallicity on the line emission. The models are described in Section 9.1 and their comparison with the data in Section 9.2.

This chapter has been published in (Buchbender et al., 2013). Exceptions are a study of the formation and destruction pathways of HCN and HCO$^+$ in the best-fit models in Section 9.1.2 and also Section 9.1.3 that discusses the modeled abundances shown in Fig. 9.2.

9.1. A sub-solar metallicity PDR model for M 33

9.1.1. Model setup

The Meudon PDR code (Le Petit et al., 2006; Gonzalez Garcia et al., 2008) solves the thermal balance, chemical network, detailed balance, and radiative transfer of a plane-parallel slab of optical extinction A_v and, constant density n_{H} illuminated from both sides by an FUV field of intensity G_0. The modeled line widths are calculated by the Meudon code via the Doppler broadening of the gas due to the kinetic temperature and the turbulent velocity of the gas. The latter dominates the line widths and is an input parameter to the Meudon code. We use the default value of the Meudon code which, expressed in terms of the FWHM of the velocity distribution, is $(\Delta v)_{\text{FWHM}} \sim 3\,\text{km}\,\text{s}^{-1}$. This is slightly lower than the observed line widths that are in the range of 4–11 km s^{-1}. We also used the defaults for additional input parameters (e.g. the cosmic-ray ionization rate and size distribution of dust grains).

Table 9.1.: Initial Abundances used in the PDR models

Species	Sun[a]	Orion[b]	M33[c]	diff. in [dex][d]
H_2	0.1	0.1	0.1	
H	0.8	0.8	0.8	
He	0.1	0.1	0.1	
C	8.43	8.37	7.77	0.60
O	8.69	8.65	8.27	0.38
N	7.83	7.92	7.31	0.61
S	7.12	6.87	6.71	0.16
Fe	7.50	6.00	5.73	0.27

Notes. Entries show $12+\log(n(X)/(2n(H_2)+n(H)))$. [a]Asplund et al. (2009); [b]Simón-Díaz & Stasińska (2011); [c]Magrini et al. (2010); Henry et al. (2000); [d]between Orion and M 33.

The grid of models has been calculated for volume densities $n_H = 0.1, 0.5, 1, 5, 10, 50, 10^2 \times 10^4 \, cm^{-3}$, FUV field strengths $G_0 = 10, 50, 100$ in Habing units, and optical extinctions $A_v = 2 - 50 \, mag$, i.e. in steps of $\log A_v \sim 0.2$.

The input range of FUV fields is motivated by the range of FUV fields derived from the TIR in the six observed clouds which vary between $G_0 = 11.3$ and 50.7, excluding position no2 with a very low G_0 of 1.8 (cf. Table 5.1). We add models of $G_0 = 100$ to cover possible higher local radiation fields. The values of A_v range from those found in translucent clouds with 2 mag to extinctions of 50 mag typically found in resolved Galactic high-mass star-forming clouds. The densities cover values found in a typical molecular cloud, covering the critical densities of the observed tracers and transitions.

We calculated this grid of models for solar and subsolar metallicities. Table 9.1 shows the abundances measured in M 33 and in the Orion nebula which we use as initial abundances for our PDR models. The abundances of the sun are listed for comparison. For the "solar" metallicity model, we adopt the abundances of O, C, N, S, Fe measured in the H ıı region of the Orion nebula by Simón-Díaz & Stasińska (2011). The heavy elements S and Fe are depleted to dust grains with respect to the abundances found in the solar photosphere.

For the subsolar metallicity PDR model, we adopt the averaged O, N, and S abundances measured in M 33 from Magrini et al. (2010) who targeted 33 H ıı regions between 1 and 8 kpc galacto-centric distance. The carbon gas-phase abundance has not been measured in M 33. We estimate it using the metallicity dependence of the C/O ratio described by (Henry et al., 2000). To derive the Fe abundance, we scale the solar Fe/O ratio by the subsolar O metallicity of M 33.

Please note that the line intensities of the molecules ^{13}CO, HNC, and C_2H are unfortunately not included in the version of the Meudon PDR code that has been used.

9.1.2. Formation and destruction of HCN and HCO$^+$ in photon-dominated regions

In this section the formation and destruction of HCN and HCO$^+$ in PDRs is investigated using the best-fitting solar metallicity model for the stacked values from Section 9.2
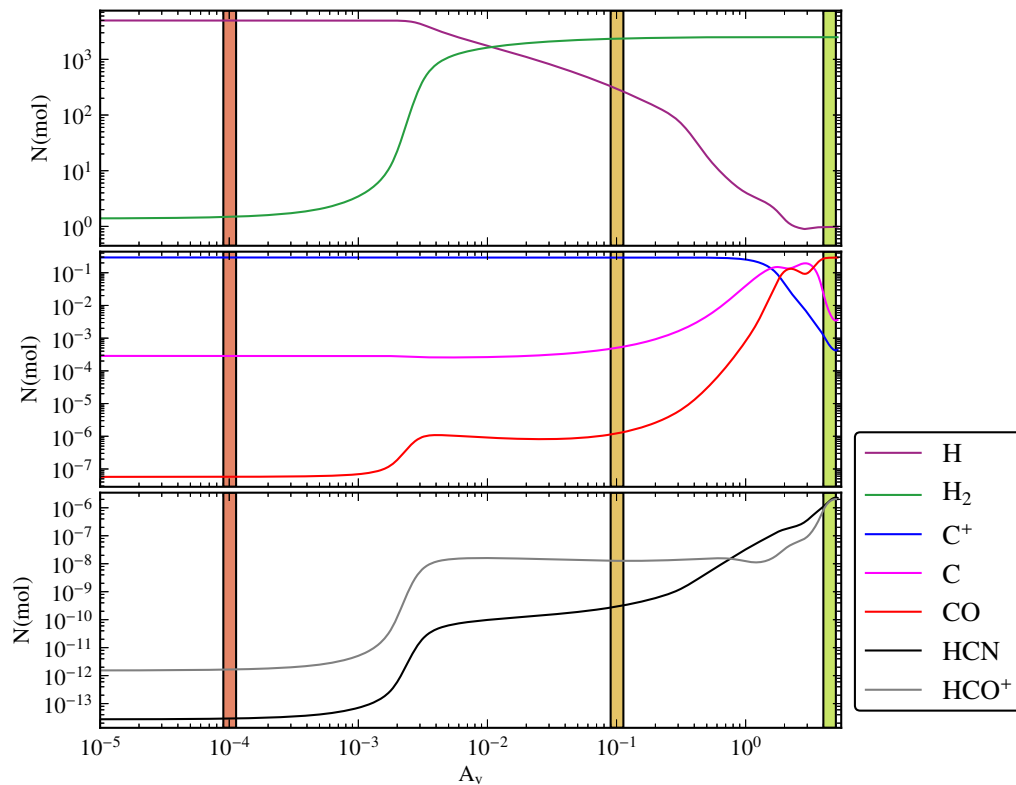
Figure 9.1.: Absolute abundances (N(mol)) of H, H$_2$, C$^+$, CO, HCN and HCO$^+$ versus A_v for a Meudon PDR model cloud with A_v=10 mag, G_0= 50, n_H=5 × 10^3 cm^{-3}, two sided-illumination as well as solar metallicity. The colored stripes mark the three points in A_v in which the chemical reactions for destruction and formation of HCN and HCO$^+$ have been evaluated (cf. Text).

below, which has the parameters A_v= 10 mag, G_0= 50, n_H=5 × 10^3 cm^{-3}. A variety of different chemical reactions can contribute to the formation of a single molecular species. Furthermore, at different depths of the cloud different reactions are responsible to form a particular species. The same is true for different densities; however, this is not discussed here. To investigate the more than 130 formation and destruction channels of HCN and HCO$^+$ that are included in the Meudon Code would not be very productive here. Therefore, the predominant formation and destruction channels of the cloud are investigated at different depths of A_v.

In Fig. 9.1 the abundances of H, H$_2$, C$^+$, C, CO, HCN and HCO$^+$ are shown with respect to the value of A_v. Note that the values are only shown up to A_v=5 mag instead of the 10 mag cloud size of the models. This is because of the 1-D geometry of the clouds and the two-sided illumination, which render the "center" of the cloud at an A_v of 5 mag such that the region 5–10 mag resembles the structure of 5–0 mag. The two transition zones H/H$_2$ and C$^+$/C/CO are clearly visible as is the gradual increase of abundance of HCN and HCO$^+$ with prominent changes in the vicinity of either transition zone. Similar to CO the abundances of HCN and HCO$^+$ change between 6–7.5 orders of magnitude from the edge of the cloud-model to the center. There is a clear connection between the increase of the CO abundance and that of HCN. This shows that the more the FUV-radiation becomes attenuated the more molecules of this

Table 9.2.: Formation and destruction of HCN at $A_v=1\,e^{-4}$, 0.1, and 5 mag.

Reaction	$A_v=1\,e^{-4}$ mag		$A_v=0.1$ mag		$A_v=5$ mag	
	Percent [%]	Rate [cm^{-3}s^{-1}]	Percent [%]	Rate [cm^{-3}s^{-1}]	Percent [%]	Rate [cm^{-3}s^{-1}]
Formation						
$H + HCN^+ \longrightarrow HCN + H^+$	98	$5\,e^{-22}$	-	-	-	-
$HCNH^+ + e^- \longrightarrow H + HCN$	1.3	$7\,e^{-24}$	53	$2\,e^{-18}$	85	$2\,e^{-17}$
$CH_2 + N \longrightarrow H + HCN$	-	-	46	$2\,e^{-18}$	4	$1\,e^{-18}$
$CH + NO \longrightarrow O + HCN$	-	-	-	-	4	$1\,e^{-18}$
$C^+NH_2 \longrightarrow H + HCN$	-	-	-	-	3	$1\,e^{-18}$
$H + HNC \longrightarrow H + HCN$	-	-	-	-	1	$3\,e^{-19}$
$HCO + N \longrightarrow H^+HCN$	-	-	-	-	1	$3\,e^{-19}$
Destruction						
$HCN + h\nu \longrightarrow H + CN$	90	$5\,e^{-22}$	92	$4\,e^{-18}$	8	$2\,e^{-18}$
$HCN + C^+ \longrightarrow H + CNC^+$	7	$6\,e^{-23}$	8	$4\,e^{-19}$	64	$2\,e^{-17}$
$HCN + H^+ \longrightarrow H + HCN^+$	3	$2\,e^{-23}$	-	-	7	$2\,e^{-18}$
$HCN + H_3^+ \longrightarrow H_2 + HCNH^+$	-	-	-	-	14	$4\,e^{-18}$
$HCN + sec.h\nu \longrightarrow H + CN$	-	-	-	-	2	$4\,e^{-19}$
$HCN + He^+ \longrightarrow H + He + CN^+$	-	-	-	-	2	$5\,e^{-19}$

Notes. [1]sec.$h\nu$ signifies "secondary photon" and means photons that have been produced in the PDR, e.g. by spontaneous emission, and did not enter from outside.

species can form. Interestingly, the abundance of HCO^+ starts to rise later than that of HCN in the C^+/C/CO transition zones. Anticipating what is said below, a possible explanation might be that the main destruction channel of HCO^+ in this example is found to be the dissociative recombination with electrons. It might therefore be that only after most of the ionized carbon (C^+) – the main source of free electrons in PDRs – has become neutral that HCO^+ can become more abundant.

The chemical pathways forming HCN and HCO^+ have been evaluated for $A_v=1\,e^{-4}$, 0.1, and 5 mag which have been chosen such that they sample the chemistry in each zone of this PDR model The results are shown in Table 9.2 for HCN and Table 9.3 for HCO^+. There, the fraction of all formations or destructions of HCN or HCO^+ as well as the reaction rates in (cm^{-3} s^{-1}) are given for every chemical-reaction at each evaluation-point. Reactions with contributions less than 1% in a specific zone have been neglected. Note that the model is iterated until the formation and destruction rates of all molecules are in balance at each point in A_v.

A quick view at the table readily shows that the reactions participating in the formation/destruction at different depths of the cloud are different in nature and/or importance. HCN, for example, is nearly solely formed by the reaction of its ion (HCN^+) with the neutral H atom at the lowest analyzed optical extinction $A_v=1\,e^{-4}$. For larger optical extinctions this formation channel is completely removed and the recombination reaction of $HCNH^+$ with electrons becomes the most important pathway. Destruction of HCN in the outer layers is dominated by photodissociation with only a small contribution from charge transfer reactions with C^+ and H^+. These play still a major role at $5\,A_v$, but also new destruction channels open up. One includes secondary photons[1].

---

[1]These are photons that are produced inside the cloud itself

Table 9.3.: Formation and destruction of HCO^+ at $A_v = 1\,e^{-4}$, 0.1, and 5 mag.

Reaction	$A_v = 1\,e^{-4}$ mag		$A_v = 0.1$ mag		$A_v = 5$ mag	
	Percent [%]	Rate [$cm^{-3}s^{-1}$]	Percent [%]	Rate [$cm^{-3}s^{-1}$]	Percent [%]	Rate [$cm^{-3}s^{-1}$]
Formation						
$O + CH_2^+ \longrightarrow H + HCO^+$	68	$2\,e^{-19}$	1	$2\,e^{-17}$	-	-
$H_2 + CO^+ \longrightarrow H + HCO^+$	21	$2\,e^{-20}$	31	$5\,e^{-16}$	6	$1\,e^{-15}$
$H_2O + C^+ \longrightarrow H + HCO^+$	10	$3\,e^{-20}$	7	$1\,e^{-16}$	6	$2\,e^{-15}$
$CH + O \longrightarrow HCO^+ + e^-$	4.2	$8\,e^{-20}$	1	$2\,e^{-17}$	-	-
$H_2 + HOC^+ \longrightarrow H_2 + HCO^+$	-	-	43	$8\,e^{-16}$	19	$5\,e^{-16}$
$O + CH_3^+ \longrightarrow H_2 + HCO^+$	-	-	16	$3\,e^{-16}$	-	-
$CO + H_3^+ \longrightarrow H_2 + HCO^+$	-	-	-	-	69	$2\,e^{-14}$
Destruction						
$HCO^+ + e^- \longrightarrow H + CO$	94	$2\,e^{-19}$	94	$2\,e^{-15}$	93	$2\,e^{-14}$
$HCO^+ + e^- \longrightarrow C + OH$	6	$2\,e^{-20}$	6	$1\,e^{-16}$	6	$2\,e^{-15}$

The major destruction channels of HCO^+ in this example are independent of the depth into the cloud and are due to dissociative recombination of HCO^+ with electrons. This reaction occurs in two different ways producing either H + CO or C + OH. The formation of HCO^+ is more rich than that of HCN and mainly due to ion-molecule reactions. It is interesting that after the two major transition zones H/H_2 and $C^+/C/CO$ a channel including H_2 and CO, respectively, becomes the dominant formation reaction for HCO^+: first the reaction of H_2 with HOC^+, then CO with H_3^+.

9.1.3. Modeled abundances

The modeled abundances of HCN, HCO^+ and ^{12}CO are shown in Fig. 9.2. The CO abundances show a clear dependence on metallicity; however, clearly different from HCN and HCO^+. For all input parameters, its abundance in the subsolar models is ~ 0.6 dex lower than in the solar models and the final abundance at the highest value of A_v stays constant for each metallicity. This directly reflects the under-abundance of carbon of 0.6 dex in the subsolar models. This shows that once CO becomes self-shielding, typically the $C^+ \rightarrow C \rightarrow CO$ transition occurs very fast in PDRs and nearly all available carbon is used to produce CO molecules[2] (e.g. Boger & Sternberg, 2005).

Strikingly, the under-abundance of nitrogen, oxygen and carbon in the subsolar models is not – or only weakly in case of HCN – reflected in the resulting abundances of HCN and HCO^+ at optical extinctions above $A_v \geq 10$ and densities above $n_H \geq 1 \times 10^5$. At low optical extinctions, however, subsolar HCN abundances are lower than solar ones by up to a factor of 0.6 dex. HCO^+ on the other hand is enhanced in the subsolar models by up to 0.7 dex at low optical extinctions and densities. For HCN and HCO^+ it holds that with increasing A_v the abundances of both metallicity-models constantly increase and approach each other.

---

[2]However, after this transition not all carbon is locked into CO, free neutral and ionized carbon atoms may still become available: at low optical extinctions via photodissociation of CO or at large optical extinctions via helium impact ionization (e.g. Boger & Sternberg, 2005).
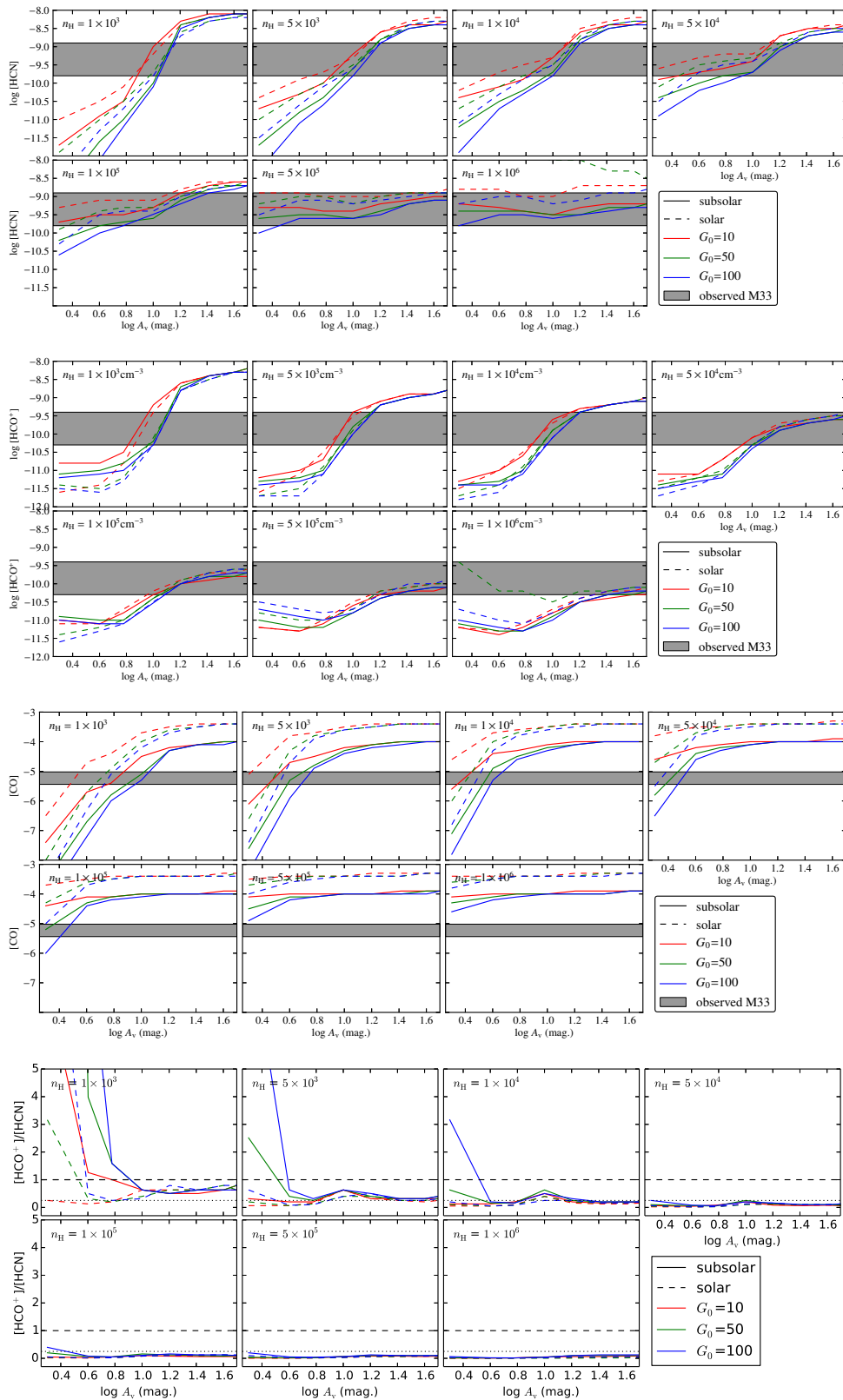
Figure 9.2.: PDR model abundances of *from top to bottom* HCN, HCO$^+$, ^{12}CO as well as the [HCO$^+$]/[HCN] abundance ratio. The abundances are shown for for subsolar (*solid lines*) and solar metallicity (*dashed lines*). Different colors indicate different FUV field strengths $G_0 = 10$ (*red*), 50 (*green*), and 100 (*blue*). Every panel of a subfigure shows the results for one density; from left to right and top to bottom $n_H = 0.1, 0.5, 1, 5, 10, 50,$ and $10^2 \times 10^4$ cm^{-3}. *Gray* areas mark the range of observed ratios in M 33. The *dashed* horizontal lines show the values from the stacked spectra. In the *bottom-most* figure the *dashed* and *dotted black* lines mark ratios of 1 and 0.25.
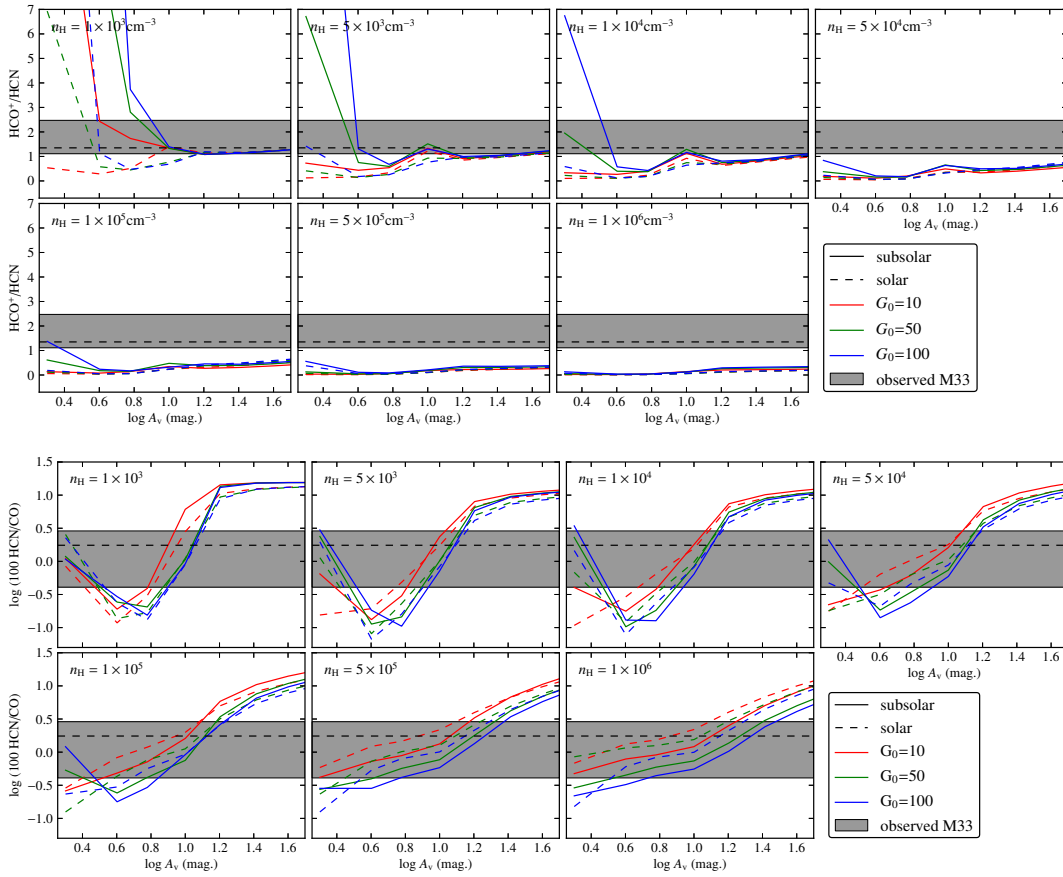
Figure 9.3.: PDR model line ratios for subsolar (*solid lines*) and solar metallicity (*dashed lines*): HCO$^+$/HCN (top) and HCN/CO (*bottom*). Different colors indicate different FUV field strengths G_0 = 10 (*red*), 50 (*green*), and 100 (*blue*). Every panel of a subfigure shows the results for one density; from *left to right and top to bottom* n_H = 0.1, 0.5, 1, 5, 10, 50, and 10^2 $\times 10^4$ cm^{-3}. *Gray* areas mark the range of observed ratios in M 33. The dashed horizontal lines show the values from the stacked spectra.

The increase in HCO$^+$ at optical extinctions lower or equal than A_v = 8 mag and densities lower or equal than n_H = 10^4 cm^{-3} can be explained by the lower carbon abundance. As discussed above in the previous section, carbon is the main source of free electrons in photon-dominated regions (e.g. Tielens, 2005). A lower abundance of carbon thus lowers the abundance of free electrons and reduces dissociative recombination reactions of HCO$^+$ with electrons, which has been identified as the major destruction channel for HCO$^+$ in the previous section (cf. Table 9.3).

The *lower* HCN abundance may as well (partly) be explained due to the lower abundance of carbon: one major formation channel of HCN, identified from the models, is HCNH$^+$ + e $\rightarrow$ H + HCN (cf. Table 9.2) and since this reaction depends on the dissociative recombination of HCNH$^+$, formation of HCN might be suppressed if fewer electrons are available.

For all three lines holds that the role of the FUV field onto the abundance is stronger the lower the optical extinction and the density becomes. For optical extinctions above $A_v \sim 10$–16 the influence of the FUV-field strengths onto the abundances of all three molecules becomes minimal. In general a higher FUV field strength results in a lower

abundance. This reflects the higher potential of a higher FUV field to photodissociate molecules an to produce more free electrons.

However, a higher FUV-field strengths does not always lead to a decrease of the HCO^+ abundance. As such it can be seen from Fig. 9.2 that at densities larger than 1×10^5 cm^{-3} no longer the lowest modeled far ultraviolet field strength $G_0 = 10$ yields the highest HCO^+ abundance but either $G_0 = 50$ or $G_0 = 100$. At high densities the electron recombination rates becomes higher but also new pathways for the formation of HCO^+ open up. Furthermore HCO^+ is nearly exclusively formed in ion molecule reactions at all densities (cf. e.g. Table 9.3), which obviously depend on the ionization degree of medium. Therefore, the actual influence of variations in the FUV-field onto the HCO^+ abundance is determined by its influence on the ratio between the formation and destruction rates of this molecule. Note that at large densities $n_H \geq 1 \times 10^5$ cm^{-3} and optical extinctions, HCN is mainly formed by reactions that are not ion-molecule reactions, in contrast to the investigated case in the previous section ($n_H = 5 \times 10^3$ cm^{-3}). This might explain that it is not affected by a larger density in the same way as HCO^+.

9.1.4. Modeled line ratios

This section has been published in Sec. 6.2 of (Buchbender et al., 2013).

The modeled HCN/CO line ratio (Fig. 9.3, Table C.1 Table C.2) hardly varies with metallicity, n_H or FUV. It varies, however strongly, with A_v. After an initial drop of up-to an order of magnitude for extinctions less than about 4 mag, it rises until A_v ~20 mag and then saturates at a value that is nearly independent of any of the input parameters.

In contrast, the modeled HCO^+/HCN ratio shows differences between the two metallicities for $A_v \lesssim 10$ mag. The subsolar model shows higher ratios than the solar model for a given A_v, FUV field, and density. Strong FUV fields and low densities increase the ratio. At higher optical extinctions the ratios are hardly influenced by changes in metallicity, A_v or FUV. This reflects the variation in HCN and HCO^+ abundances.

The HCN/CO line ratio is fairly independent of metallicity as a consequence of the ~ 0.6 dex lower abundances of HCN and CO for low A_v.

For optical extinctions in the range of $A_v \leq 8$ mag, where the bulk of molecular gas in galaxies resides (Tielens, 2005), the HCN/CO ratio increases with increasing densities. In general in LIRGs/ULIRGs where most of gas has higher density than in normal galaxies, the HCN/CO is also higher (GS04a,b).

9.2. Comparison of Data with PDR models

Fig. 9.3 shows the range in observed intensity ratios (cf. Table 5.1), where the plot shows that the optical extinctions play a decisive role in determining the line ratios. High extinctions of $A_v > 16$ mag are inconsistent with the observed HCN/CO ratios. Similarly, high densities of 10^5 cm^{-3} cannot reproduce the measured HCO^+/HCN ratios. Interestingly, metallicity only plays a minor role. In general, both metallicity models allow the observed range of line ratios to be reproduced.

To quantitatively compare the modeled and observed line ratios we calculate the summed squared residuals weighted by the observational errors between the modeled

Table 9.4.: Best-fitting PDR models

	HCO$^+$/HCN	HCN/CO [%]	A_v [mag.]	n_H [cm^{-3}]	FUV [G_0]	Φ_{A_v}[a]	Φ_{FUV}[b]	best χ^2 [c]
			subsolar metallicity Models					
Stacked	1.4 ± 0.2	1.0 ± 0.1	8 ± 3	(3 ± 4) 10^4	68 ± 24	0.5 ± 0.2	0.3 ± 0.1	0.1 ± 0.1
GMC no6	2.5 ± 0.2	1.4 ± 0.3	4 ± 2	(6 ± 4) 10^3	41 ± 16	1.7 ± 1.1	0.9 ± 0.4	1.4 ± 0.5
GMC no3	1.9 ± 0.1	0.8 ± 0.2	8 ± 2	(3 ± 2) 10^3	27 ± 20	0.7 ± 0.2	0.8 ± 0.6	0.6 ± 0.3
GMC 91	1.4 ± 0.3	0.4 ± 0.1	6 ± 2	(1 ± 5) 10^4	54 ± 44	0.9 ± 0.3	0.2 ± 0.2	0.1 ± 0.1
GMC no1	1.4 ± 0.2	1.7 ± 0.4	7 ± 4	(3 ± 4) 10^4	42 ± 40	0.3 ± 0.2	0.3 ± 0.3	0.2 ± 0.1
GMC 1	1.1 ± 0.1	2.9 ± 0.4	10 ± 3	(1 ± 2) 10^4	30 ± 37	0.6 ± 0.2	1.7 ± 2.1	0.7 ± 0.5
GMC 26	1.2 ± 0.1	1.0 ± 0.2	9 ± 2	(1 ± 3) 10^4	67 ± 24	0.3 ± 0.1	0.2 ± 0.1	0.1 ± 0.1
			solar metallicity models					
Stacked	1.4 ± 0.2	1.0 ± 0.1	10 ± 1	(5 ± 1) 10^3	47 ± 12	0.4 ± 0.0	0.5 ± 0.1	0.6 ± 0.4
GMC no6	2.5 ± 0.2	1.4 ± 0.3	2 ± 0	(5 ± 1) 10^3	100 ± 4	3.1 ± 0.8	0.4 ± 0.0	3.4 ± 1.2
GMC no3	1.9 ± 0.1	0.8 ± 0.2	6 ± 3	(2 ± 2) 10^3	81 ± 32	0.9 ± 0.5	0.3 ± 0.1	3.4 ± 0.9
GMC 91	1.4 ± 0.3	0.4 ± 0.1	4 ± 1	(1 ± 1) 10^3	98 ± 11	1.4 ± 0.3	0.1 ± 0.0	0.5 ± 0.4
GMC no1	1.4 ± 0.2	1.7 ± 0.4	7 ± 4	(5 ± 3) 10^3	50 ± 43	0.4 ± 0.2	0.3 ± 0.2	0.2 ± 0.2
GMC 1	1.1 ± 0.1	2.9 ± 0.4	11 ± 2	(3 ± 6) 10^3	26 ± 34	0.6 ± 0.1	1.9 ± 2.6	0.5 ± 0.2
GMC 26	1.2 ± 0.1	1.0 ± 0.2	9 ± 2	(5 ± 1) 10^3	52 ± 17	0.2 ± 0.1	0.2 ± 0.1	0.4 ± 0.3

Notes. [a]beam-filling factor derived from $A_v(^{12}CO)/A_v$(Model); [b]beam-filling factor derived from FUV(TIR)/FUV(Model); [c]average χ^2 of the best-fitting models.

and observed line ratios HCO$^+$/HCN and HCN/CO, for every model and for each observed cloud as

$$\chi^2 = \frac{1}{2} \sum_{i=1}^{2} \frac{(\text{Ratio}_{\text{obs},i} - \text{Ratio}_{\text{mod},i})^2}{\sigma_i^2}, \tag{9.1}$$

where σ is the observational error of the line ratios deduced from the errors of the line intensities, cf. Chapter 5. We normalize the χ^2 by dividing by $N = 2$, the number of independent observed line ratios. The minimum χ^2 gives the best-fitting model.

To get a handle on the errors of the best-fitting models, we employ a Monte Carlo simulation. We assume that the measured ratios and their errors follow a Gaussian distribution with an expected value equal to the ratio and a variance equal to σ^2.

We generate 5000 sets of HCN/CO and HCO$^+$/HCN ratios drawn randomly from their Gaussian parent distribution. For every set we calculate a χ^2 as explained above and deduce the best fits. From all best fits of all sets we derive the mean and the standard deviation of the input parameters, n_H, A_v, FUV, and χ^2 (Table 9.4).

Table 9.4 shows the input parameters A_v, n_H, and FUV of the best-fitting subsolar and solar metallicity models, i.e. those having the lowest χ^2, for the stacked values and each observed cloud.

9.2.1. Stacked ratios

The best-fitting models for reproducing the stacked HCO$^+$/HCN and HCN/CO ratios of 1.4 and 1%, respectively, that describe the averaged GMC properties are $A_v = 8$ mag, $n_H = 3\ 10^4$ cm^{-3}, and FUV $= 68\ G_0$. Emission stems from moderately dense gas with average line-of-sight column densities of 8 mag. The beam-filling factor Φ_{FUV} derived

from ratio of the beam-averaged TIR intensity to the fitted local FUV field is $\sim 30\%$; i.e., the fitted FUV field strengths are significantly higher than expected from the observations. The same holds for the beam filling factors deduced from the ratios of extinctions derived from CO and the A_v of the best-fitting models, which are about $\Phi_{A_v} = 50\%$. This is not surprising, however, and indicates that emission is clumped within the 114 pc beam. From the models of the calculated grid closest to the best fit, i.e., Av = 6 and 10 mag, $n_H = 1\,10^4$, and FUV = $50\,G_0$, we find optical depths (τ) in the centers of the lines of HCN and HCO$^+$ that lie between $0.02 - 0.1$ and $0.07 - 0.1$, respectively. Thus both lines are optically thin. ^{12}CO is moderately optically thick with optical depths of $\tau\ 4 - 25$. The line width assumed in the Meudon PDR code is $\sim 3\,\mathrm{km\,s^{-1}}$(cf. Section 9.1.1).

9.2.2. Individual regions

Here, we focus on individual regions grouped by their particular HCO$^+$/HCN ratios and thus their best-fit A_v values: GMC no6 showing a high ratio of 2.5, GMC 91, no3, and no1 have intermediate ratios of 1.4-1.9 and GMC 26, GMC 1 having ratios of 1.1-1.2.

GMC no6   This cloud shows the highest HCO$^+$/HCN ratio of 2.5, while at the same time the HCN/CO ratio is relatively low with 1.4 and weaker than expected from the linear fit to the M 33 data (cf. Section 8.1 and Fig. 8.1). GMC no6 is best fitted by subsolar models that yield a low best-fitting value for A_v of ~ 4 mag, while the best-fitting density and FUV strength are $6\,10^3\,\mathrm{cm^{-3}}$ and $40\,G_0$, respectively. The beam-filling factor derived from A_v is 1.7, indicating that emission completely fills the beam with several clouds along the line-of-sight. This cloud has the second highest star formation rate of our sample of $35.9\,\mathrm{M_\odot\,Gyr^{-1}\,pc^{-2}}$, and the same holds for the FUV field strength of $37.3\,\mathrm{G_0}$.

GMC 91, no3, and no1   The line ratios of these three clouds are best described by subsolar models. The best-fitting A_v are similar with 6–8 mag. So are the FUV 30–50 G_0 and the densities $3\,10^3\,\mathrm{cm^{-3}} - 3\,10^4\,\mathrm{cm^{-3}}$, and no1 and no3 have similar SFR rates of $\sim 13\,\mathrm{M_\odot\,Gyr^{-1}\,pc^{-2}}$, while no3 is a factor of four more massive than no1 with $M_{H_2} = 8\,10^{\,5}\,\mathrm{M_\odot}$. GMC 91 lies at only 320 pc distance in close vicinity of GMC no3 and is only slightly more massive than the same. It is the most CO intense cloud in our sample while its HCN and HCO$^+$ emission is relatively weak. This renders GMC 91 somewhat peculiar and results in a low HCO$^+$/CO ratio of 0.6 % and, as already found by RPG11, a particularly low HCN/CO intensity ratio of 0.4 % (Table 5.1). The HCN/CO ratio of GMC 91 is much lower than the ratios observed in the disk of the Milky Way by Helfer & Blitz (1997), who find 2.6 % ± 0.8 % and also in the inner disks (5–10 kpc) of normal galaxies by GS04b who find 4 % ± 2 %. The relatively weak HCN and HCO$^+$ emission may indicate a low fraction of dense mass in GMC 91, which thus may be a rather quiescent GMC with only a low SFR. Indeed, it has the lowest star formation rate of $4\,\mathrm{M_\odot\,Gyr^{-1}\,pc^{-2}}$ of all observed clouds.

GMC 1 and GMC 26   These two clouds host the lowest HCO$^+$/HCN ratios observed of $1.1 - 1.2$. Here, the solar models provide slightly better or equal fits than the subsolar models. However, since the ISM of M 33 is subsolar, here we discuss only the best fits to the subsolar models. These GMCs have similar best-fitting input parameters of A_v 9–10 mag and $n_H \sim 10^4$ cm^{-3}, while the best-fitting FUV field strengths are $\sim 30\,G_0$ and $70\,G_0$, respectively. However comparing their physical properties in Table 5.1, again, these two clouds are actually not at all alike. GMC 1 is located in the very center of M 33 and is by far the most massive cloud in our sample. It is actively forming stars at a rate of 65 M$_\odot$Gyr^{-1} pc^{-2}, the highest in our sample, and has an correspondingly high FUV field of $50.7\,G_0$. GMC 26 has much lower HCN/CO ratios, and its SFR is only 6.6 M$_\odot$ Gyr^{-1} pc^{-2} the second lowest in the sample with exception of no2.

For all best-fitting solutions of the six individual positions we find that the modeled optical depths of HCN and HCO$^+$ are $\tau \leq 0.1$, which renders emission of these lines to be likely optically thin. This also justifies the assumption of optical thin emission for the LTE analysis in Section 5.4.2. Indeed, the PDR modeled abundances of both molecules are comparable to the ones derived from LTE (cf. Table 5.4 Table C.2).

In conclusion, it is noteworthy to repeat that the line ratios studied here are fairly independent of the metallicity, SF activity, and FUV field strength of the parent GMC, while the optical extinction has a major influence on the modeled line ratios.

Chapter 10.

Summary

Bullet points 1–6 and the introductory text of this Summary have been published in Section 8 in Buchbender et al. (2013).

The observations of HCN, HCO$^+$, ^{13}CO and ^{12}CO with the 30 m telescope achieve a spatial resolution of ~ 114 pc at a frequency of 89 GHz. The molecular gas masses of the target GMCs vary by a factor of ~ 130 between 0.1×10^5 M$_\odot$ (GMC no2) and 13×10^5 M$_\odot$ (GMC 1) and the star formation rates derived from Hα and 24 μm images vary by a factor of more than 50. The FUV field strengths show a variation of more than a factor 20. Below the main results are summarized:

1. For the six GMCs where HCO$^+$ is detected, peak line temperatures (on the T_{mb} scale) vary between 6 and 12 mK. The HCO$^+$/HCN-integrated intensity line ratios lie between 1.1 and 2.5 (on the K km s^{-1} scale, (cf. Table 5.1). Similar line ratios are observed in the disk of M 31 (Brouillet et al., 2005).

2. The line intensity ratios HCN/CO and HCO$^+$/CO vary between $(0.4 - 2.9)$ % and $(0.6 - 3.5)$ %, respectively. The spread of ratios found in M 33 is slightly larger than in the spiral arms of M 31 (Brouillet et al., 2005, Fig. 8.1). GMC 91 exhibits a particularly low HCN/CO ratio of 0.4 %, which is much lower than values in the Galactic disk of 2.5 % ± 0.6 % (Helfer & Blitz, 1997) or in normal galaxies with 4 % ± 2 % (GS04a).

3. The $L_{\mathrm{TIR}}/L'_{\mathrm{HCN}}$ luminosity ratios range between 1.3×10^3 and 3.5×10^3 and are situated at the very high end of ratios found by Wu et al. (2010) in molecular clouds of the Milky Way and LIRGs/ULIRGs. This shows that HCN emission in comparison to the L_{TIR} in M 33 particularly weak.

4. Stacking of all spectra taken at the seven GMC positions leads to 3 σ detections of CCH and HNC. The HCN/HNC ratio of 5.8 is remarkable high. It is higher than values found in the LMC (Chin et al., 1997, 1998), in IC 342 (Meier & Turner, 2005), in samples of LIRGs/ULIRGs (Baan et al., 2008; Costagliola et al., 2011), in starburst and Seyfert galaxies (e.g. Aalto et al., 2002), and in Galactic molecular complexes Wootten et al. (1978), where all together no values higher than three are reported.

5. The HCO$^+$, HCN, HNC abundances, derived assuming LTE, agree with those of the LMC cloud N159 within 0.5 dex. In contrast, the Orion Bar, a Galactic massive star-forming region, shows significantly higher abundances of all three

tracers by 0.7 dex to 1.8 dex. These striking differences may reflect the factor two subsolar metallicities of both the LMC and M 33.

6. Employing the Meudon PDR code to model photon-dominated regions we investigated the influence of the metallicity on the abundances and emission of HCN and HCO$^+$. For a range of optical extinctions, volume densities, and FUV radiation field strengths, we derived two sets of models with different metallicity, one reflecting the abundances in the Orion nebula by Simón-Díaz & Stasińska (2011), the other the average subsolar metallicity of M 33 (Magrini et al., 2010).

   Both sets of models are able to describe the observed range of HCO$^+$/HCN and HCN/CO line ratios reasonably well ($\chi^2 < 3.4$). Therefore, changes in metallicity do not need to be invoked to describe the observed line ratios. The observations are described by subsolar models with optical extinctions between 2 mag and 10 mag and moderate densities of $<3 \times 10^4\,\mathrm{cm}^{-3}$, with little influence by the FUV field strength. The optical extinction has a pronounced influence on the modeled ratios, while FUV field, metallicity and even density only play minor roles. The modeled lines of HCN and HCO$^+$ of the best-fitting models are found to be optically thin with optical depths $\tau \leq 0.1$.

7. A good correlation of HCO$^+$ and L_{TIR} is found. HCN in contrast is not well correlated with the total infrared luminosity. Therefore HCO$^+$ might be a more reliably tracer of the dense gas content related to star formation in M 33.

8. Comparing the HCO$^+$/HCN ratio with L_{TIR} of the clouds it has been found that both values are very well correlated (r=0.97) when GMC 1 is excluded from the comparison. This peculiar behavior of GMC 1 may hint at different formation/excitation mechanisms of HCN and HCO$^+$ and different properties of the ISM in this cloud. Its close proximity to a luminous X-Ray binary M33-X8 ($L_{\mathrm{X}} = 2.2 \times 10^{39}\,\mathrm{erg\,s}^{-1}$ (Weng et al., 2009)) might play a role in the different emission and abundance characteristics.

9. The radially averaged temperature of the cold dust component that contributes to the dust spectral energy distribution (SED) in the disk of M 33 is found to radially decline from the center of M 33 with $T_{\mathrm{cold}} = 24$ K to $T_{\mathrm{cold}} = 13$ K in the outskirts of the detected dust disk. T_{cold} in the seven GMC pointings is varies between $T_{\mathrm{cold}} = 19$ K in GMC no2 and $T_{\mathrm{cold}} = 25$ K in GMC 1. The dust emission can be decomposed to a disk is can be decomposed into a diffuse exponential disk and a spiral-arm network.

Part III.

Small scale variations of molecular tracers: A single GMC in M 33

Chapter 11.

PdBI observations of one GMC in M 33

11.1. Introduction

In Part II single pointings of HCN, HCO$^+$ and ^{12}CO in giant molecular clouds along the major axis of M 33 have been investigated. Amongst others HCN is found to be particular under-luminous in relation to the total infrared luminosity, a proxy of the star formation rate, when compared with larger spiral galaxies (cf. Chapter 7), while HCO$^+$ seems to better trace dense star forming gas. Further, a variation of the HCO$^+$/HCN ratios in the range of 1.1—2.5 was found that is likely due to variations in the total H$_2$-column density or optical extinction as the PDR analysis in Chapter 9 suggests.

However, information on the mutual distribution of emission from both molecules in spatial as well as in velocity space within the GMCs is missing in the single pointing observations. Such information is crucial to identify physical and/or chemical causes that lead to variations in the line intensity ratios. To add this information, GMC no3, a giant molecular cloud H II-region interface-region, has been observed in the ground-state transitions of ^{12}CO, HCN, and HCO$^+$ with the PdBI with ~ 25 pc spatial resolution and 2 km s^{-1} velocity resolution in a field of view of approximately 300 pc.

The position of this GMC and the field of view of the PdBI observations are shown in Fig. 11.1 (cf. also Figs. 5.1 and 5.5). GMC no3 is situated at a galacto-centric distance of 2.2 kpc in the North. It shows the second highest HCO$^+$/HCN ratio of 1.9 within the above sample of giant molecular clouds and also a high total-infrared over HCN luminosity ratio ($L_{\text{TIR}}/L'_{\text{HCN}}$) of 3×10^3. GMC no3 is classified as an evolved cloud in a systematic ^{12}CO (2–1) survey of giant molecular clouds in M 33 by Gratier et al. (2012) due to the presence of exposed as well as embedded star formation traced by 8 μm, 24 μm, far ultraviolet and Hα emission. The [C II] emission of this region studied by Mookerjea et al. (2011) is found to show little spatial correlation with molecular gas traced by ^{12}CO.

The high HCO$^+$/HCN and $L_{\text{TIR}}/L'_{\text{HCN}}$ ratios of GMC no3 as well as proximity to the H II-region BCLMP 302 (Boulesteix et al., 1974) render this GMCs an interesting target. Its properties allow to study the source of mutual variations of HCN and HCO$^+$ relative to ^{12}CO emission, within a single giant molecular clouds and in relation to variation of the properties in the environment.
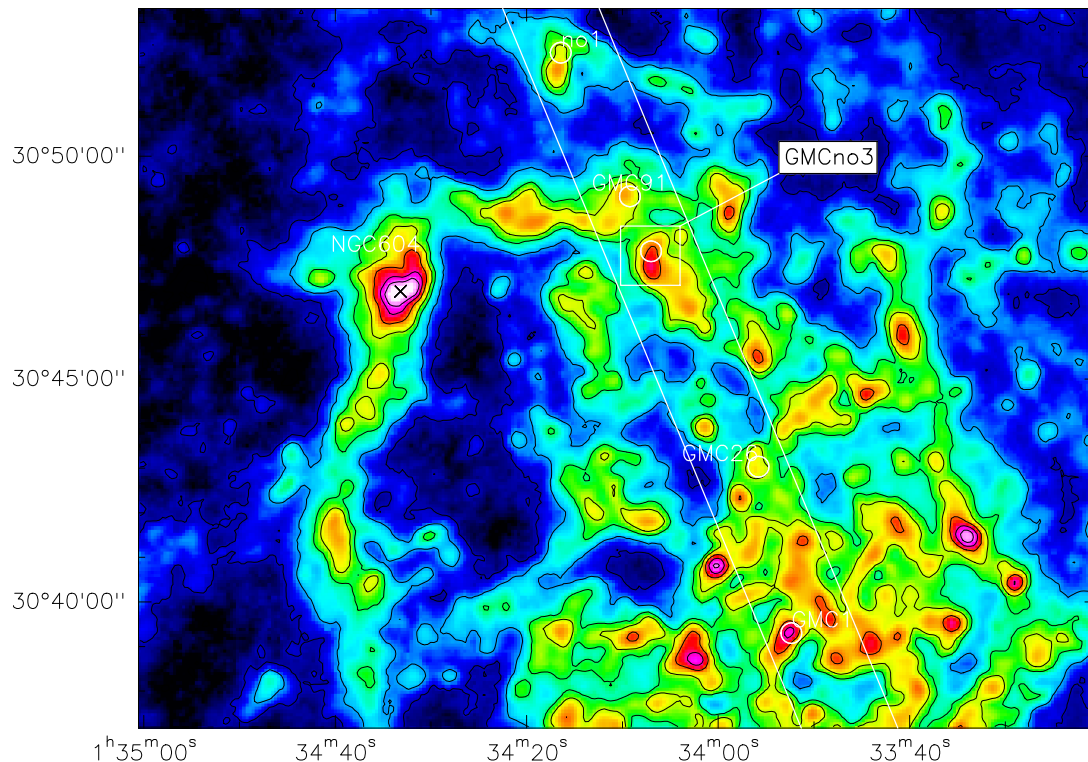
Figure 11.1.: 250 µm SPIRE/*Herschel* map of the center and the northern spiral arm of M 33 (Kramer et al., 2010). The position of the 30 m observation of GMC no3 and the PdBI FOV (*white square*) are highlighted. The positions and beam size of the GMC observations from Part II are shown (*white circles*) as well as the $2'' \times 4'''$ strip along the major axis (*white lines*) shown in Figs. 5.1 and 5.5 as well as Section 5.3.

Note that, at the time of writing, the analysis of the data presented here, is still work in progress. This Part can only give a first insight.

This chapter describes the details of the observations and the subsequent data reduction (Section 11.2) and presents the final data product in Section 11.3 where the spatial and velocity structure of GMC no3 are discussed. In Section 11.4 the PdBI data is compared with ancillary data at similar high resolution, which gives insight into the interplay of the different components of the interstellar medium and the stars in GMC no3. The emerging picture helps the interpretation of the results of the quantitative analysis from the data in Chapter 12.

11.2. Observations and data reduction

High resolution images of the lines ^{12}CO, HCN and HCO$^+$ have been obtained towards GMC no3 with the PdBI. The 30 m was used to add information on the extended emission.

11.2.1. HCN and HCO⁺ (1–0) Observations

PdBI single pointing - Project U07D   The ground state transitions of HCN and HCO⁺ towards GMC no3 have been observed in six tracks in May and June of 2011 with the IRAM Plateau de Bure Interferometer (PdBI) in its D configuration with baselines between 15.3 and 97 meters. Five of the six antennas have been used. The total telescope time was 26.3 h with an on-source integration time of 17.5 h. The phase center of the observations has been RA=01:34:07.000, DEC=30:47:52.000 (J2000). The field of view equal to the primary beam of the individual antennas is $\sim 57''$ at the frequencies of HCN and HCO⁺. The narrow band correlator was set to yield two windows centered on both lines with 40 kHz resolution and 20 MHz bandwidth in SSB mode. Furthermore, the wideband correlator WideX ("Wideband Express") with 195 kHz frequency resolution was configured such that both lines HCN and HCO⁺ fall into the 1 GHz IF chunk of the narrow correlator input Q2. The narrow band correlator data having a higher spectral resolution is used for the line emission while WideX is used to measure the 3 mm continuum. The RF bandpass was calibrated on 3C454.3. For amplitude and phase calibration the calibrator 0055+300 was observed frequently during the observations.

The calibration of the six individual tracks has been done with the "Continuum and Line Interferometer Calibration" (CLIC) software from the GILDAS[1] software package. The proposed calibration of the standard CLIC calibration pipeline gave satisfactory results for the phase correction, RF-bandpass- and phase-calibration as well as amplitude calibration. To calibrate the absolute flux the calibrator MWC349 has been used with a modeled flux of 1.12 Jy at the time of the observations. The relative flux calibration between the different tracks has been compared to assure their consistency.

Short-spacings at IRAM 30 m   The short-spacing observation have been performed between January and August 2013 in four session with a total of ~ 28 hours on source time. The data was taken mostly during stable weather conditions with precipitable water vapor columns ≤ 5 mm. The 3 mm-band of the EMIR receiver (band: E090) was tuned such that the lower-outer subband (LO) was centered on 88.91 GHz, the middle-frequency between HCN (88.6316) and HCO⁺ (89.1885). As backend the FTS with 200 kHz frequency resolution are used. Using the on-the-fly (OTF) observation mode a field of $160'' \times 160''$ was observed. The field was centered on the phase center of the PdBI observations. The offset position with an offset of -358″ in RA and 655″ in DEC was chosen to lie within ¹²CO emission-free, outer part of M 33. At this position a dedicated ¹²CO (1–0) position-switched spectrum with an off-position outside of M 33 and 12 min integration time has been obtained to verify that no CO emission is detected. Following the "rule of thumb" introduced in Sect. B.5 the optimal map size would be $120'' \times 120''$, i.e. two times the FOV of the primary beam of the PdBI. However, a larger maps size allows to remove map-edge artifacts such as higher noise, which are typical at the 30 m, in the final short-spacing map. Calibrations were done every ≈ 15 min. The scanning direction has been alternated between vertical and horizontal to minimize scanning artifacts.

---

[1] http://www.iram.fr/IRAMFR/GILDAS/

11.2.2. ^{12}CO (1–0) Observations

PdBI mosaic - Project V07C   The PdBI ^{12}CO observations of GMC no3 have been conducted in November 2011 under cloudy conditions with 10 mm pwv using the D configuration of the PdBI with baselines of 20–101 m. The on-source time was 3.4 h and the total telescope time 5.1 h. Note that the telescope time was not dictated by a certain signal-to-noise ratio but by the uv-coverage needed to obtain a reasonable clean beam. As a consequence the ^{12}CO map has a high signal-to-noise ratio. The 3 mm-receiver was tuned to 115.365 GHz in the upper-side band (USB). As for the HCN and HCO$^+$ observations both, the narrow-band correlator and WideX have been employed. The narrow-band correlator was set to 40 kHz resolution and 20 MHz bandwidth in SSB in order to cover the ^{12}CO line. The narrow-correlator input Q3 has been used. The source was covered by a 7-field hexagonal mosaic with the innermost field centered on RA=01:34:06.72, DEC=30:47:41.10 and the outer pointings were spaced by half of the primary beam size of 43″ with respect to the inner one. This mode was chosen as it yields a stable noise and a level intensity scale in the central region. Further, it accounts for the slightly smaller primary beam size of the ^{12}CO observation compared to the one of the HCN and HCO$^+$ data. For the flux calibration 2200+420 and MWC349 have been observed. The phase and amplitude calibrators used were 0202+319 and 0055+300.

Calibration of the data was straight-forward and the standard calibration pipeline of CLIC gave satisfactory results after fine-tuning the flux-calibration using the modeled flux of 1.31 Jy for MWC349 .

Short-spacings at IRAM 30 m   Short-spacing observation have been obtained with the IRAM 30 m telescope at Pico Veleta in Spain during 7 h in March 2012 under good and stable weather conditions ($\tau = 0.1$–0.2). We tuned the EMIR E090 receiver to 110.756 GHz in the upper inner (UI) sideband to allow simultaneous observation of ^{12}CO and ^{13}CO (1–0). This set-up took advantage of the large simultaneous bandwidth coverage of 32 GHz of the Fourier Transform Spectrometers (FTS) with a frequency-resolution of 195 kHz. The observations have been performed in a position switched on-the-fly (OTF) map of 160″ × 160″ – i.e. two times the maximum extent of the PdBI mosaic of ∼ 80 ″ – centered on the phase center of the ^{12}CO PdBI map (see above). As for the HCO$^+$ and HCN short-spacings, we alternated the scanning direction between vertical and horizontal in between scans. The time on source was 3.1 h.

11.2.3. Short-spacing Reduction

The raw data of all short-spacing data sets have been calibrated using MIRA[2] and time-weighted average of all off-positions for each scan. The resulting FTS-spectra were corrected for "platforming". Subsequently, those spectra were rejected that had exceptional high baseline-rms values. The rms cut-off has been empirically defined from the rms distribution of the spectra. Scans that showed a large variation in rms

---

[2]The calibration software at the 30m. Part of the GILDAS package, cf. http://www.iram.fr/IRAMFR/GILDAS/.

values due to very unstable weather conditions were rejected entirely. Altogether, 12% of the data was excluded from the analysis.

Baseline-ripples are present in the vertical polarization of the HCN and HCO^+ spectra. Including the vertical polarization into the final interferometer images leads to severely increased noise and artifacts. Here, only the horizontal polarization data were used for the reduction of the HCN and HCO^+ short-spacings. This results in the fact that while HCO^+ is detected in the final 30 m map, HCN is not. As a consequence the horizontal HCN short-spacing map leads to increased noise in the final PdBI+30 m map with respect to the pure PdBI map. The differences between both maps (imaged and cleaned) are $\lesssim 25\%$ and the distribution of emission only changes marginally. Furthermore, in the pure PdBI map of HCN no indications of missing flux, e.g. in the form of a "negative bowl", are seen. Therefore, in this preliminary data reduction the short-spacings for HCN are neglected for HCN. Note that, in contrast, the addition of the short-spacings is crucial for the HCO^+ map, because the HCO^+ shows extended emission as discussed below.

In principle the reduction of the ^{12}CO and HCO^+ short-spacing maps follow the same scheme. However, the ^{12}CO maps were generated first, to make use of their high signal-to-noise ratio. This map is used to define line-windows and support regions for the reduction of the much lower signal-to-noise data of HCN and HCO^+. Note that the usage of ^{12}CO line windows for the HCN and HCO^+ reduction is based on the assumption that the denser regions, as traced by HCN and HCO^+, are always embedded in more diffuse gas traced by ^{12}CO.

To reduce the ^{12}CO data first a baseline of zeroth-order was subtracted from each spectrum. Subsequently, the 30 m data was gridded and averaged at every pixel in order to improve signal to noise in the spectra. The calculated weights, based on the integration time per pixel, were then used to reject pixels with a too low weight as examined by eye. This truncates the map at the edges where the noise typically increases. In the following an algorithm is used that searches for line windows at every position in the cube. The line windows are defined as the range between the first and the last channel of a spectra that has an emission over 3σ. A further constraint is that at least one adjacent channel must have a flux than 3σ to reduce false-positives. If no line windows are found a default window is used based on the line-width of the integrated spectrum over the entire map. The thus defined line windows are used to subtract a baseline of order 2 from each spectrum. Using this new baseline subtracted set, the ^{12}CO line windows are defined a second time to improve their quality. The baseline subtraction is then repeated using these new windows and the resulting spectra are used to create the final 30 m map. The reduction of the HCO^+ data is similar, except that ^{12}CO defined line windows are used and thus the line-window definition and its second iteration are not performed on the HCO^+ data.

11.2.4. Imaging and Cleaning

The PdBI observations, made with the narrow-band corralator, have an intrinsic frequency resolution of 40 kHz, which corresponds to $\sim 0.13\,km\,s^{-1}$ velocity resolution. Evaluating different velocity resolutions it has been found that $2\,km\,s^{-1}$ is a sensible compromise between signal-to-noise and velocity resolution for the HCN and HCO^+

data. The final spectra have a bandwidth of $114 \, \text{km s}^{-1}$. Since the ^{12}CO map has a higher signal-to-noise ratio two versions of the ^{12}CO map have been produced, one at $0.5 \, \text{km s}^{-1}$ velocity resolution and $142 \, \text{km s}^{-1}$ bandwidth and one with $2 \, \text{km s}^{-1}$ velocity resolution with $114 \, \text{km s}^{-1}$ bandwidth.

The combination of the short-spacings with the PdBI uv-table and the subsequent cleaning of the resulting dirty image was done using the program "Mapping" from the GILDAS package and follow the steps detailed in Appendix B.4 and Appendix B.5. During cleaning of the ^{12}CO map is was assured that the cleaning converges for all channels and that no significant residuals are left. The resulting ^{12}CO map was then used to create a 3D-mask for every channel-map of the clean cube, defining regions where ^{12}CO radiation is detected. Similar to the definition of the baseline window, pixels with more than $3\,\sigma$ are considered to contain emission. Planes that do not have emission are not masked. This 3D-mask is then used to run a second cleaning with a definition of a cleaning support for every channel map based on the derived mask. The final resolution of the ^{12}CO cube is $4.89 \times 3.71''$ with a position angle (p.a.) of $63°$.

To define cleaning support regions for the HCO$^+$ map, a 3D-mask of the ^{12}CO emission is used as above. To define the mask, the cleaned ^{12}CO cube has been re-projecting to the dimensions of the HCO$^+$ map. Again it was assured that the cleaning converges in each channel map and that no residuals exist after cleaning. For the cleaning of the HCN data a different route had to be taken due to the hyperfine structure of HCN as well as the smaller extent of emission: for all channels the outlines of the cleaned HCO$^+$ emission distribution are used to define a supporting region. This was necessary to assure that the cleaning process converges. Using the 3D-mask from ^{12}CO, adapted for the hyperfine lines of HCN, did not lead to convergence in some of the channels. The final resolutions of HCN and HCO$^+$ are $6.50 \times 5.17''$ p.a. $144.9°$ and $6.85 \times 5.43''$ p.a. $145.5°$, respectively. The moment zero (cf. Section 11.2.5) of the final maps are displayed in Fig. 11.3 at their original resolution. For further analysis all PdBI maps have been converted the T_{mb} scale.

For all steps involving supporting regions or line-windows from another emission line it was assured that the results are not significantly altered with respect to a data reduction that does not make use of this information. Note, that in all cases the ^{12}CO based line-windows and support regions reduced the noise in the final images while maintaining the basic morphology and intensities of the respective lines.

Primary Correction Note, that single pointed observations with an interferometer result in an response that reveals the brightness distribution convolved with the primary beam of the telescopes, which is typically a Gaussian (here with a FWHM = $57''$). Therefore, the absolute intensities toward the edges of the map decline artificially and a quantitative comparisons with other data is not possible. To correct for this effect one can multiply the images with a Gaussian of a FWHM equal to the primary beam size of the interferometer and which is centered on the phase center of the maps. However, this procedure increases the noise towards the edges. In the following analysis the primary corrected maps are used. For reference the uncorrected images are shown in Fig. 11.2. Also note that the ^{12}CO map does not need such a treatment, as it is a hexagonal mosaic that yields a central field with constant intensity level. This is also
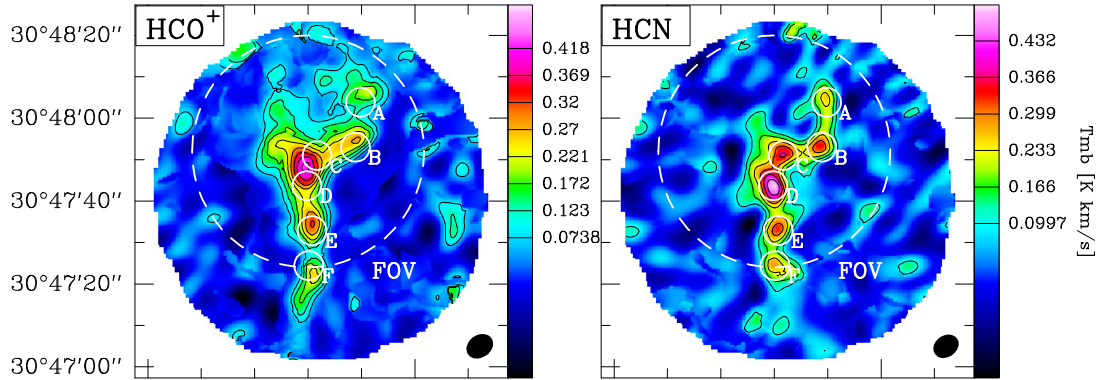
Figure 11.2.: Zeroth moment of the primary-uncorrected (cf. Section 11.2.4) HCO$^+$ and HCN maps at the original resolutions. The ellipses in the lower right corner mark the intrinsic beam sizes. Contours of the maps start at the 3σ level and are spaced by 2σ up to the peak value: $\sigma_{HCN} = 0.033$, Peak$_{HCN} = 0.5$; $\sigma_{HCO^+} = 0.025$, Peak$_{HCO^+} = 0.43$, in K km s^{-1}. The intensities corresponding to the contours are marked in the color scale to the right of the images. The dashed circle shows the FWHM field of view (FOV) of the PdBI primary beam of 57$''$. The small white circles overlayed onto the maps mark the peak positions A to F identified in the HCN map, as noted in Section 11.3.

the reason for the circular shape of the ^{12}CO maps: the maps are truncated at a radius after that the intensity scale is disturbed by the influence of the outer pointings.

3mm Continuum   Simultaneously, to the observations of HCN and HCO$^+$ the 3 mm continuum of GMC no3, near 89 GHz was obtained. The Q2 1 GHz IF chunk of the narrow correlator is used to extract the continuum information. Cleaning the pure PdBI map was unproblematic and done with the hogbom algorithm and 5000 iteration. The resulting map is shown in Fig. 11.3. In the preliminary state of the data presented here it still lacks the short spacing information and therefore more extended emission might exist. In this thesis the data is not further exploited. However in future work this data might add to the definition of the spectral energy distribution. In particular it can help to define the connection between the long wavelengths tail of the dust emission and the free-free emission.

11.2.5. Moment Zero Maps

To produce low noise moment zero maps of ^{12}CO, HCN and HCO$^+$ 3D-masks of the ^{12}CO emission are generated as explained above and used to define positional dependent integration ranges. For the ^{12}CO moment zero map the 3D-mask was derived at the original resolution of ^{12}CO. In case of the HCN and HCO$^+$ maps that have a lower resolution, the ^{12}CO map has been convolved to 7$''$ prior to the definition of the mask. To exclude spikes and edge effects a generous polygon outlining the ^{12}CO emission has been used to concentrate the 3D-mask onto the GMC region.

To construct the moment zero for each pixel all channels that are above 3σ in the ^{12}CO map are added and multiplied by the channel-width. At pixels for that no line-width is defined, due to missing ^{12}CO emission, all channels in the range of the map

Table 11.1.: Comparison of PdBI and 30 m single-pointed flux

	30 m Pointing	PdBI+30 m	Deviation
$I_{^{12}CO\,(1-0)}$ [K km s^{-1}]	9.4±0.9	8.8±0.9	7 %
$I_{HCO^+\,(1-0)}$ [mK km s^{-1}]	119±10	130±13	9 %
$I_{HCN\,(1-0)}$ [mK km s^{-1}]	61±10	72±7	18 %

Notes. A 10% absolute flux calibration error for the PdBI observations is assumed.

averaged line-width of ^{12}CO are used. As a consequence, the circular shape of the edges of the ^{12}CO map is transported to the HCO$^+$ and HCN maps.

Note that the hyperfine structure of HCN (Table 12.2) is taken into account by extending each line-width defined in the 3D-mask by -7.064 and 4.842 km s^{-1} to account for the displacements of the HCN hyperfine structure lines. The resulting zeroth moment maps are displayed in Figure 11.3.

11.2.6. Comparison of the PdBI results with the 30 m pointing towards GMC no3

To compare the calibration between the 30 m single pointings and the PdBI observations, the spectral cubes of the PdBI+30 m data have been smoothed to the resolution of the 30 m data, which is 28″ for HCN and HCO$^+$ and 21″ for ^{12}CO. Subsequently the spectra corresponding to the position of the 30 m observations (RA = 01:34:07, Dec = 30:47:52) are extracted and integrated over the line extent of the ^{12}CO line in the same way as described below in Section 12.1. The results together with the intensities found at the 30 m (cf. Table 5.1), are given in Table 11.1. The fluxes are consistent within 18% or better and thus in reasonable agreement. However, although HCN and HCO$^+$ have been obtained at the same time at the PdBI as well as the 30 m they show different deviations. This might be due to subtle differences in the cleaning procedure and the derivation of the moment zero. Further HCN is weaker than HCO$^+$ and was detected only at a signal-to-noise of $6\,\sigma$ at the 30 m telescope, therefore it might be influenced more strongly by baseline noise than HCO$^+$.

11.3. Morphology of GMC no3

In Fig. 11.3 the integrated intensity maps of ^{12}CO, HCO$^+$ and HCN and the 3 mm continuum image are shown at their original resolutions. In all lines GMC no3 is fragmented; however, to different degrees. The ^{12}CO line has the smoothest distribution and shows two distinct complexes: a large one in the north with a "Y-shaped" morphology and a smaller one in the south resembling an "hour-glass" shape. Further, ^{12}CO shows a peak above the north-western end of the "Y".
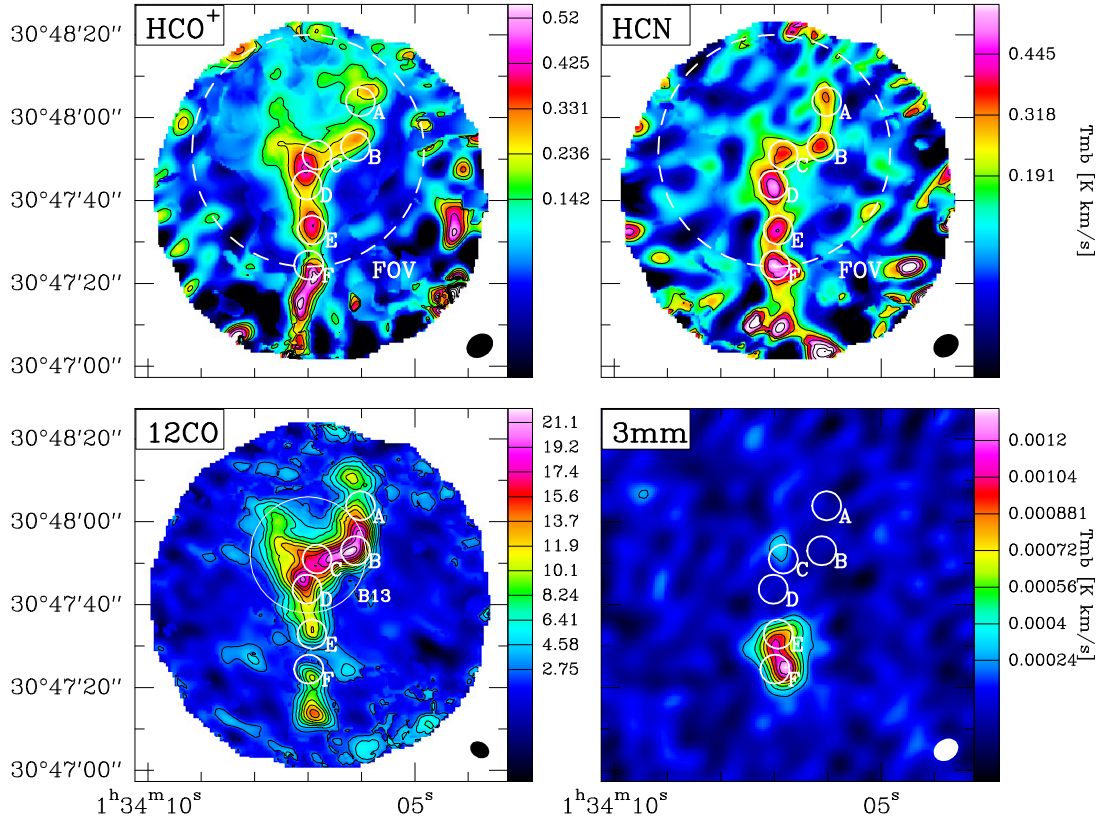
Figure 11.3.: Moment zero maps of HCO$^+$, HCN, ^{12}CO and the 3 mm continuum at their intrinsic original resolutions. The HCN and HCO$^+$ maps are primary-corrected (cf. Section 11.2.4). Note the increase of noise towards the edges as well as of intensities of the southern sources in comparison to Fig. 11.2. The *ellipses*, *dashed circle* as well as *small white circles* are the same as in Fig. 11.2. Contours start at the 3 σ level and are spaced by 2σ up to the peak value. The peak value and σ for HCN and HCO$^+$ are measured inside the PdBI FOV. The values are: $\sigma_{CO} = 0.92$, Peak$_{CO} = 22.1$; $\sigma_{HCN} = 0.06$, Peak$_{HCN} = 0.55$; $\sigma_{HCO^+} = 0.05$, Peak$_{HCO^+} = 0.44$; $\sigma_{3\,mm} = 7 \times 10^{-5}$, Peak$_{3\,mm} = 1.3 \times 10^{-3}$ in K km s^{-1}. The color scales to the right marks the intensities of the contours. The *white circle* on-top of the ^{12}CO map displays the positions and 28" beam-size of the 30 m observations presented in Part II and Buchbender et al. (2013) (B13).

HCO$^+$ follows the morphology of ^{12}CO and is similar in extent[3]; however it shows a more clumpy nature with several condensations on top of a more diffuse distribution in the north of the cloud.

In comparison the HCN emission is less extended and more clumpy than HCO$^+$ and resembles a string of clouds. The HCN emission emerges nearly exclusively from structures with sizes that are comparable to the resolution, which might indicate that HCN is not resolved.

Between five and six distinct "clumps" of emission can be identified in the HCO$^+$ and HCN maps, respectively. The "clumps" seen in HCN and HCO$^+$ have sizes of about 25 pc. As these entities are structures within one giant molecular cloud com-

---

[3]Note that it has been checked that this fact is not produced by the derivation of the moment zero maps based on the ^{12}CO emission. Moment zero maps with a constant integration range enclosing the emission yield a similar, yet noisier result.

plex, they are referred to as molecular clouds (MCs) in the following, although it is acknowledged that giant molecular clouds exist that are 25 pc or less in size (Murray, 2011). For later reference the HCN-peaks are named MC-A to MC-F[4] from north to south.

The emission peaks of the three molecules show shifts between each other. As such the main ^{12}CO peak does not coincide with the strongest HCN and HCO$^+$ emission. The peak of HCO$^+$ in the junction of the "Y" is located between MC-C and MC-D, the two less extended peaks of HCN emission[5]. Also the other positions of HCN and HCO$^+$ peaks do not perfectly overlap each other (see also Fig. 12.3). Both maps have been obtained simultaneously such that the shifts are genuine as differences in astrometry can be ruled out.

The overall distribution of emission of ^{12}CO (1–0), HCO$^+$ (1–0) and HCN (1–0) is consistent with the expected behavior due to their critical densities (n_{crit}). ^{12}CO (1–0) has a critical density about two orders of magnitude lower than HCO$^+$ (1–0) which has a critical density of $n_{\text{crit}} = 3 \times 10^4 \, \text{cm}^{-3}$. The critical density of HCN is even larger, i.e. $2 \times 10^5 \, \text{cm}^{-3}$ (Table 3.1). Therefore, HCN is the least easy to excite of the three molecules and is expected to trace dense and compact regions with densities about $1 \times 10^5 \, \text{cm}^{-3}$ and larger, HCO$^+$ can be thermalized at lower densities and thus will trace less dense and more extended regions than HCN. Consequently, ^{12}CO is expected to have the largest spatial extend and also to include more diffuse molecular gas (Baan et al., 2008). The fact that the distribution of emission in ^{12}CO is smoother than that of HCN and HCO$^+$ is most likely due to the fact that ^{12}CO is mostly optically thick and as such only shows the surface of the molecular clouds.

Velocity structure   The good velocity resolution of the PdBI maps allows to study the behavior of the molecular emission in GMC no3 in velocity space. In Figure 11.4 the position-velocity diagrams of HCO$^+$ and ^{12}CO along two cuts are shown between -265 km s^{-1} and -245 km s^{-1}. The cuts are oriented in: north-south direction (NS) cutting through MCs D, E, and F and east-west direction (EW) through MCs B and C. The velocity resolution of the displayed ^{12}CO data is 0.5 km s^{-1}, the one of HCO$^+$ 2 km s^{-1}. HCN is not included in the plot because its hyperfine structure and low signal to noise renders an image of the position-velocity cut difficult to interpret.

The position-velocity diagrams reveal clear velocity gradients within GMC no3 and a segregation of the identified molecular clouds in velocity space. This can best be seen in ^{12}CO due to its high velocity resolution. The cut NS shows a difference in velocity and line-widths between the northern cloud MC-D and the clouds E and F in the south. In cut EW a ^{12}CO velocity gradient between the HCN-peaks MC-C and MC-B is visible spanning a range of ~ 10 km s^{-1} between 251 and 260 km s^{-1}.

---

[4]Note that MC-F lies at the edge of the primary beam of the maps. It, nevertheless shows up in both, the HCN and the HCO$^+$ maps, and has a counterpart in ^{12}CO (cf. also Fig. 11.2). Therefore, it is reckoned that it is real; however, its measured intensity is certainly affected by a larger uncertainty (cf. Table 12.1).

[5]The exact HCN morphology of MC-C and MC-D in the current state of reduction depends on whether or not the HCN short-spacing data is included; if included both peaks merge to a larger one. This is however most probably due to the higher noise in the data. Nevertheless, in a future iteration it has to be clarified whether these are two single MCs or one larger complex.
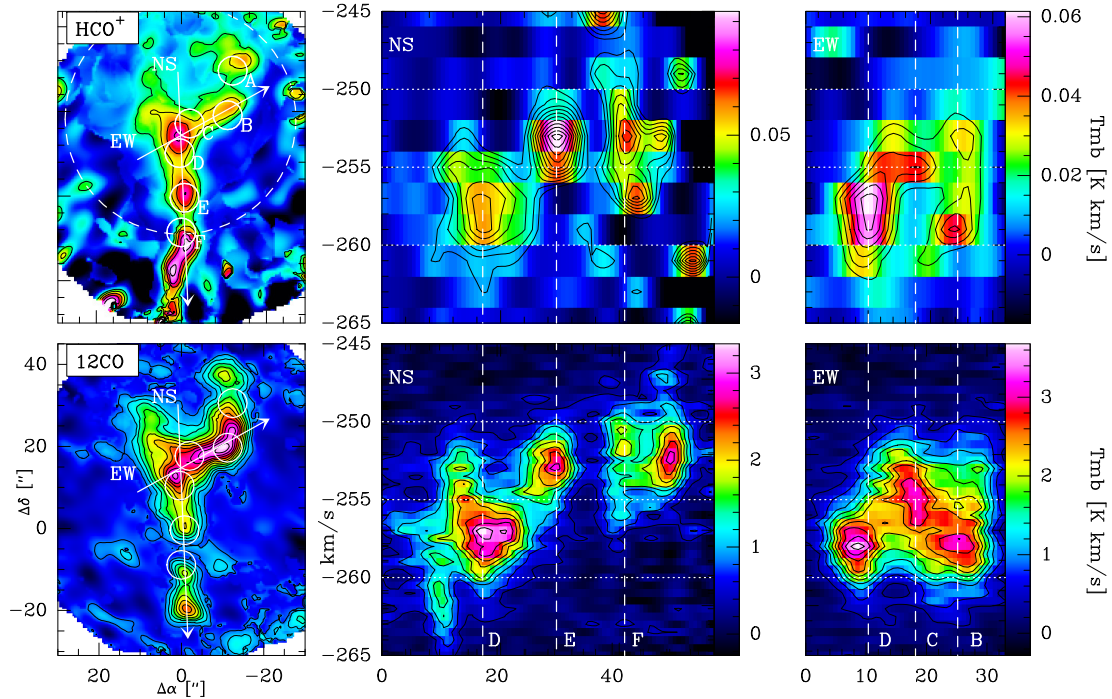
Figure 11.4.: PdBI maps of HCO$^+$ (primary-corrected) and ^{12}CO together with position-Velocity (PV) diagram of HCO$^+$ and ^{12}CO along two cuts: in north-south direction (NS) through MCs D, E, and F and in east-west (EW) through MCs C and B. The velocity resolutions are $2\,\mathrm{km\,s^{-1}}$ for HCO$^+$ and $0.5\,\mathrm{km\,s^{-1}}$ for ^{12}CO. Coordinates in arcseconds from RA = 01:34:06.985, Dec = 30:47:33.29 and displayed velocity range are the same for both maps. Contours of the maps are as in Fig. 11.3. The contours of the PV-cuts are shown from $3\,\sigma - \sigma$ is the averaged baseline rms – to the maximum of the cuts in steps of σ for HCO$^+$ and of $3\,\sigma$ for ^{12}CO. For HCO$^+$, which has a non-flat noise distribution due to the primary correction, all values, i.e. min and max intensity as well as σ, have been derived inside the primary field of view (FOV) marked by the dashed circle. The line show the approximate positions of the identified HCN-peaks (*dashed lines*) and from *top to bottom* mark the velocities -250, -255 and -260 km s^{-1} (*dottet lines*).

The HCO$^+$ velocity structure follows the morphology of ^{12}CO. MC-D shows a offset in position and a slightly broader line-width than its ^{12}CO counterpart. In the north-south cut the positions of the ^{12}CO and HCO$^+$ peaks are well aligned.

Towards cloud F, HCO$^+$ shows additional peaks towards lower $\sim$ -257 km s^{-1} velocities. This features are also visible in the HCO$^+$ spectra at this position shown in Fig. 12.1 and is most likely an artificial baseline features, since it is confined to a single channel and the cloud is situated close to the edge of the FOV of the primary beam.

11.4. Comparison with other wavelengths

Multiwavelength comparisons of GMC no3 have been done before by Gratier et al. (2012, cf. Fig. B.256) and Mookerjea et al. (2011, cf. Fig 5). Gratier et al. (2012) compared the ^{12}CO (2–1) emission with Hα, 8 μm, 24 μm and FUV emission in GMC no3 and concluded that it is an evolved cloud, due to exposed star formation seen in FUV
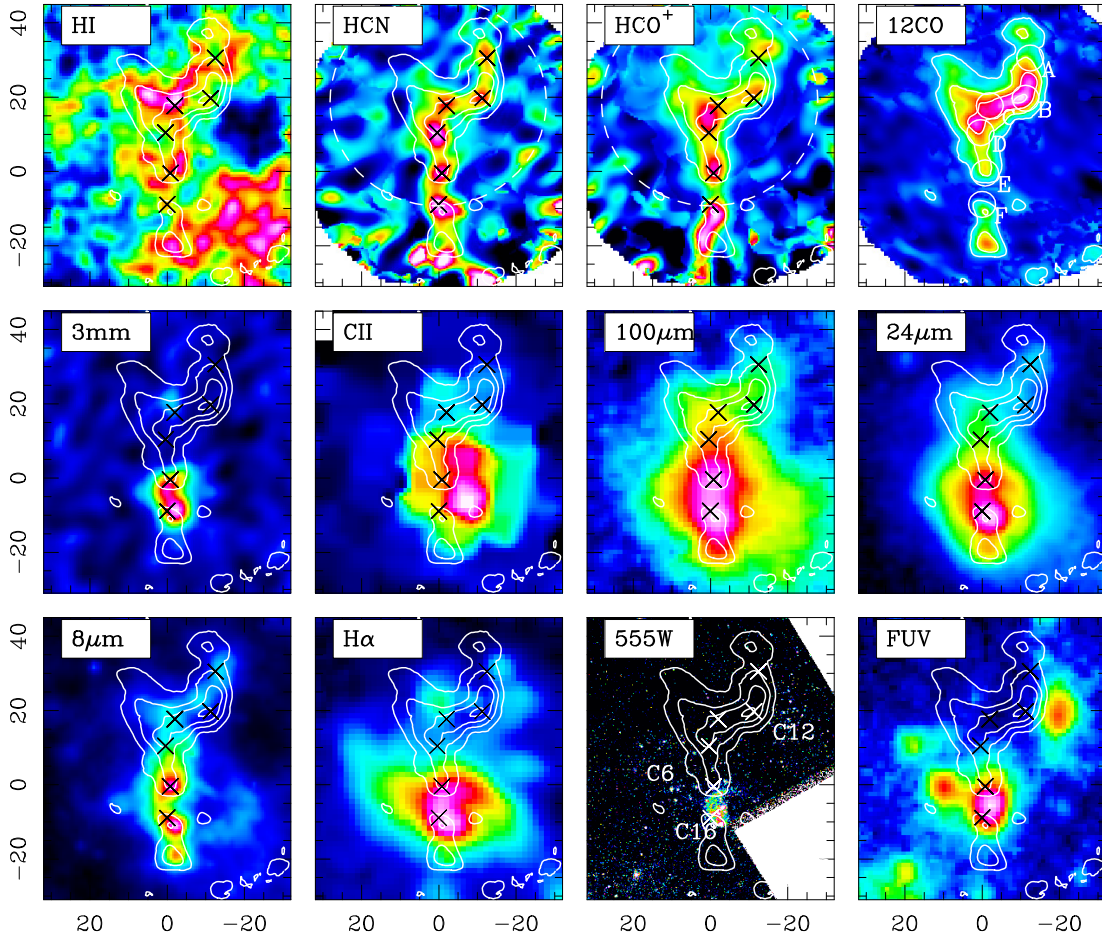
Figure 11.5.: Comparison of the PdBI observations with ancillary data of GMC no3 at resolutions better than 7″. The primary corrected HCN and HCO⁺ data are shown. The coordinates are given in offsets in arcseconds from RA = 01:34:06.985, Dec = 30:47:33.29. The [C II] data is an exception with an resolution of ∼ 12″. The maps are ordered in decreasing wavelength from *left to right* and *top to bottom*. All maps are shown on a scale ranging from their minimum to maximum flux in the displayed region. HI, HCN, HCO⁺ ^{12}CO and [C II] are shown on a linear, all other maps on a logarithmic scale. The white contours show the ^{12}CO emission and start at the $5\,\sigma$ level and are spaced by $6\,\sigma$ with $\sigma_{CO} = 0.93$. The crosses mark the positions of the HCN peaks MC-A through MC-F as shown in Fig. 11.3 and Fig. 11.2. For information on the displayed images see Section 5.3.

and Hα as well as the embedded star formation seen in 8 μm and 24μm. Gratier et al. (2012) considers evolved clouds to be precedent to cloud dispersal and ∼ 50 % of the 337 identified M 33-GMCs fall into this category. The study by Mookerjea et al. (2011) compares Hα, H I, ^{12}CO, 24 μm, 100 μm, and 160 μm with the [C II] emission from this region. They find little spatial correlation of [C II] emission with ^{12}CO, with a correlation coefficient of $r = 0.41$ over the entire map and even less with H I ($r = 0.22$). Hα and the dust emission is however found to be better correlated with correlation coefficients of about $r = 0.6$.

In Fig. 11.5 the new PdBI observations are shown next to a range of ancillary data available to the `HerM33es` project that have a resolution of better than 7″. In Section 5.3 the data-set is introduced and the corresponding references are given.

The most prominent features in the vicinity of GMC no3 are three star clusters visible in the HST 5300Å broadband image (555W). These clusters were identified in Bedin et al. (2005) in a Hubble Space Telescope WFC/ACS[6] observation in the F775W band (6400–9000Å). In Bedin et al. (2005) they are listed under IDs 6, 12 and 16 as labeled in Fig. 11.5, here they are refered to as C 6, C 12, and C 16. C 12 is classified as an association, C 6 as a low density cluster and – the most prominent cluster – C 16 as a populous cluster. C 12 and C3 are difficult to see in print but all three clusters are highlighted by their FUV emission. In the same field shown here seven further candidates for smaller clusters are identified in Bedin et al. (2005). The "cometary" shaped star cluster C 16 is situated in the ^{12}CO-gap to the south that separates the "Y" from the "hourglass" shaped ^{12}CO cloud. Its position coincides with the strongest Hα, FUV, 24 μm and 100 μm emission. Cluster C 12 is also associated with Hα emission, while C 6 shows only weak Hα emission and does not show up in the other wavelengths. Note the pronounced hole of H I in which C 6 is situated.

The H I emission in GMC no3 shows a flocculent and filamentary morphology that envelopes the ^{12}CO emission. Although H I emission is present throughout the ^{12}CO emitting region, it is weaker in regions of strong ^{12}CO, HCN or HCO$^+$ emission, cf. MC-A, MC-B, and MC-D. There is extended H I emission with no counterpart in the southwest.

The dust components traced by 8 μm emit most strongly at the positions of MC-E and MC-F near the H II region marked by the Hα emission. In the north of GMC no3, where it is relatively weak, the 8 μm emission follows the molecular gas. The 24 μm and 100 μm emission show a similar behavior as the 8μm emission, but their emission is more widespread, which may be due to some extent to the lower resolution of these maps. The 3 mm continuum emission follows the distribution of the peak fluxes of Hα and 24μm that highlight the cluster C 16.

[CII] 158 μm is shown here despite its lower resolution of 12″. The main [C II] emission peak is located outside of the molecular cloud traced by ^{12}CO and spatially not directly related to any of the other emission lines. Note that ^{12}CO emission, however weak, exists close to the peak position of [C II] while Hα and 24 μm "wrap" around the [C II] peak. Interestingly, the 8 μm emission shows a ring-like structure around the [C II] peak positions.

Proposed scenario for GMC no3 With the morphology described above in mind, it is tempting to hypothesize that the star cluster C 16 has recently formed from the molecular material of GMC no3 and has begun to dissolve the molecular cloud. It is most likely a young star cluster due to its prominent Hα emission which traces stars that have formed in the past 3-10 Myr (Murphy et al., 2011). Since the star cluster is visible and enveloped by strong dust emission from 24 μm and 100 μm, it might be that the stars are situated in front of a dust cover which it heated by the cluster. The 8 μm as well as 24 μm emission peak towards MC-E and MC-F in direct vicinity of C 16, hinting at embedded star formation within these positions, which is likely triggered by the cluster itself. Towards these two HCN and HCO$^+$ peaks, only relatively weak ^{12}CO emission is found, which might show that the denser material is better suited to resist the photo-ionizing flux from the young stars, while the diffuse gas has been

---

[6]Wide field camera of the "Advanced Camera for Surveys"

largely dissolved. Note the slight shift of the HCN-emission towards the star cluster in MC-F relative to HCO$^+$ and ^{12}CO. A similar morphology is found in NGC604, the brightest H ɪɪ-region of M 33 by (Miura et al., 2010). There, HCN emission is found in one location to face towards the ionizing flux from inside the H ɪɪ-region, while ^{12}CO peaks behind the denser region. This might show a sequential star-formation process (Miura et al., 2010).

Cluster C 12 might have formed earlier because it shows far-ultraviolet emission and no Hα. In contrast to Hα, the far-ultraviolet traces star formation over a ten times larger time scale (Murphy et al., 2011). The void of H ɪ, ^{12}CO and dust emission at the position of this cluster, suggests that it has formed sufficiently long ago to be able to clear its surroundings of cold atomic and molecular material. The large build up of the near ^{12}CO emission might equally be due to radiation and/or shocks from supernovae from this very cluster that might have compressed the adjacent parts of GMC no3.

The relative age of cluster C 6 is more difficult to estimate as its Hα emission might be induced by the brighter cluster C 16. However, C6 is likely to be older than C 16 as it is associated with little dust emission.

The spatial correlation of [C ɪɪ] with the position of the star cluster as well as the Hα emission peak shows that part of its emission must stem from ionized gas. This has already been suggested by Mookerjea et al. (2011). Comparing the [C ɪɪ] intensities with models of photo-ionization and photon-dominated regions they estimate that 20%-30% of the observed [C ɪɪ] emission emerges from ionized gas.

Finally, the lower emission from H ɪ in regions traced by strong ^{12}CO as well as HCN and HCO$^+$ emission possibly indicates a higher fraction of hydrogen in molecular form in these regions.

Chapter 12.

Analysis of HCN and HCO$^+$ clumps

In this chapter a quantitative analysis of the PdBI maps is performed. The HCN, HCO$^+$ and ^{12}CO spectra at the positions of the HCN-peaks are studied in Section 12.1. The following Section 12.2 explains complementary values that are determined at the six HCN-peak positions and discusses the relation between the total infrared luminosity and the line intensities of HCN and HCO$^+$. In Section 12.3 the spatial distribution of the HCO$^+$/HCN ratio is investigated, while the relation between ^{12}CO and HCO$^+$ as well as HCN is studied in Section 12.4. Subsequently the PDR-analysis from Chapter 9 is extended to the individual clouds within GMC no3. Finally in Chapter 13 the major conclusions from the analysis are summarized.

12.1. Spectral analysis

As argued above, the HCN emitting regions are likely not resolved at a resolution of about 7$''$. For this reason, and because HCN is less extended than HCO$^+$, the following analysis is concentrated on the HCN peaks. The spectra of MC-A through MC-E are extracted from the data cubes at 2 km s^{-1} velocity resolution after all maps have been smoothed to the highest common resolution of 7$''$. To further enhance the signal-to-noise ratio, all spectra in a 7$''$ diameter aperture around each of the six positions are averaged. These spectra are shown in Fig. 12.1.

Single Gaussian fits are applied to the lines of ^{12}CO and HCO$^+$ to determine their line-width and velocity. The line intensities are deduced from the spectra by integrating the lines over the extent of the ^{12}CO line, which is determined from the point where the fitted Gaussians reach the baseline rms level of the ^{12}CO spectrum.

Due to its hyperfine structure (hfs), HCN is treated differently. A hyperfine structure triplet of three Gaussians with identical full width at half maximum and the natural relative strengths between the hfs-lines under local thermodynamic equilibrium (cf. Table 12.2) is used to fit the HCN lines[1]. The line intensities are derived as for ^{12}CO and HCO$^+$, only that the assumed line extent determined from ^{12}CO is enlarged in velocity by the shifts of the hyperfine structure lines. The fits are shown in Fig. 12.1 and the determined intensities, center velocities and line-widths are given in Table 12.1 together with further quantities explained below. The optical depths from the LTE hyperfine structure fits are not reproduced due to the low signal-to noise of the HCN spectra.

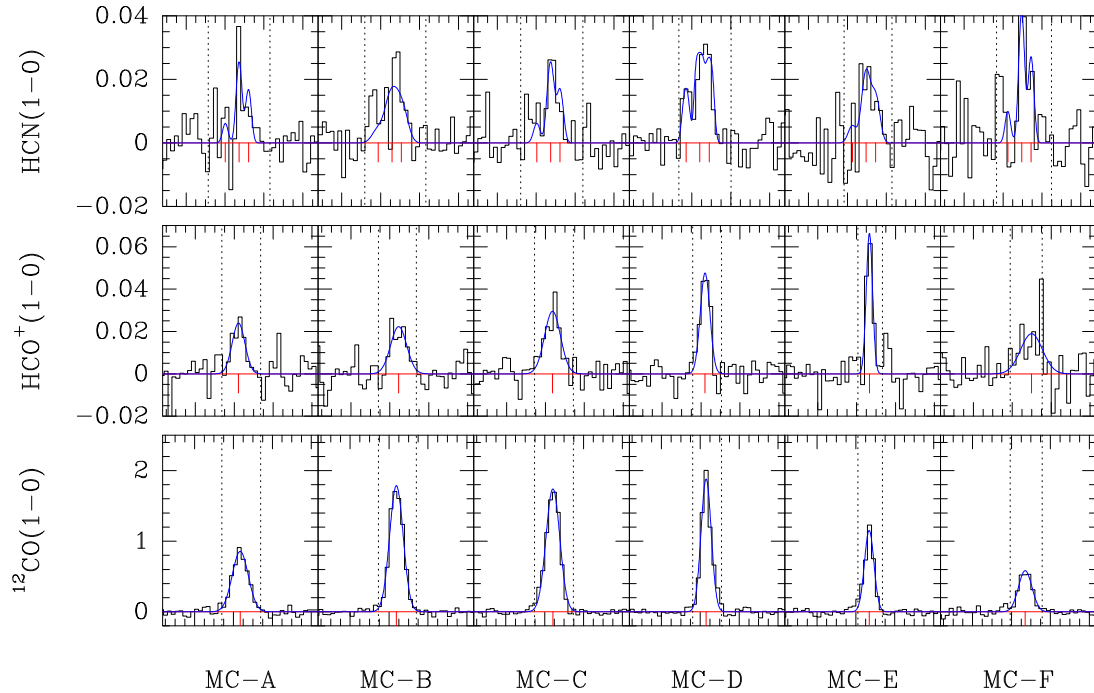[1]Using the hfs method from the CLASS/GILDAS package.

Figure 12.1.: Spectral lines of ^{12}CO, HCO$^+$, and HCN averaged over an 7″ aperture at the six peak positions identified in the HCN map (cf. Tab. 12.1). The velocity range shown is 80 km s^{-1} centered on -257 km s^{-1}. The intensity scale of the spectra is in main beam temperature T$_{mb}$. Lines mark: the baselines (*red*); Gaussian fits in case of ^{12}CO and HCO$^+$ and hyper-fine structure fit of three Gaussians for HCN (*blue*); the fitted central velocity at each position, for HCN the velocities of the individual hfs lines are shown (*vertical red*); the ^{12}CO line extent (*dotted lines*).

The determination of the σ uncertainties of the integrated line intensities is done via Eq. (5.1)[2]. A line is considered "detected" if its integrated intensity is higher than $3\,\sigma$. Here all lines are "detected" by this criterion with exception of the HCN line of MC-A.

Results   The deduced line-widths of the three molecules show interesting differences. They are displayed in Fig. 12.1 ordered from north to south. While the HCO$^+$ and ^{12}CO lines have similar line widths in the range of about 6–10km s^{-1}, the width of the HCN hfs-components are two to three times smaller and lie in the range of 3–5 km s^{-1}. One exception is MC-E where all three lines have a similar line width, i.e. 3.8–5.7 km s^{-1}. Towards MC-F the HCO$^+$ line has a significantly larger width[3] than ^{12}CO, while the opposite is true in MC-E, where the HCO$^+$ line width is comparable to that of HCN.

For the seven GMCs studied along the major axis of M 33 using the 30 m telescope at 28″ resolution, the velocity resolution of 6 km s^{-1} of the WILMA spectrometer did not allow an accurate determination of the line-widths of HCN and HCO$^+$. Gaussian

---

[2]Note the increase of uncertainty for HCN and HCO$^+$ line intensities, i.e. the values given in brackets in Table 12.1, with increasing distance to the phase center which is close to MC-C/MC-D due to the primary correction.

[3]Note that the Gaussian line fit give a similar result if the "spike" visible in the HCO$^+$ spectra of MC-F is flagged.

Table 12.1.: Observed intensities and complementary data for the seven identified clouds in GMC no3

	MC-A	MC-B	MC-C	MC-D	MC-E	MC-F
RA [J2000]	01:34:06.019	01:34:06.113	01:34:06.831	01:34:07.019	01:34:06.925	01:34:06.987
DEC [J2000]	30:48:03.85	30:47:52.99	30:47:50.98	30:47:43.74	30:47:32.87	30:47:24.42
$I_{^{12}CO\,(1-0)}$ [K km s^{-1}]	8.9 (10 %)	15.4 (10 %)	15.5 (10 %)	12.8 (11 %)	7.2 (10 %)	4.9 (10 %)
FWHM [km s^{-1}]	9.7 (5 %)	8.2 (2 %)	8.4 (2 %)	6.1 (3 %)	5.7 (5 %)	8.1 (7 %)
Velocity [km s^{-1}]	-257 (0 %)	-256 (0 %)	-256 (0 %)	-257 (0 %)	-253 (0 %)	-253 (0 %)
$I_{HCO^+\,(1-0)}$ [m K km s^{-1}]	205 (22 %)	216 (16 %)	308 (10 %)	283 (10 %)	280 (11 %)	279 (15 %)
FWHM [km s^{-1}]	7.8 (26 %)	9.8 (17 %)	9.7 (15 %)	5.8 (10 %)	3.8 (11 %)	13.2 (21 %)
Velocity [km s^{-1}]	-258.0	-255.0	-256.0	-258.0	-253.0	-250.0
$I_{HCN\,(1-0)}$ [m K km s^{-1}]	< 164	252 (15 %)	222 (18 %)	372 (10 %)	205 (23 %)	311 (20 %)
FWHM [km s^{-1}]	3.3 (7 %)	4.0 (52 %)	4.0 (21 %)	3.6 (11 %)	5.0 (29 %)	3.3 (20 %)
Velocity [km s^{-1}]	-253.0	-256.0	-253.0	-256.0	-250.0	-250.0
rms [mK]	6.9	5.0	5.0	5.1	6.8	8.1
$I_{HCO^+\,(1-0)}/I_{HCN\,(1-0)}$	> 1.2	0.9 (0.2)	1.4 (0.3)	0.8 (0.1)	1.4 (0.4)	0.9 (0.2)
$I_{HCN\,(1-0)}/I_{^{12}CO\,(1-0)}$ [%]	< 1.8	1.6 (0.3)	1.4 (0.3)	2.9 (0.4)	2.8 (0.7)	6.3 (1.4)
$I_{HCO^+\,(1-0)}/I_{^{12}CO\,(1-0)}$ [%]	2.3 (0.6)	1.4 (0.3)	2.0 (0.3)	2.2 (0.3)	3.9 (0.6)	5.7 (1.0)
L_{TIR} [10^5 L$_\odot$]	1.2 (0.0)	1.2 (0.0)	1.8 (0.1)	2.5 (0.1)	6.3 (0.2)	7.7 (0.2)
L_{TIR}/L'_{HCN} [10^3]	0.8 (0.3)	0.5 (0.1)	0.9 (0.2)	0.7 (0.1)	3.4 (0.8)	2.7 (0.5)
L_{TIR}/L'_{HCO^+} [10^3]	0.6 (0.1)	0.6 (0.1)	0.6 (0.1)	0.9 (0.1)	2.5 (0.3)	3.0 (0.5)
SFR [M$_\odot$ Gyr^{-1} pc^{-2}]	71.2 (9.9)	102.6 (14.6)	125.4 (17.5)	303.5 (43.6)	947.8 (135.6)	925.4 (128.9)
M_{HI} [10^3 M$_\odot$]	36.7 (5.5)	32.9 (4.9)	44.5 (6.7)	32.9 (4.9)	39.7 (6.0)	34.7 (5.2)
M_{H_2} [10^3 M$_\odot$]	57.0 (5.7)	98.8 (9.9)	99.4 (9.9)	82.1 (8.2)	46.2 (4.6)	31.6 (3.2)
G_0	16.4 (0.5)	16.8 (0.5)	25.0 (0.8)	33.6 (1.1)	87.0 (2.8)	105.0 (3.4)
A_v	5.0 (0.4)	7.0 (0.6)	7.7 (0.6)	6.1 (0.5)	4.6 (0.4)	3.5 (0.3)

fits to both lines result in line-widths in the range of ~ 9–$15\,\mathrm{km\,s^{-1}}$. The resolved ^{12}CO spectra – observed with the FTS-spectrometers at a higher velocity resolution – yield line widths between 4 and $11\,\mathrm{km\,s^{-1}}$. This is a similar range to that found in GMC no3 (cf. Table 5.1 and Fig. 5.3). The ^{12}CO-line width of GMC no3 was found to be $8\,\mathrm{km\,s^{-1}}$. The 30 m pointing position includes the clouds MC-B, C, and D (cf. Fig. 11.3), which show here consistent line-widths between 6 and $8\,\mathrm{km\,s^{-1}}$.

The center velocities of all three species are consistent within $3\,\mathrm{km\,s^{-1}}$ (i.e. less than two channel-widths), under exclusion of MC-A, where deviations of up to $5\,\mathrm{km\,s^{-1}}$ are found.

The HCO$^+$ integrated line intensities vary between the main peak in MC-C and the lowest value towards MC-A by about 44%. HCN shows a similar variation of 50% from cloud D to E. The ^{12}CO line intensity shows a larger dynamical range as its line intensities vary by up to 70% from the peak intensity towards MC-C. The HCO$^+$/HCN as well as HCN/CO and HCO$^+$/CO ratios are discussed in detail in Section 12.3 and Section 12.4.

The hyperfine structure triplet of HCN is marginally resolved as can best be seen in the spectrum of MC-D. The consistency of the central velocities of ^{12}CO with the center of the HCN hfs-triplet are an indication that the observed hfs-splitting of HCN is genuine. In the 30 m single pointings from Part II the hyperfine structure was not resolved due to the three times lower velocity resolution of the WILMA spectrometer of $\sim 6\,\mathrm{km\,s^{-1}}$.

The on average smaller line-width of HCN might indicate that HCN traces less turbulent, and more quiescent gas than HCO$^+$ and ^{12}CO. Note, that the actual HCN line widths are similar to those measured in individual massive dense clumps in the MW
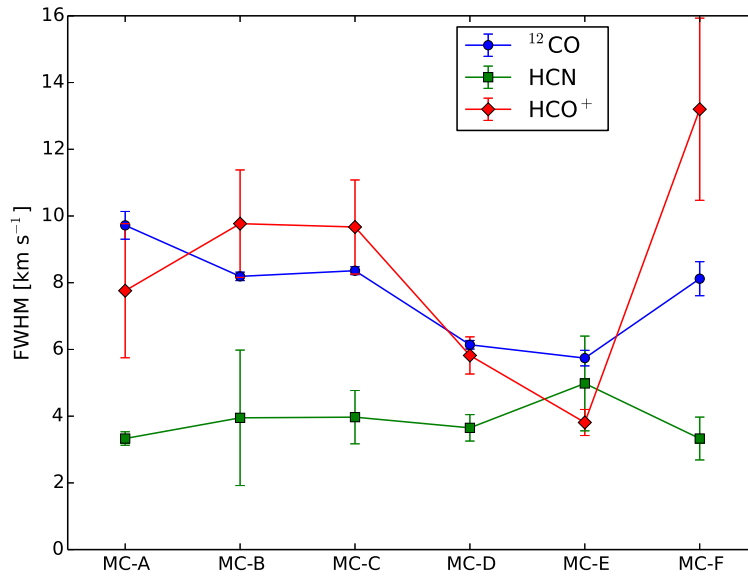
Figure 12.2.: Line-widths of ^{12}CO, HCN and HCO$^+$ plotted for the sources MC-A to MC-F.

with linear sizes of $\lesssim 2$ pc (Wu et al., 2010) and only slightly larger than those of infrared dark cores with $\sim 2\,\mathrm{km\,s^{-1}}$ (Liu et al., 2013).

12.2. Complementary quantities

The values of the total gas mass (M_{gas}), star formation rate (SFR), optical extinction (A_{v}) and far-ultraviolet field strength (G_0), given in Table 12.1 were determined for a resolution of 7$''$ in the same way as their counterparts in Part II (cf. Table 5.1). For details of their calculation please refer to the explanations in Part II.

The derivation of the total infrared luminosity and the molecular gas mass differ from the calculation explained in Section 6.4 and Section 5.6, respectively, as is described in the following.

Total infrared luminosity   For each of the clouds the total infrared luminosity (L_{TIR}) value is determined with the same technique as in Section 6.4. A linear combination of available IR bands is used to determine the L_{TIR} value following the calibration given in Boquien et al. (2010). However, here only 24 µm MIPS and 100 µm PACS date is used because these observations have a resolution better than 7$''$. Both were smoothed to 7$''$ prior to calculation of L_{TIR} via Eq. (6.2). Note that the resulting fluxes in the range of 1×10^5–8×10^5,$L_\odot$ are close to or below the lower limit in L_{TIR} where a breakdown of the L_{TIR}–L'_{HCN} relation is observed (Wu et al., 2005).

Molecular gas mass   In Section 5.6 the X_{CO} values of the observed GMCs have been scaled by the value of L_{TIR} following the relation found by Israel (1997). This relation is based on the estimation of total infrared luminosities in M 33 from Rice et al. (1990) using the *IRAS* satellite with a resolution of a few arcminutes. Therefore on the local scales observed here, this approach might become error-prone. Here, the global value of $3.2 \times 10^{20}\,\mathrm{(K\,km\,s^{-1})^{-1}\,cm^{-2}}$ that has been derived for GMC no3 in Section 5.6 is used instead for all clouds. Molecular gas masses in the range of 32×10^3

Table 12.2.: HCN hyperfine structure lines

	Frequency [GHz]	velocity shift [km/s]	rel. LTE intensity
F=0-1	88.6339357	-7.064	0.2
F=2-1	88.6318475	0	1
F=1-1	88.6304156	4.842	0.6

to $100 \times 10^3 \, M_\odot$ are found, which are up to four times higher than the corresponding H I masses.

Results Similar to the analysis of Chapter 7 the relation of the line luminosities of HCN and HCO$^+$ with L_{TIR} (SFR) is investigated. Here the linear correlation coefficients are $r_{HCN} = 0$ and $r_{HCO^+} = -0.05$ and thus no correlation is visible. This is in contrast to the good correlation of HCO$^+$ with the total infrared luminosity within the GMC sample observed with the 30 m telescope at lower resolution. This indicates a break-down of the L_{TIR}-HCO$^+$ relation at high spatial resolutions. A reason might be that not all relevant feedback from star formation and the corresponding dense gas is included within in the same resolution element. This is indicated by the distribution of the star formation rate tracers Hα FUV, 24 μm and 8 μm that peak towards the young star cluster and are not directly related to most of the HCN and HCO$^+$ peaks (cf. Fig. 11.5).

A gradually increase of star formation rate from north to south of 72 to about 950 $M_\odot \, Gyr^{-1} \, pc^{-2}$ is found. This increase is due to the strong peaks of Hα and 24 μm towards the star cluster C 16 in the south. Here higher star formation rates are found in comparison to those deduced at 28$''$ at the single pointings towards the seven GMCs with the 30 mtelescope, where 1.2–65 $M_\odot \, Gyr^{-1} \, pc^{-2}$ has been found (cf. Part II). This is, however, due to the fact that the SFR is given per parsec and that the beam filling factors of the star formation tracers are larger at 7$''$. Here, the linear correlation factor between the SFR and the total infrared luminosity is $r = 0.98$.

The deduced range of optical extinction is $A_v = 3.5–7.7$ mag while the FUV field strengths are estimated to lie between $G_0 = 16$ and $G_0 = 105$.

12.3. HCO$^+$/HCN line ratio

Figure 12.3 shows a map of the HCO$^+$/HCN line intensity ratios within GMC no3 at 7$''$ resolution. The map has been derived for pixels that have an integrated intensity above 3 σ in both maps[4]. From this figure it can be seen that the ratio varies from values below 0.5 to values higher than 1.75. The variation of ratios between 0.8 and 1.4 (cf. Table 12.1), found in the spectra of positions A to F, are more moderate because they are averaged over the 7$''$ apertures shown also in Fig. 12.3. The HCO$^+$/HCN ratio is found to be higher than unity in the regions of MCs C and E, while it is significantly lower in the vicinity of clouds D and F. Gradients in the ratio can be seen throughout the cloud in Fig. 12.3 and reflect the slight displacements of the emission peaks of

---

[4]Note that here the primary uncorrected images have been used, which is possible since the primary field-of-view of HCN and HCO$^+$ are very similar due to the similar frequencies.
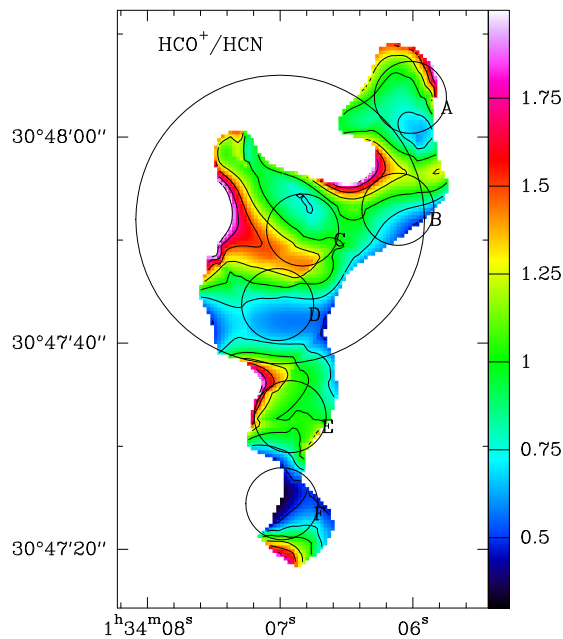
Figure 12.3.: Map of the HCO$^+$/HCN line intensity ratio shown for pixels that have a signal-to-noise of 3 σ or higher in both maps of HCN and HCO$^+$. The values of the contours are indicated in the color scale to the right. The positions of MC-A through MC-F are indicated by the circles that have a 7$''$ diameter.

the two molecules. Further, also the global HCO$^+$/HCN ratio of GMC no3 is deduced from the sum of all pixels in either map that are above the 3 σ level and found to be HCO$^+$/HCN=1.4.

From north to south, regions of high and low ratios alternate, which might indicate that the different regions within GMC no3 have differences in excitation and/or abundance of the molecules. Therefore, the line emission from both lines may not be simultaneous quantitative tracers of the same dense gas content over small spatial scales, if constant conversion factors are assumed.

In the GMC sample observed with the 30 m, HCO$^+$/HCN ratios in the range of 1.1–2.5 have been observed, where the ratio of GMC no3 of 1.9 was the second highest[5][6]. Here, with higher resolution the ratios are on average lower, which is likely due to the higher relative beam filling factors of HCN.

The variation of the HCO$^+$/HCN ratio within GMC no3 shows that single pointed observations that partly resolve a GMC, may yield significant variations in the line intensity ratio of HCO$^+$/HCN, depending on the resolution and the position of the observation. Therefore, for an unbiased comparison of the HCO$^+$ and HCN emission in between GMCs, it is important to gather the entire flux from objects that are to be compared.

12.4. HCN/CO/ vs. HCO$^+$/CO

Figure 12.4 plots HCN/CO versus HCO$^+$/CO integrated intensity ratios. The HCN/CO ratios found in GMC no3 lie in the range of 1.4–6.3%, while the HCO$^+$/CO ratios range between 1.4 and 5.7%. These values are on average higher than the ones found with the 30 m telescope in the GMC sample, where HCN/CO and HCO$^+$/CO are found

---

[5]See Fig. 12.3 for the position of the 30 m beam.

[6]Note that a ratio of 1.8 is found at the position of the pointing with the 30 m telescope after smoothing the PdBI maps to the same resolution as explained in Section 11.2.6.
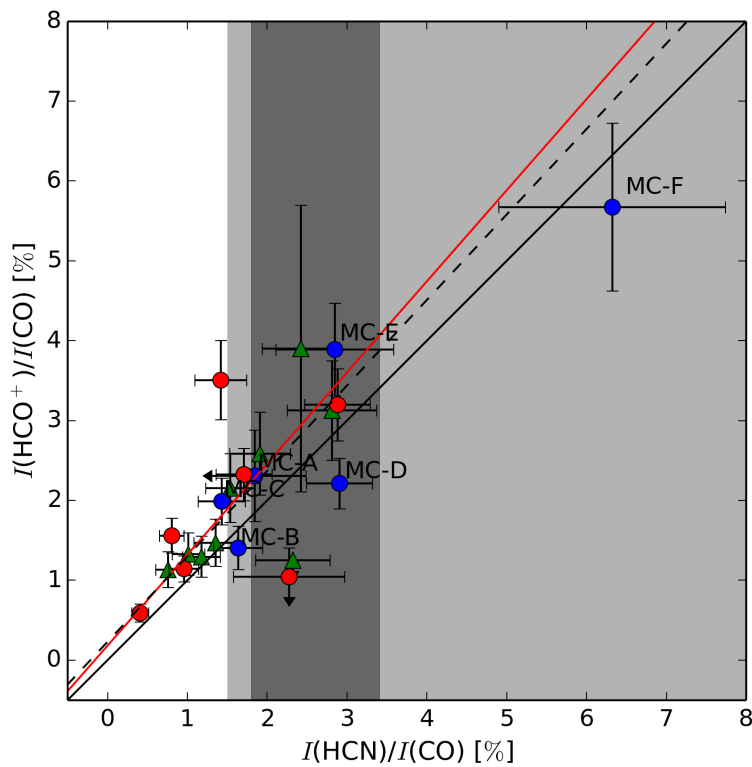
Figure 12.4.: Reproduction of Fig. 8.1 including the HCO⁺/CO vs. HCN/CO line intensity ratios for the HCN-peaks in GMC no3 (*blue*), GMCs in M 33 observed with the 30 m(*red*) and GMCs observed in M 31 by Brouillet et al. (2005) (*green*). Upper/lower limits are denoted by arrows. Lines and gray areas as in Fig. 8.1.

to be 0.4%–2.9% and 0.6%–3.5%, respectively. The deduced global value towards GMC no3 are HCN/CO=0.8% and HCO⁺/CO=1.6%. The low value of HCN/CO relative to the ones found for the HCN-peaks reflects the small filling factor of HCN in the larger beam of the 30 m telescope. In Fig. 12.4 the data points within GMC no3 are shown in comparison with those of the GMC sample and other 30 m data towards M 31. The distribution of the values from GMC no3 are situated at the upper end of the distribution.

One cloud, MC-F, exceeds the sampled range of ratios in all other GMCs/MCs by a factor of about 2. Also within the estimated errors this cloud still shows a considerably larger ratio $\gtrsim 4.7$ than the other data.

As already discussed in Section 8.1 in the solar vicinity HCN/CO ratios between 0.7%–1.9% are found while the Galactic Plane exhibits ratios in the range of 2.6±0.8% (Helfer & Blitz, 1997). Disks of normal galaxies at galacto-centric radii $\gtrsim 4$ kpc have ratios in the range of 1.5% – 3% and about 10% in their centers (Gao & Solomon, 2004b). In contrast the HCN/CO ratios in the LMC are relatively larger than the disk values of galaxies and lie between 3% and 6%.

Nevertheless, caution is needed when comparing ratios obtained in different sources and/or with different telescopes, because the ratios are sensitive to the mutual filling factors of the molecules they compare. This effect is discussed in detail for the example of HCN/CO in the Milky Way in Jackson et al. (1996). Dense Gas as traced by HCN and HCO⁺ is most likely confined to smaller structures than the ¹²CO emission. If the structure is resolved observations with different beam sizes (or at different distances) yield different relative filling factors for the compact and the more diffuse material, with the due changes in their ratio. The same effect is visible here, where we explicitly focus on the HCN emission peaks, in comparison to the single 30 m pointings with a

Table 12.3.: Best-fitting PDR models in GMC no3

	HCO⁺/HCN	HCN/CO [%]	A_v [mag.]	n_H [cm⁻³]	FUV [G_0]	Φ_{A_v}[a]	Φ_FUV[b]	best χ^{2}[c]
				subsolar metallicity Models				
MC-A	1.2 ± 0.5	1.8 ± 0.6	8 ± 5	(7 ± 19) 10⁴	46 ± 37	0.3 ± 0.2	0.4 ± 0.3	0.1 ± 0.1
MC-B	0.9 ± 0.2	1.6 ± 0.3	8 ± 4	(6 ± 12) 10⁴	39 ± 39	0.2 ± 0.1	0.4 ± 0.4	0.2 ± 0.1
MC-C	1.4 ± 0.3	1.4 ± 0.3	7 ± 4	(5 ± 6) 10⁴	58 ± 38	0.4 ± 0.3	0.4 ± 0.3	0.2 ± 0.2
MC-D	0.8 ± 0.1	2.9 ± 0.4	12 ± 6	(6 ± 4) 10⁴	98 ± 10	0.2 ± 0.1	0.3 ± 0.0	0.4 ± 0.2
MC-E	1.4 ± 0.4	2.8 ± 0.7	9 ± 5	(2 ± 7) 10⁴	45 ± 38	0.3 ± 0.2	1.9 ± 1.6	0.4 ± 0.4
MC-F	0.9 ± 0.2	6.3 ± 1.4	18 ± 7	(4 ± 13) 10⁴	61 ± 36	0.1 ± 0.1	1.7 ± 1.0	0.1 ± 0.1
				solar metallicity models				
MC-A	1.2 ± 0.5	1.8 ± 0.6	8 ± 4	(3 ± 12) 10⁴	52 ± 42	0.3 ± 0.2	0.3 ± 0.2	0.2 ± 0.3
MC-B	0.9 ± 0.2	1.6 ± 0.3	9 ± 3	(2 ± 4) 10⁴	32 ± 35	0.2 ± 0.1	0.5 ± 0.6	0.1 ± 0.1
MC-C	1.4 ± 0.3	1.4 ± 0.3	8 ± 3	(6 ± 8) 10³	37 ± 35	0.3 ± 0.1	0.7 ± 0.6	0.3 ± 0.3
MC-D	0.8 ± 0.1	2.9 ± 0.4	15 ± 2	(5 ± 3) 10⁴	90 ± 27	0.1 ± 0.0	0.4 ± 0.1	0.4 ± 0.3
MC-E	1.4 ± 0.4	2.8 ± 0.7	10 ± 4	(8 ± 30) 10³	43 ± 43	0.3 ± 0.1	2.0 ± 2.0	0.2 ± 0.3
MC-F	0.9 ± 0.2	6.3 ± 1.4	22 ± 9	(2 ± 6) 10⁴	59 ± 35	0.1 ± 0.0	1.8 ± 1.1	0.1 ± 0.1

Notes.[a]beam-filling factor derived from A_v(¹²CO)/A_v(Model); [b]beam-filling factor derived from FUV(TIR)/FUV(Model); [c]average χ^2 of the best-fitting models.

larger beam size. Therefore, to compare ratios between different sources and/or from different telescopes, it has to be assured that the data includes the total emission of both molecules from the particular sources. A quantitative comparison of the ratios in M 33, M 31 and other sources with the ratios found in GMC no3 can therefore not be conclusive.

However, inside GMC no3 a comparison between the different ratios is possible. Here, MC-F with its high ratio clearly takes a special place. Its position coincides with the Hα peak of BCLMP 302 and thus with the location of the star cluster C 16. In the proposed scenario for GMC no3 from Section 11.4 the recently formed star cluster C 16 dissolves, and at the same time compresses, its surrounding molecular material, triggering star formation within it. It is hypothesized that the dense material traced by HCN and HCO⁺ might be better suited to resist the dissolving flux than the diffuse envelope of molecular gas traced by ¹²CO. This process would result in a decrease of the ¹²CO filling factor, while the dense gas filling factor would be less affected, which would lead to changes in the line intensity ratio. A similar but less extreme scenario might happen in MC-E, situated on the other side of the "¹²CO-gap", as this cloud exhibits a high HCO⁺/CO= 4. From Table 12.1 it can be seen the ¹²CO intensity has a larger dynamical range of 70% between the strongest and weakest peak, while HCO⁺ only shows a variation of about 40%. HCN shows a smaller variation than ¹²CO as well, i.e. about 50%. This supports the above interpretation that mainly the ¹²CO filling factor is changed by the influence of the star cluster with respect to the dense gas filling factor. This might explain the large range in HCO⁺/CO and HCN/CO ratios within GMC no3.
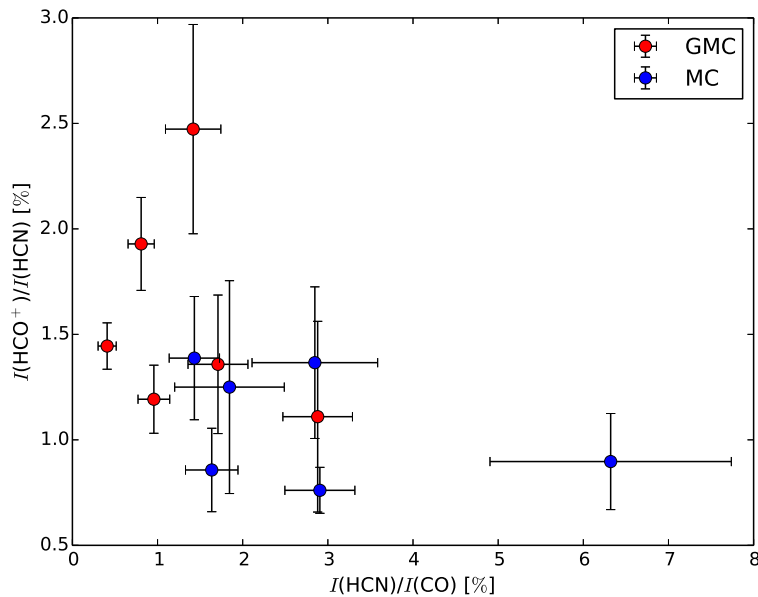
Figure 12.5.: HCN/CO vs. HCO$^+$/HCN line intensity ratios observed in single pointings with the 30 m telescope in giant molecular clouds (*red*) and in clouds within GMC no3 at the HCN-peaks (MCs) (*blue*).

12.5. Photodissociation regions

Here models of photon-dominated regions from the Meudon-PDR code (Le Petit et al., 2006; Gonzalez Garcia et al., 2008) are employed to study the six HCN-peaks. Two models are used: one resembling a solar metallicity and one that reflects the metallicity conditions of M 33. A grid of in total 288 models is used that includes volume densities of $n_H = 0.1, 0.5, 1, 5, 10, 50, 10^2 \times 10^4 \, cm^{-3}$, FUV field strengths of $G_0 = 10, 50, 100$ in Habing units, and optical extinctions $A_v = 2 - 50$ mag in steps of $\log A_v \sim 0.2$. The derivation of this grid is explained in detail in Chapter 9. Note, that the parameters of $A_v \sim$ 2-3 mag and of $G_0 \sim$ 16-100 estimated within GMC no3 fall within the sampled parameter space of the grid.

The measured HCN/CO and HCO$^+$/HCN line intensity ratios are compared with the ones derived from the grid. To determine the best-fit PDR-models for the data, summed squared residuals weighted by the observational errors are calculated Eq. (9.1). Errors on the best-fitting values are deduced from a Monte Carlo simulation. To do so, it is assumed that the measured line ratios and their uncertainties follow a Gaussian parent distribution with an expected value equal to the measured line-ratio and a variance equal to the square of the observational error (σ). These distributions are used to generate 5000 sets of HCN/CO and HCO$^+$/HCN line ratios for which the χ^2-values are calculated. The 5000 best fits are used to derive the mean and standard variation of the input parameters, these values are shown in Table 12.3.

It is found that both metallicity models are able to describe the observations in concordance with the results from the equivalent study on GMC scale in Chapter 9. In the following, as long as the qualitative results are equal, only the values of the sub-solar metallicity models will be discussed explicitly.

The range of best-fit densities in the sub-solar models for the molecular clouds in GMC no3 is $n_H = 2 \times 10^4 - 7 \times 10^4 cm^{-3}$. This displays nearly exclusively higher densities than the results from the PDR-analysis for the GMCs along the major axis of M 33 in Section 9.2, where densities $n_H = 3 \times 10^3 - 3 \times 10^4 cm^{-3}$ were found. On first sight it

is surprising that the results differ as the range in ratios observed in the seven GMCs, i.e. $HCO^+/HCN = 1.1–2.5$ and $HCN/CO = 0.4–2.9$, overlaps with the ratios observed at the HCN-peaks in GMC no3, i.e. $HCO^+/HCN = 0.8–1.4$ and $HCN/CO = 1.4–6.3$. In Fig. 12.5 both ratios are plotted against each other for all positions observed with the 30 m telescope as well as the PdBI. From this figure it can be seen that the distribution of the "GMC-points" is different than the one of the positions within GMC no3. The GMCs display on average lower HCN/CO and higher HCO^+/HCN ratios. Two "GMC-points" fall within the distribution of the values from the HCN-peaks. These correspond to GMC 1 and GMC no1 and have similar results in the PDR-analysis as the HCN-peaks, i.e. optical extinctions of 7 and 10 mag and densities of 1×10^4 cm^{-3} and 3×10^4 cm^{-3}, respectively.

The optical extinctions in the sub-solar models lie in the range of 7–18 mag, which exceeds the range of optical extinctions found at GMC scale of 4–10 mag. The two clouds in GMC no3 with the highest best-fit optical extinctions are MC-D and MC-F, with $A_v = 12$ and $A_v = 18$ mag.

Further, in the above PDR-analysis is was found that the main agent of influence on the HCO^+/HCN ratio was the value of A_v, where lower HCO^+/HCN ratios yielded larger best fit optical extinctions. Here this trend is not very pronounced, higher optical extinctions are rather found for positions with a low HCO^+/HCN ratio only in combination with a high HCN/CO ratio (cf. MC-F and MC-B). This indicates that an increase in HCN emission with respect to HCO^+ as well as ^{12}CO is favored by larger densities and larger optically depths.

The best-fit values for the FUV-field strength are not strongly constrained and fill the sampled parameter range in their errors, similar to the results at GMC-scales in Section 9.2.

In comparison to the single-pointing analysis at 114 pc scale, the results for GMC 3 show on average larger uncertainties. The uncertainties can become as high as one order of magnitude. This suggests good fitting models within the Monte-Carlo analysis with densities as high as $7–9 \times 10^5$ cm^{-3} or as low as 1×10^3 cm^{-3} for the extreme cases of MC-A and MC-F. The large errors of the A_v and n_H values for some pointings in GMC no3 are probably due to the, sometimes, large errors on the line intensity ratios. These large errors are not least due to the primary correction and increase for clouds that are further away from the phase center. In particular, comparing Table 5.1 and Table 12.1, it can be found that the uncertainties in GMC no3 are on average higher than the ones deduced for the GMC pointings. This is especially due for the HCN/CO ratio where uncertainties between 0.3–1.4 are found for the HCN-peaks in GMC no3, in contrast to uncertainties in the range of 0.1–0.4 for the GMC pointings.

Nevertheless, on average a significant trend towards higher densities and larger optical extinctions is found for the clouds within GMC no3 in comparison to the results within the GMC sample, which might be an indication that the filling factor of denser and more opaque gas is larger at the lower resolution of the PdBI observations.

Chapter 13.

Summary

In the following, the major results from the investigation of GMC no3 at high resolution are summarized:

- The spatial extent of HCO$^+$ is found to be similar to that of ^{12}CO; however more clumpy. In contrast the HCN emission is more compact and confined to six condensations that are aligned in a "string" that follows the outline of the HCO$^+$ emission. These entities are not resolved with the 7″ resolution and HCN likely emerges from regions smaller than ~ 25 pc.

- From a qualitative comparison of high resolution observations of GMC no3, including dust, Hα, [C II], H I, and FUV emission as well as an optical image at 5300 Å, it is found that most likely recently a young star cluster (C 16 Bedin et al., 2005) has formed from the GMC and now shapes the physical and chemical processes within part of the cloud.

- For most of the identified HCN-peaks, HCO$^+$ exhibits lines that are well aligned in velocity with those of ^{12}CO and also similar in line-width. This indicated that HCO$^+$ emits significant radiation from similar volumes as ^{12}CO.

- The hyperfine structure of HCN is partly resolved and the individual components have two to four times smaller line-widths than ^{12}CO and HCO$^+$ in the range of $3.3 - 5\,\mathrm{km\,s^{-1}}$. This shows that HCN emission is likely confined to less turbulent and more quiescent gas than HCO$^+$ and ^{12}CO.

- No linear correlation between the total infrared luminosity and the luminosities of the HCN and HCO$^+$ lines is found. The lack of correlation is in contrast to the good correlation found for HCO$^+$ on GMC scales. Therefore a breakdown of this HCO$^+$-L_{TIR} relation is observed at higher resolution. This breakdown is most likely due to the high resolution that might separate the relevant feedback from newborn stars and the corresponding dense gas from which they have formed.

- The HCO$^+$/HCN ratio shows a significant variation within the giant molecular cloud and exhibits ratios from below 0.5 to higher than 1.75. The total ratio of GMC no3 is found to be 1.4. The variations of HCO$^+$/HCN indicate changes in abundance and/or excitation conditions throughout the GMC, which is also reflected in the results of the PDR analysis.

- The HCN/CO and HCO$^+$/CO ratios show a larger range than seen in the single pointings along the major axis of M 33 with the 30 m. The same holds for GMC observations with the 30 m in M 31 (Brouillet et al., 2005). This is most likely due to the different spatial resolutions of the observations that lead to relative changes in the beam filling factors of the diffuse and dense component. However, the variations of the dense gas fraction within GMC no3 are mainly due the higher dynamical range of the ^{12}CO intensities in comparison with those of HCN and HCO$^+$. Since the dense gas fraction as traced by HCN/CO continuously increases towards the young star cluster in the south of the GMC, it is suggested that the dense gas traced by HCN and HCO$^+$ can better resist the photo-ionizing radiation than the more diffuse gas traced by ^{12}CO. Therefore the filling factor of ^{12}CO relative to the filling factors of HCN and HCO$^+$ decreases which gives rise to larger dense gas fractions.

- A PDR analysis of the HCN-peaks yields higher densities in the range of 2×10^4–$7 \times 10^4 \mathrm{cm}^{-3}$ and also (partly) higher optical extinctions 7–18 mag than what is found within the sample of GMCs observed with the 30 m telescope. Lower HCO$^+$/HCN ratios in combination with higher HCN/CO ratios are found to yield higher, best-fit, optical extinctions.

Part IV.

Discussion, conclusion and outlook

Chapter 14.

Discussion

The major goal of this thesis is to add to the understanding of ^{12}CO, HCN and HCO$^+$ as molecular tracers of the diffuse and dense gas and their dependence on the physical and chemical conditions of their environment.

The observations and analysis presented in this thesis cover the spatial scales of giant molecular clouds (GMCs), i.e. ~ 115 pc (Part II), and of clouds within a GMC complex, i.e. ~ 25 pc (Part III). Henceforth, for the sake of brevity, the GMC sample observed with the 30 m will be referred to as "sample 1", while the sample of "clouds" identified within GMC no3 will be called "sample 2". The global HCO$^+$/HCN line intensity ratios in sample 1 are found to vary between 1.1 and 2.5, while they range from values below 0.5 to over 1.75 in sample 2. Variations in the HCO$^+$/HCN ratio are common on all size scales from entire galaxies down to small scales of a few parsecs within the Milky Way and the Large Magellanic Cloud (e.g. Chin et al., 1997; Christopher et al., 2005; Krips et al., 2008; Baan et al., 2008; Seale et al., 2012; Liu et al., 2013). The changes in the ratio indicate that the HCO$^+$ and HCN emission is affected differently by the various physical and/or chemical properties of the individual objects. This renders the simultaneous quantitative estimation of the dense gas content of the clouds from both lines complicated and a careful evaluation is necessary to not misinterpret the data (e.g. Meier & Turner, 2012). On the other hand these differences might yield powerful diagnostic tools to probe physical and chemical conditions in the dense interstellar medium.

To better understand the mutual alterations of HCN and HCO$^+$, below in Section 14.1 the most prominent influences onto the emission characteristics of both molecules (but also of ^{12}CO) are discussed and set into relation with the results from the analysis in Part II and Part III. Subsequently, a scenario for the conditions of the interstellar medium in the observed GMCs is constructed based on the HCN, HCO$^+$ and ^{12}CO observations and the PDR-analysis. The aim of this discussion is to better understand the emission from these molecules within different environments and to develop a good idea of the conditions of the dense interstellar medium in M 33. Subsequently, Section 14.2 discusses HCN and HCO$^+$ as tracers of dense gas related to star-formation and possible reasons for the under-luminosity of HCN in M 33 with respect to the total infrared luminosity. Finally, in Section 14.3 the possibility of X-ray dominated regions in M 33 and their influence onto the HCO$^+$ and HCN line emission is considered.

14.1. The HCN, HCO$^+$, and ^{12}CO emitting gas in M 33

This section compiles physical mechanisms that may alter the line emission of HCN and HCO$^+$ with respect to each other. In general, variations of line intensity ratios between two molecules can be categorized into such that are due to: different relative abundances, different excitation conditions, and/or differences in the relative volume filling factors. All three effects are interleaved by their simultaneous dependence on the numerous underlying physical parameters (metallicity, density, temperature, ...). This makes it difficult to isolate individual effects that cause a variation in the line intensity ratios. In the following Section 14.1.1 the isolated effects of the three possible reasons for variations in the line intensity ratio are shortly considered. In Section 14.1.2 a scenario for the molecular gas that gives rise to emission in HCN, HCO$^+$ and ^{12}CO is considered.

14.1.1. Influences onto the HCO$^+$/HCN line intensity ratio

Excitation conditions   The excitation conditions of molecules within molecular clouds are determined by the kinetic gas temperatures (T_{kin}) and the H$_2$ volume densities (n_H) if collisions dominate the excitation at a given positions inside the cloud. However, for a given physical condition the intrinsic parameters of a molecule determines its level of excitation. The critical density[1] of HCO$^+$ (1–0) ($n_{crit} = 3 \times 10^4 \, cm^{-3}$) is an order of magnitude lower than the one of HCN (1–0) ($n_{crit} = 2 \times 10^5 \, cm^{-3}$), and thus HCO$^+$ is easier to excite and thermalize than HCN[2]. The emission of HCO$^+$ will therefore be always stronger in gas of lower density ($n_H \leq 10^5 \, cm^{-3}$) if both molecules are confined to the same volume of gas and if their abundances are equal. In fact, even if it is less abundant than HCN, HCO$^+$ might be brighter. This has been shown in Section 8.5 calculating the HCO$^+$/HCN line intensity ratios with RADEX for different [HCO$^+$]/[HCN] abundance ratios, temperatures and densities. There it is found, for example, that at a density of $n_H = 7 \times 10^4 \, cm^{-3}$ an abundance ratio of [HCN]/[HCO$^+$]=4 is needed to render the line intensity unity. Therefore it is important to keep in mind that molecular line intensity ratios may not linearly reflect abundance differences.

For sample 1 it was found in Section 8.5, that it is unlikely that temperature variations govern the observed HCO$^+$/HCN ratios. This is because for a given abundance ratio, the HCO$^+$/HCN line intensity ratios derived from RADEX vary only within the measurement uncertainties (cf. Table 5.1) if the temperatures vary in the range of the measured dust-temperatures, i.e. 19 K–25 K. Further, substantial changes in the mean density likely do not to play a large role in defining the HCO$^+$/HCN line intensity ratio of the observed GMCs. This is because in general the line intensity ratio of HCO$^+$/HCN should decrease if the fraction of dense gas above the critical density of HCN increases. This should also be reflected in the HCN/CO ratios. In this picture

---

[1] Given here for temperatures of 20 K, collisions with H$_2$ and neglecting opacity effects, cf. Table 3.1.

[2] As a side-note: molecular emission lines do not necessarily trace only gas at densities larger than their critical density as their effective densities (n_{eff}), defined as the density that is needed to produce a line of 1 K, may be much lower (Evans, 1999). Even for gas at a temperature of 10 K Evans (1999) reports for HCO$^+$ that $n_{eff}(10K) = 2.4 \times 10^3 \, cm^{-3}$ and for HCN that $n_{eff}(10K) = 2.9 \times 10^4 \, cm^{-3}$. At higher temperatures the effective densities are lowered.

lower HCO⁺/HCN ratios should go in hand with higher HCN/CO ratios. The correlation coefficient between both quantities in sample 1 is not significant with $r = -0.27$ and therefore such a trend is not observed in M 33. This indicates that variations of the mean gas density do not govern the HCO⁺/HCN ratios (cf. Section 8.3 and Fig. 8.4).

For sample 2 it is difficult – with the data at hand – to decide whether excitation conditions control the HCO⁺/HCN ratio. Here, no information on the temperature is available because most available dust continuum maps have a lower resolution than the PdBI observations. Further, the line-of-argument used in the previous paragraph to reject changes in density as a major influence onto the line intensity ratio, can not be used. This is because on the small spatial scales of 25 pc changes in the ¹²CO filling factor are observed within GMC no3 which are not due to differences in density. Therefore, not only densities effects affect the HCN/CO line intensity ratio: As argued in Section 12.4, the ¹²CO-filling factor is diminished towards the south of the cloud with decreasing distance to a young star cluster that likely dissolves the more diffuse gas as traced by ¹²CO.

Note that the RADEX analysis in Section 8.5 and the best-fitting PDR models for the HCN (1–0) and HCO⁺ (1–0) observations (Chapter 9 and Section 12.5) find that these lines are optically thin. Therefore, optical depths effect do not play a role, here.[3]

Volume/Area Filling factor   A difference in area filling factor between the molecules has not been considered in the PDR models and the derivation of HCO⁺/HCN ratios from RADEX. It is however likely that differences in the spatial extent between HCN and HCO⁺ exist. This is because the critical density of a certain transition determines the "visible" extent of a cloud that is larger for lower critical densities (see e.g. Papadopoulos, 2007). Therefore it is expected that HCO⁺ emission traces a larger region than HCN, including also less dense gas (e.g. Baan et al., 2008). The PdBI observations of GMC no3 with a spatial scale of about 25pc (cf. e.g. Fig. 11.3) indeed show a picture which is consistent with this: HCN is less extended and resembles a string of compact "clouds", while HCO⁺ shows more extended diffuse emission in which similar compact condensations (in size and location) are embedded. Both molecules together fall within the outlines of the less dense gas of the GMC traced by ¹²CO (1–0) ($n_{crit} = 4 \times 10^2$ cm⁻³). This difference in area filling factor may result in a bias towards higher ratios of HCO⁺/HCN, because a larger beam filling factor increases the antenna temperature of a radio-telescope. This effect is visible in our observations when comparing the 30 m telescope pointing towards GMC no3 and the corresponding PdBI

---

[3]As a side-note: For most extragalactic sources HCO⁺ (1–0) and HCN (1–0) are expected to be optically thick (Papadopoulos, 2007; Greve et al., 2009). Under high optical depth the line intensity ratio between HCO⁺/HCN would no longer depend on the underlying column density of the molecules, but approach unity. However, for HCN and HCO⁺ it has been shown that for this reason the line emission is sensitive to the underlying abundances of the molecules, even if the gas is moderately optical thick (cf. Fig. 9 in Imanishi et al., 2007, and also Imanishi et al. (2006); Knudsen et al. (2007)). This is due to the in-homogeneity of the ISM, where multiple denser "clumps" are embedded in more diffuse gas. If the molecular emission of the dense clumps is optically thick, a lower or higher abundance of a molecule would move the surface – assuming a radial profile of the clouds – where the gas becomes optically thick ($\tau \sim 1$), inwards or outwards of the clump, increasing or decreasing the area filling factor of the emission from the dense gas (Imanishi et al., 2007; Solomon et al., 1987). A larger area filling factor in turn increases the observed flux of a line.
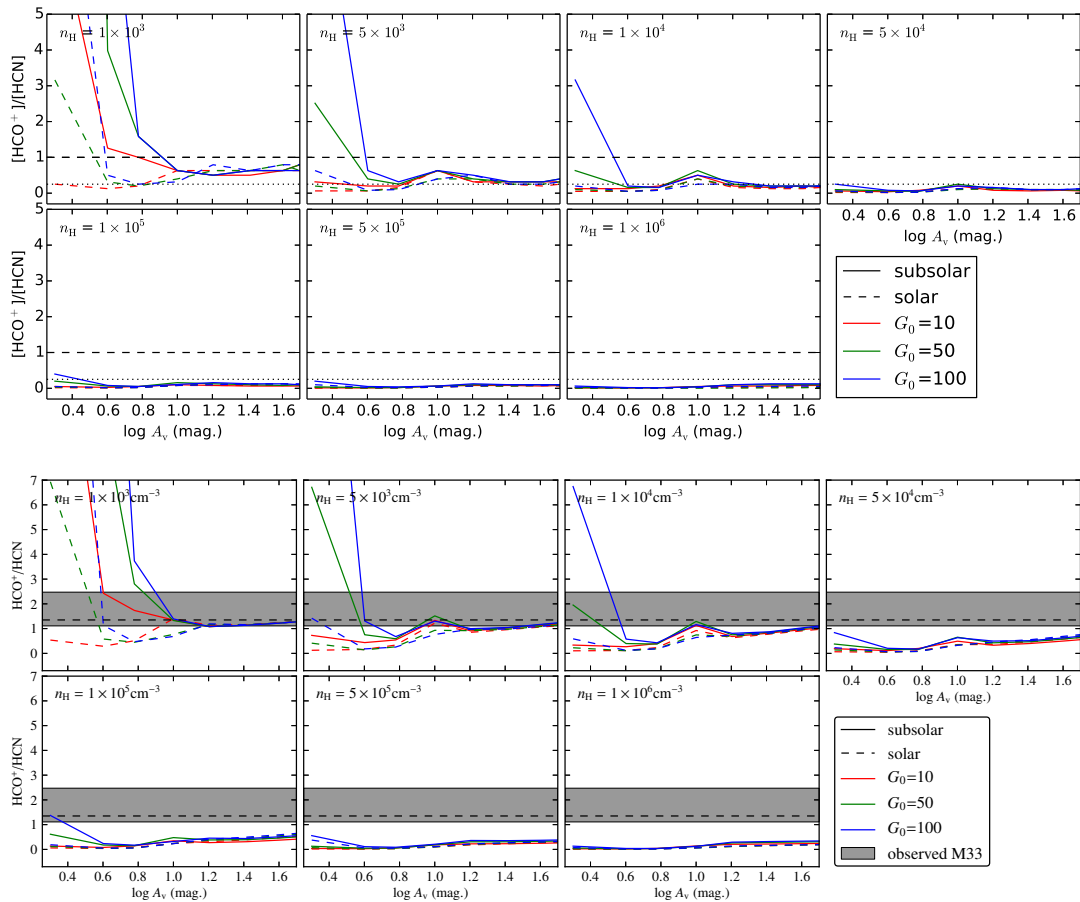
Figure 14.1.: PDR model [HCO$^+$]/[HCN] abundance ratios (*top*) and HCO$^+$/HCN line intensity ratios (*bottom*), for subsolar (*solid lines*) and solar metallicity (*dashed lines*). Different colors indicate different FUV field strengths $G_0 = 10$ (*red*), 50 (*green*), and 100 (*blue*). Every panel of a subfigure shows the results for one density; from *left to right* and *top to bottom* $n_H = 0.1, 0.5, 1, 5, 10, 50$, and $10^2 \times 10^4$ cm^{-3}. In the *top* figure the *dashed* and *dotted black* lines mark ratios of 1 and 0.25; the latter is the ratio found for [HCO$^+$]/[HCN] for the stacked spectrum. In the *bottom* figure the *dashed* horizontal lines show the values from the stacked spectra.

observations. A higher ratio is found in the single pointing. This is due to the larger extent of HCO$^+$ in comparison to HCN, which results in a larger relative are filling factor in the larger 30 m beam than in the 25 pc beam of the PdBI observations that are here evaluated at the HCN peaks.

Abundance differences in photon-dominated region chemistry   For the above reasons it is likely that the variations of HCN and HCO$^+$ in sample 1 are dominated by abundance differences and/or changes in the respective area filling factors, rather than by substantial changes in the mean excitation conditions between the GMCs. Therefore, details of the molecular formation processes and their dependence on cloud properties have a major influence on molecular line emission ratios. In the following the insight from the PDR-models is shortly re-considered.

Figure 14.1 reproduces the modeled [HCO$^+$]/[HCN] abundance ratios, shown in Fig. 9.2 and the modeled line intensity ratios shown in Fig. 9.3. From these figures it can be seen that for most models HCN is more abundant than HCO$^+$. In the solar-metallicity models, HCO$^+$ becomes only more abundant for the lowest modeled density and high FUV-field strengths (G_0=50 and G_0=100). For M 33-like metallicity, HCO$^+$ is more abundant than HCN at low densities $n_H \leq 1 \times 10^4$ cm^{-3}, and low optical extinctions $A_v \leq 4$ mag (edge-to-center)[4] if the FUV-field is strong enough. This shows on the one hand the stronger photodissociation of HCN at low optical extinctions and densities. On the other hand it reflects that HCO$^+$ is mainly destroyed in dissociative recombination reactions with electrons (Section 9.1.3). The sensitivity to the free-electron abundance of HCO$^+$ results in an increase of the [HCO$^+$]/[HCN] abundance ratios at lower metallicity, which is due to a lower abundance of carbon – the main source of free electrons. A further consequence of differences in electron abundance is the decrease of the [HCO$^+$]/[HCN] abundance ratio under higher densities that is partly due to an increase in the recombination rate of HCO$^+$ with electrons, but also due to differences in the chemical pathways at different densities. Note, that due to very high recombination rates HCO$^+$ might actually be depleted in very dense regions (e.g. Seaquist & Frayer, 2000).

The picture is similar for the HCO$^+$/HCN line intensity ratio. Due to the different critical densities of the two molecules, line intensity ratios larger than unity are possible even if the [HCO$^+$]/[HCN] abundance ratio is below unity. In general the line intensity ratio may become larger than unity for optical extinctions $A_v \leq 5$ mag (edge-to-center) up to densities of n_H=1 $\times 10^5$ cm^{-3}. A larger FUV-field strengths yields a larger HCO$^+$/HCN line intensity ratio. Also here, a lower metallicity results in higher HCO$^+$/HCN line intensity ratios.

The above could be summarized as follows: under PDR chemistry HCO$^+$/HCN line intensity ratios above unity – as they are found in sample 1 – are an indication of low mean densities ($n_H \leq 1 \times 10^4$ cm^{-3}) and relatively low mean optical extinctions ($A_v \leq 5$ mag) of the emitting medium. Further, the lower the FUV-field strength is, the lower the HCO$^+$/HCN line intensity ratio for a given density and optical extinction becomes.

Further influences onto the HCO$^+$/HCN line intensity ratios   In addition to the influences discussed above, the abundance and line-emission of HCO$^+$ as well as HCN is sensitive to: cosmic rays, alternative heating processes such as shocks, turbulent diffusion, and infrared pumping[5]. For the sake of completeness these mechanisms are shortly considered in Appendix A.1, although they were not particularly identified as an influence onto the line intensity ratios in the GMCs analyzed in this thesis.

If the chemistry diverges from the chemistry of photon-dominated regions, the abundance and excitation conditions of molecules will differ as well. Below, in Section 14.3, the possible influence of X-ray dominated regions within M 33 are discussed. The im-

---

[4]The reference values for optical extinctions are typically given from edge-to-center of the clouds. The values used in the model are however for a two-sided illuminated clouds, and thus the values in Fig. 14.1 as well as in Chapter 9 and Section 12.5 are given edge-to-edge.
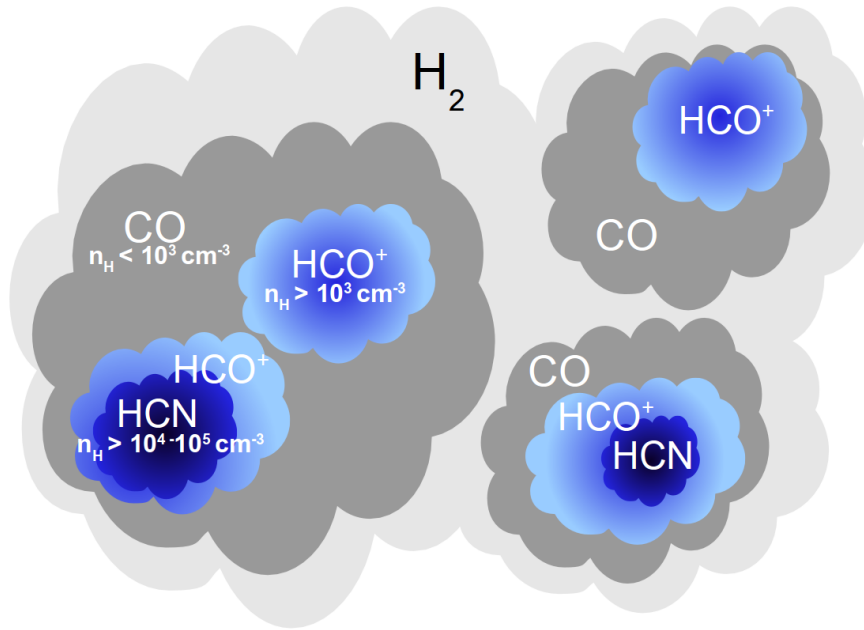
[5]This list is not exhaustive.

Figure 14.2.: Qualitative sketch of the HCN, HCO$^+$ and ^{12}CO emitting gas in the observations of M 33 based on the observations presented in this thesis. The molecules CO and HCO$^+$ that are emitting at lower densities are not exclusive from the respective higher density regions.

plications of a difference of higher gas-to-dust mass ratios – as observed for the GMCs (cf. Section 6.4.1) – are shortly considered in Section 14.1.3.

14.1.2. Scenario for the molecular gas in giant molecular clouds in M 33

For the GMCs of sample 1 the PDR-analysis (Chapter 9) yields best-fitting optical extinctions in the range of 2–5 mag from edge-to-center of the clouds (i.e. 4–10 edge-to-edge). These optical extinctions fall into the regime of translucent clouds, which are considered to be in the transition region between diffuse clouds ($A_v \leq 1$) and dense clouds ($A_v \geq 5$) (Burgh et al., 2010). In this range of optical extinctions the atomic-molecular transition zones are located, i.e. typically it is found that that the $C^+ \rightarrow C \rightarrow CO$ transition occurs at $A_v \sim 2$–4 (Hollenbach & Tielens, 1999). The resulting densities are moderate, i.e. 1×10^3–3×10^4 cm^{-3}.

However, the PDR-analysis assumes a homogeneous medium, instead of a more realistic in-homogeneous medium, where denser "clumps" are embedded in more diffuse gas. Therefore the determined quantities do not reflect the real physical conditions of the gas, but are mean quantities of the combined volume of gas that gives rise to the HCN, HCO$^+$, and ^{12}CO lines. One part of the emitting gas will therefore reside at larger, another at lower optical extinctions and densities. Considering the critical density of HCN and the insight from the PDR-analysis above, the bulk emission from this molecule likely emanates from the densest regions ($n_H \geq 1 \times 10^5$ cm^{-3}) within the 30 m beam; HCO$^+$ from somewhat less dense ($n_H \geq 1 \times 10^4$ cm^{-3}) or less opaque ($A_v \leq 5$ mag) gas. In contrast, ^{12}CO (1–0), with a much lower critical density, traces the diffuse molecular gas. For these reasons the determined values of A_v and n_H are
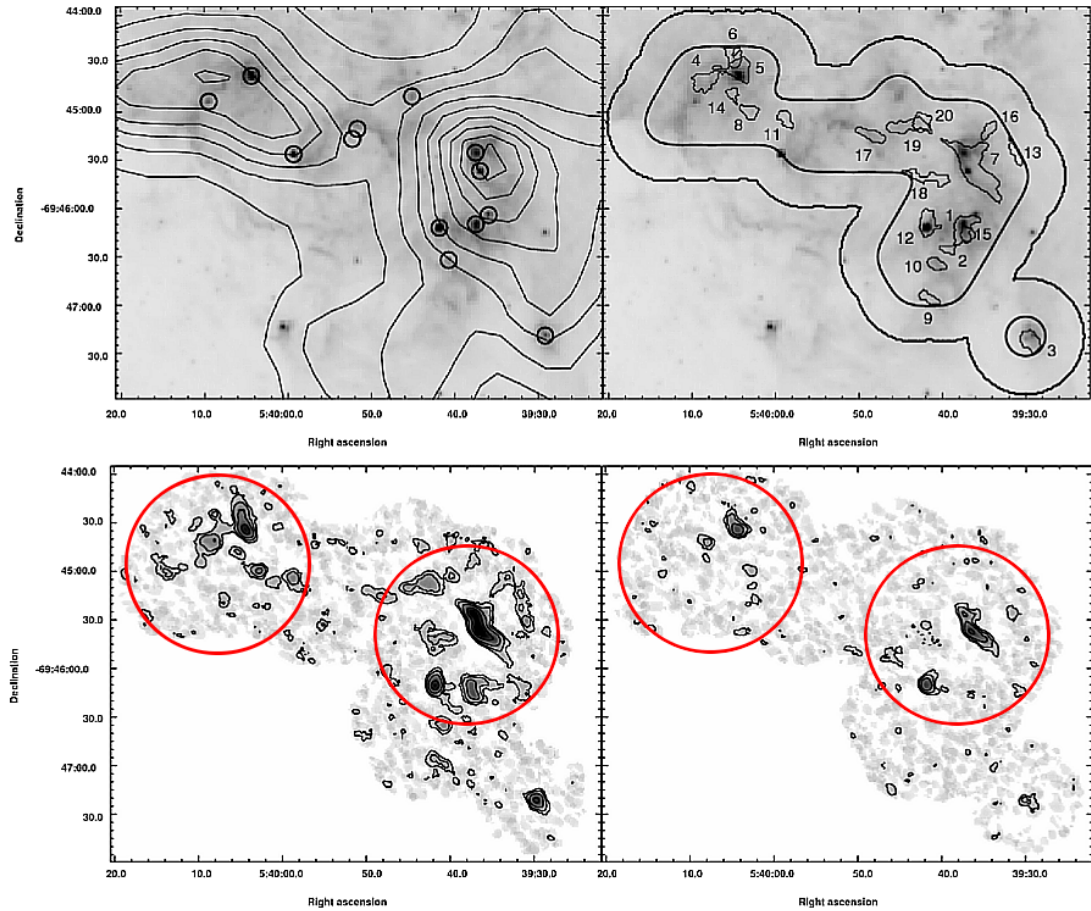
Figure 14.3.: Observation of N159 in the LMC Figure 3 in Seale et al. (2012). The *top left* panel shows a 5.8 μm *IRAC/Spitzer* image that is overlaid with contours of CO emission observed with the Mopra Telescope. *Small circles* mark young stellar objects. The *bottom left and right* panels shows Australia Telescope Compact Array (ATCA) HCO+ and HCN observations, respectively. The contours start at 2σ and are spaced by 2σ. (Seale et al., 2012). The *red circles* show the spatial resolution of the PdBI HCN and HCO+ observations in GMC no3 in this thesis. (Seale et al., 2012)

measures of the fraction of the gas (or the beam-filling factor) at high optical extinction and/or density.

Consequently, in the PdBI observations that resolve GMC no3, "clouds" of HCN and HCO+ with small filling factors are visible. These are embedded within weaker, more extended emission of HCO+, which in turn follows the outlines of the ^{12}CO emission. Concentrating the PDR-analysis on the HCN-peaks yields nearly exclusively higher densities in the range of 3×10^4–7×10^4 cm^{-3} as well as partly higher optical extinctions of up to A_v=9 mag (edge-to-center) in comparison to the results obtained in sample 1. This reflects the increase of the beam filling factors of the denser and more opaque regions within the smaller beam.

The compact HCN and HCO+ structures are unresolved in the 25 pc beam and therefore may contain substantial sub-structure. This is likely reflected by the striking difference of a factor 2–4 between the line widths of HCN and HCO+ in four out of six HCN-peaks in GMC no3 (cf. Section 12.1). For all positions HCN has a similar line-width of

3–$5\,\mathrm{km\,s^{-1}}$, while the HCO^+ line-widths are mostly larger and similar to that of ^{12}CO in the range of ~ 6–$10\,\mathrm{km\,s^{-1}}$. This indicates a higher turbulence in the HCO^+ and ^{12}CO emitting gas. If the molecular gas is sub-structured in individual clouds the difference in turbulence can be explained if only a part of the clouds have densities and optical extinctions large enough for HCN to become luminous ($n_H \gtrsim 1 \times 10^4$–$1 \times 10^5\,\mathrm{cm^{-3}}$, $A_v \gtrsim 4\,\mathrm{mag}$; cf. Section 14.1.1). The individual clouds will have a velocity dispersion in the giant molecular cloud and thus if HCN only emanates from a sub-set of the clouds it will have a smaller line-width than tracers that emit from a larger ensemble of clouds. In this scenario HCO^+ belongs to the latter. The similar line-widths of ^{12}CO and HCO^+ indicate that all clouds that emit in ^{12}CO also host regions that have densities large enough to emit strongly in HCO^+ but not in HCN. Therefore, from the results of the PDR-analysis summarized above such clouds fall in the range of densities of $n_H = 1 \times 10^3$–$1 \times 10^4\,\mathrm{cm^{-3}}$ and optical extinctions of $A_v = 1$–$5\,\mathrm{mag}$ [6]. Figure 14.2 shows a qualitative sketch of this scenario.

The above scenario is supported by observations of $HCN\,(1$–$0)$ and $HCO^+\,(1$–$0)$ in giant molecular clouds at a much higher spatial resolution of 1–$1.5\,\mathrm{pc}$ towards the star forming regions N 105, N 113, N 159, and N 44 in the Large Magellanic Cloud (LMC) by Seale et al. (2012). The metallicity of the LMC is only slightly lower than that of M 33, and is 0.3–0.5 of the solar value (Hunter et al., 2007)). It lies in a distance of $50\,\mathrm{kpc}$ (e.g. Macri et al., 2006) and thus is 16 times nearer to us than M 33. This allows to resolve individual clumps [7] within GMCs. Figure 14.3 shows the observations of N 159 by Seale et al. (2012). The red circles mark the beam-size for a spatial resolution of $25\,\mathrm{pc}$ as achieved within GMC no3 with the PdBI. From this figure it can be seen that only a few of the clumps that emit in HCO^+, are also visible in HCN. Furthermore, Seale et al. (2012) finds that for the individual clumps HCO^+ traces a larger region than HCN. Therefore they argue that the HCN emission is restricted to the higher density centers of the most dense clumps.

Conclusion   The PDR-analysis suggests that the observed GMCs are partly translucent clouds with optical extinctions of $A_v = 1$–$5\,\mathrm{mag}$. Of the three observed tracers of molecular gas, HCN is found to be a tracer of very dense gas ($n_H \gtrsim 1 \times 10^4$–$1 \times 10^5\,\mathrm{cm^{-3}}$) and opaque regions ($A_v \gtrsim 4\,\mathrm{mag}$). On the other hand, HCO^+ traces also somewhat less dense gas ($n_H \gtrsim 1 \times 10^3\,\mathrm{cm^{-3}}$) and also less opaque regions ($A_v > 1$). In contrast ^{12}CO traces the diffuse gas ($n_H \gtrsim 1 \times 10^2\,\mathrm{cm^{-3}}$). The smaller line width of HCN in comparison to that of HCO^+ and ^{12}CO, hints at substructure of unresolved regions within GMC no3. As a possible scenario it is proposed that only a part of the unresolved clouds have densities large enough to be bright in HCN, while HCO^+ and ^{12}CO are present in most of these clouds.

14.1.3. The role of the gas-to-dust mass ratio

In the Milky Way most molecular gas is found at optical extinctions of $A_v \le 8\,\mathrm{mag}$ (Hollenbach & Tielens, 1999). From the PDR analysis it is found that parts of the ^{12}CO

---

[6] This is not to say that HCO^+ does not emit at larger densities and optical extinctions, but under these conditions HCN should become visible as well.

[7] In the sense

emitting clouds are likely translucent with A_v=1–5 mag. However, the PDR analysis presented in this thesis did not incorporate differences in the dust-to-gas mass ratio (GDR) in the scope of a lower metallicity into the analysis. The gas-to-dust mass ratios are typically higher in low-metallicity galaxies due to a reduced dust content (e.g. Bolatto et al., 2008; Leroy et al., 2013). In Kramer et al. (2010) we found ratios between 120–200 averaged over galacto-centric rings of 2 kpc width (cf. also Chapter 6). In contrast, averaged over larger regions (Leroy et al., 2011) find gas-to-dust ratios of 140–160 in M 33. Nevertheless, in this thesis the gas-to-dust masses of the observed GMCs are found to be in the range of $\sim$ 170-290 (cf. Section 6.4.1), and are thus higher than those typically found in the Milky Way of $\sim$ 100-150 (e.g. Draine et al., 2007).

Higher gas-to-dust ratios would have a decisive influence on the PDR chemistry if accounted for in the models. Under higher gas-to-dust ratios, FUV-photons can penetrate deeper into the cloud due to less absorption by the dust. This would push the molecular transition zone C/CO to larger depths into the cloud[8]. This effect has been observed in translucent regions and is also used to explain low CO brightness in low metallicity systems (e.g. Bolatto et al., 1999; Leroy et al., 2009). This effect could be in favor of an increase in the HCO⁺/HCN abundance ratio[9] because the fraction of regions within clouds at high A_v is reduced where HCN in general, forms more efficiently than HCO⁺ as discussed above.

Further, a higher gas-to-dust ratio would have additional influences onto the clouds. For example the photoelectric heating rate (cf. Section 4.3.1) could decrease and thus also the gas temperature might be affected, which in turn controls the excitation of the molecules. Also, more free electrons might be present at larger depths into the cloud for two reasons: the lower shielding from photo-ionizing radiation as well as the lower abundance of polycyclic-hydrocarbon (PAH) that absorb a large amount of the free electrons (Tielens, 2005). Thus the rate of dissociative recombination reactions, but also the production of ions is influenced by the gas-to-dust mass ratio.

All together, predicting the effects of a higher dust-to-gas mass ratio onto the modeled HCO⁺/HCN and HCN/CO line ratios can only be speculative, due to the complexity of the chemical networks and physical conditions. To understand the true influence of a lowered metallicity (i.e. lower elemental abundance and larger gas-to-dust mass ratio) onto HCN and HCO⁺ abundances and emission, dedicated PDR-models that include variations in gas-to-dust mass ratio would be needed.

14.2. HCN and HCO⁺ as a tracer of star forming gas in M 33

Gas with a density of $\geq 10^5$ cm^{-3} is estimated to be the fuel for star formation (Krumholz & McKee, 2005). The HCN (1–0) line has a critical density that matches this density regime closely and is the molecule of choice in a variety of studies that investigate

---

[8]Note that if the H_2 is self shielding and dominates over shielding by dust as in the Milky Way the H$-$ > H_2 transition will not move further into the cloud. Thus the molecular cloud would not change its size for a lower GDR, but its ^{12}CO-emitting core will become smaller (Bolatto et al., 2008).

[9]Note that the HCO⁺/HCN observations e.g. in the LMC, which has a slightly lower metallicity than M 33, shows even higher ratios of up to 3.5 (cf. Fig. 8.3 Chin et al., 1997, 1998).

the star formation relation with the dense gas (e.g. Gao & Solomon, 2004a; Wu et al., 2005; Gao et al., 2007; Graciá-Carpio et al., 2008a; Wu et al., 2010; García-Burillo et al., 2012). A tight linear correlation between the star formation rate (SFR) – as traced by the total infrared luminosity (L_{TIR}) – and the HCN line luminosity (L'_{HCN}) was recently found in these studies (cf. Section 7.1). This correlation holds over several magnitudes in total infrared luminosity from individual massive star forming clumps in the Milky Way to entire galaxies including normal galaxies and (U-)LIRGs. The HCN emission of sample 1 has been found to be under-luminous with respect to this relation and also found not to be correlated with the total infrared luminosity. The values of $L_{\mathrm{TIR}}/L'_{\mathrm{HCN}}$ are found to be 1300–3500 $L_{\odot}$/K km s^{-1} pc^2. In comparison to the above studies this range of $L_{\mathrm{TIR}}/L'_{\mathrm{HCN}}$ values lies in the "(U-)LIRGs-regime"[10], while normal galaxies have $\sim 600\pm70\,L_{\odot}$/K km s^{-1} pc^2. Note, however that sample 1 is widely different from the objects for which the tight L_{TIR}–L'_{HCN} relation has been found – individual massive clumps in an early stage of star formation (Wu et al., 2010) and entire galaxies (e.g. García-Burillo et al., 2012) – in the sense that it is not assured that the giant molecular clouds in sample 1 host dense gas that is currently forming stars.

The following three scenarios might explain the "under-luminosity" of HCN in M 33:

1. **Sample of Evolved Clouds** Four of the clouds in sample 1 – GMCs no6, 1, 26 and no3 – have been classified as evolved clouds in a systematic ^{12}CO (2–1) survey of M 33 at 12″resolution (Gratier et al., 2012)[11] based on signs of exposed star formation, i.e. association with Hα and/or the FUV emission. If star-forming gas with densities of n_{H}=> 10^5 cm^{-3} is traced reliably by the HCN line intensity, the latter should decrease during the evolution of a star-forming giant molecular cloud. This is because the dense gas is depleted by the star formation and dispersed by the feedback of newly formed stars. Based on this argumentation the HCN/CO ratio is used as an evolutionary trace of starbursts in galaxies Baan et al. (2008, cf. also Chapter 8). In this sense the under-luminosity of HCN could be an artifact of the evolutionary stage of the clouds. The Hα emission that accompanies the evolved clouds shows that stars must have formed recently in the past 3–10 Myrs (cf. Chapter 7). Therefore, the clouds traced by HCN could be in a stage where the dense gas is already depleted, while the signposts of former star formation are still present. A similar effect has been discussed as an explanation, for the a high star formation efficiency observed for the low-metallicity dwarf galaxy IC 10 (Leroy et al., 2009).

2. **High Gas-to-dust mass ratio** Alternatively the under-luminosity of HCN in M 33 might be due to the higher gas-to-dust ratio of M 33, which might reduce the fraction of clouds at high optical extinctions (A_{v}). HCN is sensitive to photodissociation and only becomes sufficiently abundant in well shielded regions

---

[10]Note that the highest value reported in extragalactic observations is $\geq$ 3500 $L_{\odot}$/K km s^{-1} pc^2 found in the galaxies NGC 1614 and II Zw96, while the highest efficiency was observed in Galactic star forming cores $\sim 3900\,L_{\odot}$/K km s^{-1} pc^2 on much smaller scales.

[11]Gratier et al. (2012) classified the GMCs into three evolutionary stages of (A) clouds not associated with star formation (B) clouds with embedded star formation traced via 8 and 24 μmemission and (C) clouds that show exposed star formation in Hα and/or the FUV. About half the GMCs in M 33 where classified as type C.

of molecular clouds (cf. Section 14.1.1, see also Boger & Sternberg (2005)). The same argumentation is used to describe weak emission of CO in low metallicity systems (e.g. Bolatto et al., 2008). For CO this effect is exemplified by the study of Leroy et al. (2013) in a sample of about 30 nearby spiral galaxies observed at kpc scales. They show that in general low-mass, low-metallicity, late-type spiral galaxies exhibit higher star formation efficiencies of gas traced by ^{12}CO than larger spirals, if a constant X_{CO} conversion factor is used. They show that a variable X_{CO}-factor based on the gas-to-dust ratio of the galaxies can explain the strongest variations of star formation efficiency between the galaxies.

3. **High star formation efficiency** The L_{TIR}/L'_{HCN} is commonly interpreted as a tracer of the star formation efficiency of the dense gas (SFE$_{dense}$). In this sense the dense gas in M 33 as traced by HCN could be forming stars more efficiently in comparison to normal spiral galaxies. Without further investigation this possibility can not be excluded. A high SFE for the giant molecular clouds in M 33 as traced by ^{12}CO has been claimed before by e.g. Heyer et al. (2004); Gardan et al. (2007). Based on ^{12}CO observations, these studies find SFEs an order of magnitude larger than those of larger spirals (thus more-metal rich) in the local universe. However, these studies are based on standard $X_{CO} = 2 \times 10^{20}$ (K km s^{-1})$^{-1}$ cm^{-2} conversion factor. This might underestimate the true H$_2$ column densities in low metallicity environments (Leroy et al., 2013; Bolatto et al., 2008), as described in the previous item. However a high star formation efficiency of the dense gas does not explain the absence of a correlation between total infrared luminosity and L'_{HCN}. Thus this scenario is more unlikely than the first two to explain the characteristics of the HCN emission in M 33.

Correlation of HCO⁺ with total infrared luminosity In contrast to the lack of a correlation of HCN with total infrared luminosity a good correlation for HCO⁺ was observed (cf. Chapter 7). [12] In the following the correlation of HCO⁺ with total infrared luminosity in sample 1 is considered for the three scenarios above.

If scenario *(1)* applies, the correlation with HCO⁺ could be explained by the proposed scenario for the dense gas in M 33 above (cf. Section 14.1.2), in which only such clouds emit HCN radiation that are dense enough ($n_H \gtrsim 1 \times 10^5$ cm^{-3}). The same clouds would be the sites where stars form. HCO⁺, on the other hand, would additionally emanate from clouds at intermediary densities ($n_H \gtrsim 1 \times 10^3$ cm^{-3}), where the gas is not depleted by the star formation process, and thus the HCO⁺ emission might be less affected than HCN by the depletion. In this scenario the correlation of HCO⁺ with total infrared luminosity despite the fact that less dense clumps do not participate in the star-formation process, would hint at a correlation between "clumps" at high and intermediary density and/or a continuous density-spectrum of the clumps in GMCs.

If scenario *(2)* applies, the lower critical density and lower sensitivity to photoionization of HCO⁺ in comparison to HCN might explain why HCO⁺ is less affected by a lower shielding by dust from photo-ionizing radiation. Further, the abundance of

---

[12]Note that similar to the study of (Wu et al., 2010) using HCN, a correlation of thee HCO⁺ line with total infrared luminosity luminosity is found in a sample of galactic massive star forming clumps by (Ma et al., 2012).
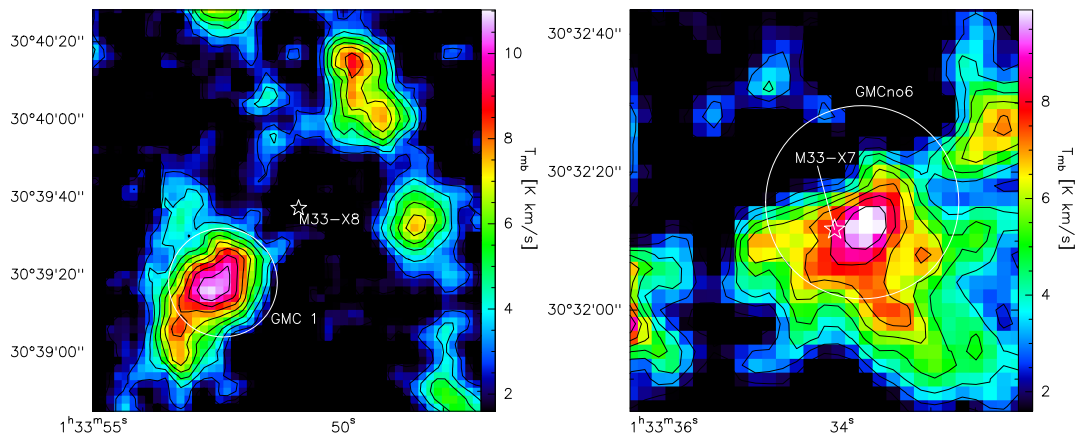
Figure 14.4.: Positions of the X-ray sources X8 and X7 in the vicinity of GMC 1 (*left*) and GMC no6 (*right*). The color scale shows ^{12}CO (2–1) emission. *Contours* start at the the $3\,\sigma$ level (i.e. $1.5\,\mathrm{K\,km\,s^{-1}}$) of the ^{12}CO (2–1) moment zero map and are spaced by $2\,\sigma$. *White circles* show the position and beam size, i.e. $114\,\mathrm{pc}$, of the 30 m observations.

HCO$^+$ is increased in the low-metallicity models (cf. Section 14.1) in contrast to HCN. For these reasons HCO$^+$ could prove to be a more robust tracer of dense gas related to star formation in low-metallicity systems.

As already said above, scenario *(3)* would only explain the lower HCN emission but not the a lack of a correlation between HCN and L_{TIR}. Therefore the correlation with HCO$^+$ should equally be unaffected.

In conclusion, further investigation is needed to decide which effect renders the HCN emission under-luminous in M 33. A larger sample of M 33-GMCs, that includes clouds at all evolutionary stages, would allow to find out whether HCN in our sample is under-luminous because of evolutionary effects. Further, the inclusion of a higher gas-to-dust mass ratio in the grid of PDR models would allow to quantify the implication onto emission of HCN and HCO$^+$. In general HCO$^+$ might prove to be a substitute for HCN as a molecular tracer of star-forming gas in low metallicity and/or evolved GMCs.

14.3. X-ray dominated regions in M 33

X-ray sources may create X-ray dominated regions (XDRs) in the interstellar gas in which the formation and destruction pathways of HCN and HCO$^+$ differs from that in photon-dominated regions. The atomic and molecular cross-sections are small at high energies [13]. Therefore, X-rays can penetrate deeper into clouds and affect the chemistry at larger depths than e.g. FUV photons. Also, in contrast to FUV photons, X-rays can ionize atoms with an ionization threshold above 13.6 eV like hydrogen, helium, oxygen and nitrogen. Further, X-rays can doubly ionize some species. (Stäuber et al., 2005).

From the XMM-Newton X-ray source-catalog from (Pietsch et al., 2004a) that contains 408 sources in the field of M 33 it has been found that GMC 1 and GMC no6 are

---

[13]For 1 keV photon the cross-section is $\sim 2.5 \times 10^{-22}\mathrm{cm}^{-2}$ and decreases with λ^3 (Stäuber et al., 2005).

situated close to the luminous X-ray sources M33-X8 and M33-X7, respectively. In Fig. 14.4 the constellation in both regions is shown.

M 33-X8 is the most powerful steady X-ray source in the local group with an X-ray luminosity of $\sim 2.2 \times 10^{39}$ erg s^{-1} (Weng et al., 2009, luminosity for a distance of 840 kpc). This source is classified as an ultra-luminous X-ray source (ULX)[14] and it is located 27″ away from the central 30 m pointing towards GMC no1. This corresponds to a spatial scale of about 110pc. The mean X-ray flux from M33-X8 averaged over the 28″ beam of the 30 m observation is $F_X = 2 \times 10^{-3}$ erg s^{-1} cm^{-2}. Therefore the energy input per hydrogen atom becomes $P = 2 \times 10^{-7}$ erg cm s^{-1}, if one assumes a mean density of the cloud of $n_H = 1 \times 10^4$ cm^{-3} as derived from the PDR analysis Section 9.2. From the analysis in Chapter 7 an indication for different physical and/or chemical processes in GMC 1 in comparison to the other observed GMCs in sample 1 has been found. Figure 7.3 shows the relation between the total infrared luminosity and the HCO$^+$/HCN line intensity ratio. Both quantities exhibit a significant linear correlation for all clouds, except GMC 1, which has a too low HCO$^+$/HCN line intensity ratio of 1.1 with respect to its total infrared luminosity in comparison to the other clouds.

The second X-ray source M 33-X7 is associated with GMC no6 and is an eclipsing X-ray binary with a luminosity of 5×10^7 cm^{-3}. Therefore it is less luminous than M33-X8 (Pietsch et al., 2004b). It is however situated within the observed GMC. Further, it is also the most massive X-ray binary known (Valsecchi et al., 2010) and associated with the dense O-B association HS-13 (Humphreys & Sandage, 1980). The mean X-ray flux averaged over the 28″ beam is $F_X = 0.13$ erg s^{-1} cm^{-2}. This energy input per hydrogen atom becomes $P = 2.2 \times 10^{-5}$ erg cm s^{-1} for a mean density of $n_H = 6 \times 10^3$ cm^{-3} as determined from the PDR analysis. Thus the energy input per hydrogen atom is 30 times larger than for the case of GMC 1 and M33-X8. However, unlike for GMC 1, no particular difference of GMC no6 has been observed with respect to the other clouds in the analysis. This cloud has with HCO$^+$/HCN=2.5 however the highest HCO$^+$/HCN line intensity ratio found within sample 1.

Models of XDRs by Meijerink & Spaans (2005); Meijerink et al. (2007) (see also Baan et al., 2008, for a summary) [15] predict for XDRs with an energy deposition rate per hydrogen nucleus of $P \sim 5 \times 10^{-6}$ erg cm s^{-1} and/or low Hydrogen column densities $N_H < 3.2 \times 10^{22}$ cm^{-2} that the [HCO$^+$]/[HCN] abundance ratios are below unity. For radiation fields that are stronger and yield $P \geq 5 \times 10^{-4}$ erg cm s^{-1} together with hydrogen column densities above $N_H = 3.2 \times 10^{22}$ cm^{-2} the models yield [HCO$^+$]/[HCN] abundance ratios above unity.

The hydrogen column densities derived from the H I- and ^{12}CO-data (cf. Table 5.2) data are similar for GMC 1 and GMC no6 and are about $N_H = 1.2 \times 10^{22}$ cm^{-2}. Both sources are below the hydrogen column density threshold of $N_H = 3.2 \times 10^{22}$ cm^{-2} of the Meijerink et al. (2007) models. Therefore both GMCs fall into the predicted regime in which HCO$^+$/HCN abundance ratios lower than unity are produced in the X-ray dominated regions. This is in contrast with the observed HCO$^+$/HCN ratios that lie

---

[14]Ultra-luminous X-ray sources are intermediate between X-ray binaries with luminosities $L_X \leq 10^{38}$ erg s^{-1} and Seyfert galaxies with $L_X \geq 10^{42-44}$ erg s^{-1} (Weng et al., 2009).

[15]Note that these models have been tailored for larger X-ray fluxes found in active galactic nuclei ($F_X = 1.6$–160 erg s^{-1} cm^{-2}), but have energy inputs per hydrogen atom in the range of 1×10^{-4} – $5 \times 10^{--6}$ similar to the ones derived for GMC 1 and GMC no6. The energy input per hydrogen atom defines the XDR structure.

at opposite sides of the observed range of line intensity ratios, i.e. $1.1 - 2.5$. However, both sources are also associated with Hα and 24 μm emission and have the highest star formation rates found in sample 1. Therefore, the chemistry in these clouds is most likely a mix of XDR- and PDR-chemistry. For this reason and because the Meijerink et al. models do not reflect the exact properties of the observed GMCs, a dedicated XDR (and PDR) modeling of the clouds is necessary to confirm the hypothesis that XDR chemistry alters the HCN and HCO$^+$ emission in these M 33 GMCs. Note that unfortunately the Meudon PDR code does not offer the option to account for X-rays.

Such a study would add to the on-going discussion whether the HCO$^+$/HCN line intensity ratio can be used as a probe if X-ray vs. photon-dominated regions (e.g. Kohno, 2005; Usero et al., 2004; Krips et al., 2008; Imanishi et al., 2007). The HCO$^+$/HCN line intensity ratio is discussed to be usable to distinguish (ultra-)luminous infrared galaxies ((U-)LIRGs) between such that host an AGN (HCO$^+$/HCN<1 – XDR) and such that are pure star-burst galaxies (HCO$^+$/HCN>1 – PDR)[16]. This use is however controversial, not least because XDR-models do not show such a clear cut picture (Meijerink & Spaans, 2005; Meijerink et al., 2007). Furthermore, observational results by Baan et al. (2008); Costagliola et al. (2011) challenge this interpretation.

14.4. Summary

In the following the main conclusions of this chapter are summarized:

- In general the line intensity ratio of HCO$^+$/HCN is not a linear tracer of the [HCO$^+$]/[HCN] abundance ratio due to the differences in critical densities of the molecules. [HCN]/[HCO$^+$] abundance ratios above unity are necessary to render the line intensity ratio unity if the gas densities are lower than the critical density of HCN.

- The differences in critical densities further results in the fact that HCO$^+$ might have systematically larger area/volume filling factors. A difference in area filling factor may result in a bias towards higher ratios of HCO$^+$/HCN because a larger beam filling factor increases the antenna temperature of a radio-telescope.

- Under PDR chemistry HCO$^+$/HCN line intensity ratios above unity are an indication of low mean densities ($n_{\mathrm{H}}=1 \times 10^3$–$1 \times 10^4$ cm^{-3}) and relatively low mean optical extinctions ($A_{\mathrm{v}} \leq 5$ mag) of the emitting medium. Further, the lower the FUV-field strength is, the lower the HCO$^+$/HCN line intensity ratio for a given density and optical extinction becomes. In photon-dominated regions a lower elemental abundance of carbon favors the formation of HCO$^+$ while HCN is depleted.

- Based on the fact that HCN has a two to four times lower line-widths than HCO$^+$ and ^{12}CO in the PdBI observations, a scenario is proposed in which the emission

---

[16]Using the HCO$^+$/HCN as a diagnostic tool for the type of chemistry in such sources is attractive as it would allow to distinguish (U-)LIRGs between pure starbursts and such that contain a "buried" AGN, i.e. one that does not produce a narrow line region due to a large central concentrations of dust.

within the 25 pc beam is clumpy. The smaller line-width of HCN is interpreted to indicate that only a sub-set of the unresolved clouds have a large enough density ($n_H \geq 1 \times 10^4$–1×10^5 cm^{-3}) to efficiently emit in HCN (1–0). In this scenario HCO$^+$ (1–0) emission however emanates also from clouds with lower densities and from a similar ensemble of clouds as ^{12}CO. This scenario is in accordance with findings for clumps within GMCs of the Large Magellanic Cloud at much higher resolution of 1–1.5 pc (Seale et al., 2012). There HCN is found to only emanate from the densest and most massive clumps. In HCO$^+$ also clumps with lower densities are detected.

- A higher than galactic gas-to-dust mass ratio has been observed for the GMCs in M 33 but not included in the PDR modeling. It is reckoned that a higher gas-to-dust mass ratio might have a decisive effect onto the line emission and formation of HCN and HCO$^+$ as it might reduce the fraction of the clouds at large optical extinctions.

- The under-luminosity of HCN with respect to the total infrared luminosity and to findings towards massive star-forming clumps in the Milky way as well as normal galaxies and (ultra-) luminous infrared galaxies might have several reasons:

  – The observed GMC sample consists largely of evolved clouds. In such systems a large part of the dense gas associated with star formation has likely been consumed and/or gas reservoirs are observed that do not form stars.

  – Alternatively the higher gas-to-dust ratios might decrease the fraction of the clouds at high A_v and thus HCN might be more readily photodissociated in M 33 than in systems with higher metallicities.

  – The dense gas might have a higher star formation efficiency. This possibility is however unlikely.

- GMC 1 and GMC no6 are found to be associated with the luminous X-ray sources M33-X8 ($L_X = 2.2 \times 10^{39}$ erg s^{-1}) and M33-X7 ($L_X = 5 \times 10^{37}$ erg s^{-1}), respectively (Pietsch et al., 2004b; Weng et al., 2009). GMC 1 shows a HCO$^+$/HCN intensity ratio of 1.1. This value is low in relation to its total infrared luminosity compared to the other sources in the sample and indicates different physical and/or chemical processes. It is argued that the influence of X-ray radiation from M33-X8 might drive the chemical processes away from the chemistry of photon-dominated regions to an X-ray dominated one. However, no models of X-ray dominated regions (XDR) are available to us that cover the observed properties of GMC 1 and GMC no6. A dedicated study of combined XDR and PDR models for these regions is pending to confirm the hypothesis of X-ray dominated regions in these sources.

Chapter 15.

Conclusions and Outlook

This thesis presents a study of the ground state transitions of HCN, HCO^+ and ^{12}CO – tracers of the dense and diffuse gas – in a sample of giant molecular clouds in the nearby galaxy M 33. These molecules have been observed towards seven giant molecular clouds along the major axis with the IRAM 30 m telescope at a spatial resolution of 115 pc ("sample 1"). Furthermore, high resolution maps of a single giant molecular cloud have been obtained with the IRAM Plateau de Bure Interferometer (PdBI). The maps have a spatial resolution of about 25 pc and a field-of-view of about 300 pc. The "clouds" identified within the PdBI maps are referred to as "sample 2" in the following. The analysis of the data was performed with the goal to better understand the emission characteristics of the observed molecules on the underlying physical parameters of their environment such as metallicity, optical extinction, density, far-ultraviolet field as well as the star formation rate. To this end two models of photon-dominated regions using the Meudon PDR code (Le Petit et al., 2006)) have been employed; one with a solar metallicity and the other with a lower metallicity tailored to reflect the conditions in M 33.

As stated in the Introduction (Chapter 1) to this thesis, several topical questions related to molecular emission in the field of star formation in galaxies have motivated this study. Below the main conclusion of this thesis are given categorized by the topics they address. An exhaustive summary of all key conclusions are presented at the end of the individual parts of the thesis and can be found in Chapters 10 and 13 and Section 14.4.

What are good tracers of the dense gas? The analysis in this thesis shows that the two observed tracers of dense gas, the ground state transitions of HCN and HCO^+, do not trace the same volumes of gas. Due to its lower critical density of $n_{crit} = 3 \times 10^4 \, cm^{-3}$, the $HCO^+ \, (1–0)$ transition might be stronger than the HCN (1–0) transition in gas with a volume density below the critical density of HCN (1–0) ($n_{crit} = 2 \times 10^5 \, cm^{-3}$). Therefore, the HCO^+/HCN line intensity ratio might become larger than unity even if HCO^+ is less abundant than HCN. The observations in this thesis show that the HCO^+/HCN line intensity ratios vary within a single giant molecular cloud (0.5–1.75) as well as between the GMCs of sample 1 (1.1–2.5). Thus, a significant variation of the ratio is found locally and globally along the major axis of M 33. The HCO^+/HCN line intensity ratios in GMCs of M 31 are found to be in the range of 0.5–1.5 (Brouillet et al., 2005) and thus on average lower than in the GMCs of sample 1. In comparison with GMCs in the Large Magellanic Cloud (LMC), where ratios up to 3.5 are observed (Chin et al., 1997, 1998), the HCO^+/HCN line intensity ratios of sample 1 are similar or lower.

In the high resolution observations with the PdBI with 25 pc spatial resolution a string of compact and unresolved structures of HCN and HCO$^+$ with small filling factors is found to be embedded in weaker, more extended emission of HCO$^+$. The emission of ^{12}CO envelopes the emission of HCN and HCO$^+$. The hyperfine structure of HCN is partly resolved and the line widths of the individual components – in the range of $3.3 - 5\,\mathrm{km\,s}^{-1}$ – are two to four times smaller than those of ^{12}CO and HCO$^+$. Therefore, the emission of HCN likely emerges from less turbulent gas than that of HCO$^+$. To explain this difference, it is proposed that an unresolved ensemble of clouds/clumps exists in the 25 pc beam of which only the densest clumps, with densities of $n_{\mathrm{H}} > 1 \times 10^4$–$1 \times 10^5\,\mathrm{cm}^{-3}$, emit in HCN (1–0)[1]. In this scenario, HCO$^+$ (1–0) emission would emanate from a larger ensemble of clouds that, in addition to the clouds seen in HCN, also includes clouds with lower densities and/or a lower optical extinction (see below). The similar line-widths of HCO$^+$ and ^{12}CO consequently show that both stem from a similar ensemble of clouds. In general emission lines trace the velocity dispersion of the emitting gas-clouds and thus the HCN lines, which emerge from fewer clouds than HCO$^+$ and ^{12}CO, would have a smaller line-width. This scenario is supported by observations of clumps within GMCs of the Large Magellanic Cloud by (Seale et al., 2012), where HCN is found to trace only the densest and most massive clumps, while HCO$^+$ is detected in a larger sample of clumps.

All together, in this thesis it is found from the observations and the PDR-analysis that the HCN (1–0) line emission is better suited as a tracer of dense gas with densities above $n_{\mathrm{H}} > 1 \times 10^5\,\mathrm{cm}^{-3}$ and/or optical extinctions of $A_{\mathrm{v}} > 5$ mag than HCO$^+$ (1–0). This is because of the presence of significant HCO$^+$ (1–0) emission also in less dense regions ($\geq 1 \times 10^3\,\mathrm{cm}^{-3}$) and/or regions with lower extinctions ($A_{\mathrm{v}} < 5$).

What are good molecular tracers of star formation in galaxies?   The HCN emission in the sample of GMCs is found not to be correlated with the total infrared luminosity. This is in contrast to the good correlation between HCN and the total infrared luminosity that is found to hold from galactic massive star forming clumps over normal galaxies to (ultra-) luminous infrared galaxies (e.g. Wu et al., 2010; García-Burillo et al., 2012). In comparison with the these findings HCN is particularly weak in M 33. The $L_{\mathrm{TIR}}/L'_{\mathrm{HCN}}$ luminosity ratios range between 1.3×10^3 and 3.5×10^3 $L_\odot/\mathrm{K\,km\,s^{-1}\,pc^2}$ and are situated at the very high end of ratios found in the Milky Way as well as in LIRGs/ULIRGs (Wu et al., 2010; García-Burillo et al., 2012). The gas-to-dust mass ratios of the observed giant molecular clouds are found to be in the range of 170–290 and thus higher than values of 100-150 typically found in the Milky Way (Draine et al., 2007). Here it is argued that the higher gas-to-dust mass ratio might account for the under-luminosity of HCN because it might reduce the fraction of the giant molecular clouds at high optical extinction, which is where HCN is efficiently produced and excited within photodissociation-regions. Alternatively, selection-effects for sample 1 might play a role because it includes mostly evolved giant molecular clouds (Gratier et al., 2012)[2]. These clouds might have consumed and dispersed a significant amount of the dense gas traced by HCN in recent star formation processes. Therefore, the present observations might include a considerable amount of gas traced in HCN that

---

[1] The range if densities given here is motivated by the results of the PDR-analysis.
[2] Defined as clouds that show exposed star formation in Hα and FUV.

is not currently associated with star formation. This is in contrast to the objects for which the HCN–L_{TIR} correlation is found – i.e. massive star forming clumps and entire galaxies (Wu et al., 2010; García-Burillo et al., 2012) – where inclusion of dense, star-forming gas is assured.

In contrast HCO$^+$ is found to be well correlated with the total infrared luminosity within sample 1. This is possibly due to the fact that it additionally traces regions with lower densities (1×10^3 cm^{-3}) and/or lower optical extinctions (A_v<5 mag) than HCN. Only gas with densities above 10^5 cm^{-3} is estimated to be the fuel for star formation (Krumholz & McKee, 2005). Therefore, a part of the gas reservoirs traced in HCO$^+$ might be less affected by the evolutionary stage of the GMCs. Further, from the PDR-analysis HCO$^+$ is found to be less sensitive to photo-ionization than HCN. It is reckoned that if the higher gas-to-dust ratios leads to a under-luminosity of HCN, the abundance of HCO$^+$ might be less affected by the consequently lower optical extinction of the clouds.

However, at a high spatial resolution of 25 pc, which resolves the observed GMCs in M 33, a break-down of the correlation of HCO$^+$ with the tracers of star formation (Hα, 24 μm, L_{TIR}) is found. This is attributed to a separation of the feedback of newborn stars and the corresponding dense gas from which they have formed.

All together these results show that HCN fails to be a direct tracer of star-forming gas in the low metallicity and/or evolved conditions of the observed sample of giant molecular clouds. However, under these conditions HCO$^+$ might prove to be a substitute for HCN as a molecular tracer of star-forming gas, when averaged over the size scales of GMCs. At smaller spatial scales, however, the relation between molecular tracers and tracers of star formation breaks down.

Which impact has metallicity on the molecular tracers? To get a handle on the influence of metallicity, models of photon-dominated regions using the Meudon PDR code (Le Petit et al., 2006; Gonzalez Garcia et al., 2008) have been employed. The models have been tailored to reflect the elemental abundances of a M 33 (Magrini et al., 2010) as well as the higher (solar) elemental abundances of the Orion nebula (Simón-Díaz & Stasińska, 2011). The models have been evaluated for a range of optical extinctions, volume densities, and far-ultraviolet radiation field strengths.

It was found that both metallicity-models are able to describe the observed range of HCO$^+$/HCN and HCN/CO line intensity ratios equally well for the clouds in sample 1 and 2. However, the input parameters are slightly different and higher densities are found for the sub-solar models. Nevertheless, differences in elemental abundances do not need to be invoked to explain the emission characteristics of HCN, HCO$^+$ and ^{12}CO in M 33. The observations of sample 1 are described by subsolar models with low optical extinctions of A_v=1–5 mag for the cloud centers as well as moderate densities of n_H< 3×10^4 cm^{-3}, with only little influence by the FUV field strength. For the resolved clouds within the PdBI observations nearly exclusively higher densities are found in the range of 3×10^4 cm^{-3}–7×10^4 cm^{-3}, and also (partly) higher optical extinctions 3–9 mag in the cloud centers. Note that although the measured HCN/CO and HCO$^+$/HCN ratios in sample 1 and 2 overlap, differences in best-fitting densities and optical extinctions exist. This is due to the fact that the parameter-space for both samples is different: sample 1 hosts largely low HCN/CO ratios in combination with

high HCO$^+$/HCN ratios, while sample 2 exhibits high HCN/CO ratios in combination with low HCO$^+$/HCN ratios.

Nevertheless, despite the fact that a lower metallicity is not needed to describe the observations, it is noted that a lower elemental abundance of carbon in the models favors the formation of HCO$^+$, while the HCN abundance is decreased. At the same time the total amount of ^{12}CO decreases linearly with a lower carbon abundance.

How do cloud parameters control the properties of molecule emission?   A variety of processes are discussed that lead to change in the intensities of HCN and HCO$^+$ as well as their line intensity ratio. The effects of variations of temperature and density onto the excitation conditions of HCO$^+$and HCN are studied with the statistical equilibrium radiative transfer code RADEX (van der Tak et al., 2007). Temperature estimates for the GMCs are obtained from the cold dust-component temperatures of the GMCs, which are in the range of 19–25 K. With RADEX it is found that for a given [HCO$^+$]/[HCN] abundance ratio this temperature range can not describe the observed variation of the HCO$^+$/HCN line intensity ratios between the GMCs. Also significant variations in mean density between the clouds are neglected as a major influence of the HCO$^+$/HCN line intensity ratios. This is because an increase of the fraction of dense gas above the critical density of HCN should be reflected by a decrease of the HCO$^+$/HCN line ratio, together with an increase of the HCN/CO line ratios. Thus, the two ratios should be anti-correlated, but this is not observed. Therefore, it is unlikely that changes in the mean excitation conditions between the GMCs dominate the mutual variations of HCN and HCO$^+$ in sample 1.

Further it is argued that because the critical density of HCN is an order of magnitude larger than the one of HCO$^+$, the latter might have systematically larger area/volume filling factors. A difference in area filling factor may result in a bias towards higher ratios of HCO$^+$/HCN because a larger beam filling factor increases the antenna temperature of a radio-telescope.

For the above reasons it is likely that the variations of HCN and HCO$^+$ in sample 1 are dominated by abundance differences and/or changes in the respective area filling factors. From the analysis of models of photon-dominated regions it was found that an HCO$^+$/HCN line intensity ratio above unity is an indication of a low mean gas density ($n_H \leq 1 \times 10^4$ cm^{-3}) and a relatively low mean optical extinction ($A_v \leq 5$ mag) of the emitting medium. Further, the lower the FUV-field strength is, the lower the HCO$^+$/HCN line intensity ratio for a given density and optical extinction becomes. This shows the sensitivity of HCN to photoionization. HCO$^+$ on the other hand reacts strongly to the free electron abundance, because – being an ion – it is readily destroyed by dissociative recombinations. Due to this reason HCO$^+$ might even be depleted in very dense regions due to higher recombination rates (e.g. Seaquist & Frayer, 2000).

The comparison of the measured HCN/CO and HCO$^+$/HCN line intensity ratios with those obtained from the PDR models shows that the optical extinction (A_v) has a major influence on the best-fitting models, while density, FUV-field strength and even metallicity play only minor roles. The best-fit optical extinctions are found to range between 2–5 mag (edge-to-center of the clouds). This falls into the regime of translucent clouds (Burgh et al., 2010). The optical extinctions that are found for molecular clouds in the Milky Way are typically higher with $A_v < 8$ mag (Hollenbach & Tielens,

1999). Here it is argued that this might reflect the relatively high gas-to-dust ratios of 170–290 measured for the observed GMCs.

Does the HCO⁺/HCN ratio indicate the prevalent type of chemistry (XDR/PDR)?

Two giant molecular clouds of the observed sample – GMC 1 and GMC no6 – are found to be associated with the luminous the X-ray sources M33-X8 and M33-X7. M33-X8 is the most luminous, steady X-ray source in the Local Group and has a luminosity of $\sim 2.2 \times 10^{39}$ erg s^{-1} (Weng et al., 2009). M33-X7 is the most massive X-ray binary known (Valsecchi et al., 2010) and exhibits a luminosity of $\sim 5 \times 10^{37}$ erg s^{-1}(e.g. Pietsch et al., 2004b). The energy input per hydrogen atom (P) averaged over the 28″ beam of the 30 m telescope is $P = 2 \times 10^{-7}$ erg cm s^{-1} and $P = 2.2 \times 10^{-5}$ erg cm s^{-1}, for GMC 1 and GMC no6. Both GMCs host a hydrogen column density of $N_{\mathrm{H}} = 1.2 \times 10^{22}$ cm^{-2} for which models of X-ray dominated regions from Meijerink & Spaans (2005) and Meijerink et al. (2007) predict [HCO⁺]/[HCN] abundance ratios below unity. However, the models do not resemble the properties of the GMCs well because they are tailored for the physical conditions present in active galactic nuclei. Nevertheless, an indication for different physical and/or chemical processes in GMC 1 in comparison to the other GMCs of sample 1 has been found. GMC 1 deviates from the otherwise good correlation between the total infrared luminosity and the HCO⁺/HCN line intensity ratio in the sample. Therefore, it is reckoned that the chemical processes in GMC no1 might be influenced by the X-ray emission. The additional affiliation of both clouds with Hα and 24 μm emission indicates that, if X-rays play a role, the chemistry in these clouds might be a mix of XDR- and PDR-chemistry. For this reason and because the Meijerink et al. models do not reflect the exact properties of the observed GMCs, a dedicated XDR (and PDR) modeling of the clouds is necessary to confirm the hypothesis that XDR chemistry alters the HCN and HCO⁺ emission in these GMCs of M 33. Such a study is particularly interesting in the light of the controversial use of the HCO⁺/HCN line intensity ratio as a distinctive tracer of X-ray dominated regions against PDR-regions (e.g. Kohno, 2005; Usero et al., 2004; Krips et al., 2008; Imanishi et al., 2007). If XDR chemistry plays a role in M 33, in the sources associated with M 33-X8 and M 33-X7 regions are observed where XDR (combined with PDR) chemistry produces both, a high (2.5, GMC no6) and a low (1.1, GMC 1) ratio of HCO⁺/HCN. Therefore, this ratio might prove to not be a robust tracer of X-ray dominated regions against PDR-regions.

Is the HCN/CO a tracer of the dense gas fraction? How does the interpretation change with the environment?

The line intensity ratios of HCN/CO and HCO⁺/CO are found to vary between $(0.4 - 2.9)\,\%$ and $(0.6 - 3.5)\,\%$, respectively, between the giant molecular clouds observed with the 30 m telescope. This range of ratios is slightly larger than in the spiral arms of M 31 (Brouillet et al., 2005, Fig. 8.1). One GMC of the sample (GMC 91) exhibits a particularly low HCN/CO ratio of 0.4 %, which is much lower than values found in the Galactic disk of $2.5\,\% \pm 0.6\,\%$ (Helfer & Blitz, 1997) or in normal galaxies with $4\,\% \pm 2\,\%$ (GS04a). Albeit a very massive cloud with a molecular gas mass of $M_{\mathrm{H_2}} = 88 \times 10^4 \mathrm{M}_\odot$, GMC 91 has a low star formation rate of 4 $\mathrm{M}_\odot$ Gyr^{-1} pc^{-2} in comparison to the other observed GMCs. This renders it a quiescent cloud which is consistent with a small dense gas fraction.

Furthermore, a lack of a correlation of the HCN/CO and HCO$^+$/CO line intensity ratios with the ^{12}CO intensity is found, which indicates that the fraction of the denser gas traced by HCN and HCO$^+$ does not depend on the total amount of molecular gas of a specific GMC as traced by ^{12}CO.

In the observations with the PdBI the HCN/CO and HCO$^+$/CO ratios show a range of 1.4–6.3% and 1.4–5.7% respectively. This range is somewhat larger than the one found for the GMCs in sample 1. The observed fraction of dense gas is higher in this sample probably because the dense gas covers a larger relative area in the smaller beam of 25 pc.

Within the resolved GMC, it is found that the dense gas fraction as traced by HCN/CO increases steadily towards a young star cluster situated in direct vicinity in the south of the observed GMC. This increase in the ratio is mainly due to a variation in the ^{12}CO flux, which shows a larger dynamical range within the observed GMC. Therefore, it is suggested that the dense gas traced by HCN and HCO$^+$ can better resist the photo-ionizing radiation than the more diffuse gas traced by ^{12}CO. This shows that evolutionary processes effect the observed dense gas fraction.

15.1. Outlook

> Science never solves a problem without creating ten more.
>
> *(George Bernard Shaw)*

The analysis in this thesis has shown that some properties of the observed line emission of HCN, HCO$^+$ and ^{12}CO can not be fully understood without further investigation. In particular the observed under-luminous HCN emission might be due to different scenarios that can not be distinguished in the present state of the analysis. Further, the influence of X-ray emission on the emitting gas in the sources GMC no6 and GMC 1 has to be quantified to be able to confirm or neglect the presence of X-ray dominated regions. In the following ways to refine and extend the presented work in this thesis are shortly considered.

The very first step for future work is to complete the analysis of the PdBI observations of GMC no3 because the results presented in this thesis are but a first insight. First a revision of the short-spacing data of HCN and HCO$^+$ is planned. In the present state this data could not be fully exploited due to severe baseline-problems in the vertical polarization. Further, here only the integrated spectra at the position of the HCN-peaks have been investigated. However, a pixel-to-pixel comparison of the HCN, HCO$^+$ and ^{12}CO maps with high-resolution ($<7''$) complementary data – i.e. 24 µm, 100 µm, Hα, [C II] H I and FUV emission – allows to quantify the mutual correlation of the tracers in different regions of the cloud and will form part of the further exploitation of the data.

The suspicion has been raised that the higher gas-to-dust mass ratio – that is not taken into account in the PDR modeling – might be responsible for the under-luminous HCN emission found for the GMCs in M 33 in this work. Building upon the foundation of the existing PDR analysis, variations of the gas-to-dust ratio can be incorporated into

the PDR model grid. So far only the lower elemental abundance of a lower metallicity has been exploited. The extended grid would therefore better reflect the conditions of dense molecular gas in low-metallicity systems. In particular such a grid can be used to quantify the effects of a higher gas-to-dust mass ratio onto the molecular tracers and to decide if the same is a cause for under-luminous HCN emission with relation to the L_{TIR}–L'_{HCN} relation of Gao et al. (2007); Wu et al. (2010).

Another possible reason for the under-luminous HCN emission is the fact that the sample of GMCs consists of largely evolved clouds, where probably a significant amount of dense gas has been consumed during the star-formation process. Therefore, it would be desirable to observe a larger sample that includes clouds at different evolutionary stages. With a larger sample it can be studied whether the evolutionary stage of the clouds has an impact on the emission of HCN. Together with the extended PDR-grid it would be possible to find out which of the proposed scenarios leads to the under-luminous HCN emission in M 33. Further, the larger sample would enable us to probe the possible use of HCN and HCO$^+$ in combination with ^{12}CO as a tracer of the evolutionary stage of individual giant molecular clouds.

The PDR-models in the current state of analysis are compared with only two line ratios. To be able to better constrain the models it would be beneficial to include further lines. Although ^{13}CO has been observed in all GMCs, no use could be made of this information. This is because at the time of the generation of the PDR-model grid the Meudon PDR code (v. 1.4.2) did not include the isotopologues of CO into the radiative transfer calculations. In newer versions they are included and therefore ^{13}CO is readily available to refine the PDR-analysis.

Obviously, further line observation of dense gas tracers would be beneficial. However, this work has shown that, for example, HNC is very weak in the GMCs of M 33. This molecule has only been detected in the stacked spectrum. Therefore, the intent to detect its emission would be very time consuming. Note that the observations of HCN, HCO$^+$, ^{12}CO and ^{13}CO in the seven GMCs at the 30 m telescope add up to 109 hours of telescope time and another 64 hours were needed for the PdBI maps. In both HNC has not been detected in the individual spectra. Nevertheless, another promising tracer of dense gas could be CN. The CN (1–0) hyperfine transitions fell into the frequency range of the ^{12}CO and ^{13}CO observations with the 30 m telescope presented in this thesis. However, they have not been detected at a $3\,\sigma$ level of ~ 5 mK in the stacked spectrum (cf. Fig. 5.4b). The rms-level of the ^{12}CO and ^{13}CO stacked spectrum is however still about five times larger than that of the individual HCN and HCO$^+$ observations. CN has a critical density that is a factor of 5 lower than HCN and thus intermediary between HCO$^+$ and HCN (Aalto et al., 2002). The HCN/CN ratio shows significant variations in galaxies and a decrease with increasing total infrared luminosity is observed (Aalto, 2004). This would render CN an interesting additional tracer of physical conditions to add to the existing data set. Further, higher transitions of ^{12}CO with critical densities close to the one of HCN could be added to the line inventory; for example ^{12}CO (3–2) with a critical density of $\gtrsim 10^5$.

In general ALMA or Noema (the future extended PdBI) are an option to observe dense gas tracing lines with low intensities, due to their large collecting surface and the increase of the beam filling factors of line emission when observed at higher resolution.

Observation of higher transitions of the observed molecules would be necessary to quantify the actual densities and excitation temperatures in the medium that gives rise to the emission of the molecules. This information would also help to construct a more realistic PDR-model of the emitting regions that involves PDRs with different densities and different filling factors. However, sub-thermal excitation of HCN and HCO^+ is common in extragalactic observations of HCN and HCO^+ as has been shown via higher transitions (4–3 and 3–2) in a variety of galaxies including M82, Mrk231, NGC4945, NGC6240 and NGC253 (Seaquist & Frayer, 2000; Papadopoulos, 2007; Wang et al., 2004; Greve et al., 2009; Knudsen et al., 2007, ; see the latter for a compilation). Partly these objects host strong starburst and are on average more energetic environments than M 33. HCN and HCO^+ might therefore be also sub-thermally excited in M 33. In this case the higher transitions would yield even lower main beam brightness temperatures than the ground transition with the due demands on telescope time. However, to test whether it is feasible to detect the HCN (3–2) and HCO^+ (3–2) transitions GMC 1 should be targeted. It has two to three times larger HCN and HCO^+ intensities than the other clouds and is found to host the most energetic environment of the observed clouds in this thesis.

Finally, indications of local X-ray dominated regions in M 33 call for further investigation. To this end models of X-ray dominated regions might be exploited to quantify the impact of the X-ray sources M 33-X8 and M 33-X7 on the surrounding material. However, the models should also account for the far-ultraviolet radiation field that is estimated to be strong in GMC no6 and GMC 1 – the GMCs in the vicinity of M 33-X8 and M 33-X7. Until now the extragalactic studies of HCN and HCO^+ in X-ray dominated regions have been restricted to observations in active galactic nuclei (e.g. Kohno, 2005; Usero et al., 2004; Krips et al., 2008; Imanishi et al., 2007). If GMC no6 and GMC 1 prove to indeed host X-ray dominated regions, this would allow extend the investigation of the impact of X-ray emission onto the abundance and emission of HCN and HCO^+ to less extreme environments and lower X-ray fluxes.

Part V.

Appendix

Appendix A.

Side-tracks

A.1. Additional influences onto HCO$^+$ and HCN

Further mechanism exist that influence the line intensities of HCO$^+$ and HCN that have not been discussed above in Chapter 14 and which are (partly) not accounted for in the used Meudon PDR-models. Here they are listed for the sake of completeness.

Cosmic ray ionization   Shocks from supernova remnants are seen to increase HCO$^+$ with respect to CO through an increase of cosmic rays which may yield a higher ionization degree of the medium an thus an increase of formation of HCO$^+$ (Elitzur, 1983). However, this effect depends on the density of the clouds because HCO$^+$ may react sensitive to high densities, where possibility of recombination with electrons becomes higher. Therefore, cosmic rays may enhance the HCO$^+$ abundance in lower density regions and at high densities may lead to a decrease of the HCO$^+$ abundance (Seaquist & Frayer, 2000; Baan et al., 2008). Shocks further can heat the gas which might lead to an increase of the HCN abundance via an effect that is discussed in the next section. Note, that a cosmic ray ionization is included in the PDR models of the Meudon PDR code used in this thesis and the cosmic ray flux was fixed to $\xi = 5 \times 10^{-17} \mathrm{s}^{-1}$.

Alternative heating processes   Under high temperatures in the range of 100-200 K, the activation barrier of the reaction HNC + H $\rightarrow$ HCN + H can be overcome. This reaction transforms HNC into HCN and thus increases the HCN abundance. Gas with such high temperatures is typically related to shocks[1]. Radiative heating alone is unable to produce the temperatures needed. Therefore Loenen et al. (2008) discusses the possibility of additional mechanical heating, which may come from supernovae and/or outflows of young stellar objects. These authors argue that high galactic supernova rates of $1/10\,\mathrm{yr}^{-1}$ are needed such the gas is sufficiently heated over large scales. The supernova rate estimated for M 33 by Tammann et al. (1994) is much lower: $1/147\,\mathrm{yr}^{-1}$. Therefore, it is unlikely that mechanical heating from SNe strongly affects the ISM and the HNC/HCN ratio in M 33. Young stellar objects are unlikely to play a significant role in mechanical heating on large scales. This is because the majority of PDRs and stars would have to be at a similar evolutionary stage, which is unlikely (Loenen et al., 2008).

---

[1]Note that the imprint of a shock onto the gas chemistry can actually persists a long time of up to 10^5 yrs after it has passed (Schilke et al., 1992).

Infrared Pumping   In particular sources, infrared pumping can have an influence onto the line emission of both, HCN and HCO$^+$, via photo-pumping of their vibrational lines at 14 μm and 12 μm, respectively (Aalto et al., 1995). Guélin et al. (2007) discusses that this effect however would affect both molecules in a similar way due to the close lying wavelength of the vibrational transitions. Thus, it is improbable that this effect leads to variations of the HCN to HCO$^+$ ratio.

Turbulent diffusion   Turbulence might allow the diffusion of the ion- and electron-rich outer layers of molecular clouds inward of the clouds. This might suppress the HCO$^+$ formation at larger depth into the cloud by almost 2 orders of magnitude (Xie et al., 1995).

A.2. Implications of the high HCN/HNC ratio

HNC remains undetected in M 33 in the individual 30 m telescope spectra. The detection in the stacked spectrum of all sources yields a global HCN/HNC line intensity ratio of 5.9. This ratio is higher than what is observed in many galactic and extra-galactic observations as discussed in Section 8.2. Similarly the abundance ratio of [HCN]/[HNC], derived in the LTE analysis (Section 5.4), is with ∼ 19 also very high as a compilation of HCN/HNC abundance ratios in (Baan et al., 2008) shows: quiescent and cold gas, as for example is present in infrared dark clouds, has low ratios ≲ 0.3 (Liu et al., 2013; Churchwell et al., 1984), warmer gas in GMCs gives higher ratios in the range of 2–5 as found by (Irvine, 1987) while in the center of the Orion Hot core high values between 5–76 are found (Schilke et al., 1992).

Both molecules have similar Einstein A as well as collision coefficients (which results in a similar critical density cf. Eq. (3.18)) and their upper energy states as well as frequencies do not differ much. Therefore, the HCN/HNC ratio should be rather insensitive to changes in excitation (Meier & Turner, 2012). Depending on the conditions in the clouds both molecules have different formation pathways. If only neutral-neutral reactions are considered, the canonical ratio of the HCN/HNC abundance ratio would be ∼ 1.1 (Baan et al., 2008). In an ionized medium, such as present in PDRs, the dissociative recombination of HCNH$^+$ forms both molecules at an equal rate. Therefore in regions where these two pathways are dominant, abundance and line intensity ratios[2] close to unity are expected.

One chemical pathway that may produce HCN/HNC abundance (and thus line intensity ratios) that are larger than unity, occurs in translucent PDR-like gas. In this regime HCN is able to form via the reaction N + CH$_2$ → HCN + H that solely forms HCN (cf. alsoTable 9.2 Turner et al., 1997; Meier & Turner, 2012). Due to this additional formation-pathway HCN can become more abundant than HNC. As discussed in Section 14.1.2 on average the giant molecular clouds are likely translucent over large scales, which might be the reason for the high HCN/HNC ratio. However, it is argued that the clouds might be on average translucent due to a lower metallicity with a higher

---

[2]Note that due to the hfs-splitting of HCN in contrast to HNC, a carefull evaluation of the excitation conditions and optical depths are needed, as they may have a different effects on the conversion between line intensity and abundance in both molecules (Turner et al., 1997).

gas-to-dust mass ratio. For this reason one might suspect that other low-metallicity systems yield similar high HCN/HNC ratios. This is however in contrast to the values found in the Large Magellanic Cloud, with a similar metallicity to M 33, that are no higher than 3.6 and comparable to those found in Galactic GMCs (Chin et al., 1998; Heikkilä et al., 1999) as discussed in Section 8.1.

Another formation pathway, that might unbalance the [HCN]/[HNC] abundance ratios is HNC + H $\longrightarrow$ HCN + H and can only occurs under high temperatures of 100-200 K (Schilke et al., 1992; Loenen et al., 2008). This has been already discussed in Appendix A.1, where it is found that it is unlikely to play a large role in M 33.

Appendix B.

Observing techniques

The aim of any astronomical observation is to measure a source as accurately as possible. This holds for single pointed observations with the aim to obtain the intensity and velocity of a source as well as imaging observations with the goal to measure the brightness distribution of the emission. However, all observations are restricted and altered by the telescopes itself. A thorough understanding of the relationship between the original brightness distribution and the telescope response is mandatory to successfully build and operate telescopes and to understand and interpret the data they produce.

The molecular lines that have been analyzed in this thesis have been observed with the two IRAM observatories the 30 m single dish and the Plateau de Bure Interferometer (PdBI) which are introduced in Appendix B.1. To understand radio interferometry, clearly one has to understand also the functioning of a single dish telescope. However, a thorough discussion of the basics of single dish telescopes and observation is neglected here, for sake of brevity. In Appendix B.2 only the concepts of the brightness temperature and antenna pattern are introduced, which are needed for the later discussion of the basic principles of interferometric observations in Appendix B.3.

B.1. IRAM observatories

The HCN and HCO$^+$ data of M 33, that has been obtained for this thesis, was taken with the two radioastronomical observatories operated by the "Institut de Radioastronomie

(a) PdBI   **(b)** 30m

Figure B.1.: a) Plateau de Bure Interferometer in the French alps. (© Rebus) **b)** 30m telescope located in the Sierra Nevada in Spain.

Millimétrique" (IRAM). The two telescopes are the 30 m Single-Dish telescope[1] in the Sierra Nevada near Granada, Spain and the Plateau de Bure Interferometer (PdBI) in the French Alps; both are shown in Fig. B.1.

B.1.1. PdBI Interferometer

The IRAM PdBI is located ~ 100 km from Grenoble in the french Alps at Plateau de Bure in 2560 m altitude. In its current configuration it consists of six 15 m antennas with a surface accuracy of 35-50 μm. It has two correlators. One is the 2×1 GHz wide-band correlator WideX with a fixed resolution of with 2 MHz. The second, the narrow-band correlator, is more flexible but can only handle bandwidths between 20-320 MHz, however, at higher resolutions 0.039–2.5 MHz. The heterodyne receivers of the PdBI work in the 3, 2, 1.3, 0.9 mm atmospheric windows.

B.1.2. 30 m telescope

The IRAM 30 m is a single-dish telescope with a diameter of 30 m and is located near Granada in Spain in the Sierra Nevada at 2850 m altitude. Currently it has two heterodyne receivers: the "Eight Mixer Receiver" (EMIR) and the "Heterodyne Receiver Array" (HERA). EMIR has four bands with an instantaneous bandwidth of 16 GHz in two polarizations that cover the 3, 2, 1 and 0.9 mm atmospheric windows. HERA consists of nine receivers arranged in a square and operates in the 1 mm window with a bandwidth of 500 Mhz. HERA is thus optimized for mapping purposes. Three different backends are available: one Fast Fourier transform spectrometer that is able to cover 32 GHz simultaneously at 200 kHz frequency resolution or 8 GHz at 50 kHz frequency resolution; one autocorrelator (WILMA) with 16 GHz bandwidth and 2 MHz resolution; and VESPA, a versatile autocorrelator with less bandwidth (10-512 MHz) but high frequency resolution of up to 3.3 kHz depending on the configuration.

B.2. A glimpse of single-dish radio astronomy

In radio-astronomy it is common to express the observed intensities in form of a temperature T_B called brightness temperature. T_B is defined as the temperature of a virtual Blackbody $B_\nu(T_\mathrm{B})$[2] that has the same intensity I_ν as the one that is measured with the telescope. The definition of T_B uses the Rayleigh-Jeans Approximation of the Planck Function:

$$B_\nu(T_B) = \frac{2h\nu^3}{c^2}\left(\exp\left(\frac{h\nu}{kT_B}\right) - 1\right) \approx \frac{2\nu^3}{c^2}kT_B \text{for } h\nu \ll kT_B \tag{B.1}$$

Hence,

$$T_B = \frac{c^2}{2k\nu^2}I_\nu. \tag{B.2}$$

---

[1]hereafter simply the "30 m"
[2]Described by the Planck function.

where c the speed of light, k the Boltzmann constant and ν the frequency of the emission.

The angular extent from that a radio-telescopes is able to receive radiation is called antenna pattern. Parabolic radio-telescopes are build such that they have a high directivity. In other words the region from which emission can be received is made as narrow as possible. A true pencil beam, one that has no angular extend is, however, is not achievable. Further, the beam-size depends on the observed frequency. The beam-shape of a circular aperture like that of a single dish telescope is a sinc function. This gives rise to more or less high side- and back-lobes, which can be somewhat lowered by tapering the illumination of the dish trough feed horns. The main-beam has a Gaussian shape which defines the resolution of a telescope via its the Full Width Half Maximum (FWHM).

The temperature that one measures directly with a radio telescope, however, is not the brightness temperature (T_B) but the Antenna Temperature (T_A). The latter also includes the signal of the source reduced by atmospheric absorption and telescope efficiencies. T_A is therefore lower than T_B. To account for this another temperature is in use which is called the main beam temperature (T_{mb}), being the fraction of all power that is received by the main beam of the telescope:

$$T_{mb} = \frac{F_{eff}}{B_{eff}} T_A^*.$$
(B.3)

B.3. Interferometric principles

This section aims to sketch out the basic principles of an imaging interferometer. It is meant to provide a very basic understanding of such an instrument and the basic nomenclature needed to discuss the PdBI observations presented in Part III. Obviously, a detailed discussions of all aspects of interferometry and a thorough development of their theoretical foundation is not subject of this thesis. The important topics of calibration, observation modes as well as technical details of the receiver, correlator and antenna systems are therefore altogether neglected. Good references for a in-depth introduction to all of these topics are Wilson et al. (2009); Thompson et al. (1986) and especially the lecture notes from Klein (2006), all of which serve as general references for this chapter. A further valuable source of information, which is also used in this chapter, are the online available lectures from the 7th interferometry School at IRAM, Grenoble[3] that amongst others, shed light on the more technical details of the PdBI.

The angular resolution of a telescope is $\Theta = k\lambda/D$, where D is the diameter of the antenna, λ the wavelength of the radiation received and k a factor of order unity depending on the antenna illumination. Therefore, the resolution of a radio telescope at a certain wavelength is proportional to the diameter of its aperture. To increase the resolution, the diameter has to be increased. This is only possible to some extend due to the physical and material limitations to the size of single-dish telescopes. The worlds largest movable radio telescopes, the Green Bank and Effelsberg telescope, have diameters of about 100 m, while the largest single-dish telescope, the 305 m Arecibo telescope, is stationary.

---

[3]http://www.iram-institute.org/EN/content-page-212-7-67-182-212-0.html

To achieve higher resolution a different type of instrument, the interferometer, has to be used. An interferometer consists of multiple single-dish telescopes and its resolution depends on the largest separation, or "baseline" (hereafter denoted by D), present between any two of its antennas. For ground-based interferometers, the separation is only limited by the diameter of the earth $R_{\oplus} \approx 17.000$ km; however plans exists to extend the available baselines through radio-antennas in space.
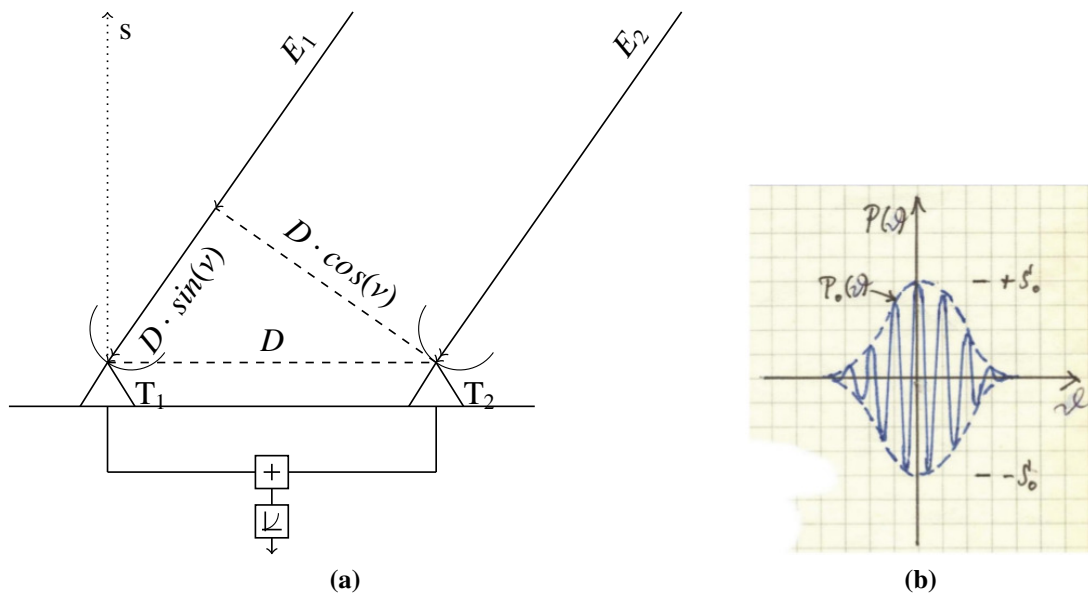
B.3.1. Two-element interferometer

Figure B.2.: a) Geometrical Layout of an two-element interferometer. Reproduced from (Klein, 2006). **b)** Interferometer Response. (Klein, 2006).

Most modern radio-interferometers employ multiple antennas; however, the basic principles of interferometry can be introduced by considering an interferometer made of two antennas. Such an instrument functions equivalent to its earlier optical counterparts, such as the Michelson interferometer or the Young's Hole experiment. The geometrical layout of such an instrument is depicted in Fig. B.2a: two parabolic-single dish antennas T_1 and T_2, separated by a baseline D, track the same source and receive a monochromatic, coherent and plane electromagnetic wave-front incident from a direction **s** under an angle v to the direction to the zenith (v=0). After the emission is detected by each antennas the two signals are combined.

The way the signals of the different antennas are combined defines the final response of the interferometer. Nowadays mostly "Correlation Interferometers" are used which multiply and integrate the two signals. This is in contrast to the "Adding Interferometers" used in early days of radio-interferometry, which, as their name suggest, simply added both signals. This method was technically easier to implement since it demanded less computational power. It has however been proven to be less sensitive than the "Correlation Interferometer", which has the advantage that uncorrelated signals, such as voltage fluctuations in the individual receiver systems of the antennas, are

canceled out in the final response of the interferometer. This improves the interferometers sensitivity to incoming radiation.

A monochromatic, coherent and plane electromagnetic wave-front incident on a interferometer does in general not reach both antennae at the same time but with a time lag that is (cf. Fig. B.2):

$$\tau_g = \frac{D}{c} \sin \nu, \tag{B.4}$$

depending on the angle ν and the baseline D. A result of the time lag between the telescopes is the typical "fringe pattern" of an interferometer, i.e. alternating regions of amplification and cancellation of the signal due of the phase variation between the two antennas. This response is shown in Fig. B.2b for a correlation interferometer.

To fully understand the response of an interferometer, one first has to consider the response of a single antenna to incident radiation. In the case of astronomy the radiation comes from very distant sources and can be considered as a plane electromagnetic wave. The output voltage U of each antenna (T_1 and T_2) is proportional to the incoming radiation and:

$$U_1 \propto E e^{i\omega(t-\tau_g)}, \tag{B.5}$$

$$U_2 \propto E e^{i\omega t}, \tag{B.6}$$

where E is the amplitude of the electromagnetic wave and ω the angular frequency. Since the output of the two antennas is correlated (multiplied and integrated) the response of an interferometer becomes:

$$R(\tau) \propto \frac{E^2}{T} \int_0^T e^{i\omega t} e^{-i\omega(t-\tau_g)} dt \tag{B.7}$$

where T the integration time. This can be simplified to:

$$R(\tau) \propto \frac{1}{2} E^2 e^{i\omega \tau_g}, \tag{B.8}$$

if one assumes that T is much longer than the time of a full oscillation period t_{osc} of the incident electromagnetic wave $t_{\text{osc}} = 2\pi/\omega$. In this case the integral will not be very different to the integration over one full period.

The latter formula tells us that the response of an interferometer decisively depends on the geometrical delay τ_g between the antennas which in turn depends on the direction to the source **s**. Due to the rotation of the earth, astronomical sources constantly move in the sky and **s** changes while the telescopes track a source. As an result the interference pattern changes with time. The frequency of this change is called "fringe frequency" or "fringe rate" and is proportional to the angular frequency of the earth's rotation ($\omega_e = 7.27 \cdot 10^{-5} \text{rad s}^{-1}$) and the separation of the telescopes. Fringe rates for the longest baselines of large interferometers such as the "Very Large Array" (VLA) can be in the range of 100 MHz–200 MHz. To recover all information that can be obtained from the incoming radiation "Nyquist sampling" must be achieved. This means that one has to take at least two samples per period of the fringe rate, which would result in very high data rates. It is therefore desirable to reduce or even entirely elim-

inate the fringe rate. This can be done by introducing an instrumental delay (τ_i) that varies as **s** changes and keeps the total phase difference constant for each antenna pair. This process is called "fringe stopping" and has the effect that the baseline between both telescopes seems constant to incoming radiation, although the projected baseline changes with time.

The response of an interferometer further depends on its geometrical configuration as well as on the properties of the individual antennas and receiver systems. The configuration and antenna characteristics together define the effective antenna surface $A_{\text{eff}}(s)$, which – similar to that antenna pattern of a single dish telescope (cd. Appendix B.2) – describes the direction-dependent sensitivity of the instrument. The effective antenna surface is connected with the antenna pattern F of the interferometer via:

$$A_{\text{eff}}(s) = A(0) \cdot \frac{F(s)}{F(0)} := A_{\text{eff}}(0)A_{\text{eff}}^{\text{N}}(s) \tag{B.9}$$

where $A_{\text{eff}}(0)$ and $F(0)$ the effective antenna surface and the antenna diagram in the direction of the phase center and $A_{\text{eff}}^{\text{N}}(s)$ the normalized effective antenna surface in direction s. The antenna diagram $F(s)$ can be described as the Fourier transformation of the aperture-field distribution $\bar{E}(x_v)$, i.e. the geometrical layout of the interferometer.

After the incoming radiation has been collected by the antennae it is channeled into the receivers where it is detected and converted into a measurable voltage. The Receivers have a finite bandwidth (Δv) and thus are sensitive to a range of frequencies. Since astronomical sources in general do not emit monochromatic light, one has to take the entire bandwidth of the receivers into account to derive the power received from a source. In the following the brightness distribution of a source is denoted by $B(s)$. Altogether the power received by an interferometer in a solid-angle element $d\Omega$ from a brightness distribution B(**s**) is:

$$dP = \frac{1}{2}A(s)B(s)d\Omega\Delta v, \tag{B.10}$$

here 1/2 accounts for the fact that the radio-receivers are in general only sensitive to one polarization.

The final response of an interferometer to a brightness distribution is the "visibility function":

$$V(b) = \iint\limits_{\text{source}} A_{\text{eff}}^{N}(s)B(s) \cdot e^{-i2\pi \cdot (D \cdot s)}d\Omega \tag{B.11}$$

Note, that this function is in the form of a Fourier transform and therefore allows to recover the brightness distribution as seen by the telescope, i.e. $A_{\text{eff}}^{N}(s)B(s)$, from the measured visibility through an inverse Fourier transform. This shows that an interferometer may be used to map the brightness distribution of a source. This fact is theoretically justified by the Van-Cittert-Zernike theorem, which describes the mutual coherence function of a source in the far-field, measured at two points in a plane. Detailed discussions of this theorem is given in Born & Wolf (1980); Wilson et al. (2009); Klein (2006).

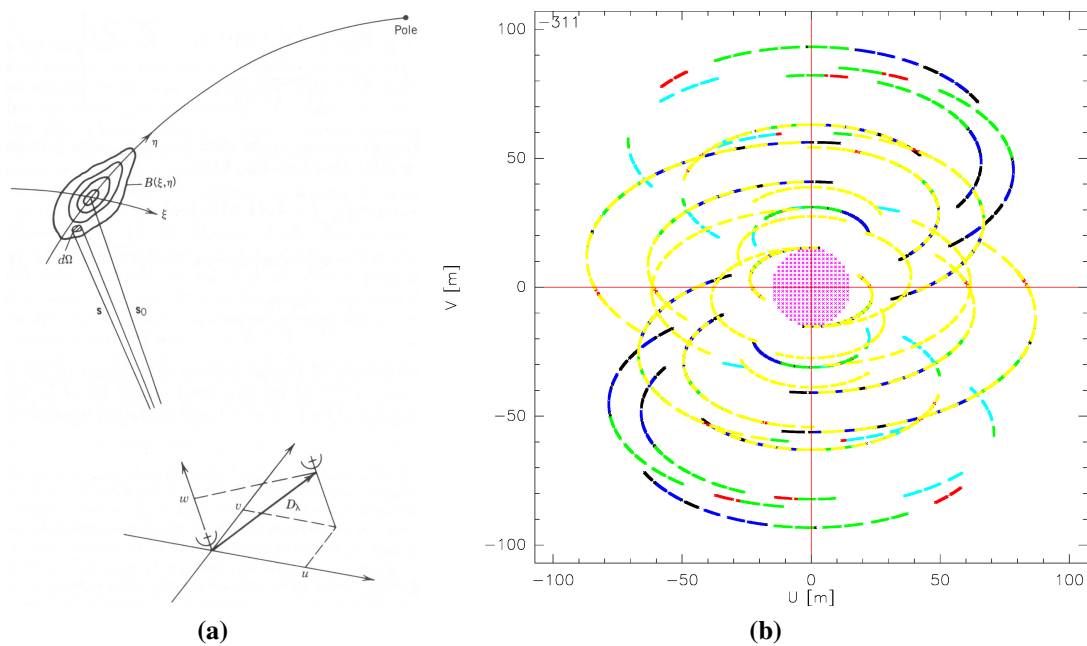## B.3.2. The uv-plane and aperture synthesis

Figure B.3.: a) Graphical representation of the coordinate system that defines the uv-plane (Thompson et al., 1986), **b)** Example uv-coverage. Different colors indicate different tracks. Pink points in the middle show the short spacing pseudo-visibilities (this work).

To perform the Fourier transformation of the measured visibilities and reconstruct the brightness distribution a convenient coordinate system is needed in which both the visibilities as well as the brightness distribution can be described. Fig. B.3a illustrates the coordinate-system of choice used in radio-interferometry. The visibilities are dependent on the specific baselines D. A plane perpendicular to the direction to the source **s** is defined that is spanned by the two parameters u and v. A third parameter w points in direction of s_0 towards the center of the field that is to be observed. The coordinates in which the brightness distribution is described are the directional cosines of the vector **s** with respect to the u, v, and w, i.e. ξ=cos(s∠u), η=cos(s∠v) and ζ=cos(s∠w). When **s** and D are expressed in these coordinates, the complex visibility (Eq. (B.11)) can be written as:

$$V(u, v, w) = \iint A_{\text{eff}}^{N}(\xi, \eta) B(\xi, \eta) \frac{1}{\zeta} exp(-i2\pi[u\xi + v\eta + w(\zeta - 1)]) d\xi d\eta \qquad \text{(B.12)}$$

Note that in this form the brightness distribution is described as a projection onto a plane that is tangential to the center of the field s_0.

Contemplating Eq. (B.12) it can be seen that each point in the uv-plane measures only a small part of the Fourier components of the brightness distribution. The range of points observed in the uv-plane is called the uv-coverage. Now consider an interferometer with multiple antennas. Adding more antennas does not change the basic functionality of an interferometer but increases the number of simultaneous baselines. Thus a better coverage of the uv-plane is achieved.

To obtain an unambiguous image of a given source, a high *uv*-coverage is needed. This means that many different baseline configurations have to be observed. The number of instantaneous baselines (or antenna pairs) that an interferometer has is N(N-1)/2, where N is the number of antennas in the array. Modern interferometers are configured such that they intrinsically cover a good range of the *uv*-plane for all elevations of the source with little redundancy between the baselines. However, since the number of antennas are limited only few interferometers with many antennas, such as the Very Large Array (VLA) or the Atacama Large Millimeter/submillimeter Array (ALMA), have an *uv*-coverage that allows to observe in a "snap-shot mode", i.e. short observations employing only the instant *uv*-coverage of the array.

Most interferometers have considerably fewer antennas, such as for example the PdBI with (currently) 6 antennas and thus 30 baselines. To fill the *uv*-plane the rotation of the earth is employed. In terms of the above coordinate system the rotation of the earths results in a rotation of the *uv*-plane with respect to the source, which in turn results in a change of the *u* and *v* components of the baseline vector. Therefore, while the interferometer observes and the source moves due to the ration of the earth, the *uv*-plane is gradually filled up. In Fig. B.3 an example *uv*-coverage from the HCN and HCO$^+$ observations, presented in Part III is shown. Note that the baseline vectors describe elliptical motions that depend on the elevation of the source. Furthermore, most interferometers have the possibilities to change their geometrical configuration by changing the location of all or individual antennas and as such increase the number of available baselines. In case of the PdBI four different configurations are used that are labeled A through D, where A the most extended and D the most compact configuration.

B.4. Reconstruction of the image

This section discusses the reconstruction of the brightness distribution from the measured interferometer response following the line-of-argument in (Klein et al., 2006). The *uv*-coverage of an interferometer can never be complete and is only defined at discreet positions. Especially very small and very long baselines are not covered, which, respectively, leads to insensitivity to extended structures (cf. Appendix B.5) and a finite resolution. Let in the following $S(u,v)$ be the sampling function that is unity where visibilities have been measured and zero elsewhere. The measured brightness distribution B_{meas} becomes

$$B_{\mathrm{meas}} = \mathcal{F}^{-1} S(u, v) \cdot V(u, v) \qquad (B.13)$$

where $\mathcal{F}^{-1}$ is the inverse Fourier transform and $V(u,v)$ the true visibility function induced by the source.

Dirty Beam   To be able to reconstruct the brightness distribution one has to know the so called "dirty beam shape" of the interferometer, i.e. the antenna pattern that corresponds to the final aperture distribution (*uv*-coverage) of the interferometer. Recalling Eq. (B.11), the visibility of a source is the Fourier transform of the brightness distribution folded with the antenna diagram. The antenna diagram is directly related with the

effective antenna surface (or aperture distribution) via Eq. (B.9). The actual aperture distribution of an interferometer is thus the multiplication of the sampling function $S(u,v)$ with the aperture size of the individual telescopes within the array:

$$A_{\text{eff}} = S(u, v) \cdot B_{\text{primary}}. \tag{B.14}$$

The antenna pattern F that corresponds to A_{eff} resembles the dirty beam of the observation.

Weighting Just like in the case of a single dish (cf. tapering) it is desirable to have a way to control the shape of the dirty beam or, equivalently, the illumination of the aperture distribution. This can be achieved by digitally applying weights to the measured visibilities before performing the Fourier transformation to reconstruct the brightness distribution. The weights have the general form of

$$W(u_l, v_l) = \sum_{\text{uvcov}} R_l \cdot T_l \cdot D_l \cdot \delta^2(u - u_l, v - v_l) \tag{B.15}$$

where δ the Delta-Function and:

- R_l - sets the weighting in case different telescopes have been used with different sizes or receiver systems, bandwidth, etc.,

- T_l - modifies the illumination and thus controls the beam shape,

- D_l - sets the weights for the density of the measured visibilities.

The choice for D_l allows to control how much weight is given to certain parts of the *uv*-plane and thus influences the final resolution of the image. For example, if more weight is given to large spatial frequencies the resolution becomes higher.

Deconvolution Once the visibilities are weighted the Fourier transform can be performed to obtain the so called "dirty-image". The dirty image is effectively the measured brightness distribution multiplied by the dirty beam. The latter does not have a Gaussian form and has more or less strong sidelobes and other features that dependent on the actual *uv*-coverage. The dirty image is therefore a rather distorted image of the brightness distribution.

Therefore, a further step has to be employed to obtain an image that can be exploited qualitatively as well as quantitatively. This process is called "cleaning" and consists in principal of a deconvolution of the image with the dirty beam and subsequent convolution with a Gaussian beam of the size of the main lobe of the dirty beam. Several algorithms exists to achieve this, each has advantages and disadvantages. Here only the "Högbom CLEAN" algorithm is discussed, which was used to clean the interferometer maps of M 33 presented in this thesis. With the dirty image and dirty beam B_{dirty} at hand the following steps are executed:

- The peak of the brightness distribution I_{max} is determined. At this position $\gamma B_{\text{dirty}} I_{\text{max}}$ is subtracted from the map; the "loop gain" γ controls the speed of

the cleaning process. The map from that the peaks are subtracted is called in the following "residual map". Further, a Dirac δ-peak of height γI_{max} is written at the corresponding position to an temporary working array.

- The first step is re-executed until a stopping criterion is reached chosen by the user (number of iterations, residual noise, ...). Gradually the working array becomes a "point source model" of the brightness distribution.

- When the point source model is finished it is convolved by the user defined "clean beam", which is usually a Gaussian of size of the main-lobe of the dirty beam.

- Finally, the residual map and the convolved point-source model are added to form the clean image I_{clean}.

B.5. Short spacings

Despite aperture synthesize and different geometrical configurations, an interferometer is not able to observe baselines smaller than the diameter of its antennas. The diameter of one antenna is the absolute minimum baseline in the case two antennas are placed so close to each other that they nearly touch[4]. The result is a gap in the *uv*-plane for small values of *u* and *v*. The consequence of this gap for the final image (the Fourier transformation from the observed Visibilities V(u,v,w)) can be deduced from the Similarity-Theorem of Fourier transformation, which says that if $f(x)$ has the Fourier transform $\mathcal{F}(s)$ then,

$$\mathcal{F}(a \cdot x) = \frac{1}{|a|}\mathcal{F}(\frac{s}{a}), \qquad (B.16)$$

where $\mathcal{F}$ denotes the Fourier transformation. The formula states that small values of x ($a \rightarrow 0$) correspond to large values of s. In the case of an interferometer this means that small baselines measure large spatial scales in the brightness distribution. Therefore, an interferometer filters out the information from extended structures with an angular size larger than λ/b_{min}, with b_{min} the minimal baseline[5]. To refer to this lack of information from small baselines the term "missing short-spacings" is commonly used.

To correct for this the same source can be observed with a single-dish telescope or alternatively with an interferometer array with smaller antennas or shorter baselines. In the case that single-dish observations are used the absolute minimum possibility is a single pointing towards the (in this case preferably unresolved) source. Such an observation is referred to as "zero-spacing observation" and delivers an estimate for the total flux of the source, which helps in the deconvolution step.

Better, however, is to map the source with the single-dish telescope. The estimation of the optimal short-spacings map-size and observation time at the 30 m for a specific PdBI observation is not straightforward as is discussed in detail in the "IRAM Memo

---

[4]Which is not very practical as it may lead, e.g. to shadowing between the antennas

[5]Note that in the same way the resolution of an interferometer is determined by the longest baseline.

2008-2 on single-dish observations" by N.J Rodriguez-Fernandez, J. Pety and F. Gueth. The latter reference, however, gives the following boundary conditions:

- the map size must not be smaller than the field-of-view (FOV) of the interferometer map ,

- the maps should have a uniform noise distribution,

- larger maps help to interpret the noisier signals in the edges of the map.

The minimal and maximum integration times that can be calculated from these conditions are normally very small or unsensible large. At the IRAM facilities an empirical "rule of thumb" is therefore suggested which is that the short spacing observations should cover a field that is two-times larger than the FOV of the interferometer map and the observation time should be the same as the time spent at the interferometer.

Amongst other techniques, interferometer observations can be combined with a single-dish maps by decomposing the latter into so-called "pseudo-visibilities" which are combined in the *uv*-plane with the visibilities measured at the interferometer before imaging and deconvolution (see Appendix B.4). For details of this process please refer to the "IRAM Memo 2008-2 on single-dish observations".

Appendix C.

PDR Model results

These tables and the following text have been published in Appendix E of Buchbender et al. (2013). The modeled abundances and intensity ratios of the ground-state transition of HCN, HCO, and ^{12}CO using the Meudon PDR code for subsolar and solar etallicities are shown in Tables C.1 and C.2. Both tables are subdivided in three blocks one for each modeled radiation field of $G_0 = 10, 50,$ and 100 in Habing units, which illuminates the modeled clouds from both sides. The other two input parameters that have been varied are the density with values of $n_H = 0.1, 0.5, 1, 5, 10, 50, 10^2 \times 10^4$ cm^{-3} and the optical extinctions with values of $A_v = 2, 4, 6, 10, 16, 26, 40,$ and 50 mag.

Table C.1.: Results of the PDR models with subsolar metallicities for M 33 (cf. Sect. 9.1.4).
Notes. ^{a} logarithmic relative abundance X(mol)= log(N(mol)/N(H$_2$))

A_v (mag.)	n_H (cm^{-3})	X(HCO$^+$)^a	X(HCN)^a	X(CO)^a	HCN/CO %	HCO$^+$/CO %	HCO$^+$/HCN
				$G_0 = 10$			
2.0	1 10^3	-10.8	-11.7	-7.4	1.11	19.57	17.63
2.0	5 10^3	-11.2	-10.7	-6.1	0.65	0.47	0.73
2.0	1 10^4	-11.3	-10.4	-5.6	0.40	0.14	0.34
2.0	5 10^4	-11.1	-9.9	-4.6	0.22	0.04	0.19
2.0	1 10^5	-11.0	-9.7	-4.4	0.26	0.04	0.14
2.0	5 10^5	-11.2	-9.3	-4.1	0.42	0.02	0.04
2.0	1 10^6	-11.2	-9.2	-4.1	0.47	0.01	0.02
4.0	1 10^3	-10.8	-10.9	-5.7	0.19	0.46	2.43
4.0	5 10^3	-11.0	-10.3	-4.7	0.13	0.06	0.43
4.0	1 10^4	-11.0	-10.1	-4.4	0.18	0.05	0.27
4.0	5 10^4	-11.1	-9.7	-4.2	0.37	0.04	0.11
4.0	1 10^5	-11.1	-9.5	-4.1	0.48	0.04	0.08
4.0	5 10^5	-11.3	-9.3	-4.0	0.73	0.02	0.03
4.0	1 10^6	-11.4	-9.3	-4.0	0.79	0.01	0.02
6.0	1 10^3	-10.5	-10.5	-5.4	0.39	0.68	1.73
6.0	5 10^3	-10.7	-10.0	-4.5	0.30	0.16	0.54
6.0	1 10^4	-10.6	-9.9	-4.3	0.38	0.15	0.40
6.0	5 10^4	-10.7	-9.6	-4.1	0.61	0.12	0.20
6.0	1 10^5	-10.8	-9.5	-4.1	0.71	0.10	0.14
6.0	5 10^5	-11.1	-9.4	-4.0	0.89	0.05	0.06
6.0	1 10^6	-11.2	-9.4	-4.0	0.91	0.04	0.04
10.0	1 10^3	-9.2	-9.0	-4.5	6.10	8.22	1.35
10.0	5 10^3	-9.4	-9.2	-4.2	2.36	3.14	1.33

Table C.1.: Continued

A_v (mag.)	n_H (cm^{-3})	X(HCO$^+$)^a	X(HCN)^a	X(CO)^a	HCN/CO %	HCO$^+$/CO %	HCO$^+$/HCN
10.0	1 10^4	-9.6	-9.3	-4.1	1.79	2.02	1.13
10.0	5 10^4	-10.1	-9.4	-4.0	1.62	0.80	0.49
10.0	1 10^5	-10.3	-9.3	-4.0	1.61	0.56	0.35
10.0	5 10^5	-10.6	-9.4	-4.0	1.33	0.24	0.18
10.0	1 10^6	-10.8	-9.5	-4.0	1.21	0.17	0.14
16.0	1 10^3	-8.6	-8.3	-4.2	14.29	15.42	1.08
16.0	5 10^3	-9.1	-8.6	-4.1	7.98	7.25	0.91
16.0	1 10^4	-9.3	-8.6	-4.0	7.42	5.05	0.68
16.0	5 10^4	-9.8	-8.7	-4.0	6.71	2.20	0.33
16.0	1 10^5	-10.0	-8.9	-4.0	5.86	1.60	0.27
16.0	5 10^5	-10.3	-9.2	-4.0	3.30	0.74	0.22
16.0	1 10^6	-10.5	-9.3	-3.9	2.52	0.52	0.20
26.0	1 10^3	-8.4	-8.1	-4.1	15.30	17.49	1.14
26.0	5 10^3	-8.9	-8.4	-4.0	10.34	10.55	1.02
26.0	1 10^4	-9.2	-8.4	-4.0	10.14	8.30	0.82
26.0	5 10^4	-9.7	-8.5	-4.0	10.81	4.32	0.40
26.0	1 10^5	-9.9	-8.7	-4.0	10.45	3.24	0.31
26.0	5 10^5	-10.2	-9.1	-3.9	6.79	1.56	0.23
26.0	1 10^6	-10.4	-9.2	-3.9	5.06	1.10	0.22
40.0	1 10^3	-8.3	-8.1	-4.0	15.52	19.00	1.23
40.0	5 10^3	-8.9	-8.4	-4.0	11.44	12.98	1.14
40.0	1 10^4	-9.1	-8.4	-4.0	11.59	11.11	0.96
40.0	5 10^4	-9.6	-8.5	-3.9	13.63	6.79	0.50
40.0	1 10^5	-9.8	-8.6	-3.9	14.05	5.25	0.37
40.0	5 10^5	-10.2	-9.0	-3.9	10.59	2.63	0.25
40.0	1 10^6	-10.3	-9.2	-3.9	8.08	1.86	0.23
50.0	1 10^3	-8.2	-8.1	-4.0	15.51	19.81	1.28
50.0	5 10^3	-8.8	-8.3	-4.0	11.89	14.17	1.19
50.0	1 10^4	-9.1	-8.3	-4.0	12.23	12.53	1.02
50.0	5 10^4	-9.6	-8.4	-3.9	14.97	8.28	0.55
50.0	1 10^5	-9.8	-8.6	-3.9	15.82	6.54	0.41
50.0	5 10^5	-10.1	-9.0	-3.9	12.80	3.35	0.26
50.0	1 10^6	-10.3	-9.2	-3.9	9.96	2.39	0.24
				$G_0 = 50$			
2.0	1 10^3	-11.1	-13.0	-8.7	1.19	219.55	185.29
2.0	5 10^3	-11.3	-11.7	-7.6	2.38	15.95	6.71
2.0	1 10^4	-11.4	-11.2	-7.1	2.29	4.48	1.95
2.0	5 10^4	-11.4	-10.4	-5.8	0.98	0.37	0.38
2.0	1 10^5	-10.9	-10.2	-5.2	0.53	0.33	0.61
2.0	5 10^5	-11.0	-9.6	-4.5	0.27	0.04	0.13
2.0	1 10^6	-11.1	-9.4	-4.3	0.29	0.02	0.06
4.0	1 10^3	-11.0	-11.6	-6.7	0.24	2.34	9.64
4.0	5 10^3	-11.2	-10.8	-5.3	0.11	0.09	0.75
4.0	1 10^4	-11.3	-10.5	-4.9	0.10	0.04	0.40
4.0	5 10^4	-11.2	-10.0	-4.4	0.18	0.03	0.16

Table C.1.: Continued

A_v (mag.)	n_H (cm^{-3})	$X(HCO^+)^a$	$X(HCN)^a$	$X(CO)^a$	HCN/CO %	HCO$^+$/CO %	HCO$^+$/HCN
4.0	1 10^5	-11.0	-9.8	-4.3	0.24	0.04	0.18
4.0	5 10^5	-11.2	-9.5	-4.1	0.40	0.02	0.05
4.0	1 10^6	-11.3	-9.4	-4.1	0.45	0.01	0.03
6.0	1 10^3	-10.8	-11.0	-5.8	0.20	0.57	2.81
6.0	5 10^3	-11.0	-10.4	-4.8	0.14	0.09	0.59
6.0	1 10^4	-11.0	-10.2	-4.5	0.18	0.07	0.38
6.0	5 10^4	-11.1	-9.8	-4.2	0.34	0.05	0.16
6.0	1 10^5	-11.0	-9.7	-4.1	0.41	0.06	0.15
6.0	5 10^5	-11.2	-9.5	-4.1	0.57	0.03	0.05
6.0	1 10^6	-11.3	-9.4	-4.0	0.59	0.02	0.03
10.0	1 10^3	-10.2	-10.0	-5.1	1.06	1.41	1.33
10.0	5 10^3	-9.8	-9.6	-4.3	1.02	1.54	1.51
10.0	1 10^4	-9.9	-9.7	-4.2	0.84	1.08	1.29
10.0	5 10^4	-10.3	-9.7	-4.1	0.74	0.48	0.65
10.0	1 10^5	-10.4	-9.6	-4.0	0.75	0.36	0.48
10.0	5 10^5	-10.8	-9.6	-4.0	0.77	0.14	0.18
10.0	1 10^6	-10.9	-9.5	-4.0	0.74	0.09	0.12
16.0	1 10^3	-8.7	-8.4	-4.3	13.57	14.65	1.08
16.0	5 10^3	-9.2	-8.8	-4.1	6.49	6.21	0.96
16.0	1 10^4	-9.4	-8.8	-4.1	5.54	4.16	0.75
16.0	5 10^4	-9.9	-9.0	-4.0	4.23	1.80	0.43
16.0	1 10^5	-10.0	-9.1	-4.0	3.43	1.31	0.38
16.0	5 10^5	-10.4	-9.4	-4.0	1.79	0.55	0.31
16.0	1 10^6	-10.5	-9.5	-4.0	1.38	0.36	0.26
26.0	1 10^3	-8.4	-8.2	-4.1	15.23	17.30	1.14
26.0	5 10^3	-9.0	-8.5	-4.0	9.56	9.90	1.04
26.0	1 10^4	-9.2	-8.5	-4.0	8.88	7.56	0.85
26.0	5 10^4	-9.7	-8.7	-4.0	8.42	3.97	0.47
26.0	1 10^5	-9.8	-8.8	-4.0	7.58	2.97	0.39
26.0	5 10^5	-10.2	-9.2	-4.0	4.22	1.30	0.31
26.0	1 10^6	-10.3	-9.3	-4.0	3.02	0.85	0.28
40.0	1 10^3	-8.3	-8.1	-4.0	15.47	18.89	1.22
40.0	5 10^3	-8.9	-8.4	-4.0	10.74	12.44	1.16
40.0	1 10^4	-9.1	-8.4	-4.0	10.36	10.40	1.00
40.0	5 10^4	-9.6	-8.6	-4.0	11.18	6.47	0.58
40.0	1 10^5	-9.8	-8.7	-4.0	10.91	5.01	0.46
40.0	5 10^5	-10.1	-9.1	-3.9	6.97	2.27	0.33
40.0	1 10^6	-10.3	-9.3	-3.9	5.03	1.50	0.30
50.0	1 10^3	-8.2	-8.1	-4.0	15.46	19.72	1.28
50.0	5 10^3	-8.8	-8.4	-4.0	11.22	13.68	1.22
50.0	1 10^4	-9.1	-8.4	-4.0	10.99	11.84	1.08
50.0	5 10^4	-9.6	-8.5	-4.0	12.46	8.00	0.64
50.0	1 10^5	-9.7	-8.7	-4.0	12.57	6.30	0.50
50.0	5 10^5	-10.1	-9.1	-3.9	8.65	2.92	0.34

Table C.1.: Continued

A_v (mag.)	n_H (cm^{-3})	$X(HCO^+)^a$	$X(HCN)^a$	$X(CO)^a$	HCN/CO %	HCO$^+$/CO %	HCO$^+$/HCN
50.0	1 10^6	-10.2	-9.2	-3.9	6.33	1.95	0.31
				$G_0 = 100$			
2.0	1 10^3	-11.2	-13.6	-9.3	1.08	536.12	498.10
2.0	5 10^3	-11.4	-12.4	-8.4	2.97	69.85	23.49
2.0	1 10^4	-11.4	-11.9	-7.8	3.43	23.10	6.74
2.0	5 10^4	-11.5	-10.9	-6.5	2.10	1.76	0.84
2.0	1 10^5	-11.0	-10.6	-6.0	1.21	1.66	1.37
2.0	5 10^5	-10.7	-10.0	-4.9	0.28	0.16	0.56
2.0	1 10^6	-11.0	-9.8	-4.6	0.22	0.03	0.13
4.0	1 10^3	-11.1	-12.1	-7.2	0.29	6.97	23.75
4.0	5 10^3	-11.3	-11.1	-5.9	0.18	0.24	1.31
4.0	1 10^4	-11.4	-10.7	-5.3	0.13	0.07	0.58
4.0	5 10^4	-11.3	-10.2	-4.6	0.14	0.03	0.20
4.0	1 10^5	-11.1	-10.0	-4.4	0.18	0.04	0.23
4.0	5 10^5	-10.9	-9.6	-4.2	0.28	0.03	0.11
4.0	1 10^6	-11.2	-9.5	-4.2	0.32	0.01	0.04
6.0	1 10^3	-11.0	-11.2	-6.0	0.15	0.57	3.73
6.0	5 10^3	-11.1	-10.6	-4.9	0.10	0.07	0.68
6.0	1 10^4	-11.1	-10.3	-4.6	0.13	0.05	0.43
6.0	5 10^4	-11.2	-10.0	-4.3	0.24	0.04	0.17
6.0	1 10^5	-11.1	-9.8	-4.2	0.29	0.05	0.17
6.0	5 10^5	-11.0	-9.6	-4.1	0.41	0.04	0.09
6.0	1 10^6	-11.3	-9.5	-4.1	0.44	0.02	0.04
10.0	1 10^3	-10.3	-10.1	-5.3	0.92	1.27	1.39
10.0	5 10^3	-10.0	-9.8	-4.4	0.72	0.93	1.30
10.0	1 10^4	-10.1	-9.8	-4.3	0.64	0.74	1.16
10.0	5 10^4	-10.4	-9.7	-4.1	0.59	0.37	0.63
10.0	5 10^5	-10.8	-9.6	-4.0	0.58	0.12	0.21
10.0	1 10^6	-11.0	-9.6	-4.0	0.56	0.07	0.12
16.0	1 10^3	-8.8	-8.5	-4.3	13.03	14.15	1.08
16.0	5 10^3	-9.2	-8.9	-4.2	5.81	5.81	1.00
16.0	1 10^4	-9.4	-8.9	-4.1	4.71	3.81	0.81
16.0	5 10^4	-9.9	-9.1	-4.0	3.32	1.64	0.50
16.0	1 10^5	-10.0	-9.2	-4.0	2.62	1.19	0.45
16.0	5 10^5	-10.4	-9.5	-4.0	1.35	0.49	0.36
16.0	1 10^6	-10.5	-9.5	-4.0	1.04	0.30	0.29
26.0	1 10^3	-8.4	-8.2	-4.1	15.16	17.18	1.13
26.0	5 10^3	-9.0	-8.5	-4.1	9.34	9.75	1.04
26.0	1 10^4	-9.2	-8.5	-4.0	8.40	7.31	0.87
26.0	5 10^4	-9.7	-8.7	-4.0	7.50	3.84	0.51
26.0	1 10^5	-9.8	-8.9	-4.0	6.53	2.87	0.44
26.0	5 10^5	-10.2	-9.2	-4.0	3.42	1.21	0.35
26.0	1 10^6	-10.3	-9.4	-4.0	2.42	0.77	0.32
40.0	1 10^3	-8.3	-8.1	-4.1	15.43	18.82	1.22
40.0	5 10^3	-8.9	-8.4	-4.0	10.58	12.39	1.17

Table C.1.: Continued

A_v (mag.)	n_H (cm^{-3})	$X(HCO^+)^a$	$X(HCN)^a$	$X(CO)^a$	HCN/CO %	HCO$^+$/CO %	HCO$^+$/HCN
40.0	1 10^4	-9.1	-8.4	-4.0	9.92	10.21	1.03
40.0	5 10^4	-9.6	-8.6	-4.0	10.22	6.38	0.62
40.0	1 10^5	-9.7	-8.8	-4.0	9.69	4.92	0.51
40.0	5 10^5	-10.1	-9.1	-4.0	5.80	2.14	0.37
40.0	1 10^6	-10.2	-9.3	-3.9	4.12	1.37	0.33
50.0	1 10^3	-8.3	-8.1	-4.0	15.49	19.71	1.27
50.0	5 10^3	-8.8	-8.4	-4.0	11.06	13.65	1.23
50.0	1 10^4	-9.1	-8.4	-4.0	10.55	11.67	1.11
50.0	5 10^4	-9.5	-8.6	-4.0	11.47	7.93	0.69
50.0	1 10^5	-9.7	-8.7	-4.0	11.28	6.23	0.55
50.0	5 10^5	-10.1	-9.1	-3.9	7.26	2.76	0.38
50.0	1 10^6	-10.2	-9.3	-3.9	5.23	1.78	0.34

Table C.2.: Results of the PDR models with solar metallicities.
Notes. [a] logarithmic relative abundance X(mol)= log(N(mol)/N(H_2))

A_v (mag.)	n_H (cm^{-3})	X(HCO$^+$)[a]	X(HCN)[a]	X(CO)[a]	HCN/CO %	HCO$^+$/CO %	HCO$^+$/HCN
				$G_0 = 10$			
2.0	1 10^3	-11.6	-11.0	-6.5	0.84	0.45	0.54
2.0	5 10^3	-11.6	-10.4	-5.1	0.15	0.02	0.12
2.0	1 10^4	-11.5	-10.2	-4.6	0.11	0.01	0.10
2.0	5 10^4	-11.3	-9.6	-3.8	0.18	0.01	0.07
2.0	1 10^5	-11.1	-9.3	-3.7	0.29	0.02	0.06
2.0	5 10^5	-11.2	-8.9	-3.5	0.59	0.01	0.02
2.0	1 10^6	-11.2	-8.8	-3.4	0.68	0.01	0.01
4.0	1 10^3	-11.4	-10.5	-4.7	0.12	0.03	0.29
4.0	5 10^3	-11.1	-9.9	-3.8	0.19	0.03	0.16
4.0	1 10^4	-11.0	-9.7	-3.7	0.29	0.03	0.12
4.0	5 10^4	-11.1	-9.3	-3.5	0.64	0.03	0.05
4.0	1 10^5	-11.1	-9.1	-3.5	0.83	0.03	0.04
4.0	5 10^5	-11.3	-8.9	-3.4	1.22	0.02	0.01
4.0	1 10^6	-11.3	-8.8	-3.4	1.33	0.01	0.01
6.0	1 10^3	-10.8	-10.1	-4.4	0.30	0.15	0.51
6.0	5 10^3	-10.5	-9.7	-3.7	0.48	0.16	0.34
6.0	1 10^4	-10.5	-9.5	-3.6	0.65	0.15	0.23
6.0	5 10^4	-10.7	-9.2	-3.5	1.03	0.10	0.10
6.0	1 10^5	-10.7	-9.1	-3.4	1.19	0.09	0.08
6.0	5 10^5	-11.0	-9.0	-3.4	1.46	0.04	0.03
6.0	1 10^6	-11.1	-9.0	-3.4	1.52	0.03	0.02
10.0	1 10^3	-9.4	-9.2	-3.7	2.81	3.92	1.40
10.0	5 10^3	-9.5	-9.3	-3.5	1.74	2.12	1.22
10.0	1 10^4	-9.7	-9.3	-3.5	1.56	1.44	0.92
10.0	5 10^4	-10.1	-9.2	-3.4	1.79	0.64	0.36
10.0	1 10^5	-10.2	-9.1	-3.4	1.99	0.48	0.24
10.0	5 10^5	-10.5	-9.0	-3.4	2.17	0.23	0.10
10.0	1 10^6	-10.7	-9.0	-3.4	2.19	0.16	0.07
16.0	1 10^3	-8.6	-8.4	-3.5	10.58	11.99	1.13
16.0	5 10^3	-9.1	-8.6	-3.4	6.79	5.78	0.85
16.0	1 10^4	-9.3	-8.5	-3.4	6.63	4.18	0.63
16.0	5 10^4	-9.7	-8.7	-3.4	5.79	2.05	0.35
16.0	1 10^5	-9.9	-8.8	-3.4	5.01	1.55	0.31
16.0	5 10^5	-10.2	-9.0	-3.3	3.97	0.72	0.18
16.0	1 10^6	-10.4	-8.7	-3.3	4.03	0.49	0.12
26.0	1 10^3	-8.4	-8.2	-3.4	12.46	14.49	1.16
26.0	5 10^3	-8.9	-8.3	-3.4	9.03	8.66	0.96
26.0	1 10^4	-9.2	-8.3	-3.4	9.03	7.03	0.78
26.0	5 10^4	-9.6	-8.5	-3.4	8.94	4.13	0.46
26.0	1 10^5	-9.7	-8.6	-3.4	8.26	3.21	0.39
26.0	5 10^5	-10.1	-8.9	-3.3	6.74	1.53	0.23
26.0	1 10^6	-10.2	-8.7	-3.3	6.86	1.05	0.15

Table C.2.: Continued

A_v (mag.)	n_H (cm^{-3})	$X(HCO^+)^a$	$X(HCN)^a$	$X(CO)^a$	HCN/CO %	HCO$^+$/CO %	HCO$^+$/HCN
40.0	1 10^3	-8.3	-8.1	-3.4	13.15	16.22	1.23
40.0	5 10^3	-8.9	-8.2	-3.4	10.14	10.78	1.06
40.0	1 10^4	-9.1	-8.2	-3.4	10.38	9.44	0.91
40.0	5 10^4	-9.5	-8.4	-3.3	11.17	6.46	0.58
40.0	1 10^5	-9.7	-8.6	-3.3	10.92	5.20	0.48
40.0	5 10^5	-10.0	-8.9	-3.3	9.75	2.58	0.27
40.0	1 10^6	-10.2	-8.7	-3.3	10.02	1.78	0.18
50.0	1 10^3	-8.3	-8.1	-3.4	13.41	17.13	1.28
50.0	5 10^3	-8.8	-8.2	-3.4	10.62	11.84	1.11
50.0	1 10^4	-9.0	-8.2	-3.4	11.01	10.68	0.97
50.0	5 10^4	-9.5	-8.4	-3.3	12.26	7.85	0.64
50.0	1 10^5	-9.6	-8.6	-3.3	12.26	6.44	0.53
50.0	5 10^5	-10.0	-8.8	-3.3	11.49	3.28	0.29
50.0	1 10^6	-10.1	-8.7	-3.3	11.88	2.28	0.19
				$G_0= 50$			
2.0	1 10^3	-11.4	-11.9	-8.0	2.55	17.66	6.93
2.0	5 10^3	-11.7	-11.0	-6.6	1.14	0.47	0.41
2.0	1 10^4	-11.7	-10.7	-6.0	0.68	0.15	0.23
2.0	5 10^4	-11.5	-10.1	-4.7	0.18	0.03	0.14
2.0	1 10^5	-11.4	-9.9	-4.3	0.12	0.01	0.12
2.0	5 10^5	-10.8	-9.2	-3.7	0.23	0.02	0.07
2.0	1 10^6	-9.4	-7.1	-3.6	0.85	0.02	0.02
4.0	1 10^3	-11.5	-11.0	-5.7	0.14	0.08	0.58
4.0	5 10^3	-11.5	-10.3	-4.3	0.08	0.01	0.14
4.0	1 10^4	-11.4	-10.1	-4.0	0.12	0.01	0.11
4.0	5 10^4	-11.2	-9.5	-3.7	0.32	0.02	0.06
4.0	1 10^5	-11.2	-9.4	-3.6	0.43	0.02	0.04
4.0	5 10^5	-11.0	-9.0	-3.5	0.73	0.02	0.02
4.0	1 10^6	-10.2	-7.5	-3.5	1.16	0.01	0.01
6.0	1 10^3	-11.2	-10.5	-4.9	0.17	0.07	0.45
6.0	5 10^3	-10.9	-10.0	-3.8	0.23	0.06	0.27
6.0	1 10^4	-10.9	-9.8	-3.7	0.33	0.06	0.18
6.0	5 10^4	-11.0	-9.4	-3.5	0.62	0.05	0.08
6.0	1 10^5	-11.0	-9.3	-3.5	0.76	0.04	0.06
6.0	5 10^5	-11.0	-9.0	-3.4	1.02	0.03	0.03
6.0	1 10^6	-10.2	-7.9	-3.4	1.25	0.02	0.02
10.0	1 10^3	-10.1	-9.7	-4.0	1.11	0.85	0.77
10.0	5 10^3	-9.9	-9.5	-3.6	1.02	0.95	0.93
10.0	1 10^4	-9.9	-9.5	-3.5	0.97	0.73	0.75
10.0	5 10^4	-10.3	-9.3	-3.4	1.05	0.36	0.34
10.0	1 10^5	-10.4	-9.3	-3.4	1.12	0.27	0.24
10.0	5 10^5	-10.7	-9.2	-3.4	1.27	0.12	0.10
10.0	1 10^6	-10.5	-8.0	-3.4	1.55	0.08	0.05
16.0	1 10^3	-8.8	-8.6	-3.6	9.36	10.90	1.16
16.0	5 10^3	-9.2	-8.8	-3.5	4.95	4.54	0.92

Table C.2.: Continued

A_v (mag.)	n_H (cm^{-3})	$X(HCO^+)^a$	$X(HCN)^a$	$X(CO)^a$	HCN/CO %	HCO$^+$/CO %	HCO$^+$/HCN
16.0	1 10^4	-9.4	-8.7	-3.4	4.67	3.21	0.69
16.0	5 10^4	-9.8	-8.9	-3.4	3.76	1.58	0.42
16.0	1 10^5	-9.9	-9.0	-3.4	3.20	1.19	0.37
16.0	5 10^5	-10.2	-9.0	-3.4	2.60	0.53	0.20
16.0	1 10^6	-10.2	-8.0	-3.4	2.98	0.34	0.11
26.0	1 10^3	-8.5	-8.3	-3.5	12.16	14.10	1.16
26.0	5 10^3	-9.0	-8.4	-3.4	7.76	7.55	0.97
26.0	1 10^4	-9.2	-8.4	-3.4	7.55	6.07	0.80
26.0	5 10^4	-9.6	-8.6	-3.4	6.94	3.61	0.52
26.0	1 10^5	-9.7	-8.7	-3.4	6.15	2.81	0.46
26.0	5 10^5	-10.1	-8.9	-3.4	4.94	1.26	0.26
26.0	1 10^6	-10.2	-8.3	-3.3	5.29	0.81	0.15
40.0	1 10^3	-8.3	-8.2	-3.4	12.97	15.95	1.23
40.0	5 10^3	-8.9	-8.3	-3.4	8.88	9.64	1.08
40.0	1 10^4	-9.1	-8.3	-3.4	8.88	8.42	0.95
40.0	5 10^4	-9.5	-8.5	-3.4	9.11	5.91	0.65
40.0	1 10^5	-9.6	-8.7	-3.4	8.64	4.76	0.55
40.0	5 10^5	-10.0	-8.9	-3.3	7.58	2.20	0.29
40.0	1 10^6	-10.1	-8.3	-3.3	8.18	1.43	0.17
50.0	1 10^3	-8.3	-8.1	-3.4	13.25	16.90	1.28
50.0	5 10^3	-8.8	-8.3	-3.4	9.35	10.66	1.14
50.0	1 10^4	-9.0	-8.3	-3.4	9.47	9.61	1.01
50.0	5 10^4	-9.5	-8.5	-3.4	10.14	7.29	0.72
50.0	1 10^5	-9.6	-8.6	-3.3	9.92	5.99	0.60
50.0	5 10^5	-10.0	-8.9	-3.3	9.16	2.84	0.31
50.0	1 10^6	-10.1	-8.5	-3.3	9.77	1.85	0.19
				G_0= 100			
2.0	1 10^3	-11.5	-12.6	-8.6	2.27	69.47	30.54
2.0	5 10^3	-11.7	-11.5	-7.4	1.97	2.80	1.42
2.0	1 10^4	-11.8	-11.1	-6.8	1.46	0.85	0.59
2.0	5 10^4	-11.7	-10.5	-5.5	0.47	0.11	0.23
2.0	1 10^5	-11.6	-10.3	-5.0	0.23	0.04	0.19
2.0	5 10^5	-10.5	-9.5	-4.0	0.12	0.05	0.38
2.0	1 10^6	-10.7	-9.2	-3.8	0.15	0.01	0.07
4.0	1 10^3	-11.6	-11.3	-6.3	0.24	0.27	1.13
4.0	5 10^3	-11.7	-10.6	-4.7	0.07	0.01	0.18
4.0	1 10^4	-11.6	-10.3	-4.3	0.08	0.01	0.12
4.0	5 10^4	-11.4	-9.7	-3.8	0.21	0.01	0.07
4.0	1 10^5	-11.3	-9.5	-3.7	0.30	0.01	0.05
4.0	5 10^5	-10.7	-9.1	-3.6	0.53	0.03	0.06
4.0	1 10^6	-11.0	-9.0	-3.5	0.60	0.01	0.02
6.0	1 10^3	-11.3	-10.7	-5.1	0.13	0.06	0.47
6.0	5 10^3	-11.1	-10.1	-3.9	0.16	0.04	0.26
6.0	1 10^4	-11.0	-9.9	-3.8	0.23	0.04	0.18
6.0	5 10^4	-11.1	-9.5	-3.6	0.45	0.04	0.08

A_v (mag.)	n_H (cm^{-3})	$X(HCO^+)^a$	$X(HCN)^a$	$X(CO)^a$	HCN/CO %	HCO$^+$/CO %	HCO$^+$/HCN
6.0	1 10^5	-11.1	-9.4	-3.5	0.56	0.03	0.06
6.0	5 10^5	-10.8	-9.1	-3.5	0.80	0.04	0.05
6.0	1 10^6	-11.1	-9.0	-3.4	0.83	0.02	0.02
10.0	1 10^3	-10.3	-9.8	-4.2	0.90	0.61	0.68
10.0	5 10^3	-10.0	-9.6	-3.6	0.83	0.64	0.76
10.0	1 10^4	-10.1	-9.5	-3.6	0.82	0.52	0.64
10.0	5 10^4	-10.3	-9.4	-3.5	0.88	0.28	0.32
10.0	1 10^5	-10.5	-9.4	-3.4	0.93	0.21	0.23
10.0	5 10^5	-10.7	-9.2	-3.4	1.01	0.11	0.11
10.0	1 10^6	-10.8	-9.2	-3.4	0.99	0.06	0.06
16.0	1 10^3	-8.8	-8.7	-3.7	8.80	10.47	1.19
16.0	5 10^3	-9.2	-8.9	-3.5	4.15	4.05	0.98
16.0	1 10^4	-9.4	-8.8	-3.5	3.85	2.85	0.74
16.0	5 10^4	-9.8	-9.0	-3.4	3.03	1.40	0.46
16.0	1 10^5	-10.0	-9.0	-3.4	2.59	1.06	0.41
16.0	5 10^5	-10.3	-9.1	-3.4	2.15	0.47	0.22
16.0	1 10^6	-10.4	-9.1	-3.4	2.13	0.29	0.14
26.0	1 10^3	-8.5	-8.3	-3.5	12.27	14.21	1.16
26.0	5 10^3	-9.0	-8.4	-3.4	7.31	7.17	0.98
26.0	1 10^4	-9.2	-8.4	-3.4	7.04	5.74	0.82
26.0	5 10^4	-9.6	-8.6	-3.4	6.23	3.45	0.55
26.0	1 10^5	-9.7	-8.8	-3.4	5.44	2.68	0.49
26.0	5 10^5	-10.0	-9.0	-3.4	4.41	1.18	0.27
26.0	1 10^6	-10.2	-8.9	-3.4	4.47	0.73	0.16
40.0	1 10^3	-8.3	-8.2	-3.4	13.13	16.13	1.23
40.0	5 10^3	-8.9	-8.3	-3.4	8.45	9.27	1.10
40.0	1 10^4	-9.1	-8.3	-3.4	8.37	8.09	0.97
40.0	5 10^4	-9.5	-8.5	-3.4	8.38	5.76	0.69
40.0	1 10^5	-9.6	-8.7	-3.4	7.86	4.64	0.59
40.0	5 10^5	-10.0	-8.9	-3.3	6.96	2.10	0.30
40.0	1 10^6	-10.1	-8.9	-3.3	7.22	1.32	0.18
50.0	1 10^3	-8.3	-8.2	-3.4	13.42	17.11	1.27
50.0	5 10^3	-8.8	-8.3	-3.4	8.91	10.28	1.15
50.0	1 10^4	-9.0	-8.3	-3.4	8.94	9.28	1.04
50.0	5 10^4	-9.4	-8.5	-3.4	9.40	7.14	0.76
50.0	1 10^5	-9.6	-8.7	-3.4	9.10	5.88	0.65
50.0	5 10^5	-9.9	-8.9	-3.3	8.51	2.71	0.32
50.0	1 10^6	-10.1	-8.8	-3.3	8.92	1.72	0.19

Christof Buchbender

Curriculum Vitae

Personal data

Nationality   German

Date of birth   10 January 1983

Education

2009–present   **PhD student**, *University of Granada and IRAM*, Granada, Spain.

2003–2009   **Study of Physics – Diplom**, *Rheinische Friedrich-Wilhelms-Universität*, Bonn, Germany.

1993–2002   **A-levels**, *Jugenddorf-Christophorusschule*, Königswinter,Germany.

Diploma thesis

Title   *An indepth study of the interstellar medium in the barred spiral galaxy NGC3627*

Advisor   Prof. Dr. Karl Menten; Dr. Axel Weiss; Max Planck Institute for Radioastronomy, Bonn

Experience

2009–2013   **Astronomer on Duty**, *IRAM 30m telescope*, Granada, Spain.

2009/2011   **Teaching Assistent**, *5th & 6th IRAM Summer School*, Pradollano, Spain.

2006–2007   **Student Assistent**, *Max-Planck-Institute for Radioastronomy*, Bonn, Germany.

2007   **„Taiwan Summer Institute Program"**, *Academia Sinica Institute for Astronomy and Astrophysics*, Taiwan, Taipeh.
- Two-Month Internship funded by the „German Academic Exchange Service" (DAAD) and the „National Science Council" (NSC) of Taiwan.
- Project: „Detection of new brown dwarf candidates using proper motion measurements"

Conferences and scientific schools

Contributed Talk   **"Dense Gas and Dust in M 33"**, *21th UCL Colloquium*, Cumberland Lodge, Windsor, England, 5–8th July, 2010.
Buchbender, C.; Kramer, C.; Gonzalez-Garcia, M.

Poster   **"Dense Gas and Star Formation Along the Major Axis of M33 (HERM33ES)"**, *The Molecular Universe, 280th Symposium of the IAU*, Toledo, 30th May – 3rd June.
Buchbender, C.; Kramer, C.; Rosolowsky, E.

Participant   **"7th IRAM Interferometry School"**, *IRAM*, Grenoble, France, 4–8th October 2010.

Publication list

Buchbender, C., C. Kramer, et al. "Dense gas in M 33 (HerM33es)". In: *A&A* 549, A17 (Jan. 2013), A17.

Kramer, C., **Buchbender, C.**, et al. "PACS and SPIRE photometer maps of M 33: First results of the HERschel M 33 Extended Survey (HERM33ES)". In: *A&A* 518, L67 (July 2010), p. L67.

Mookerjea, B., C. Kramer, **Buchbender, C.**, et al. "The Herschel M 33 extended survey (HerM33es): PACS spectroscopy of the star-forming region BCLMP 302". In: *A&A* 532, A152 (Aug. 2011), A152.

Xilouris, E. M., F. S. Tabatabaei, M. Boquien, C. Kramer, **Buchbender, C.**, et al. "Cool and warm dust emission from M 33 (HerM33es)". In: *A&A* 543, A74 (July 2012), A74.

Saintonge, A., G. Kauffmann, J. Wang, C. Kramer, L. J. Tacconi, **Buchbender, C.**, et al. "COLD GASS, an IRAM legacy survey of molecular gas in massive galaxies - II. The non-universality of the molecular gas depletion time-scale". In: *mnras* 415 (July 2011), pp. 61–76.

Saintonge, A., G. Kauffmann, C. Kramer, L. J. Tacconi, **Buchbender, C.**, et al. "COLD GASS, an IRAM legacy survey of molecular gas in massive galaxies - I. Relations between H_2, H I, stellar content and structural properties". In: *mnras* 415 (July 2011), pp. 32–60.

Braine, J., P. Gratier, C. Kramer, E. M. Xilouris, E. Rosolowsky, **Buchbender, C.**, et al. "Cool gas and dust in M 33: Results from the HERschel M 33 Extended Survey (HERM33ES)". In: *A&A* 518, L69 (July 2010), p. L69.

Combes, F., M. Boquien, C. Kramer, E. M. Xilouris, F. Bertoldi, J. Braine, **Buchbender, C.**, et al. "Dust and gas power spectrum in M 33 (HERM33ES)". In: *A&A* 539, A67 (Mar. 2012), A67.

Boquien, M., D. Calzetti, C. Kramer, E. M. Xilouris, F. Bertoldi, J. Braine, **Buchbender, C.**, et al. "100 μm and 160 μm emission as resolved star-formation rate estimators in M 33 (HERM33ES)". In: *A&A* 518, L70 (July 2010), p. L70.

Verley, S., M. Relaño, C. Kramer, E. M. Xilouris, M. Boquien, D. Calzetti, F. Combes, **Buchbender, C.**, et al. "Properties of compact 250 μm emission and H II regions in M 33 (HERM33ES)". In: *A&A* 518, L68 (July 2010), p. L68.

Kramer, C., J. Abreu-Vicente, S. García-Burillo, M. Relaño, S. Aalto, M. Boquien, J. Braine, **Buchbender, C.**, et al. "Gas and dust cooling along the major axis of M 33 (HerM33es). ISO/LWS [C ii] observations". In: *A&A* 553, A114 (May 2013), A114.

Relaño, M., S. Verley, I. Pérez, C. Kramer, D. Calzetti, E. M. Xilouris, M. Boquien, J. Abreu-Vicente, F. Combes, F. Israel, F. S. Tabatabaei, J. Braine, **Buchbender, C.**, et al. "Spectral energy distributions of H ii regions in M 33 (HerM33es)". In: *A&A* 552, A140 (Apr. 2013), A140.

List of Figures

List of Tables

Bibliography

Aalto, S. 2004, in Astronomical Society of the Pacific Conference Series, Vol. 320, The Neutral ISM in Starburst Galaxies, ed. S. Aalto, S. Huttemeister, & A. Pedlar, 3–14

Aalto, S., Booth, R. S., Black, J. H., & Johansson, L. E. B. 1995, A&A, 300, 369

Aalto, S., Polatidis, A. G., Hüttemeister, S., & Curran, S. J. 2002, A&A, 381, 783

Abel, N. P., Ferland, G. J., Shaw, G., & van Hoof, P. A. M. 2005, ApJS, 161, 65

Agladze, N. I., Sievers, A. J., Jones, S. A., Burlitch, J. M., & Beckwith, S. V. W. 1996, ApJ, 462, 1026

Asplund, M., Grevesse, N., Sauval, A. J., & Scott, P. 2009, ARA&A, 47, 481

Baan, W. A., Henkel, C., Loenen, A. F., Baudry, A., & Wiklind, T. 2008, A&A, 477, 747

Baan, W. A., Loenen, A. F., & Spaans, M. 2010, A&A, 516, A40+

Banwell, C. 1983, Fundamentals of Molecular Spectroscopy (McGraw-Hill)

Barvainis, R., Maloney, P., Antonucci, R., & Alloin, D. 1997, ApJ, 484, 695

Bedin, L. R., Piotto, G., Baume, G., et al. 2005, A&A, 444, 831

Bekki, K. 2008, MNRAS, 390, L24

Bell, T. A., Viti, S., Williams, D. A., Crawford, I. A., & Price, R. J. 2005, MNRAS, 357, 961

Benjamin, R. A., Churchwell, E., Babler, B. L., et al. 2005, ApJ, 630, L149

Bensch, F., Leuenhagen, U., Stutzki, J., & Schieder, R. 2003, ApJ, 591, 1013

Bevington, P. R. & Robinson, D. K. 1992, Data reduction and error analysis for the physical sciences (McGraw-Hill)

Black, J. H. & van Dishoeck, E. F. 1987, ApJ, 322, 412

Blitz, L. 1993, in Protostars and Planets III, ed. E. H. Levy & J. I. Lunine, 125–161

Boger, G. I. & Sternberg, A. 2005, ApJ, 632, 302

Bohlin, R. C., Savage, B. D., & Drake, J. F. 1978, ApJ, 224, 132

Boissier, S., Prantzos, N., Boselli, A., & Gavazzi, G. 2003, MNRAS, 346, 1215

Böker, T., Laine, S., van der Marel, R. P., et al. 2002, AJ, 123, 1389

Bolatto, A. D., Jackson, J. M., & Ingalls, J. G. 1999, ApJ, 513, 275

Bolatto, A. D., Leroy, A. K., Rosolowsky, E., Walter, F., & Blitz, L. 2008, ApJ, 686, 948

Bolatto, A. D., Wolfire, M., & Leroy, A. K. 2013, ARA&A, 51, 207

Boquien, M., Calzetti, D., Combes, F., et al. 2011, AJ, 142, 111

Boquien, M., Calzetti, D., Kramer, C., et al. 2010, A&A, 518, L70

Born, M. & Wolf, E. 1980, Principles of Optics: Electromagnetic Theory of Propagation, Interference and Diffraction of Light (Cambridge University Press)

Boselli, A., Ciesla, L., Cortese, L., et al. 2012, A&A, 540, A54

Boudet, N., Mutschke, H., Nayral, C., et al. 2005, ApJ, 633, 272

Boulesteix, J., Courtes, G., Laval, A., Monnet, G., & Petit, H. 1974, A&A, 37, 33

Braine, J., Gratier, P., Kramer, C., et al. 2012, A&A, 544, A55

Braine, J., Gratier, P., Kramer, C., et al. 2010, A&A, 520, A107

Brouillet, N., Muller, S., Herpin, F., Braine, J., & Jacq, T. 2005, A&A, 429, 153

Brown, J. & Carrington, A. 2003, Rotational Spectroscopy of Diatomic Molecules, Cambridge Molecular Science (Cambridge University Press)

Brunthaler, A., Reid, M. J., Falcke, H., Greenhill, L. J., & Henkel, C. 2005, Science, 307, 1440

Brunthaler, A., Reid, M. J., Menten, K. M., et al. 2011, Astronomische Nachrichten, 332, 461

Buchbender, C. 2009, Diplomarbeit, Rheinische-Friedrich-Wilhelms-Universität Bonn

Buchbender, C., Kramer, C., Gonzalez-Garcia, M., et al. 2013, A&A, 549, A17

Burgh, E. B., France, K., & Jenkins, E. B. 2010, ApJ, 708, 334

Calzetti, D., Kennicutt, R. C., Engelbracht, C. W., et al. 2007, ApJ, 666, 870

Casoli, F., Dupraz, C., & Combes, F. 1992, A&A, 264, 55

Chapin, E. L., Chapman, S. C., Coppin, K. E., et al. 2011, MNRAS, 411, 505

Chin, Y.-N., Henkel, C., Millar, T. J., Whiteoak, J. B., & Marx-Zimmer, M. 1998, A&A, 330, 901

Chin, Y.-N., Henkel, C., Millar, T. J., Whiteoak, J. B., & Mauersberger, R. 1996, A&A, 312, L33

Chin, Y.-N., Henkel, C., Whiteoak, J. B., et al. 1997, A&A, 317, 548

Christopher, M. H., Scoville, N. Z., Stolovy, S. R., & Yun, M. S. 2005, ApJ, 622, 346

Churchwell, E., Nash, A. G., & Walmsley, C. M. 1984, ApJ, 287, 681

Colin, J. & Athanassoula, E. 1981, A&A, 97, 63

Compiègne, M., Abergel, A., Verstraete, L., & Habart, E. 2008, A&A, 491, 797

Corbelli, E. 2003, MNRAS, 342, 199

Corbelli, E. & Salucci, P. 2000, MNRAS, 311, 441

Corbelli, E., Schneider, S. E., & Salpeter, E. E. 1989, AJ, 97, 390

Corbelli, E. & Walterbos, R. A. M. 2007, ApJ, 669, 315

Costagliola, F., Aalto, S., Rodriguez, M. I., et al. 2011, A&A, 528, A30+

Curran, S. J., Polatidis, A. G., Aalto, S., & Booth, R. S. 2001a, A&A, 368, 824

Curran, S. J., Polatidis, A. G., Aalto, S., & Booth, R. S. 2001b, A&A, 373, 459

Dale, D. A., Helou, G., Contursi, A., Silbermann, N. A., & Kolhatkar, S. 2001, ApJ, 549, 215

Dame, T. M., Hartmann, D., & Thaddeus, P. 2001, ApJ, 547, 792

de Boer. 2007, Physics and the Intersellar Medium; Lecture notes (Rheinische Friedrich-Wilhelms-Universität, Bonn)

de Vaucouleurs, G. 1959, Handbuch der Physik, 53, 275

de Vaucouleurs, G., de Vaucouleurs, A., Corwin, Jr., H. G., et al. 1991, Third Reference Catalogue of Bright Galaxies (Springer)

Dickman, R. L., Snell, R. L., & Schloerb, F. P. 1986, ApJ, 309, 326

Draine, B. T. 1978, ApJS, 36, 595

Draine, B. T. 2003, ARA&A, 41, 241

Draine, B. T. 2011, Physics of the Interstellar and Intergalactic Medium (Princeton University Press)

Draine, B. T., Dale, D. A., Bendo, G., et al. 2007, ApJ, 663, 866

Draine, B. T. & Li, A. 2007, ApJ, 657, 810

Dunne, L. & Eales, S. A. 2001, MNRAS, 327, 697

Elitzur, M. 1983, ApJ, 267, 174

Evans, II, N. J. 1999, ARA&A, 37, 311

Ferland, G. J., Korista, K. T., Verner, D. A., et al. 1998, PASP, 110, 761

Fixsen, D. J. 2009, ApJ, 707, 916

Freedman, W. L., Wilson, C. D., & Madore, B. F. 1991, ApJ, 372, 455

Frerking, M. A., Langer, W. D., & Wilson, R. W. 1982, ApJ, 262, 590

Galleti, S., Bellazzini, M., & Ferraro, F. R. 2004, A&A, 423, 925

Galliano, F., Madden, S. C., Jones, A. P., Wilson, C. D., & Bernard, J.-P. 2005, A&A, 434, 867

Gao, Y., Carilli, C. L., Solomon, P. M., & Vanden Bout, P. A. 2007, ApJ, 660, L93

Gao, Y. & Solomon, P. M. 2004a, ApJS, 152, 63

Gao, Y. & Solomon, P. M. 2004b, ApJ, 606, 271

García-Burillo, S., Usero, A., Alonso-Herrero, A., et al. 2012, A&A, 539, A8

Gardan, E., Braine, J., Schuster, K. F., Brouillet, N., & Sievers, A. 2007, A&A, 473, 91

Genzel, R., Tacconi, L. J., Gracia-Carpio, J., et al. 2010, MNRAS, 407, 2091

Gil de Paz, A., Boissier, S., Madore, B. F., et al. 2007, ApJS, 173, 185

Godard, B., Falgarone, E., Gerin, M., Hily-Blant, P., & de Luca, M. 2010, A&A, 520, A20

Goldsmith, P. F. 2001, ApJ, 557, 736

González Delgado, R. M. & Pérez, E. 2000, MNRAS, 317, 64

Gonzalez Garcia, M., Le Bourlot, J., Le Petit, F., & Roueff, E. 2008, A&A, 485, 127

Graciá-Carpio, J., García-Burillo, S., & Planesas, P. 2008a, Ap&SS, 313, 331

Graciá-Carpio, J., García-Burillo, S., & Planesas, P. 2008b, Ap&SS, 313, 331

Graciá-Carpio, J., García-Burillo, S., Planesas, P., & Colina, L. 2006, ApJ, 640, L135

Gratier, P., Braine, J., Rodriguez-Fernandez, N. J., et al. 2012, A&A, 542, A108

Gratier, P., Braine, J., Rodriguez-Fernandez, N. J., et al. 2010, A&A, 522, A3

Grebel, E. K. 2001, in Astronomical Society of the Pacific Conference Series, Vol. 239, Microlensing 2000: A New Era of Microlensing Astrophysics, ed. J. W. Menzies & P. D. Sackett, 280

Greve, T. R., Papadopoulos, P. P., Gao, Y., & Radford, S. J. E. 2009, ApJ, 692, 1432

Guélin, M., Salomé, P., Neri, R., et al. 2007, A&A, 462, L45

Habing, H. J. 1968, Bull. Astron. Inst. Netherlands, 19, 421

Heikkilä, A., Johansson, L. E. B., & Olofsson, H. 1999, A&A, 344, 817

Helfer, T. T. & Blitz, L. 1997, ApJ, 478, 233

Helou, G., Khan, I. R., Malek, L., & Boehmer, L. 1988, ApJS, 68, 151

Henry, R. B. C., Edmunds, M. G., & Köppen, J. 2000, ApJ, 541, 660

Heyer, M. H., Corbelli, E., Schneider, S. E., & Young, J. S. 2004, ApJ, 602, 723

Hippelein, H., Haas, M., Tuffs, R. J., et al. 2003, A&A, 407, 137

Hogerheijde, M. R. & Sandell, G. 2000, ApJ, 534, 880

Hollenbach, D. J. & Tielens, A. G. G. M. 1999, Reviews of Modern Physics, 71, 173

Hoopes, C. G. & Walterbos, R. A. M. 2000, ApJ, 541, 597

Hubble, E. P. 1926, ApJ, 64, 321

Huettemeister, S., Henkel, C., Mauersberger, R., et al. 1995, A&A, 295, 571

Humphreys, R. M. & Sandage, A. 1980, ApJS, 44, 319

Hunter, I., Dufton, P. L., Smartt, S. J., et al. 2007, A&A, 466, 277

Imanishi, M., Nakanishi, K., & Kohno, K. 2006, AJ, 131, 2888

Imanishi, M., Nakanishi, K., Tamura, Y., Oi, N., & Kohno, K. 2007, AJ, 134, 2366

Irvine, W. M. 1987, in IAU Symposium, Vol. 120, Astrochemistry, ed. M. S. Vardya & S. P. Tarafdar, 245–251

Israel, F. P. 1997, A&A, 328, 471

Jackson, J. M., Heyer, M. H., Paglione, T. A. D., & Bolatto, A. D. 1996, ApJ, 456, L91+

Jansen, D. J., van Dishoeck, E. F., Black, J. H., Spaans, M., & Sosin, C. 1995, A&A, 302, 223

Johansson, L. E. B., Olofsson, H., Hjalmarson, A., Gredel, R., & Black, J. H. 1994, A&A, 291, 89

Juvela, M. & Ysard, N. 2012, A&A, 541, A33

Kamp, I. & Bertoldi, F. 2000, A&A, 353, 276

Kamp, I. & van Zadelhoff, G.-J. 2001, A&A, 373, 641

Kaufman, M. J., Wolfire, M. G., Hollenbach, D. J., & Luhman, M. L. 1999, ApJ, 527, 795

Kelly, B. C., Shetty, R., Stutz, A. M., et al. 2012, ApJ, 752, 55

Kennicutt, R. C., Calzetti, D., Aniano, G., et al. 2011, PASP, 123, 1347

Kennicutt, R. C. & Evans, N. J. 2012, ARA&A, 50, 531

Kennicutt, Jr., R. C. 1998, in Astronomical Society of the Pacific Conference Series, Vol. 142, The Stellar Initial Mass Function (38th Herstmonceux Conference), ed. G. Gilmore & D. Howell, 1

Kennicutt, Jr., R. C. 2008, in Astronomical Society of the Pacific Conference Series, Vol. 381, Infrared Diagnostics of Galaxy Evolution, ed. R.-R. Chary, H. I. Teplitz, & K. Sheth, 103

Kennicutt, Jr., R. C., Armus, L., Bendo, G., et al. 2003, PASP, 115, 928

Kewley, L. J., Geller, M. J., Jansen, R. A., & Dopita, M. A. 2002, AJ, 124, 3135

Klein, B., Philipp, S. D., Krämer, I., et al. 2006, A&A, 454, L29

Klein, U. 2006, Lecture Notes: Radio Astronomy: tools, applications and impacts (Rheinische Friedrich-Wilhelms-Universität, Bonn)

Knudsen, K. K., Walter, F., Weiss, A., et al. 2007, ApJ, 666, 156

Kohno, K. 2005, in American Institute of Physics Conference Series, Vol. 783, The Evolution of Starbursts, ed. S. Hüttmeister, E. Manthey, D. Bomans, & K. Weis, 203–208

Kramer, C., Buchbender, C., Xilouris, E. M., et al. 2010, A&A, 518, L67+

Krips, M., Neri, R., García-Burillo, S., et al. 2008, ApJ, 677, 262

Krügel, E. 2003, The physics of interstellar dust (The physics of interstellar dust, by Endrik Kruegel. IoP Series in astronomy and astrophysics, ISBN 0750308613. Bristol, UK: The Institute of Physics, 2003.)

Krügel, E. & Siebenmorgen, R. 1994, A&A, 288, 929

Krumholz, M. R. & McKee, C. F. 2005, ApJ, 630, 250

Kuno, N., Nakai, N., Handa, T., & Sofue, Y. 1995, PASJ, 47, 745

Langer, W. D. & Penzias, A. A. 1993, ApJ, 408, 539

Lauer, T. R., Faber, S. M., Ajhar, E. A., Grillmair, C. J., & Scowen, P. A. 1998, AJ, 116, 2263

Le Bourlot, J., Pineau Des Forets, G., Roueff, E., & Flower, D. R. 1993, A&A, 267, 233

Le Petit, F., Nehmé, C., Le Bourlot, J., & Roueff, E. 2006, ApJS, 164, 506

Lee, H.-H., Herbst, E., Pineau des Forets, G., Roueff, E., & Le Bourlot, J. 1996, A&A, 311, 690

Leroy, A. K., Bolatto, A., Bot, C., et al. 2009, ApJ, 702, 352

Leroy, A. K., Bolatto, A., Gordon, K., et al. 2011, ApJ, 737, 12

Leroy, A. K., Walter, F., Brinks, E., et al. 2008, AJ, 136, 2782

Leroy, A. K., Walter, F., Sandstrom, K., et al. 2013, AJ, 146, 19

Liszt, H. S., Pety, J., & Lucas, R. 2010, A&A, 518, A45

Liu, L. & Gao, Y. 2012, Science China Physics, Mechanics and Astronomy, Volume 55, Issue 2, pp.347-353, 55, 347

Liu, X.-L., Wang, J.-J., & Xu, J.-L. 2013, MNRAS, 431, 27

Lockman, F. J., Free, N. L., & Shields, J. C. 2012, AJ, 144, 52

Loenen, A. F., Spaans, M., Baan, W. A., & Meijerink, R. 2008, in EAS Publications Series, Vol. 31, EAS Publications Series, ed. C. Kramer, S. Aalto, & R. Simon, 183–185

Ma, B., Tan, J. C., & Barnes, P. J. 2012, ArXiv e-prints

Macri, L. M., Stanek, K. Z., Bersier, D., Greenhill, L. J., & Reid, M. J. 2006, ApJ, 652, 1133

Magrini, L., Stanghellini, L., Corbelli, E., Galli, D., & Villaver, E. 2010, A&A, 512, A63+

Magrini, L., Vílchez, J. M., Mampaso, A., Corradi, R. L. M., & Leisy, P. 2007, A&A, 470, 865

Maíz-Apellániz, J., Pérez, E., & Mas-Hesse, J. M. 2004, AJ, 128, 1196

Maloney, P. & Black, J. H. 1988, ApJ, 325, 389

Martin, D. C., Fanson, J., Schiminovich, D., et al. 2005, ApJ, 619, L1

Martín, S., Mauersberger, R., Martín-Pintado, J., Henkel, C., & García-Burillo, S. 2006, ApJS, 164, 450

Mateo, M. L. 1998, ARA&A, 36, 435

McConnachie, A. W., Irwin, M. J., Ibata, R. A., et al. 2009, Nature, 461, 66

McKee, C. F. & Ostriker, E. C. 2007, ARA&A, 45, 565

Meier, D. S. & Turner, J. L. 2005, ApJ, 618, 259

Meier, D. S. & Turner, J. L. 2012, ApJ, 755, 104

Meijerink, R. & Spaans, M. 2005, A&A, 436, 397

Meijerink, R., Spaans, M., & Israel, F. P. 2007, A&A, 461, 793

Minniti, D., Olszewski, E. W., & Rieke, M. 1993, ApJ, 410, L79

Miura, R., Okumura, S. K., Tosaki, T., et al. 2010, ApJ, 724, 1120

Mookerjea, B., Kramer, C., Buchbender, C., et al. 2011, A&A, 532, A152+

Müller, H. S. P., Schlöder, F., Stutzki, J., & Winnewisser, G. 2005, Journal of Molecular Structure, 742, 215

Müller, H. S. P., Thorwirth, S., Roth, D. A., & Winnewisser, G. 2001, A&A, 370, L49

Murphy, E. J., Condon, J. J., Schinnerer, E., et al. 2011, ApJ, 737, 67

Murray, N. 2011, ApJ, 729, 133

Omont, A. 2007, Reports on Progress in Physics, 70, 1099

Onodera, S., Kuno, N., Tosaki, T., et al. 2010, ApJ, 722, L127

Padovani, M., Walmsley, C. M., Tafalla, M., Galli, D., & Müller, H. S. P. 2009, A&A, 505, 1199

Papadopoulos, P. P. 2007, ApJ, 656, 792

Papadopoulos, P. P., Thi, W.-F., & Viti, S. 2002, ApJ, 579, 270

Paradis, D., Bernard, J.-P., & Mény, C. 2009, A&A, 506, 745

Paradis, D., Bernard, J.-P., Mény, C., & Gromov, V. 2011, A&A, 534, A118

Paturel, G., Petit, C., Prugniel, P., et al. 2003, A&A, 412, 45

Peres, G., Reale, F., Collura, A., & Fabbiano, G. 1989, ApJ, 336, 140

Pietsch, W., Misanovic, Z., Haberl, F., et al. 2004a, A&A, 426, 11

Pietsch, W., Mochejska, B. J., Misanovic, Z., et al. 2004b, A&A, 413, 879

Planck Collaboration, Ade, P. A. R., Aghanim, N., et al. 2011, A&A, 536, A16

Polk, K. S., Knapp, G. R., Stark, A. A., & Wilson, R. W. 1988, ApJ, 332, 432

Putman, M. E., Peek, J. E. G., Muratov, A., et al. 2009, ApJ, 703, 1486

Regan, M. W. & Vogel, S. N. 1994, ApJ, 434, 536

Reid, M. J., Menten, K. M., Zheng, X. W., et al. 2009, ApJ, 700, 137

Rice, W., Boulanger, F., Viallefond, F., Soifer, B. T., & Freedman, W. L. 1990, ApJ, 358, 418

Riechers, D. A., Walter, F., Carilli, C. L., et al. 2011, ApJ, 726, 50

Riquelme, D., Bronfman, L., Mauersberger, R., May, J., & Wilson, T. L. 2010, A&A, 523, A45

Rohlfs, K. & Wilson, T. L. 2000, Tools of Radio Astronomy (K. Rohlfs, T.L. Wilson. New York : Springer, 2000. (Astronomy and Astrophysics library, ISSN0941-7834))

Röllig, M., Abel, N. P., Bell, T., et al. 2007, A&A, 467, 187

Röllig, M., Ossenkopf, V., Jeyakumar, S., Stutzki, J., & Sternberg, A. 2006, A&A, 451, 917

Rosolowsky, E., Pineda, J. E., & Gao, Y. 2011, MNRAS, 415, 1977

Sánchez, N., Añez, N., Alfaro, E. J., & Crone Odekon, M. 2010, ApJ, 720, 541

Sandage, A. 1975, Classification and Stellar Content of Galaxies Obtained from Direct Photography, ed. A. Sandage, M. Sandage, & J. Kristian (the University of Chicago Press), 1

Schilke, P., Walmsley, C. M., Pineau Des Forets, G., et al. 1992, A&A, 256, 595

Schmidt, M. 1959, ApJ, 129, 243

Schöier, F. L., van der Tak, F. F. S., van Dishoeck, E. F., & Black, J. H. 2005, A&A, 432, 369

Seale, J. P., Looney, L. W., Wong, T., et al. 2012, ApJ, 751, 42

Seaquist, E. R. & Frayer, D. T. 2000, ApJ, 540, 765

Shaw, G., Ferland, G. J., Abel, N. P., Stancil, P. C., & van Hoof, P. A. M. 2005, ApJ, 624, 794

Shu, F. H., Adams, F. C., & Lizano, S. 1987, ARA&A, 25, 23

Simón-Díaz, S. & Stasińska, G. 2011, A&A, 526, A48

Snow, T. P. & McCall, B. J. 2006, ARA&A, 44, 367

Solomon, P., Vanden Bout, P., Carilli, C., & Guelin, M. 2003, Nature, 426, 636

Solomon, P. M., Rivolo, A. R., Barrett, J., & Yahil, A. 1987, ApJ, 319, 730

Sparke, L. S. & Gallagher, III, J. S. 2000, Galaxies in the universe : an introduction (Cambridge University Press)

Stäuber, P., Doty, S. D., van Dishoeck, E. F., & Benz, A. O. 2005, A&A, 440, 949

Sternberg, A. & Dalgarno, A. 1989, ApJ, 338, 197

Sternberg, A. & Dalgarno, A. 1995, ApJS, 99, 565

Stoerzer, H., Stutzki, J., & Sternberg, A. 1996, A&A, 310, 592

Tabatabaei, F. S., Beck, R., Krause, M., et al. 2007, A&A, 466, 509

Takano, M., Mitsuda, K., Fukazawa, Y., & Nagase, F. 1994, ApJ, 436, L47

Tammann, G. A., Loeffler, W., & Schroeder, A. 1994, ApJS, 92, 487

Tan, Q.-H., Gao, Y., Zhang, Z.-Y., & Xia, X.-Y. 2011, Research in Astronomy and Astrophysics, 11, 787

Taylor, J. R. 1996, An Introduction to Error Analysis: The Study of Uncertainties in Physical Measurements, 2nd edn. (University Science Books)

Taylor, S. D., Hartquist, T. W., & Williams, D. A. 1993, MNRAS, 264, 929

Thilker, D. A., Hoopes, C. G., Bianchi, L., et al. 2005, ApJ, 619, L67

Thompson, A., Moran, J., & George W. Swenson, J. 1986, Interferometry and Synthesis in Radio Astronomy (John Wiley & Sons)

Tielens, A. 2005, The Physics and Chemistry of the Interstellar Medium (Cambridge University Press)

Tielens, A. G. G. M. & Hollenbach, D. 1985, ApJ, 291, 722

Turner, B. E. 2000, ApJ, 542, 837

Turner, B. E., Pirogov, L., & Minh, Y. C. 1997, ApJ, 483, 235

Usero, A., García-Burillo, S., Fuente, A., Martín-Pintado, J., & Rodríguez-Fernández, N. J. 2004, A&A, 419, 897

Valsecchi, F., Glebbeek, E., Farr, W. M., et al. 2010, Nature, 468, 77

van den Bergh, S. 2000, The Galaxies of the Local Group (Cambridge)

van den Bergh, S. 2003, ArXiv Astrophysics e-prints

van der Marel, R. P., Besla, G., Cox, T. J., Sohn, S. T., & Anderson, J. 2012, ApJ, 753, 9

van der Tak, F. F. S., Black, J. H., Schöier, F. L., Jansen, D. J., & van Dishoeck, E. F. 2007, A&A, 468, 627

van Dishoeck, E. F. & Black, J. H. 1988, ApJ, 334, 771

Verley, S., Hunt, L. K., Corbelli, E., & Giovanardi, C. 2007, A&A, 476, 1161

Verley, S., Relaño, M., Kramer, C., et al. 2010, A&A, 518, L68

Wall, W. F. 2007, MNRAS, 379, 674

Walter, F., Brinks, E., de Blok, W. J. G., et al. 2008, AJ, 136, 2563

Wang, M., Henkel, C., Chin, Y.-N., et al. 2004, A&A, 422, 883

Weiss, A. 2000, PhD thesis, Rheinische-Friedrich-Wilhelms-Universität Bonn

Weiß, A., Kovács, A., Güsten, R., et al. 2008, A&A, 490, 77

Weiß, A., Neininger, N., Hüttemeister, S., & Klein, U. 2001, A&A, 365, 571

Weng, S.-S., Wang, J.-X., Gu, W.-M., & Lu, J.-F. 2009, PASJ, 61, 1287

Wilson, T. L. 1999, Reports on Progress in Physics, 62, 143

Wilson, T. L., Rohlfs, K., & Hüttemeister, S. 2009, Tools of Radio Astronomy (Springer-Verlag)

Wolfire, M. G., McKee, C. F., Hollenbach, D., & Tielens, A. G. G. M. 2003, ApJ, 587, 278

Wootten, A., Evans, II, N. J., Snell, R., & vanden Bout, P. 1978, ApJ, 225, L143

Wu, J., Evans, II, N. J., Gao, Y., et al. 2005, ApJ, 635, L173

Wu, J., Evans, II, N. J., Shirley, Y. L., & Knez, C. 2010, ApJS, 188, 313

Xie, T., Allen, M., & Langer, W. D. 1995, ApJ, 440, 674

Xilouris, E. M., Tabatabaei, F. S., Boquien, M., et al. 2012, A&A, 543, A74

Ysard, N., Juvela, M., Demyk, K., et al. 2012, A&A, 542, A21

Zaritsky, D., Elston, R., & Hill, J. M. 1989, AJ, 97, 97

Zielinsky, M. 1999, PhD thesis, Universität zu Köln